Mukhdeep Singh Manshahia
Valeriy Kharchenko
Gerhard-Wilhelm Weber
Pandian Vasant *Editors*

Advances in Artificial Intelligence for Renewable Energy Systems and Energy Autonomy

EAI

RESEARCH MEETS INNOVATION

Springer

EAI/Springer Innovations in Communication and Computing

The impact of information technologies is creating a new world yet not fully understood. The extent and speed of economic, life style and social changes already perceived in everyday life is hard to estimate without understanding the technological driving forces behind it. This series presents contributed volumes featuring the latest research and development in the various information engineering technologies that play a key role in this process. The range of topics, focusing primarily on communications and computing engineering include, but are not limited to, wireless networks; mobile communication; design and learning; gaming; interaction; e-health and pervasive healthcare; energy management; smart grids; internet of things; cognitive radio networks; computation; cloud computing; ubiquitous connectivity, and in mode general smart living, smart cities, Internet of Things and more. The series publishes a combination of expanded papers selected from hosted and sponsored European Alliance for Innovation (EAI) conferences that present cutting edge, global research as well as provide new perspectives on traditional related engineering fields. This content, complemented with open calls for contribution of book titles and individual chapters, together maintain Springer's and EAI's high standards of academic excellence. The audience for the books consists of researchers, industry professionals, advanced level students as well as practitioners in related fields of activity include information and communication specialists, security experts, economists, urban planners, doctors, and in general representatives in all those walks of life affected ad contributing to the information revolution.

Indexing: This series is indexed in Scopus, Ei Compendex, and zbMATH.

About EAI - EAI is a grassroots member organization initiated through cooperation between businesses, public, private and government organizations to address the global challenges of Europe's future competitiveness and link the European Research community with its counterparts around the globe. EAI reaches out to hundreds of thousands of individual subscribers on all continents and collaborates with an institutional member base including Fortune 500 companies, government organizations, and educational institutions, provide a free research and innovation platform. Through its open free membership model EAI promotes a new research and innovation culture based on collaboration, connectivity and recognition of excellence by community.

Mukhdeep Singh Manshahia • Valeriy Kharchenko •
Gerhard-Wilhelm Weber • Pandian Vasant
Editors

Advances in Artificial Intelligence for Renewable Energy Systems and Energy Autonomy

Springer

EAI
RESEARCH MEETS INNOVATION

Editors
Mukhdeep Singh Manshahia 🆔
Department of Mathematics
Punjabi University Patiala
Patiala, Punjab, India

Valeriy Kharchenko 🆔
Federal Scientific Agroengineering
Center VIM
Moscow, Russia

Gerhard-Wilhelm Weber 🆔
Institute of Applied Mathematics
Middle East Technical University
Ankara, Turkey

Pandian Vasant 🆔
Ton Duc Thang University
Ho Chi Minh City, Vietnam

Dedicated to
Green Earth

Foreword

During the past decade, different analytical tools of applied mathematics, data science, information science, and statistics have gained the attention of numerous researchers and practitioners from all over the world, providing a strong impact on information technology, finance, engineering, and computer science applications. The purpose of this book, *Advances in Artificial Intelligence for Renewable Energy Systems and Energy Autonomy*, is to inquire, reflect, and comprehensively expose the rapidly growing field of artificial intelligence (AI) research in the important field of investigation and high-performance facilities for original, innovative, and novel real-world applications in the modern world and the area of renewable energy.

Nowadays, artificial intelligence and Internet of Things (IoT) are two burgeoning technologies, full of promise for businesses in all industries. However, the real potential of these two technologies is probably their convergence, which would lead to a new paradigm of information and knowledge. These technologies are standing on the frontline of technological and scientific enhancements that represent real and potential transitions within smart and sustainable living. While environmental issues and the need for new managerial concepts remain at the forefront of operational research, renewable energy has become an important area of study. Moreover, while smart technology continues to rise while being refined, its applications broaden and enhance their potential impact on regime switching and paradigm shifts, and even revolutionize views and entire projects about sustainability. This potential can be fully realized only with a thorough comprehension of the most recent breakthroughs in the fields of renewable energy and energy autonomy in and of themselves.

Conventional energy sources have drawbacks, such as environmental degradation and global warming, that have led to the development of clean energy sources to satisfy power demand. Optimization and decision-making must find out and propose methods of power generation that are not only environment-friendly but also implementable with moderate complexity. The solutions should be accepted by organizations and governments. In such situations, machine learning techniques can make a big difference and emerge as a major tool in the future, as represented in this book in impressive ways.

This book, *Advances in Artificial Intelligence for Renewable Energy Systems and Energy Autonomy,* is a global innovative research compendium that explores the recent steps forward in the direction of smart applications in sustainable modern and future industries, economies, and societies. This book focuses on dealing with the most recent issues in areas that integrate smart technology, alternative energy sources, and the methods and models associated with them through mathematical optimization. This edited collection of interesting and exciting research chapters has been proposed, prepared, reviewed, and successfully completed. Covering a wide scope of themes, including machine learning applications and neural control, evolutionary algorithms, electric charging, MPPT, and ecology, this book is designed and well suited for both professionals and researchers working in the emerging areas of energy efficiency, energy saving technologies, RES-based energy supply systems, and different kinds of renewable technologies.

I express my thanks to the publishing house *EAI-Springer Publishing* and to the editors, *Prof. Dr. Mukhdeep Singh Manshahia* (Punjabi University, Patiala, India), *Prof. Valeriy Kharchenko* (Federal Scientific Agro engineering Center, VIM, Moscow, Russia), *Prof. Dr. Gerhard-Wilhelm Weber* (Poznan University of Technology, PUT, Poznan, Poland), and *Prof. Dr. Pandian Vasant* (MERLIN Research Centre, Ton Duc Thang University, Vietnam), for providing this opportunity for many experts to publish their research achievements and contributions.

I wish all of you much joy in reading this exciting work, and hope that great benefit is gained from it, both professionally and socially.

Sincerely yours,

Ex. Dean (Research & Consultancy),   Mayank Dave
National Institute of Technology, Kurukshetra India

Preface

Requirements for problem-solving are exponentially increasing in demand. New technologies in artificial intelligence (AI), data analytics, big data, and innovative optimization have reduced the dimension of data coverage worldwide. Thus, recent inventions in data science have inched toward reducing the gaps and coverage of domains. Specialized software solutions and sophisticated models have been developed to handle data quantity and diversity. In turn, this has given rise to articulated software architectures that combine diverse components and interact successfully. The digging of information in large data and soft-computing techniques has contributed to the strength of prediction, analysis, and decision potentials in niche areas, such as smart cities, renewable energy, agro-engineering, operational research, computational intelligence, data technology, engineering management, social computing, Internet of Things (IoT), and green computing. Nurturing research in data technology and smart computing will help to find the correct pattern in the ocean of data. This book covers a broad range of green energy-related topics, including the emerging fields of neuro-computational models and simulations under uncertainty, such as fuzzy-based computational models and fuzzy trace theory, stochastic neural computation, and neural/brain modeling with stochastic differential equations and stochastic regime models.

The book includes a description of a series of case studies for the investigation of new technological methods and technical means that ensure the organization of renewable energy systems with the application of the above-mentioned computerized approaches, optimization, and modeling processes that should accelerate and make cheaper the path from new ideas to their practical implementation. Definite attention has been paid to works aimed at organizing an efficient production process and social comfort in the face of scarcity of energy resources and the need to rationally use them. In general, the book is intended to represent broad public advanced achievements in the field of electro-technologies, renewable energy sources (RESs), and energy autonomy, which will be useful to a wide range of readers and have a positive impact on sustainable development.

The target audience of this book comprises professionals and researchers working in the fields of energy efficiency, energy-saving technologies, RES-based energy

supply systems, and different kinds of renewable technologies. Moreover, the book will provide insights and support executives concerned with the development of renewable energy systems in new territories and their sustainable development. The book will be useful to a wide range of persons, such as students of agro-engineering and power specialties, experts and heads of municipal unions, managers of ministries, and other organizations responsible for the development of new smart territories.

The book comprises 13 chapters, presenting recent advances in AI for renewable energy systems and energy autonomy with a variety of models, algorithms, and application domains. They represent United States, Russia, India, Ethiopia, South Africa, Vietnam, Uzbekistan, Pakistan, Ireland, Italy, and Mauritius. This worldwide representation clearly demonstrates the interest of the global research community to this book. A brief overview of the chapters is presented below:

In Chap. 1, the authors discuss various methods for calculating the electrical load of agricultural objects based on the available initial data and different options for supplying it using a solar photovoltaic system. Information on methods for calculating the electrical loads of agricultural consumers was analyzed and systematized according to the necessary initial data.

Chapter 2 proposes a radial basis function neural network (RBFNN)-based controller as a maximum power point tracker (MPPT) to extract the maximum power available from the wind. The proposed controller is used for wind turbines to produce maximum power output by adjusting the duty cycle of the converter. The control tracks the optimal rotor speed of the wind energy conversion system (WECS) to provide maximum power above and below the rated speed of the wind turbine. MATLAB/SIMULINK-based simulations provided better results in compression with FLC and MLFFNN.

Chapter 3 presents a unique configuration for the future development of an all-wheel drive (AWD)–plug-in hybrid electric vehicle (PHEV), which has a mechanical connection to both the front and rear axles. The control methodology is designed for renewable energy sources to help reduce greenhouse gas emissions from car tailpipe exhausts and contributes to the preservation of the environment, thus reducing the severity of global warming. This AWD–PHEV configuration offers optimal vehicle performance in three different driving modes [electric vehicle (EV), series, and parallel]. The chapter covers the development of the complete model for implementation of the AWD–PHEV, including all powertrain components/controllers, accessories, cooling systems, and a hybrid control strategy designed inside the supervisor hybrid controller unit (HCU). Simulation results were obtained during the US06 driving cycle to illustrate the vehicle's performance, energy consumption, efficiency, and performance of the powertrain components.

Chapter 4 explores the existing flexibility management techniques and some crucial areas of AI deployment in energy management systems toward meeting the flexibility needs of modern energy supply systems. The outputs of renewable energy generators are intermittent, and thus create an imbalance between the instantaneous load demand and available supply at different instances of time. Different concepts of AI are deployed as a solution provider to numerous complex

power system operational problems, especially in resource forecasting, electricity market dynamics prediction, intelligent decision-making for generator scheduling, etc.

Chapter 5 provides a detailed overview of some key applications of AI and machine learning (ML) for renewable energy, with a particular focus on challenges, available resources, and potential future research opportunities. In detail, this chapter discusses AI and ML applications in weather forecasting, power production, energy consumption forecasting, smart grids, and prognostic maintenance of renewable energy systems. An overview of the most commonly used AI and ML algorithms in the domain, along with a detailed description of some of the publicly available datasets for training and evaluation of these algorithms to perform different tasks in the renewable energy sector, is also provided.

Chapter 6 describes an integrated approach for solving existing problems in the development of new technologies for the smelting of technical silicon, which can reduce energy costs, improve product quality, and reduce the severity of environmental problems in this production. Methods to increase the profitability of carbothermal electric arc melting of technical silicon are described by returning to the process of fine waste from the preparation of charge materials and microsilica-dusty wastes from the production of silicon itself in the form of briquettes. The use of these pulverized wastes for the synthesis of liquid glass glue, concrete and building mixtures, and micro- and nano-sized silicon carbide powders is also discussed.

Chapter 7 suggests metaheuristic-based methods of simultaneous reconfiguration of the distribution network and photovoltaic system placement (RDN-PVSP) to minimize the power loss of the distribution network (DN). To search for the optimal RDN-PVSP solution, two algorithms, namely, the recent Golden Jackal optimization (GJO) and well-known particle swarm optimization (PSO), are applied. The performance of the two methods was validated on two test DNs consisting of 33-buses and 69-buses in two cases: RDN and RDN-PVSP, respectively. The results showed that GJO outperformed PSO in terms of the optimal solution and statistical results.

Chapter 8 discusses the technology of smelting one of the well-known modifications of multisilicon, namely, secondary cast polycrystalline silicon, and options for its application for production of a solar cell and the manufacture of heavily-doped silicon substrates. The proposed multisilicon is intentionally subjected to overdoping, which must be carried out by adding one or a group of impurities to the solubility limit and simultaneously using a charge from a mixture of the highest grades of technical silicon. It is emphasized that film growth, as the base region of solar cells, should be carried out under conditions of guaranteed suppression of autodoping by known methods.

Chapter 9 presents a critical analysis of ML methods and techniques for renewable energy systems, showing the advantages of introducing these novel approaches in future energy scenarios by discussing relevant case studies. ML helps obtain accurate predictions of variable renewable energy (VRE) generation, energy demand, or possible network outages, conferring to power system operators the

possibility to perform the required actions to balance load and generation in intra-day and day-ahead scheduling with benefits for operational costs, environmental impact, and system reliability.

In Chap. 10, a customer baseline load (CBL)-centered electricity cost optimization model is implemented to minimize electricity cost and peak power demand. The proposed algorithm has been successfully validated on smart-home residential loads of various categories, as well as real data of static and dynamic electricity pricing applicable to two utilities, the Tehran Power Distribution Company, Iran, and the Kerala State Electricity Board (KSEB), India. The proposed algorithm validates its performance in minimizing electricity cost and peak power demand simultaneously, and optimal scheduling of appliances facilitates both residential consumers and utilities.

In Chap. 11, the placement of photovoltaic generators (PVGs) and wind power generators (WGs) in distribution networks is optimized for both size and location to minimize the power loss as much as possible. An IEEE 85-bus radial distribution power network was employed to simulate the effectiveness of PVGs and WGs. The optimal solutions to the problem are determined by applying three novel meta-heuristic methods, including Northern Goshawk optimization (NGO), Bonobo optimizer (BO), and transient search optimization (TSO). By evaluating the results obtained from these methods, NGO proved to be the most effective, and its performance was superior to both BO and TSO in all compared criteria, such as minimum loss value (Min.loss), mean loss value (Mean.loss), maximum loss value (Max.loss), and the standard deviation (STD).

Chapter 12 documents some properties of a new modification of the well-known semiconductor material silicon, the so-called granular silicon being a silicon powder of a given grain size, whose particles are not sintered or fused but simply mechanically pressed together with a known force. The new material has shown high radiation resistance and stability in the parameters of heat energy converters made by subjecting it to high-intensity laser radiation. Methods for reducing granular silicon resistivity are discussed, and designs of thermal energy converters using natural or man-made heat, including concentrated solar radiation as a heat source, are presented.

Chapter 13 considers two evolutionary algorithms: the genetic algorithm (GA) and particle swarm optimization (PSO) to solve constrained unit commitment problems in a power system. Renewable resources, such as wind power, are incorporated into the system. Given the fluctuating and intermittent nature of the wind, different wind scenarios were considered. The wind power and its associated probabilities were derived using a universal generating function (UGF). Constraints, such as the generation limit, power balance, minimum up time and down time, were considered. The transmission losses were considered, and in certain cases, a security constraint was applied. The GA and PSO were tested on an IEEE 6-bus system and an IEEE 30-bus system to confirm their effectiveness. The results were compared based on the total costs, and numerical results suggested that the PSO was slightly better than the GA.

The editors strongly believe that the information obtained from this book will undoubtedly be interesting and useful for a wide range of readers, beginning from students to exalted scientists. This edition should disseminate new information among interested scholars, engineers, professors, and students involved in the renewable energy industry, as well as intelligent computing activities in different fields of science and engineering.

Patiala, India   Mukhdeep Singh Manshahia
Moscow, Russia   Valeriy Kharchenko
Ankara, Turkey   Gerhard-Wilhelm Weber
Ho Chi Minh City, Vietnam   Pandian Vasant

Acknowledgment

Contents

About the Editors

Mukhdeep Singh Manshahia, Ph.D., is an assistant professor at Punjabi University Patiala, Punjab, India. He obtained his Ph.D. in 2016 from Punjabi University Patiala. He works in Sustainable Computing, Artificial Intelligence, Wireless Sensor Networks, the Internet of Things (IoT), Nature Inspired Computing, Energy Harvesting, and Renewable Energy Systems. He has edited three books, published 46 international and national research papers, and presented 30 research papers at international and national conferences/seminars. He has guided four Master dissertations, 55 undergraduate projects, and two Ph.D. dissertations. He has 17 years of working experience at universities. He is a reviewer for many WoS journals and is a member of the Computer Society of India, IEEE, and IAENG.

Valeriy Kharchenko, Ph.D., is Chief Scientific Officer at FSBSI Federal Scientific Agroengineering Center VIM, Moscow. He is a researcher and consultant in a wide range of energy-saving fields, including energy policy at the national and international levels, energy RTD strategy, RUE, and RES. Dr. Kharchenko's education includes Tacis Training Programme (Manager in Energy, 1994–1995); Tashkent State Technical University, Uzbekistan (Professor, 1994); State Higher Training Courses on Patenting and Invention (Certificate with Distinction, 1987); Institute of Electronics, Moscow (Doctor of Engineering Sciences Degree, 1987); Institute of Inorganic Chemistry, Novosibirsk (Candidate of Chemistry Degree, 1969); Tashkent Polytechnic Institute

(Technology Engineer, 1956–1961). His international activity includes counterpart expert in the Project of EU "Monitoring and evaluation of the energy (nonnuclear) projects implementation in Uzbekistan" (carried out by European companies, 1994–1996); expert for evaluation of submitted proposals INTAS (1998–2000); senior expert of the Central Asia Energy Advisory Group (a project under the EC DG XVII's SYNERGY Programme) with responsibility for the formation of expert groups, peering and estimation of their reports, and preparing general Interim and final annual reports (1996–2000); Global Environmental Facility, Government of Uzbekistan (Joint Project UZB/98/G42/A/1G/99), an expert at the premises (2000–2001 UNDP). He is a reviewer for several international journals, including *Solar Energy*, Deputy Editor-in-Chief of the *European Journal of Renewable Energy*; member of the editorial boards of several international journals, including the *International Journal of Energy Optimization and Engineering* (IJEOE) and the *Journal of Cases on Information Technology* (JCIT); and an honorary professor at the Institute of Hydropower and Renewable Energy of the National Research University.

Gerhard-Wilhelm Weber, Ph.D., is a professor in the Faculty of Engineering Management at Poznan University of Technology, Poznan, Poland. His research is on mathematics, statistics, operational research, data science, machine learning, finance, economics, optimization, optimal control, management, neuro-, bio-, and earth sciences, medicine, logistics, development, cosmology, and generalized space-time research. He is involved in the organization of scientific life internationally. He received a Diploma and Doctorate in Mathematics and Economics/ Business Administration at RWTH Aachen and Habilitation at TU Darmstadt. He replaced Professorships at the University of Cologne, and TU Chemnitz, Germany. He was Professor of Financial Mathematics and Scientific Computing and Assistant to the Director at the Institute of Applied Mathematics, Middle East Technical University (METU), Ankara, Turkey. He has been a member of five other graduate schools, institutes, and depart-

ments at METU. Dr. Weber also has affiliations at the University of Siegen (Germany), Federation University (Ballarat, Australia), University of Aveiro (Portugal), University of North Sumatra (Medan, Indonesia), Malaysia University of Technology, Chinese University of Hong Kong, KTO Karatay University (Konya, Turkey), Vidyasagar University (Midnapore, India), Mazandaran University of Science and Technology (Babol, Iran), Istinye University (Istanbul, Turkey), and Georgian International Academy of Sciences. He is an advisor to EURO Conferences for the Association of European OR Societies and the International Federation of OR Societies (IFORS). Professor Weber is an IFORS Fellow, a member of many national OR societies, an honorary chair of some EURO working groups, a subeditor of the IFORS Newsletter, a member of the IFORS Developing Countries Committee and Pacific Optimization Research Activity Group. He has supervised many M.Sc. and Ph.D. students, authored and edited numerous books and articles, and given presentations on diverse areas in theory, methods, and practice. He has been a member of many international journal editorial, special issue, and award boards, participated in numerous research projects, and received various recognitions from students, universities, conferences, and scientific organizations.

Pandian Vasant is a research associate at MERLIN Research Centre, TDTU, HCMC, Vietnam, and Editor-in-Chief of the *International Journal of Energy Optimization and Engineering* (IJEOE). He holds a Ph.D. in Computational Intelligence from UNEM, Costa Rica, an M.Sc. in Engineering Mathematics from the University Malaysia Sabah, Malaysia, and a B.Sc. (Hons, Second Class Upper) in Mathematics from the University of Malaya, Malaysia. His research interests include soft computing, hybrid optimization, innovative computing, and applications. He has co-authored research articles in journals, conference proceedings, presentations, special issues, and chapters and was the General Chair of the EAI International Conference on Computer Science and Engineering in Penang, Malaysia (2016) and Bangkok, Thailand (2018). In the years 2009 and 2015, he was awarded top reviewer and outstanding reviewer for the journal *Applied Soft*

Computing. He has 32 years of university working experience (teaching, research, and editorial). He is currently the General Chair of the International Conference on Intelligent Computing and Optimization and a member of the AMS (USA), NAVY Research Group (TUO, Czech Republic), and MERLIN Research Centre (TDTU, Vietnam).

General Approaches to Assessing Electrical Load of Agro-industrial Complex Facilities When Justifying the Parameters of the Photovoltaic Power System

Yulia Daus, Valeriy Kharchenko [ORCID], and Igor Yudaev

1 Introduction

In the period of modern development at various levels of the agricultural management system [1], there appears objective need for technological re-equipment and modernization of the industry. The main strategic goal of agricultural development is the intrusion of digital technologies into the agricultural sector, designing digital platforms for the evolution of the agro-industrial complex. The idea of agriculture digitalization is quite new, and, despite the high positive potential effect, digitalization is used only in the small part of agricultural facilities (5–10%). Moreover, consequently, most of the agro-industrial complex and enterprises still operate inefficiently, causing the detriment of natural resources, soil quality, and low labor productivity [2, 3, 52]. With the growth of the population, enterprises are forced to work more intensively, which adversely affects the quality of land resources. Soil is worn out, water bodies are depleted and polluted, and livestock suffers. Numerous problems and limited opportunities for growth in production and product quality objectively contribute to the necessity of introduction of digital technologies [4–7]. This can be possible if to use natural resources as efficiently as possible at high level of labor productivity and optimization of the personnel of various categories, which, in turn, will have a positive effect on the liquidity of enterprises [8, 9]. Many scientists dealt with the problems of socioeconomic and technological development of the country's agriculture [10–14].

Y. Daus (✉) · I. Yudaev
Kuban State Agrarian University, Krasnodar, Russia

V. Kharchenko
Federal Scientific Agroengineering Center VIM, Moscow, Russia

The main tasks of digitalization are to organize gradual transition of agricultural enterprises to a new level through the introduction of digital technologies and to search for information for the creation and implementation of regional programs for the modern development of the agricultural sector; rapid assessment of problem areas in the digitalization of agricultural production; quantitative internal assessment of the prospects for digitalization of agriculture; assessment of the state of technological processes in the industry and areas of development; and identification of technological barriers hindering the development of the agricultural sector of the economy [53].

It is also necessary to consider that food security is one of the key objectives of sustainable development of the world community. The spread of the COVID-19 pandemic across the globe revealed an urgent need to support and intensively develop the agro-industrial sector of the world economy [1, 10–12].

However, any modernization, associated with the use of up-to-date tools [2, 3, 11, 13, 15], requires additional energy inputs from sources that would meet the requirements of high-tech processes introduced into agriculture [2, 5, 6, 16, 17]. Today, rural areas are characterized by a shortage of free capacities, which directs the search vector towards renewable energy sources, the functioning of which is characterized by local characteristics, and the energy generated by them can be used directly at the point where consumers are connected to them [18–20].

Motivation and significance of the study. However, all this caused an urgent need to search for energy supply reserves, since the old engineering systems are not designed for the increasing consumer capacity of agricultural producers and are characterized by a high level of wear and tear and low reliability [21–23, 48, 50]. Therefore, in rural areas, the search for new energy sources is especially relevant, for which renewable energy sources are the most promising option, since they are universally available and have a simple technological and environmentally friendly cycle of work [18, 24, 25, 49]. Low-power generating plants can both be connected to existing networks and create distributed generation systems on their basis [18, 26, 27]. In this case, the most promising are photovoltaic installations, which are very easy to maintain and have a long service life and a huge potential as a primary energy source [28–30, 47, 64, 65].

Given the world's population growth which is expected to reach more than 9 billion people by 2050, the global demand for food will drastically rise, threatening food security as a critical component of sustainable development. Recent developments of urbanism and agro-industrialization have imposed pressure on agriculture with a decisive role in supplying the global food demand. Statistics reveal that in the shadow of the COVID-19 pandemic, world hunger has been increased so that the prevalence of undernutrition reached nearly 9.9% in 2020 from the value of 8.4% in 2019 [68].

Human activities are estimated to cause global warming of around 1 °C compared to preindustrial levels. If warming continues at current rates, it is likely to reach 1.5 °C by between 2030 and 2050. The Intergovernmental Panel on Climate Change has reported that the climate-related risks for natural systems will increase if the global temperature rise reaches 1.5 °C. Despite these upcoming challenges, we

need to secure the nutrition of an expanding global population while reducing greenhouse gas emissions and protecting the environment [67]. The agricultural and food processing industries are considered key sectors aligned with sustainable development goals, as they play an important role in sustainable rural development. About 30% of global energy is used in these sectors, particularly thermal energy in both heating and cooling applications. Research considers solar energy technologies to be promising ways to increase system flexibility and lead to climate mitigation impacts [69]. For many years, solar energy has been utilized in the agricultural sector to supply energy requirements of various operations from traditional applications such as open sun drying and crop cultivation in greenhouses to modern agricultural practices using solar-powered farm robots and machinery. After several years of research and development in relative technologies, solar energy has been proved to be the most compatible energy source for use in agricultural and food production systems [66].

At the same time, photovoltaic systems for converting solar energy come to the fore, characterized by a relatively simple technology for converting insolation into electrical energy, environmental friendliness, ease of operation, and maintenance [23, 25, 8, 31, 61].

When justifying the parameters of the photovoltaic power plant or installation for the agricultural consumer, it is necessary to take into account the fact that the typical schedule of the electrical load of such a consumer is characterized by day and evening maximum load according to the specific technological process, and the graph of the coming solar radiation on the receiving surface has its well known, different from the consumption graph shape with a maximum at noon [32–34, 45, 51]. As a result, it is necessary to install duplicate and/or accumulating energy sources at the photovoltaic power plant, which leads to additional material and financial costs. Therefore, it is necessary to pay special attention to the available initial information (the list and capacity of the consumer's electrical consumers, load schedules of the entire enterprise or separately for each outgoing line from the substation switchgear, etc.), since this affects the final capacity of the solar system and accumulating or redundant devices [29, 35].

Having information about the electrical load, the required power of the supply system, switching, measuring electrical equipment, and electrical equipment of a number of electrical protections, current carrying equipment can be selected according to the condition of permissible heating, calculate losses, and voltage fluctuations [59]. Depending on the availability of the initial information, specific method for calculating the electrical load is used [36–38, 46]. Therefore, the choice of the method and source of information for determining the load has a significant impact on the parameters of the photovoltaic system. The uniqueness of this study consists in the data analysis on costs obtained by practical and computational methods.

Methods for calculating electrical loads are divided into actual and practical methods [38–40, 55–62]. Practical methods include empirical (methods of the demand coefficient, the coefficient of difference in time of maxima, specific indicators for electricity consumption and load density, two-term empirical expressions,

technological graph), analytical (methods of ordered diagrams according to the principle of the maximum average load and the coefficient of calculated active load and the statistical method), and complex (methods of electrical consumption of products, professional analysis, forecasting of time series, specific capacities of electrical loads, total annual consumption, average annual demand coefficient, specific annual consumption of electrical energy) methods. Static voltage stability approaches [55], regardless of the complexity and variety of the dynamic behavior of the facilities in power systems [56, 57], still present some particular advantages. Voltage collapses are always accompanied by a heavy load; therefore, the maximum loading point [58], or alternatively the load margin, is regarded as an efficient evaluation for the static voltage stability of power systems [59]. Therefore, the continuation power flow [54, 56, 57] is presented to solve the parameterized load flow formulations with alternating predictor and corrector steps. An improved hybrid load flow calculation algorithm and its simplified and approximate version is presented in [60, 63] for weakly meshed distribution systems with PV nodes. The initial data for each method are presented in Table 1.

For newly constructed facilities or in the absence of information on the power consumption of operated ones, it is recommended to use a stochastic method for calculating the electrical load, based on the results of a statistical survey. For the agro-industrial complex, guidelines have been designed for calculating electrical loads in networks of 0.38–110 kV for agricultural purposes under the title "Guidelines for the Design of Agricultural Power Supply System" [40].

Guidelines for the design of power supply systems for agricultural facilities are a single methodological instruction, presented as a reference material to all design organizations, engaged in the design and calculation of electrical loads in 0.38–110 kV agricultural networks. These guidelines unify the initial data for calculating power grids at different design stages, taking into account the actual load of power grid elements (transformers, power lines, etc.).

The method for determining loads, when calculating electrical networks for agricultural purposes, is based on the summation of the calculated loads, presented in probabilistic form at the inputs of consumers or on the buses of transformer substations for the third settlement year. Estimated loads of residential buildings in 0.38 kV networks are determined, taking into account the achieved level of electricity consumption for intra-apartment needs and industrial, public, and utility consumers – according to the norms.

Estimated loads in networks 0.38–110 kV are determined, taking into account the actual load, achieved by the initial year of the operating transformer substations.

The design load is considered to be the largest of the average values of the total power over an interval of 30 minutes (half an hour maximum), which can occur at the input to the consumer or in the supply network for the seventh design year with a probability of at least 0.95.

For a group of electrical consumers with the production cycle interval of 1 year, the number of hours of use of the maximum electrical load is applied: during this time, a group of electrical consumers, working at maximum load, consumes the same amount of electricity as working according to the real load schedule for a

Table 1 Methods for calculating electrical loads

Method	Initial data
Empirical (in the absence of technological and operational information)	
1. Demand coefficient method	Rated full power of electrical equipment, kVA Cost of electrical receivers, o.e. Installed power, total rated electric power of the same type of electrical machines, kW Rated power, electrical power of electrical equipment at 100% load, kW Design power, installed power, taking into account the type of electrical installation, its mode of operation, and other indicators using design factors, kW The number of the same type of electrical receivers
2. The coefficient of the difference in timing of the maxima	Designed full power, installed power, taking into account the type of electrical installation, its mode of operation, and other indicators using design factors, kVA Designed active power, installed power, taking into account the type of electrical installation, its mode of operation, and other indicators using calculated coefficients, kW Designed reactive power, installed power, taking into account the type of electrical installation, its mode of operation using design factors, kVAr
3. Method of two-term empirical expressions	The largest load, kW Additive determined by the Guidelines [40], kW
4. Methods of specific indicators	Release per unit change Electricity consumption per unit of production, kWh Shift duration, h Specific design load per 1 m^2, kW/m^2 Production area, m^2
5. Method of technological graphics	Data of the technological mode of operation of electrical receivers
Analytical (mathematical models of electrical loads and thermal models of conductors)	
1. Method of ordered charts	Maximum load factor Load utilization factor Average (per cycle) power, average value of the total calculated active power for a time interval (cycle), kW Heating time constant, for conductors up to 1 kV $\approx$ 10 min
2. Statistical method	Calculation reliability factor Load variance Average (per cycle) power, average value of the total calculated active electrical power for a time interval (cycle), kW
Complex (calculating electrical loads, it relies on analogues of created and operated facilities, using existing calculation methods)	
1. By electrical capacity of products	Electrical capacity of products Volume of production The number of hours of use of the maximum loads
2. According to the total annual electricity consumption W or the average annual power	Number of hours per year, 8760 hours Maximum load factor Average (per cycle) power, average value of the total calculated active electrical power for a time interval (cycle), kW

Table 1 (continued)

Method	Initial data
3. According to the specific annual electricity consumption	Maximum load factor Volume of production Number of hours per year, 8760
4. According to the average annual demand coefficient	Demand factor Installed power, total rated electric power of the same type of electrical machines, kW
5. By specific power of electrical loads	Specific design load per 1 m², kW/m² Production area, m²
6. Time series forecasting	Matrix of indicators defined by a time series
7. Professional logical analysis	Matrix of electrical indicators characterizing the total power consumption of the facility

year (8760 h). The number of hours of using the maximum Tm for power loads of enterprises for one shift equals 1500–2000 h/year, for two shift it equals 2500–4000 h/year, for three shifts it equals 4500–6000 h/year, for continuous operation it equals 6500–8000 h/year [41].

The average hourly active power of load types of enterprises is determined by the following formula [41]:

$$W = \frac{P_{\text{inst guidelines}} \cdot T_{\text{m}}}{8760} \tag{1}$$

where $P_{\text{inst guidelines}}$ is the installed power of the consumer according to the Guidelines, W.

For reconstructed objects, in the presence of information about the existing level of power consumption, obtained during the survey of consumers, it is recommended to use methods for calculating electrical load, based on the drawing up of graphs of electrical loads of the consumer. To build a graph of electrical loads, it is necessary to know the technological cycle of operation of electrical equipment and take into account the full design power in the daytime and evening maximums of electrical loads. For industrial consumers of electricity, the calculation of electrical load is carried out by the method of the utilization rate of electrical equipment, for residential and public buildings; by the method of the demand coefficient, for agricultural consumers; and by the method of load factors of electrical receivers.

The purpose of the research is to study various methods for calculating the electrical load of agricultural objects based on the available initial data and different options of supplying it by means of the solar photovoltaic system, taking into account the peculiarities of the consumer load graph.

The object of research is the power supply system of the agricultural enterprise "Sorghum Plant", located in Zernograd, Rostov region, Russian Federation (hereinafter – the enterprise). The general plan of the enterprise is presented in Fig. 1.

The enterprise is the complex of facilities for storing large quantities of grain in the highly mechanized silo-type granary, bringing it to a conditioned state [42].
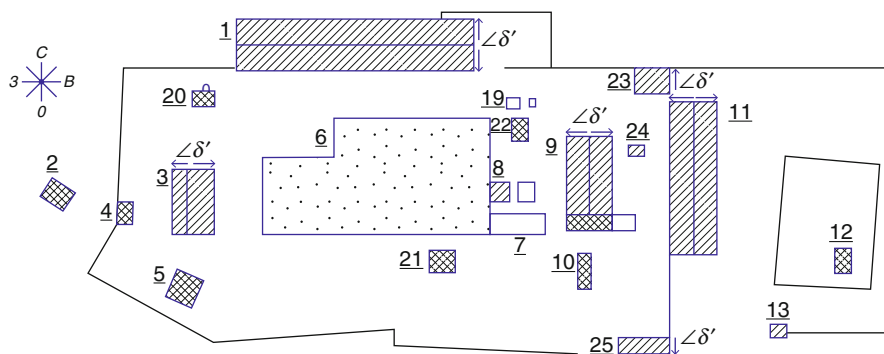
Fig. 1 Layout of electrical consumers of the research object

The main consumers of electrical energy at the facility include drying and cleaning tower with the silo 9 (Fig. 1), machine building 7, and warehouse for finished products 6. In addition, on the territory there are weighing station 5, laboratory 2, checkpoint 4, office building 3, warehouses 1 and 11, workshop 8, station of fuels and lubricants 12, gatehouse 13, cargo vehicle unloader 10, and emergency and non-electrified structures 19–25.

The source of electrical energy for the enterprise is the transformer substation CTS 10/0.4 with 630 kVA transformer, from which the plant's consumers are supplied through five main radial lines: L1, power consumers 1–5; L2, electrical consumers 6–8; L3, electrical consumers 11–13; L4, power consumers 7; and L5, power consumers 9.

2 Materials and Methods

The difference between the hourly values of the generated and consumed electrical energy is determined by the formula:

$$\delta W_t = W_t \cdot \eta_{\text{inv}} - W_{t_{\text{const}}}, \tag{2}$$

where W_t and $W_{t_{\text{const}}}$ are the hourly values of electricity generated by photovoltaic modules and consumed load, kWh, and η_{inv} is the inverter efficiency.

The existing modes of operation of photovoltaic installation can be classified into the following types:

1. The electricity generated by photovoltaic modules is completely consumed by the load: $\delta W_t = 0$. The power distribution equation in such power supply system has the form:

$$W_{t_{\text{const}}} = W_t \cdot \eta. \tag{3}$$

2. Photovoltaic modules generate excess electrical energy, and batteries do not need to be charged: $\delta W_t \geq 0$. The power distribution equation in such power supply system has the form:

$$W_{t_{const}} = W_t \cdot \eta_{inv} - W_{t_{network}}, \tag{4}$$

where $W_{t_{network}}$ is the electricity, generated by photovoltaic modules to the network, kWh.

3. Photovoltaic modules generate excess electrical energy, and batteries require charging: $\delta W_t \geq 0$. The value of the power supplied to the battery, taking into account the load, is determined by the formula:

$$W_{ab} = \left(W_t \cdot \eta_{inv} - W_{t_{const}}\right) \cdot \eta_{contr}, \tag{5}$$

where η_{contr} is the charge controller efficiency.

4. In the system, there is not enough electricity generated by photovoltaic modules; the difference is covered by batteries: $\delta W_t < 0$. The power distribution equation in such power supply system has the form:

$$W_{t_{const}} = (W_t + W_{ab} \cdot \eta_{contr}) \cdot \eta_{inv}. \tag{6}$$

where W_{ab} is the electricity that is consumed by load, covered by batteries, kWh.

5. The batteries are discharged; the difference is covered by a diesel generator or from the network: $\delta W_t < 0$. The power distribution equation in such power supply system has the form:

$$W_{t_{const}} = W_t \cdot \eta_{inv} + W_{dg} = W_t \cdot \eta_{inv} + W_{tnetwork}. \tag{7}$$

There were considered two types of graphs: the first graph is constant with rated power of 1.38 kW (lighting system of the flour-grinding areas of the enterprise, $T = 24$ hours; the second graph is according to Fig. 2 (agricultural processing enterprise [40]) for rated power of 1.38 kW.

The necessary calculations of the operating mode of the installation with identically spatially installed photovoltaic modules, focused on the maximum degree of solar energy utilization at noon, when the insolation is the biggest during the daylight hours were conducted.

The graph, presented in Fig. 2, is characterized by two maximum loads: morning peak load, which is of 100% of the rated power of the consumer, and the evening value of 77% of the rated power of the consumer.

According to the above-described modes of operation of photovoltaic installation, there are considered three options for load coverage, using modules FSM-200 for the layout of the photovoltaic installation [38]:

Option 1: $\delta W_{14} \leq 0$ (mode 1)
Option 2: $\sum_{t=7}^{21} W_t \geq \sum_{t=7}^{21} W_{t \, cons}$ (mode 3, 4)
Option 3: $\delta W_{beggining \, of \, daylight \, hours} \geq 0$, $\delta W_{end \, of \, daylight \, hours} \geq 0$ (mode 2)
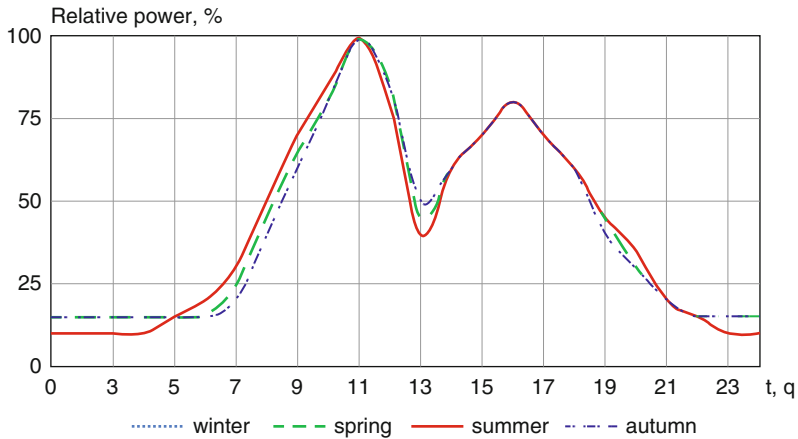
Fig. 2 Daily schedule of active load of agricultural processing enterprise

3 Results and Discussion

3.1 Construction of Annual and Daily Charts of Electric Loads by the Calculation Method

There was determined the total active electric power of the enterprise for the estimated production periods: "July–August," "September–October," "November–February," "March–April," and "May–June," which allows to build annual electrical load schedule. The total active power in the daytime and evening maximum loads at the enterprise for all calculation periods is presented in Table 2.

According to Table 2, the annual schedule of electricity consumed by the enterprise, determined by the calculation method, is built (Fig. 3). The highest consumption of electric energy is projected from July to October (the time of intensive agricultural production); the increase in load from November to March is caused by the operation of the electric heating system.

Taking as a basis, the technological process of the enterprise there was determined the daily power consumption for four characteristic days on March 15, July 1, September 15, and December 15. Daily graphs of electricity consumed by the enterprise, determined by the calculation method, are presented in Fig. 4.

The highest consumption of electric energy was obtained for a summer day (time of intensive agricultural production), the lowest consumption of electric energy is typical for a spring day, and a greater value of consumed electric energy in autumn and winter days is associated with the operation of the electric heating system.

Table 2 The total designed active electrical power consumed during the year by the enterprise for five characteristic production periods

Season	July–August	September–October	November–February	March–April	May–June
Number of months	2	2	4	2	2
Day/evening maximum load on the working days, kW	169.6 5.12	125.4 5.12	120.5 18.7	42.7 18.7	19.5 5.12
Day/evening maximum load on the off-hour days, kW	5.2/6.3	5.2/6.3	18.7/19.8	18.7/19.8	5.2/6.3
Working days	31 + 31	21 + 23	20 + 22 + 17 + 20	20 + 22	18 + 19
Off-hour days	–	9 + 8	10 + 9 + 14 + 8	11 + 8	13 + 11
Working hours	12	8 (+1)	8 (+1)	8 (+1)	8 (+1)
Night hours	12	15	15	15	15
Off-hour hours: day/night	–	11/13	8/15	12/12	16/8
Working hours for the season	744	352	632	336	296
Night hours for the season	744	660	1185	630	555
Off-hour hours for the season: day/night	–	187/221	328/615	228/228	384/192
Day/evening power consumption on the working day, kWh	126182.4 3809.3	44140.8 3379.2	76156.0 22159.5	14347.2 11781.0	5772 2841.6
Day/evening power consumption on the weekend, kWh	–	972.4 1392.3	6133.6 12,177	4263.6 4514.4	1996.8 1209.6
Seasonal total power consumption, kWh	129991.7	47520.0	98315.5	26128.2	8613.6
Total average monthly power consumption, kWh	64995.8	23760.0	24578.9	13064.1	4306.8

Wmonth, MWh/month
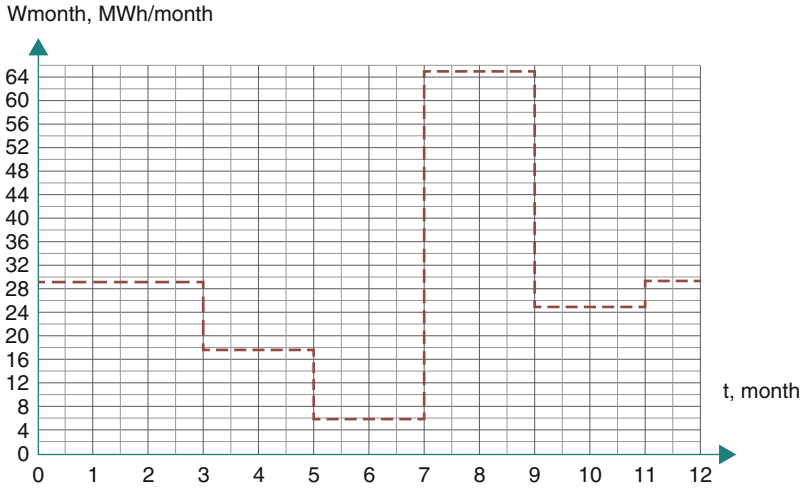
Fig. 3 Annual schedule of electricity consumed by the enterprise, determined by the calculation method

Wday, kWh/day
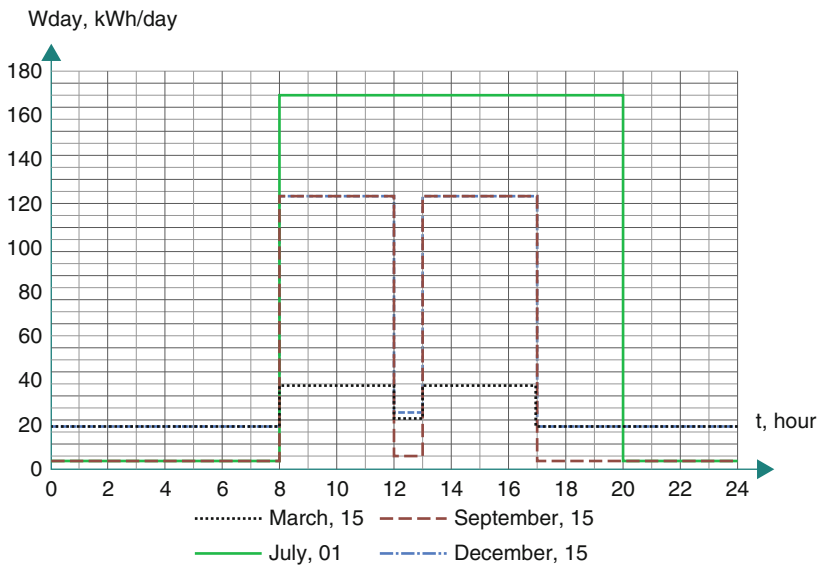
Fig. 4 Daily graphs of electricity consumed by the enterprise, determined by the calculation method

3.2 Construction of Annual and Daily Schedules of Electrical Loads According to the Guidelines

The total maximum nominal active power of the studied enterprise is 214.9 kW. According to the Guidelines, this installed capacity is close to facility No. 309 grain cleaning and drying complex KZR-5 with installed power of 250 kW [40]. This data is achieved by collecting and analyzing information on real load graphs of agricultural enterprises of different types.

The enterprise has seasonal electrical load with the maximum power consumption of the total active power in July and August.

According to [40], the average annual total active electricity consumed per hour is 57.1 kWh as determined for the enterprise, which has a one-shift work schedule (Tm = 2000 h/year) [41].

The annual schedule of electricity consumed by the enterprise, in accordance with the methodology of the Guidelines, is presented in Fig. 5.

According to the Guidelines, the lowest electricity consumption for the considered type of agricultural enterprise is projected from March to May; the period with the maximum value of electricity consumption is projected from July to January.
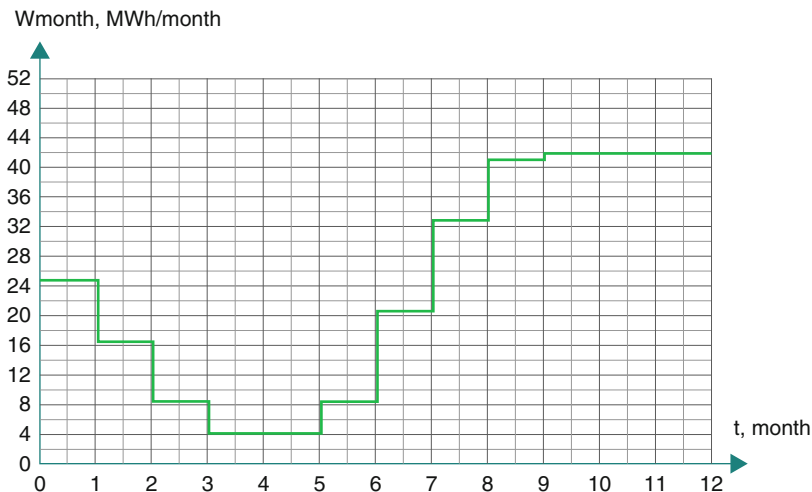
Fig. 5 The annual schedule of electricity consumed by the enterprise, in accordance with the methodology of the Guidelines

3.3 Construction of Annual and Daily Schedules of Electrical Loads by Monitoring the Actual Consumed Electricity

The enterprise receives electrical energy from the 10/0.4 kV high−/low-voltage kiosk-type tap-off complete transformer substation [43, 46].

On the buses of the low-voltage switchgear of 0.38 kV CTS 10/0.4 kV, commercial electricity metering unit is installed, consisting of three current transformers TA1–TA3 of the IEK trademark with rated voltage of 0.66 kV, rated primary/secondary current of 600/5, accuracy class of 0.5, and rated full power on the secondary winding of 10 VA. A three-phase electric energy meter (made by ENERGOMERA, TsE6803VM brand) with rated voltage of 3x220 V (380 V) and secondary current of 5 A (1-7.5 A) is connected through current transformers TA1 - TA2.8. The data on energy consumption by months obtained using the commercial metering unit for 2017–2020 are presented in Table 3.

When designing power supply facilities for agricultural enterprises, which in most cases have seasonal electricity consumption schedules, it is necessary to take into account not the total maximum electricity consumption but the designed maximum electricity consumption by seasons during the year. When designing a backup power source, such as a solar power plant using photovoltaic modules, at operating enterprises of the agro-industrial complex, it is necessary to take into account not only the seasonality of the operation of the enterprise but also the actual annual, monthly, and daily schedule of electricity consumption and a number of technical features of the designed backup power source.

The annual graphs of electricity consumed by the enterprise, constructed according to various methods, are presented in Fig. 6. Daily graphs of electricity consumed by the enterprise for March 15, for July 1, for September 15, and for December 15, built according to various methods, are presented in Fig. 7.

Table 3 Annual consumption of electrical energy by the enterprise for 2017–2020 (kWh/year)

Month	2017	2018	2019	2020	Average 2017–2020
January	9600	12,120	12,240	7680	10,410
February	12,360	11,280	10,440	8400	10,620
March	6360	11,160	8400	4680	7650
April	6000	5640	6360	4080	5520
May	2640	2040	1320	2640	2160
June	2280	2040	3960	2520	2700
July	21,360	32,040	27,480	24,960	26,460
August	18,360	23,880	21,960	17,880	20,520
September	13,200	9960	6960	10,320	10,110
October	9000	8280	5520	6720	7680
November	9360	13,920	5160	9480	9480
December	10,080	10,440	9840	10,120	10,120
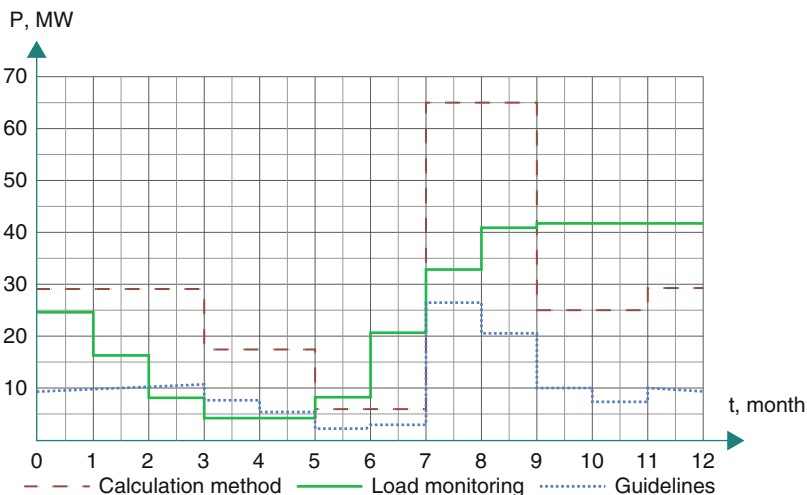
Fig. 6 Annual graphs of electrical energy consumed by the enterprise, constructed according to various methods
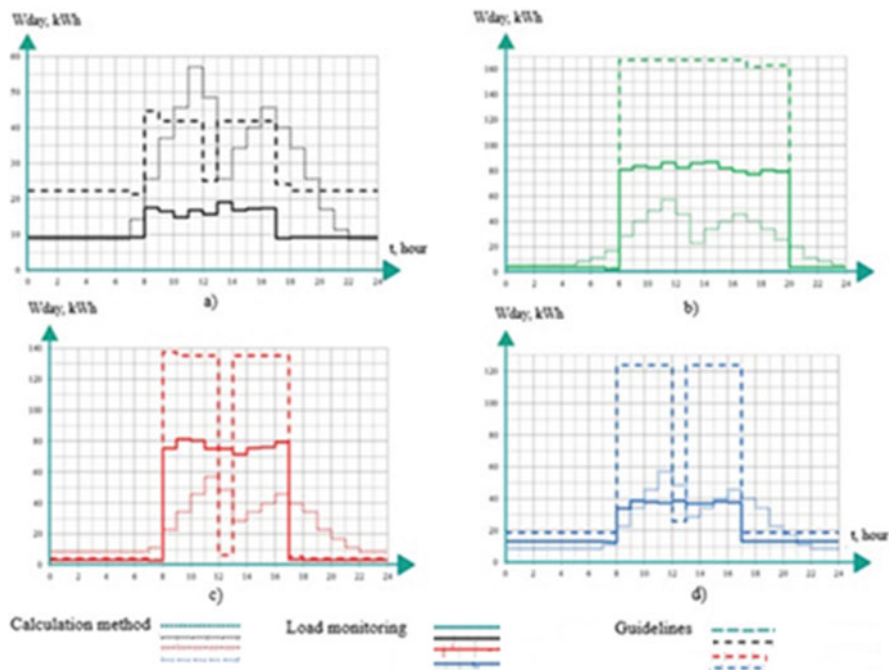
Fig. 7 Daily graphs of electricity consumed by the enterprise (**a**) for March 15, (**b**) for July 07, (**c**) for September 15, (**d**) for December 15, built according to various methods

Figure 6 reveals that the consumption of electric energy by months is the highest when calculation method is used, while the difference with the monitoring data is from 100% to 200%. Data, according to the Guidelines, predicts smaller values of consumed electrical energy than according to real data monitoring.

The data obtained by the Guidelines have clearly expressed two maximum loads for all characteristic days of the year, while they are practically the same in value for the same day. The calculation method also results in daily load graph that is characteristic of the typical agricultural consumer: two maximums at 11^{00} and 14^{00}. Both forecasting methods give overestimated load values in comparison with the data obtained by monitoring the load by metering devices.

Table 4 presents the comparative characteristics of methods for determining the annual consumption of electrical energy at the enterprise.

3.4 Analysis of Operation Modes of Photovoltaic Modules Considering Load Graph of the Consumer

Methods of supplying electrical load by means of the solar photovoltaic system were considered according to the solution options for those specific days of the year: March 21 ($n = 79$), June 22 ($n = 172$), September 22 ($n = 264$), and December 22 ($n = 356$). The calculation results for the first type of schedule (consumption constantly throughout the day) are presented in Table 5. In brackets for Option 3 according to $n = 172$ each, the number of photovoltaic modules is indicated for the time of day $t = 9$ and $t = 19$ hours $\delta W_9 \geq 0$, $\delta W_{19} \geq 0$, as for the rest of the days, the calculation was carried out according to these hours.

The first option for covering the typical load of the agricultural consumer is presented at Figure 9. For the selected number of PV modules for the day $n = 172$, all the generation curves lie below the load graph, while the coverage of daily consumption ranges from 8.8% in winter to 36.7% in summer. If to consider Fig. 9b, it can be seen that the generation of electric energy throughout the year, except for summer, does not exceed its consumption. The surplus of generation occurs in the period from 12^{00} to 16^{00} with the coverage of the daily demand for electric energy by 42.3%. In the rest of the year, the consumption of electricity from the network is reduced by 10.2% in winter and 30.0% in autumn.

With the use of 18 FSM-200 [44] photovoltaic modules ($n = 79$), the overgeneration of electrical energy in the autumn months will be observed from 12^{00} to 16^{00} and in the summer from 11^{00} to 17^{00}, while half of the required amount of energy is generated in the summer, from 30.9% to 36.0% in the spring-autumn period and 12.2% in winter. Application of the results of choosing the number of photovoltaic modules for $n = 356$ allows reducing the load on the network by 93% in summer, by 2/3 in spring and autumn, and by 22.4% in winter.

Thus, the use of the first approach to the selection of the combination of power generation and load schedule for June 22 allows, without using additional storage

Table 4 Comparative analysis of methods for determining the annual consumption of electrical energy at the enterprise

Methods	According to the recommendations of the Guidelines	Calculation method	Monitoring the actual electrical load curve
Material and technical base	Guidelines and educational-methodical complex	Educational-methodical complex	Educational and methodical complex, devices or complex of devices that register the actual consumed electricity
Time duration of methods	Acquaintance with the Guidelines, calculation	Study of the features of the technological process, electrical schematic diagrams, determination of rated power of electrical equipment	Collecting data on the amount of electricity consumed during set period
Initial data	The Guidelines data	Feature of the technological process; electrical schematic diagrams; rated power of electrical equipment	Data of commercial electricity metering unit or device that registers the actual consumed electricity
Advantages	Calculation of $W_{\text{av. an.}}$ in a short period of time	$\frac{W_{\text{actual year}}}{W_{\text{desighed year}}} \cdot 100\% = 33.8 \ldots 68.4\%$ $\frac{W_{\text{actual year}}}{W_{\text{desighed year}}}_{\text{average\%year}} = 47.8\%$ Constant monthly deviations in calculations for 10 months of 41.6, 52.5%)	High accuracy of annual power consumption by months, (days, hours)
Disadvantages	Calculation accuracy: $\frac{W_{\text{actual year}}}{W_{\text{desighed year}}} \cdot 100\% = 4.8 \ldots 64.7\%$ $\frac{W_{\text{actual year}}}{W_{\text{desighed year}}}_{\text{average\%year}} = 25.5\%$	The complexity and duration of the calculation W_{year} High calculation error of 47.8% (on average).	Annual monitoring of electrical load, the need for technical devices, or a set of devices to monitor consumed electricity

devices, to reduce consumption from the electric network. Since the forms of the production and load schedules are different, for the rest of the specific days, it is necessary to use additional equipment to utilize excess electrical energy in the peaks of solar radiation intensity, which will lead to an increase in the cost of the photovoltaic installation. In addition, the batteries will not use up their entire resource, that is, the period of their operation will be shortened.

The second option for the combination of power generation and load was considered (Fig. 8).

Table 5 Results of calculating load coverage options for the first type of graph

n		Option 1	Option 2	Option 3
79	N, pcs.	18	61	80
	Wgen, kWh/day	10.2	34.4	46.5
172	N, pcs.	13	37	157 (31)
	Wgen, kWh/day	12.05	34.3	150.06 (29.6)
264	N, pcs.	15	52	71
	Wgen, kWh/day	9.9	34.2	48.2
356	N, pcs.	33	153	630
	Wgen, kWh/day	7.4	34.1	144.9
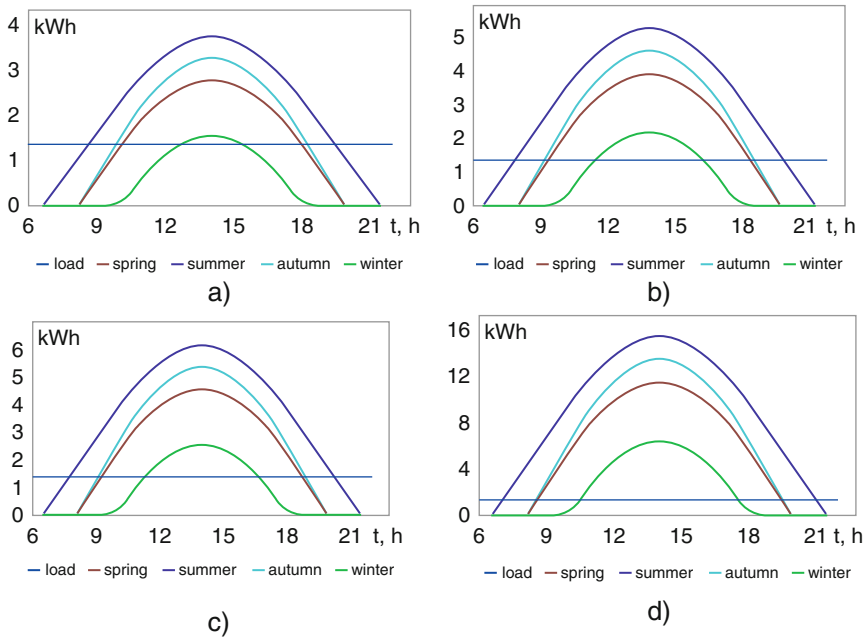
Fig. 8 Seasonal daily graphs of generation for the second option of load coverage, selected on different specific days: June 22 (**a**), September 22 (**b**), March 21 (**c**), December 22 (**d**)

If to use 37 FSM-200 photovoltaic modules, the daily load is fully covered in summer, by 63.5% and 74.1%, respectively, in the spring-autumn period and by a quarter in winter. But in view of the difference in the shape of the generation and consumption schedules, it is required to put into operation storage batteries at the solar power plant in the period from 830 to 1930 in the summer, from 10^{00} to 18^{00} in the fall and spring, and from 13^{00} to 15^{00} in winter, in order to accumulate an excess of electrical energy for its further implementation under conditions of low intensity of solar radiation or its absence.

Applying the number of photovoltaic modules selected from the condition of ensuring the daily load for $n = 79$ and $n = 264$, the overgeneration of electrical

Table 6 Results of calculating load coverage options for the typical electrical load graph of the agricultural consumer

n		Option 1	Option 2	Option 3
79	N, pcs.	11	34	61
	Wgen, kWh/day	6.2	19.7	34.4
172	N, pcs.	7	21	95 (27)
	Wgen, kWh/day	6.5	19.7	88.1 (25.0)
264	N, pcs.	9	30	56
	Wgen, kWh/day	5.9	19.7	36.9
356	N, pcs.	19	93	570
	Wgen, kWh/day	4.2	20.7	127.2

energy in the summer will be from 46.6% to 72.0%, which requires the reorganization of the technological process by connecting additional consumers, that is, to reconfigure power supply systems, which is not always technically feasible.

The photovoltaic installation equipped with 153 FSM-200 photovoltaic modules generates 2.6–4.3 times more daily electricity consumption per day except for winter.

The application of the third approach to determining the ratio of generation and load capacities leads to the fact that the schedules of electric power generation completely cover the load schedule, but the total output per day is tens of times greater than consumption.

The similar analysis of load coverage options for typical electrical load schedule for agricultural consumer was carried out (see Fig. 1). Table 6 shows the results of calculating the number of photovoltaic modules of the FSM-200 type for various options for the ratio of power generation and load for specific days of the year.

The first option for covering the typical load of the agricultural consumer is presented at Fig. 9.

For the selected number of photovoltaic modules for $n = 172$, all generation curves lie below the load graph, while the coverage of daily consumption is 35.9% in summer; 20.6% and 24.1%, respectively, and 7.9% in spring and autumn; and 7.9% in winter. When 19 photovoltaic modules ($n = 356$) are used, seasonal daily curves of electric power generation, except for the winter season, exceed the consumption schedule: from 1030 to 1830 in summer and from 1130 to 1730 in the spring-autumn period. At the same time, in summer, the daily load is provided by 93.1% and by 56.5–65.6% in spring and autumn.

Figure 9c shows that the winter and spring generation schedules are located below the load schedule for electricity consumption from the network, decreasing by 12.2% in winter and by 38.0% in spring. In autumn, there is a slight overgeneration of electrical energy at the peak of the intensity of solar radiation from 12^{30} to 14^{00}, which can be utilized due to the reorganization of the technological process and the connection of additional capacities. In the summer period, the excess of electrical energy (from 12^{00} to 17^{00}) from the photovoltaic installation is significant and equivalent to the daily total load, that is, for its use, it is necessary to additionally introduce storage battery into the structure of the power installation, or completely

Fig. 9 Seasonal daily generation schedules for the first option for covering the typical load schedule for the agricultural consumer, selected for various specific days: June 22 (**a**), September 22 (**b**), March 21 (**c**), December 22 (**d**)

reconfigure the technological process or the consumer's power supply system, which does not always seem to be possible.

For the number of photovoltaic modules selected for the date of September 22, the excess of power generation over consumption of electric energy is observed in the summer from 12^{30} to 15^{00} with a total daily generation of 44.1% more than the load. In the rest of the year, there is no surplus, and the reduction in electricity consumption from the network is from 10.0% in winter to 31.1% in autumn.

Thus, the use of the first approach to the selection of the combination of power generation and load for June 22 allows, without using additional storage devices, to reduce consumption from the electric network by 7.9% in winter and 35.9% in summer. Since the forms of the production and load schedules are different, for the rest of the specific days, it is necessary to use additional equipment to utilize excess electrical energy in the peaks of solar radiation intensity, which will ultimately lead to the increase in the cost of the generated electrical energy. In addition, the batteries will not use up their entire resource (the period of their operation is limited by two seasons of the year), which will shorten the period of their exploitation.

Let's consider the second option of the combination of power generation and load (Fig. 10).
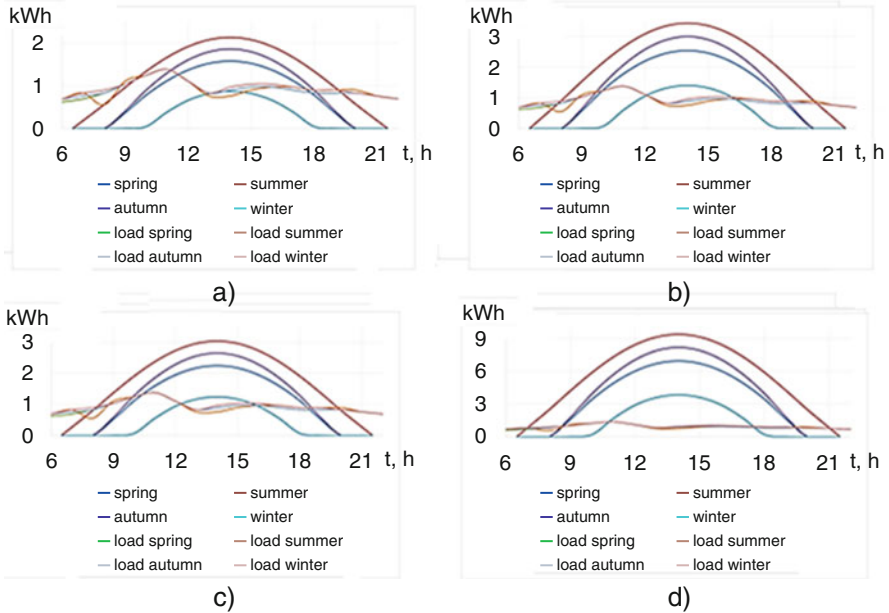
Fig. 10 Seasonal daily generation schedules for the second option of covering the typical load schedule for the agricultural consumer, selected for various specific days: June 22 (**a**), September 22 (**b**), March 21 (**c**), December 22 (**d**)

When the photovoltaic installation is equipped with 21 photovoltaic modules of the FSM-200 type, the load of the agricultural consumer is provided by 22.6% in winter, 60.8% in spring, and 70.4% in autumn and completely in summer.

For the number of photovoltaic modules $n = 264$ in summer, generation per day exceeds the load by 42.7%, and in spring and winter, the lack of electricity from the photovoltaic installation is 13.6% and 67.7%, respectively.

When photovoltaic modules in the amount corresponding to the date of March 22 are used, daily generation exceeds the load not only in summer by 61.7% but also in autumn by 14.0%, and in winter, electricity consumption is provided by only 36.3%.

To provide the daily amount of electrical energy required to carry out the technological process in winter, 93 modules of the FSM-200 type are needed to be installed on the photovoltaic installation. But the total generation per day from the installation will be 2.7–4.4 times higher than the load in the rest of the year.

Thus, when equipping photovoltaic installation with the storage battery, it is advisable to provide fully the consumer of electrical energy from it only for the summer period – the period of the highest intensity of solar radiation. In the rest of the year, more modules are required, which will lead to the need to reconfigure the power supply system or reorganize the technological process, which is not always possible.
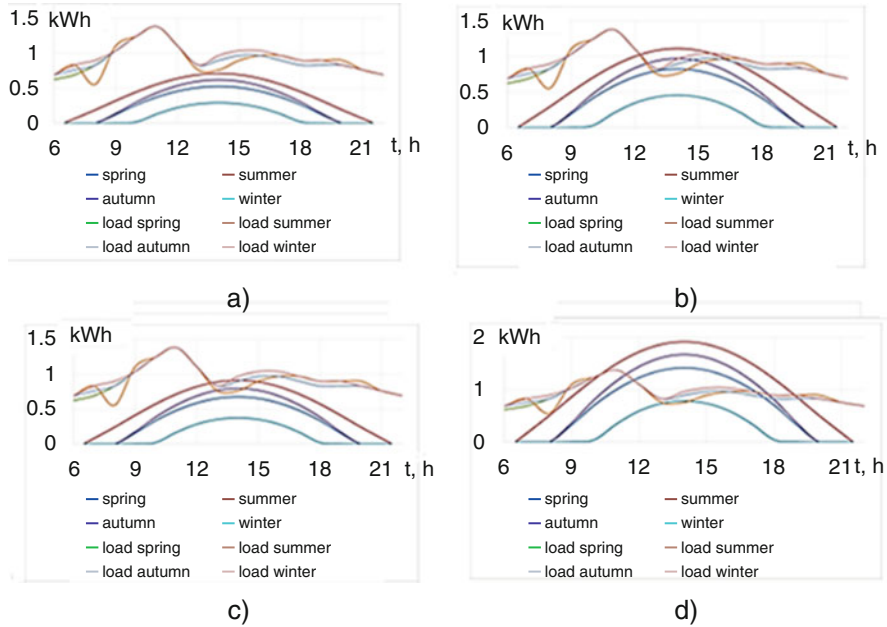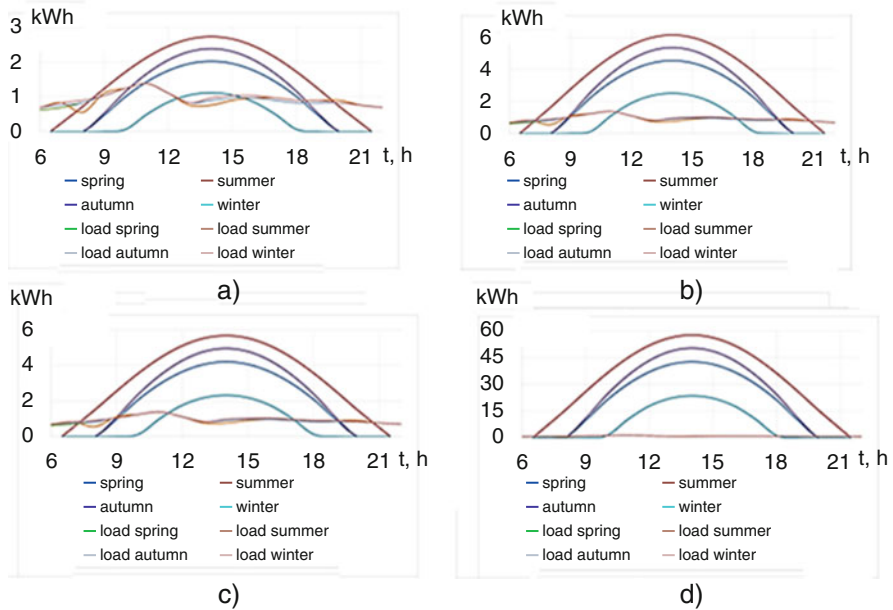
Fig. 11 Seasonal daily generation schedules for the third option for covering the typical load schedule for the agricultural consumer, selected for various specific days: June 22 (**a**), September 22 (**b**), March 21 (**c**), December 22 (**d**)

Figure 11 shows seasonal daily schedules for the generation and consumption of electrical energy for the third option to cover the load of the agricultural consumer.

The application of the third approach to the determination of the ratio of the power generation to the load leads to the fact that the total production of electrical energy per day at the photovoltaic installation significantly exceeds the amount required to ensure the technological process. In addition, the full coverage of the electric load schedule requires too many photovoltaic modules themselves, additional storage equipment, as well as a revision of the operating mode of the entire power supply system.

4 Conclusions

One of the main tasks in designing a solar power plant is to select optimal parameters for both photovoltaic modules and auxiliary equipment, duplicating and accumulating energy sources, which makes it possible to justify economically the electrical energy generation. Coordination of the graphs of electrical energy generation and consumption is most often carried out by introducing energy storage installations or additional generating equipment into the solar power plant, or

by organizing the discharge of excess generated electricity into the power grid. All this leads to a significant increase in the cost of the project, which in some cases amounts to a two- or threefold increase in material costs, and makes the conversion of solar energy into electrical energy economically inexpedient. That is why it is necessary to take into account the nature of changes in solar radiation on the considered territory throughout the year, and the influence of atmospheric phenomena, as well as the graph of electricity consumption, which will help to predict the operating mode of the installation and coordinate the schedules of generation and consumption.

The purpose of the research is to study various methods for calculating the electrical load of agricultural objects based on the available initial data and different options of supplying it by means of the solar photovoltaic system, taking into account the peculiarities of the consumer load graph. The load graph of the studied enterprise is very close to the typical agricultural processing enterprise load graph. The significance of the presented study consists in taking into account the effect of choosing the method and information source for determining the load of the consumer, which has a significant impact on the justification of the photovoltaic system parameters. The uniqueness of this study consists in the analysis of consumer load data obtained by various practical and calculation methods.

Application results of the recommendations of the Guidelines are characterized by the calculation accuracy of 4.8–64.7%. Besides, the less amount of initial information is required when determining the load according to the Guidelines. The chosen calculation method, according to available initial data, resulted in high calculation complexity and duration with a calculation error of 47.8% on average. Monitoring the actual electrical load curve was revealed to need technical devices or a set of devices to monitor consumed electricity and long time period of observation.

There were considered two types of graphs: the first graph is constant (lighting system of the flour-grinding areas of the enterprise); the second graph is a typical graph for an agricultural processing enterprise. For those load graphs, there were considered three options for load coverage. The application of the first approach to the selection of the power generation and load schedule combination for summer period allows, without using additional storage devices, to reduce consumption from the electric network. Since the forms of the production and load schedules are different, for the rest of the specific days, it is necessary to use additional equipment to utilize excess electrical energy in the peaks of solar radiation intensity, which will lead to an increase in the cost of the photovoltaic installation. In addition, the batteries will not use up their entire resource, that is, the period of their operation will be shortened. Applying the number of photovoltaic modules selected from the condition of ensuring the daily load for spring and autumn period, the overgeneration of electrical energy in the summer will be from 46.6% to 72.0%, which requires the reorganization of the technological process by connecting additional consumers, that is, to reconfigure power supply systems, which is not always technically feasible. The application of the third approach to determining the ratio of generation and load capacities results in the complete cover of the load

graph by the electric power generation graph, but the total output per day is tens of times greater than consumption.

Future studies require additional consideration of technical and economic indicators of photovoltaic system layout options and development of criteria for substantiating the parameters of a photovoltaic system for power supply of the agricultural consumer.

Conflicts of Interest: The authors declare no conflict of interest. The funders had no role in the design of the study; in the collection, analyses, or interpretation of the data; in the writing of the manuscript; or in the decision to publish the results.

References

1. Yudaev, I. V., Popov, M. Y., Seregin, A. A., Popova, R. V., & Daus, Y. V. (2021). Balance of heat flows in autonomous bio-vegetation complex as basis for its design. *IOP Conference Series-Earth and Environmental Science, 659*, 012036.

2. Nekrasov, A., Kharchenko, V., & Nekrasov, A. (2021). Evaluation of damages due to failures of electric motors in technological equipment of enterprises. *International Journal of Energy Optimization and Engineering., 1*(10), 1–15.

3. Kurin, S. Y., Antipov, A. A., Roenkov, A. D., Barash, I. S., Helava, H. I., Menkovich, E. A., Tarasov, S. A., Lamkin, I. A., Shmidt, N. M., & Makarov, Y. N. (2013). UV LEDs for high-current operation. *Journal of Physics Conference Series., 461*, 012028.

4. Sychov, A., Kharchenko, V. V., Vasant, P., & Uzakov, G. (2019). Application of various computer tools for the optimization of the heat pump heating systems with extraction of low-grade heat from surface watercourses. *Advances in Intelligent Systems and Computing, 866*, 310–319.

5. Vasil'yev, S. I., Mashkov, S. V., Syrkin, V. A., Gridneva, T. S., & Yudaev, I. V. (2018). Results of studies of plant stimulation in a magnetic field. *Research Journal of Pharmaceutical Biological and Chemical Sciences., 9*(4), 706–710.

6. Yudaev, I. V., Daus, Y. V., Gamaga, V. V., Grachev, S. E., & Kuligin, V. S. (2018). Plant tissue sensitivity to electrical impulse. *Research Journal of Pharmaceutical Biological and Chemical Sciences., 9*(4), 734–739.

7. Lipsits, I. V., & Kosov, V. V. (1996). *Investitsionnyy proyekt: metody podgotovki i analiza: uchebno–spravochnoye posobiye* [Investment project: Methods of preparation and analysis: Study guide]; Izdatel'stvo BEK. (In Russian).

8. Cagnin, C., Havas, A., & Saritas, O. (2013). Future-oriented technology analysis: Its potential to address disruptive transformations. *Technological Forecasting and Social Change, 80*, 379–385.

9. Oborin, M. S. (2021). Transformation of agriculture in the digital economy, Vestnik Nizhegorodskogo universiteta im. N.I. Lobachevskogo. *Seriya: Sotsial'nyye nauki., 1*(61), 14–21.

10. Baev, V. I., & Yudaev, I. V. (2008). Efficiency estimation of type of the electrical exposure on plants at their processing. *AD Alta-Journal of Interdisciplinary Research., 8*(1), 252–257.

11. Izmaylov, A. Y., Sidorov, S. A., Khoroshenkov, V. K., Khlusova, E. I., & Ryabov, V. V. (2017). Novel high-alloy boron-containing steels for driven elements of tilling machines. *Metal Science and Heat Treatment., 59*(3–4), 208–210.

12. Kovalev, A. A., Kovalev, D. A., Panchenko, V., & Kharchenko, V. (2021). Intellectualized control system for anaerobic bioconversion of liquid organic waste. *International Journal of Energy Optimization and Engineering., 10*(1), 56–81.

13. Ksenz, N. V., Yudaev, I. V., Taranov, M. A., Sidorcov, I. G., Semenikhin, A. M., & Chernovolov, V. A. (2019). Determination of the efficiency of the operation mode of nonflowing installation for electroactivation of water and aqueous solutions. *International Journal of Automation Technology, 13*(4), 539–544.

14. Mashkov, S. V., Kuznetsov, M. A., Fatkhutdinov, M. R., Gridneva, T. S., & Yudaev, I. V. (2020). Estimation of the accuracy parameters of automatic regulation of the flow of bulk materials on mobile vehicles under random external influences. *Research Journal of Pharmaceutical Biological and Chemical Sciences., 9*(4), 1077–1088.

15. Mazing, D. S., Matyushkin, L. B., Aleksandrova, O. A., Mikhailov, I. I., Moshnikov, V. A., & Tarasov, S. A. (2014). Synthesis of cadmium selenide colloidal quantum dots in aquatic medium. *Journal of Physics Conference Series., 572*, 012028.

16. Yarymbash, D. S., Yarymbash, S. T., Kotsur, M. I., & Litvinov, D. O. (2018). Computer simulation of electromagnetic field with application the frequency adaptation method. *Radio Electronics Computer Science Control, 1*, 65–74.

17. Mikhailov, I. I., Tarasov, S. A., Solomonov, A. V., Aleksandrova, O. A., Matyushkin, L. B., & Mazing, D. S. (2014). The study of CdSe colloidal quantum dots synthesized in aqueous and organic media. *Journal of Physics Conference Series., 572*, 012029.

18. Daus, Y. V., Kharchenko, V. V., & Yudaev, I. V. (2021). Optimizing layout of distributed generation sources of power supply system of agricultural object. *International Journal of Energy Optimization and Engineering., 10*(3), 70–84.

19. Daus, Y. V., Kharchenko, V. V., & Yudaev, I. V. (2021). Research of solar energy potential of photovoltaic installations on enclosing structures of buildings. *International Journal of Energy Optimization and Engineering., 10*(4), 18–34.

20. Bayindir, R., Colak, I., Fulli, G., & Demirtas, K. (2016). Smart grid technologies and applications. *Renewable and Sustainable Energy Reviews., 66*, 499–516.

21. Daus, Y., & Yudaev, I. (2017). Estimation of solar energy potential under conditions of urban development. In *Proceedings of the International conference actual issues of mechanical engineering 2017 (AIME 2017)*, Tomsk, Russia, July 27–29; Malozyomov, B. V., Vilberger, M. E., & Martyushev, N., Eds. (2017). (vol. 133, pp 156−161). Atlantis Press.

22. Panchenko, V. (2020). Roofing solar panels of planar and concentrator designs. *International Journal of Energy Optimization and Engineering, 4*(9), 20–40.

23. Panchenko, V. (2021). Photovoltaic thermal module with paraboloid type solar concentrators. *International Journal of Energy Optimization and Engineering., 2*(10), 1–23.

24. Atwater, M., & Ball, J. T. (1978). A numerical solar radiation model based on standard meteorological observation. *Solar Energy., 21*, 163–170.

25. Panchenko, V., Izmailov, A., Kharchenko, V., & Lobachevskiy, Y. (2020). Photovoltaic solar modules of different types and designs for energy supply. *International Journal of Energy Optimization and Engineering, 2*(9), 74–94.

26. Gu, W., Wu, Z., Bo, R., Liu, W., Zhou, G., Chen, W., & Wu, Z. (2014). Modeling, planning and optimal energy management of combined cooling, heating and power microgrid: A review. *International Journal of Electrical Power & Energy Systems., 54*, 26–37.

27. Hoppmann, J., Volland, J., Schmidt, T. S., & Hoffmann, V. H. (2014). The economic viability of battery storage for residential solar photovoltaic systems – A review and a simulation model. *Renewable and Sustainable Energy Reviews., 39*, 1101–1118.

28. Panchenko, V., Kharchenko, V., & Vasant, P. (2019). Modeling of solar photovoltaic thermal modules. *Advances in Intelligent Systems and Computing, 866*, 108–116.

29. Koohi-Kamali, S., Rahim, N. A., & Mokhlis Sam, H. (2014). Smart power management algorithm in microgrid consisting of photovoltaic, diesel, and battery storage plants considering variations in sunlight, temperature, and load. *Energy Conversion and Management., 84*, 562–582.

30. Strebkov, D. S., & Kharchenko, V. V. (2012). Innovative technologies developed for renewable energy sources. *Problemele Energeticii Regionale, 3*, 64–75.

31. Edalati, S., Ameri, M., Iranmanesh, M., Tarmahi, H., & Gholampour, M. (2016). Technical and economic assessments of grid–connected photovoltaic power plants: Iran case study. *Energy, 114*, 923–934.

32. Daus, Y. V., Pavlov, K. A., Yudaev, I. V., & Dyachenko, V. V. (2019). Increasing solar radiation flux on the surface of flat-plate solar power plants in Kamchatka Krai conditions. *Applied Solar Energy (English translation of Geliotekhnika), 55*(2), 101–105.
33. Yudaev, I. V., Daus, Y. V., Zharkov, A. V., & Zharkov, V. Y. (2020). Private solar power plants of Ukraine of small capacity: Features of exploitation and operating experience. *Applied Solar Energy (English translation of Geliotekhnika)., 56*(1), 54–62.
34. Daus, Y. V., & Yudaev, I. V. (2016). Designing of software for determining optimal tilt angle of photovoltaic panels. In *Proceedings of the International conference on education, management and applied social science (EMASS 2016).* PEOPLES R CHINA, November 20–21, 2016; Destech Publicat Inc.: Lancaster.
35. Koohi-Kamali, S., Tyagi, V. V., Rahim, N. A., Panwar, N., & Mokhlis, H. (2013). Emergence of energy storage technologies as the solution for reliable operation of smart power systems: A review. *Renewable and Sustainable Energy Reviews., 25*, 135–165.
36. Kudrin, B. I. (2015). Raschet elektricheskikh nagruzok potrebiteley: istoriya, sostoyaniye, kompleksnyy metod [Calculation of electrical loads of consumers: History, state, complex method]. *Industrial Energy, 5*, 14–22.
37. Leshchinskaya, T. B., & Naumov, I. V. (2015). *Elektrosnabzheniye sel'skogo khozyaystva: uchebnoye posobiye* [Electricity supply for agriculture: Textbook]; BIBKOM, TRANSLOG. (In Russian).
38. Fadeyeva, G. A., & Fedin, V. T. (2009). *Proyektirovaniye raspredelitel'nykh elektricheskikh setey: uchebnoye posobiye* [Design of electrical distribution networks: Textbook]; Vysha shkola. (In Russian).
39. Yershov, A. M. (2018). *Sistemy elektrosnabzheniya. Chast' 2: Elektricheskiye nagruzki. Kompensatsiya reaktivnoy moshchnosti: kurs lektsiy* [Power supply systems. Part 2: Electrical loads. Reactive power compensation: A course of lectures]; Izdatel'skiy tsentr YUUrGU. (In Russian).
40. RD 34.20.178-82. (1981). Rukovodyashchiye materialy po proyektirovaniyu elektrosnabzheniya sel'skogo khozyaystva. Metodicheskiye ukazaniya po raschetu elektricheskikh nagruzok v setyakh 0.38–110 kV sel'skokhozyaystvennogo naznacheniya [Agricultural Power Design Guidelines. Methodical instructions for calculating electrical loads in networks of 0.38–110 kV for agricultural purposes], Moscow. (In Russian).
41. Amerkhanov, R. A., Bogdan, A. V., Verbitskaya, S. V., & Gar'kavyy, K. A. (2010). Proyektirovaniye sistem energoobespecheniya: uchebnik dlya studentov vuzov po napravleniyu «Agroinzheneriya» [Designing power supply systems: A textbook for university students in the direction of "Agroengineering"]; Energoatomizdat. (In Russian).
42. Zernovoy elevator [Grain elevator]. https://ru.wikipedia.org/wiki/Zernovoy_elevator. Accessed May 21, 2020.
43. Budzko, I. A., & Zul', N. M. (1990). *Elektrosnabzheniye sel'skogo khozyaystva: uchebnoye posobiye* [Electrical supply of agriculture: Textbook]; Energoatomizdat. (In Russian).
44. Solar Power System. (n.d.). *Solar battery FSM-200.* http://solar-power-system.ru/id/solnechnaya-batareya-fsm-200-m-5.html. Accessed August 21, 2021.
45. Jo, J. H., Loomis, D. G., & Aldeman, M. R. (2016). Optimum penetration of utility–scale grid–connected solar photovoltaic systems in Illinois. *Renewable Energy, 60*, 20–26.
46. Yundin, M. A. (2011). *Tokovaya zashchita elektroustanovok: uchebnoye posobiye* [Current protection of electrical installations: A tutorial.]; Izdatel'stvo «Lan'». (In Russian).
47. Vick, B. D., & Moss, T. A. (2013). Adding concentrated solar power plants to wind farms to achieve a good utility electrical load match. *Solar Energy., 92*, 298–312.
48. Weniger, J., Tjaden, T., Bergner, J., & Quaschning, V. (2016). Sizing of battery converters for residential PV storage systems. *Energy Procedia, 99*, 3–10.
49. Weniger, J., Tjaden, T., & Quaschning, V. (2014). Sizing of residential PV battery systems. *Energy Procedia, 46*, 78–87.
50. Xu, Y., Yan, C., Liu, H., Wang, J., Yang, Z., & Jiang, Y. (2020). Smart energy systems: A critical review on design and operation optimization. *Sustainable Cities and Society., 62*, 102369.

51. Zhou, K., Yang, S., Chen, Z., & Ding, S. (2014). Optimal load distribution model of microgrid in the smart grid environment. *Renewable and Sustainable Energy Reviews., 35*, 304–310.
52. Abdulaal, A., Moghaddass, R., & Asfour, S. (2017). Two-stage discrete-continuous multi-objective load optimization: An industrial consumer utility approach to demand response. *Applied Energy., 206*, 206–211.
53. Stevanović, D. (2014). Remarks on dynamic load balancing of integer loads and integral graphs. *Applied Mathematics and Computation., 226*, 38–43.
54. Rodriguez, A., Smith, S. T., & Potter, B. (2022). Sensitivity analysis for building energy audit calculation methods: Handling the uncertainties in small power load estimation. *Energy, 238, A*, 121511.
55. Dong, X., Wang, C., Yun, Z., Han, X., Liang, J., Wang, Y., & Zhao, P. (2018). Calculation of optimal load margin based on improved continuation power flow model. *International Journal of Electrical Power & Energy Systems., 94*, 225–233.
56. Saccomanno, F. (2009). Dynamic behavior of network elements and loads. In *Electric power system: Anal control* (pp. 352–485).
57. Borghetti, A., Caldon, R., Mari, A., & Nucci, C. A. (1997). On dynamic load models for voltage stability studies. *IEEE Transactions on Power Apparatus and Systems, 12*(1), 293–303.
58. Chiang, H. D., & Jean, J. R. (1995). A more efficient formulation for computation of the maximum loading points in electric power systems. *IEEE Transactions on Power Systems, 10*(2), 635–646.
59. Tavares, B., Bedriñana, M., & Castro, C. A. (2011). Practical method for computing the maximum loading point using a load flow with step size optimization. *IET Generation Transmission and Distribution, 5*(12), 1250–1258.
60. Li, H., Jin, Y., Zhang, A., Shen, X., Chao, L., & Kong, B. (2006). An improved hybrid load flow calculation algorithm for weakly-meshed power distribution system. *International Journal of Electrical Power & Energy Systems, 74*, 437–445.
61. Pecas, J. A., Lopes, N., Hatziargyriou, J. M., et al. (2007). Integrating distributed generation into electric power systems: A review of drivers, challenges and opportunities. *Electric Power Systems Research, 77*(9), 1189–1203.
62. Keyhani, A., Abur, A., & Hao, S. (1989). Evaluation of power flow techniques for personal computers. *IEEE Transactions on Power Apparatus and Systems, 4*(2), 817–826.
63. Luo, G. X., & Semlyen, A. (1990). Efficient load flow for large weakly meshed networks. *IEEE Transactions on Power Apparatus and Systems, 5*(4), 1309–1316.
64. Daus, Y. V., Kharchenko, V. V., Yudaev, I. V., Desyatnichenko, D. A., & Stepanchuk, G. V. (2020). Improving the efficiency of the power supply to agricultural facilities by means of roof-top photovoltaic installations. *Applied Solar Energy, 56*(3), 207–211.
65. Daus, J., Desyatnichenko, D., & Stepanchuk, G. (2020). *Analysis of approaches to determining solar radiation intensity at preset geographical point*. Proceedings - 2020 International Conference on Industrial Engineering, Applications and Manufacturing, 9111932d.
66. Gorjian, S., Kamrani, F., Fakhraei, O., Samadi, H., & Emami, P. (2022). Chapter 12 – Emerging applications of solar energy in agriculture and aquaculture systems. In *Solar energy advancements in agriculture and food production systems* (pp. 425–469).
67. Amir Ghalazman, E., Das, G. P., Gould, I., Zarafshan, P., Vishnu Rajendran, S., Heselden, J., Badiee, A., Wright, I., & Pearson, S. (2022). Chapter 10 – Applications of robotic and solar energy in precision agriculture and smart farming. In *Solar energy advancements in agriculture and food production systems* (pp. 351–390).
68. Gorjian, S., Ebadi, H., Jathar, L. D., & Savoldi, L. (2022). Chapter 1 – Solar energy for sustainable food and agriculture: Developments, barriers, and policies. In *Solar energy advancements in agriculture and food production systems* (pp. 1–28).
69. AmirVadiee. (2022). Chapter 7 – Solar heating and cooling applications in agriculture and food processing systems. In *Solar energy advancements in agriculture and food production systems* (pp. 237–270).

RBFNN for MPPT Controller in Wind Energy Harvesting System

Tigilu Mitiku Dinku and Mukhdeep Singh Manshahia ⓘ

1 Introduction

Due to several problems such as pollution, global warming, international energy crises, and others, the world's electric energy consumption continues to increase [1]. Wind energy is a type of renewable energy which has been growing at a faster rate in most parts of the world [2]. Based on their range of operation, WECS is classified as a variable speed wind turbine (VSWT) and a fixed speed wind turbine (FSWT). Medium- to high-performance applications widely use variable speed WECS. The VSWT are generally operated with permanent magnet synchronous generator (PMSG). PMSG is preferred often for its better efficiency and use without gear box. For WECS to produce maximum energy, it must function at its maximum efficiency. In the last few years, several MPPT techniques have been applied to increase the efficiency of the system [3]. The main drawback of conventional methods is they perform effectively at constant wind speed [4].

RBFN has the ability to approximate any complicated nonlinearity infinitely with fault tolerance. It has a faster convergence property having simpler network structure as compared to common multilayer perceptron (MLP) neural networks [5]. RBFNN was proposed in [6] to extract the maximum power by controlling the duty cycle of boost converter. In [7], RBFNN was applied to manage the pitch angle by acting on the generator speed above the rated wind zone. Better result was obtained as compared to proportional integral (PI) controller. In [8], a hybrid method for control of generator torque was presented for the MPPT region to produce maximum

T. M. Dinku
Department of Mathematics, Bule Hora University, Bule Hora, Ethiopia

M. S. Manshahia (✉)
Department of Mathematics, Punjabi University Patiala, Patiala, Punjab, India

power. The PI controller was applied to regulate the generator torque. In [9], RBF was developed in two stages. The first one is a two-stage conversion with a diode bridge rectifier and boost converter unit, whereas the second one is a single-stage conversion unit with the boost-type Vienna Rectifier.

In this study, RBFNN-based MPPT controller is proposed for wind turbines to produce maximum output power by adjusting the duty cycle of the converter. The control tracks optimal rotor speed of WECS to give the maximum power above and below the rated speed of wind turbine.

The paper is arranged as follows: Sect. 2 presents about wind turbine dynamic model and PMSG model. The proposed technique is detailed in Sect. 3. In Sect. 4, simulation results are presented and discussed before conclusion and future scopes.

2 Wind Energy Harvesting System

The overall block diagram of variable speed stand-alone WEHS proposed in this paper is shown in Fig. 1. It contains wind turbine, directly driven PMSG-based wind turbine, a bridge rectifier, a DC-DC boost converter, battery banks for backup, and a DC-DC bidirectional buck-boost converter.
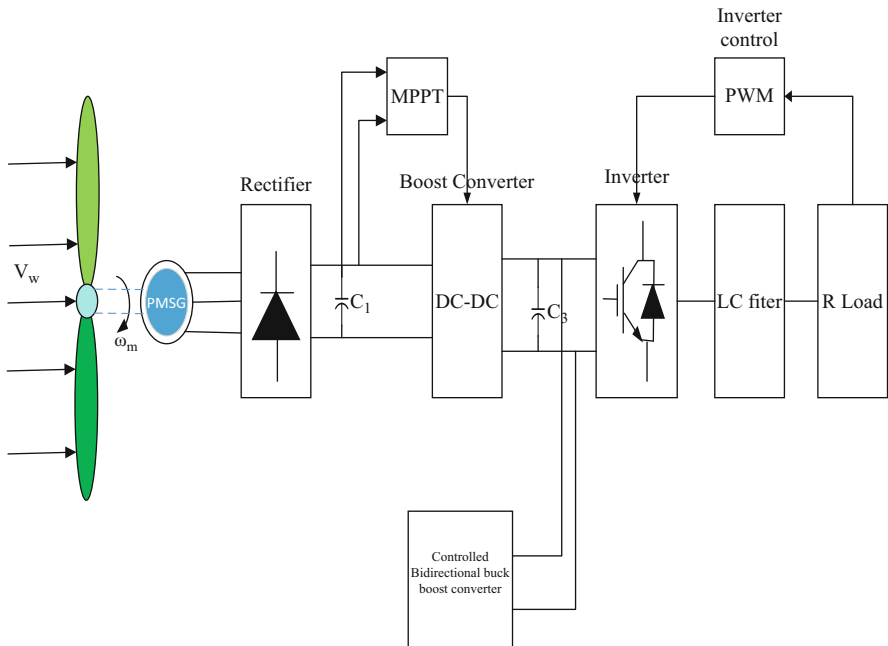
Fig. 1 Block diagram of wind turbine system

2.1 Model of Wind Turbine

The maximum mechanical power produced by turbine can be written as [10]

$$P_{m\_opt} = \frac{1}{2} C_{P\_max} \pi \frac{R}{\lambda_{opt}}^5 \omega_{m\_opt}^3 = K_{opt} \omega_{m\_opt}^3 \tag{1}$$

where C_p is a nonlinear function of β and λ given by [11]

$$C_p(\lambda, \beta) = 0.5716 \left(\frac{116}{\lambda_i} - 0.4\beta - 5 \right) e^{\frac{-21}{\lambda_i}} + 0.0068\lambda_i \tag{2}$$

with

$$\frac{1}{\lambda_i} = \frac{1}{\lambda + 0.08\beta} - \frac{0.035}{\beta^3 + 1} \tag{3}$$

where

$$\lambda_{opt} = \frac{\omega_{m\_opt} V_w}{R} \tag{4}$$

The optimum torque can be given by

$$T_{m\_opt} = K_{opt} \omega_{m\_opt}^2 \tag{5}$$

Wind turbine power characteristics are shown in Fig. 2. Based on the variation of wind speeds, the operations of turbine can be separated into four parts with different control strategies. Region one is when wind speed is less than V_{cut_in}, the turbine doesn't rotate, as the energy produced is not enough to cover the internal consumption. Hence, it is switched off. The second region is when the wind speed is between V_{cut_in} and V_{rated}, the turbine is controlled to produce maximum power. Hence, this region is called MPPT region. Region 3 is when the turbine is between V_{rated} and V_{cutout}, the turbine pitch angle is controlled. This region is called full-load region. The last region is when the wind speed is greater than V_{cutout}, the turbine is totally close to safeguard the turbine from damage. The values of V_{cut_in}, V_{rated}, and V_{cutout} are 3 m/s, 12 m/s and 25 m/s, respectively.

2.2 Modeling of the PMSG

The model of the turbine, the generator, and the bridge rectifier that converts the AC to DC is show in Fig. 3.
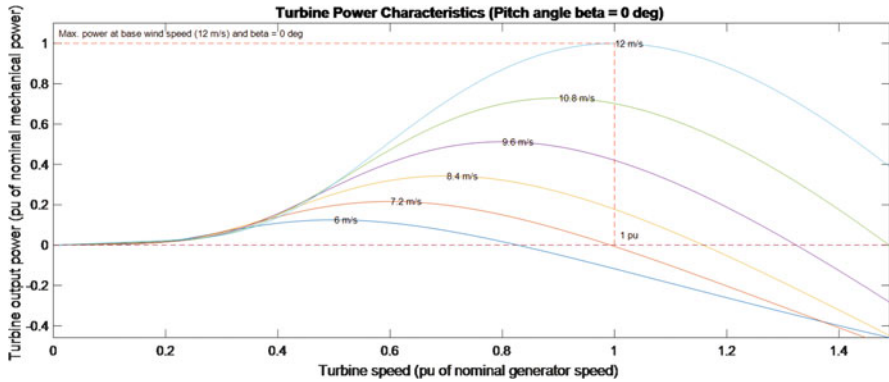
Fig. 2 Wind turbine power characteristics
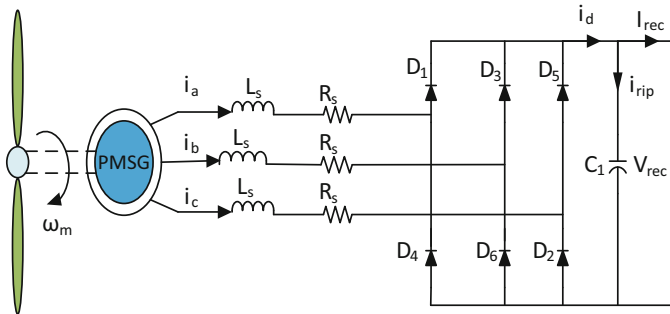
Fig. 3 Direct-drive PMSG connected to the rectifier

3 Proposed Control Strategies

Artificial intelligence (AI) plays an important role in WEHS to efficiently optimize
the power output. The uncertain or unknown variations in plant parameters can be
dealt more effectively by using AI techniques [12].

3.1 Radial Basis Function (RBF)

RBF is one of the different types of ANNs which uses RNFs as activation functions.
It is a type of feedforward network MLP proposed by Broomhead and Lowe in
1988 [13]. The hidden layer of RBFNN contains the hidden nodes that perform
computation using radial basis function. The weights are modified during training.
The performance of the RBFNN depends on the interconnection pattern, weights,
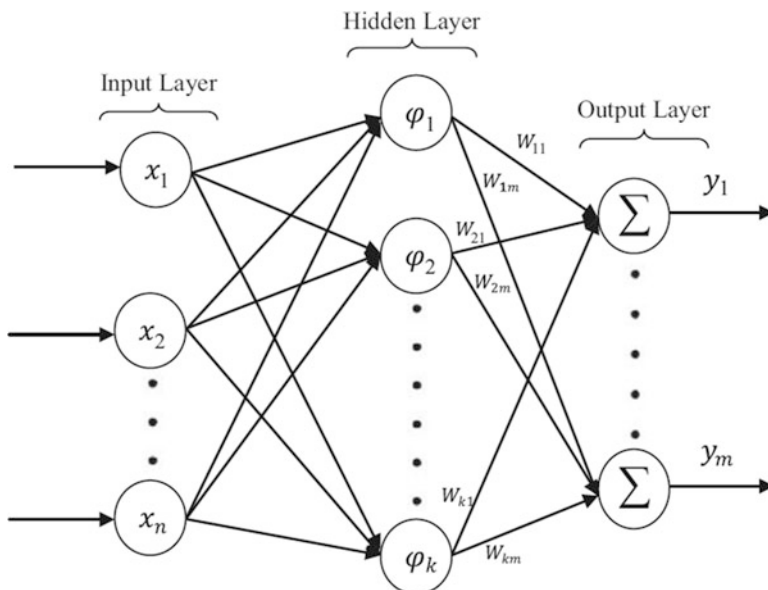
Fig. 4 RBFNN structure

and activation function present in the system and on the center of activation functions and the distribution of center of activation functions [14] (Fig. 4).

RBFN training process is performed in two steps. The first is unsupervised methods in which the parameters directing the basis function are estimated. The supervised training method on the basis of gradient descent is employed in second step to adjust the RBFN parameters [15, 16]. The calculated error is used based on the training patterns to regulate the parameters W_{ij}, c_{ij}, and σ_{ij} of the RBFN. Figure 5 shows the training performance of RBFNN.

The RBFN parameters considered are given in Table 1.

4   Simulation Results and Discussion

The WECS contains a 20 kW wind turbine and PMSG, a boost converter, a 10 kW battery with DC-DC bidirectional buck boost converter, an inverter, filters, a total 10 kW load, measuring units, and controllers. The voltages are fixed at 400 V and 50 Hz. The SPWM-based VSI has a 5 kHz switching frequency. Discrete time control is concluded with a sampling time of 5 μs. The simulated system is shown in Fig. 6. The parameters of the system used are given in Table 2.

The system is subjected to a step change of wind speed for 5 seconds with average wind speed of 12 m/s as shown in Fig. 7.
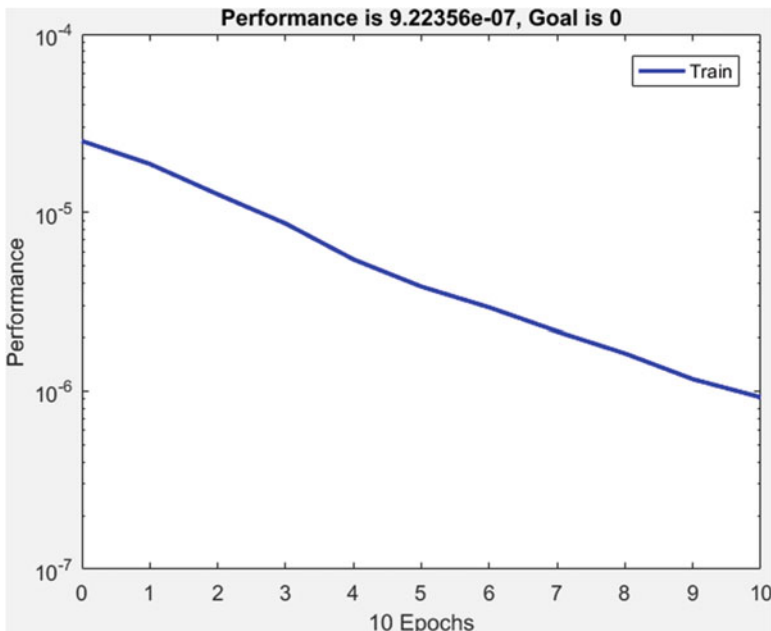
Fig. 5 Mean square error performance of RBF-NN

Table 1 Parameters of
trained RBFNN

Parameters	Values
Input neurons	1
Hidden neurons	20
Output neurons	1
Learning rate	0.1
Basis width (spread)	0.39
Training time	0.88

The rotational speed, tip speed ratio, and power coefficient are given in Figs. 8, 9, and 10, respectively. The rotational speed of the generator follows the changes of wind speed in order to bring the operating points around its optimal value where WEHS is at its high level of efficiency as shown in Fig. 8. Despite the rapid changes of the wind speed as shown in Figs. 8 and 9, respectively, this result verifies the performance of the MPPT algorithm.

The turbine mechanical power and output electrical power are shown in Fig. 11. The electrical power follows the change in wind speed, and it is matching with the theoretical power. The power losses are almost negligible. Hence, the electrical power output of the generator is also 20 kW at rated wind speed.

Figure 12 shows DC voltage at the terminal of boost converter. The voltage across the DC-link capacitor is maintained to reference voltage of 800 V. The output power of boost converter and battery is given in Fig. 13. There is slight difference between
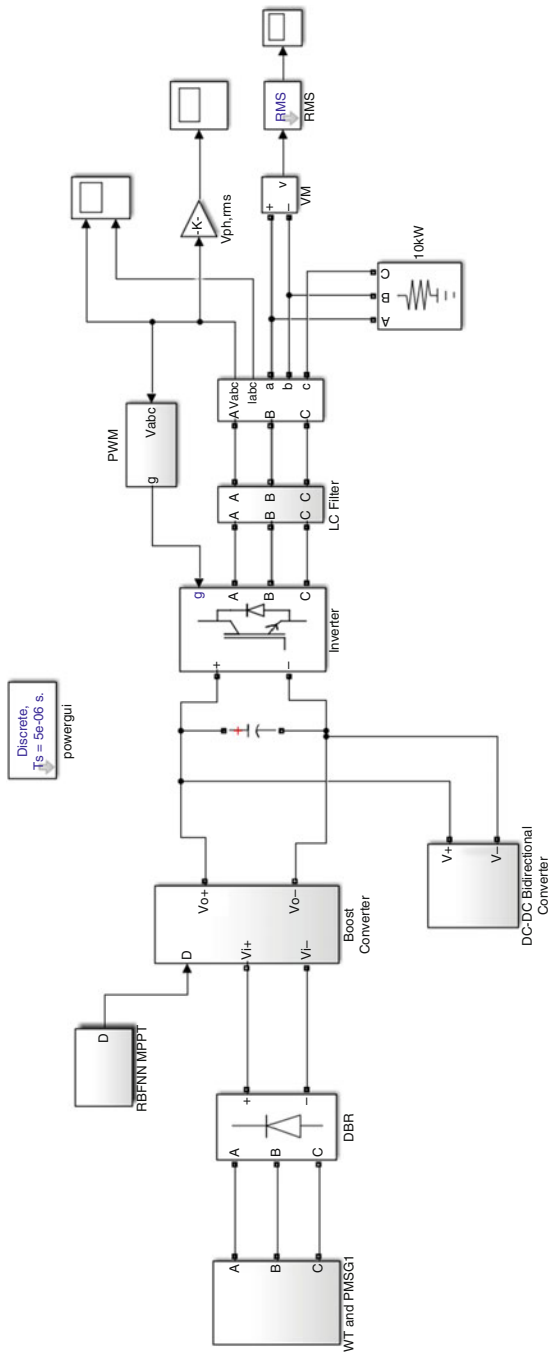
Fig. 6 Simulation of WECS with ANN MPPT

Table 2 Parameters of wind
turbine and PMSG

PMSG	
Rated power	20 kW
Rated speed	22 rad/s
Armature resistance, Rs	0.1764 ohm
Stator inductance, ls	0.0048 H
No of poles	36
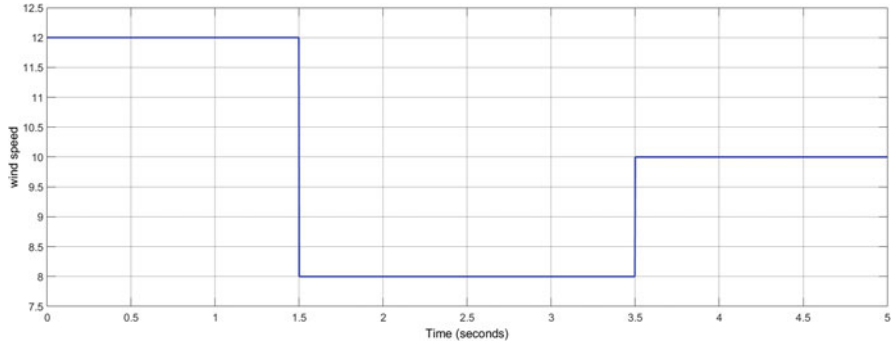
Fig. 7 Wind speed
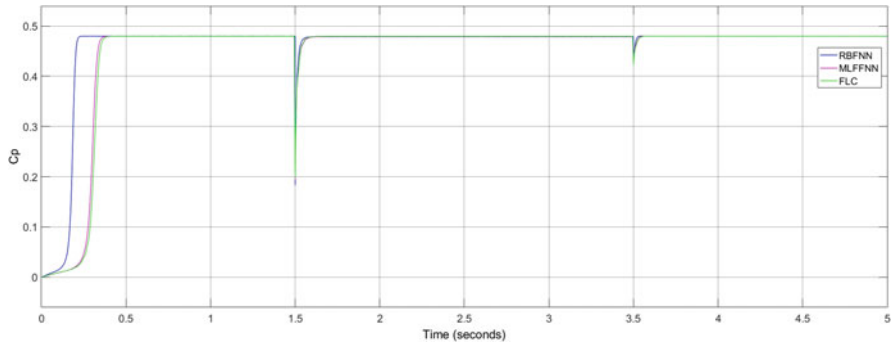
Fig. 8 Power coefficient of wind turbine

P_{dc} and P_{bat} because of the power losses corresponding to the converters. When the load is supplied by wind power, the battery power is negative as it is in charging mode. When wind is not sufficient to supply the load, the battery starts supplying power to the load and keeps the DC link voltage constant.

The output voltage of SPWM-based VSI is shown in Fig. 14. A constant 400 V AC voltage is obtained after filtering at the load terminal with a constant frequency of 50 Hz and reaches this value at 0.02 s.

The performance comparison of FLC, MLFFNN, and RBFN based on extracted maximum turbine power at base wind speed is given in Table 3. It shows that RBFN gives better results as compared to FLC.
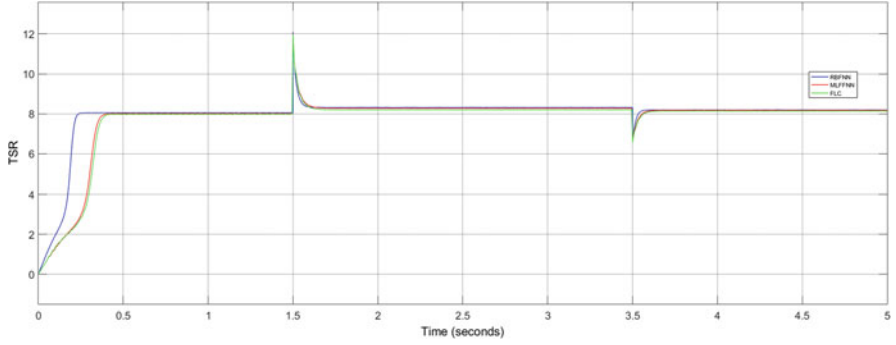
Fig. 9 TSR of wind turbine
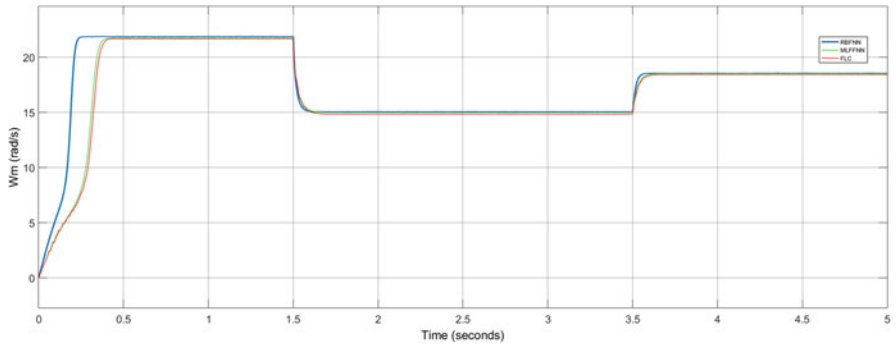
Fig. 10 Generator speed
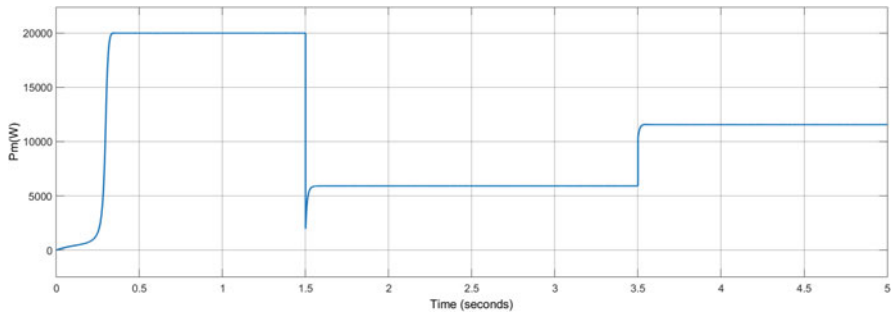
Fig. 11 Mechanical output power of wind turbine
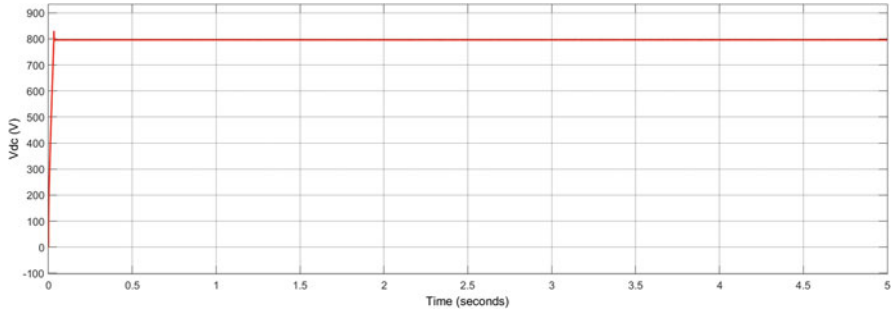
Fig. 12 Boost converter output voltage
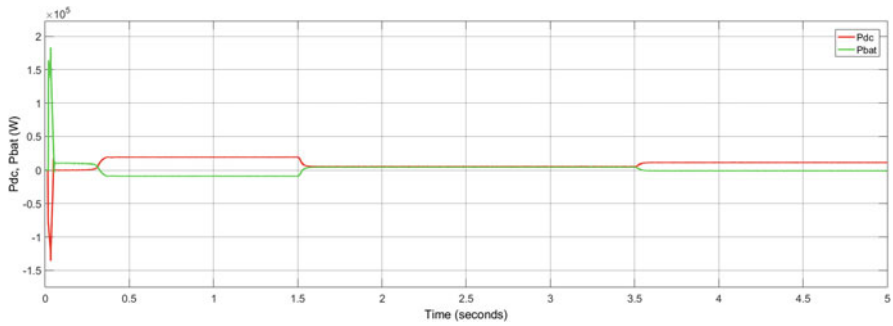
Fig. 13 Boost converter and battery output power
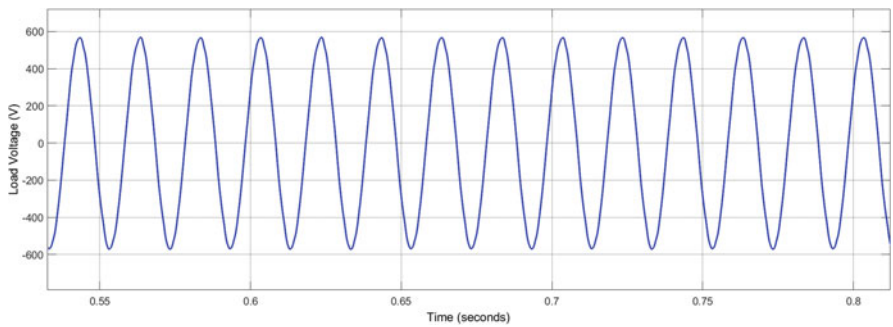
Fig. 14 Load line voltage (v)

The THD value of AC voltage and current computed for three cycles is found to be 0.66% (Fig. 15a). Similarly, it is found that the THD in load current (Fig. 15b) is 0.66%.

Table 3 Performance comparison between FLC and RBFNN

Controller type	Average power (Pm)
RBFNN	20 kW
MLFFNN	19.5 kW
FLC	19.01Kw
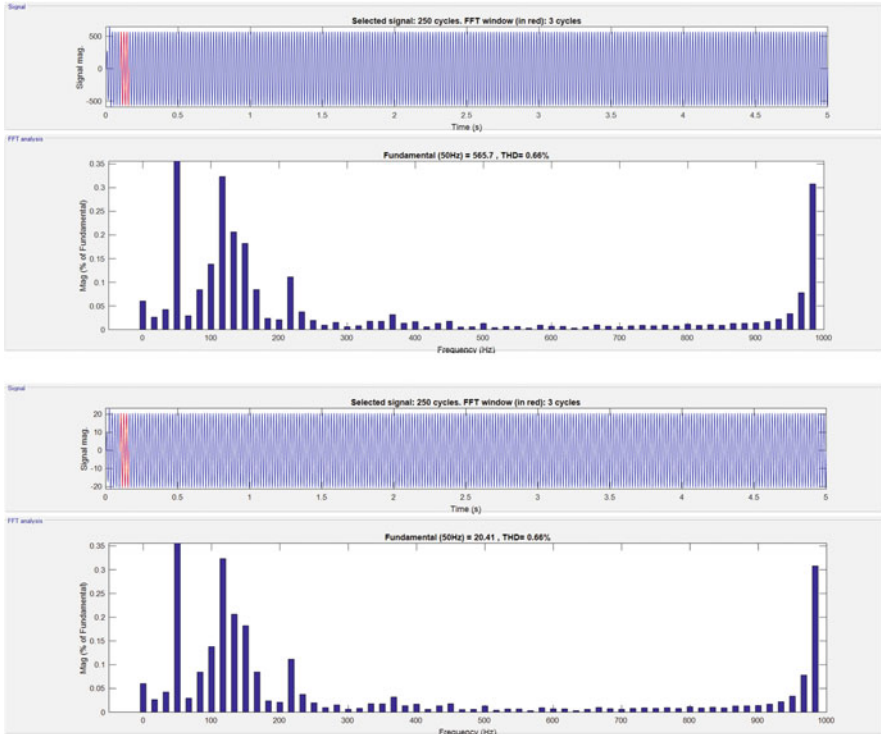
Fig. 15 THD value: (**a**) THD of load voltage and (**b**) THD of load current

5 Conclusion

This paper presents AC-DC-DC-AC-based energy conversion system through RBFN controller. The battery banks along with controller supply constant power to the load. These simulations show that the proposed controller gives better results under variable wind. It satisfies the load demand without the effect of wind speed change with better quality of the battery charging/discharging process. The performance of the proposed controller gives better results as compared to FLC and MLFFN. As a future work, it is better if the system is combined with a solar system to guarantee the supply power to remote areas and decrease the number of batteries.

References

1. Gaied, E. A. H. (2022). *Comparative analysis of MPPT techniques for enhancing a wind energy conversion system*.
2. GWEC-Global-Wind-Report. (2022).
3. El Aissaoui, H., El Ougli, A., & Tidhaf, B. (2021). Neural networks and fuzzy logic based maximum power point tracking control for wind energy conversion system. *Advances in Science, Technology and Engineering Systems, 6*, 586–592.
4. Sitharthan, R., Karthikeyan, M., Sundar, D. S., & Rajasekarana, S. (2020). Adaptive hybrid intelligent MPPT controller to approximate effectual wind speed and optimal rotor speed of variable speed wind turbine. *ISA Transactions, 96*, 479–489.
5. Huang, C.-H. (2014). Modified neural network for dynamic control and operation of a hybrid generation systems. *Journal of Applied Research and Technology, 12*, 1154.
6. Kumar, R., Agrawal, H. P., Shah, A., & Bansal, H. O. (2019). Maximum power point tracking in wind energy conversion system using radial basis function based neural network control strategy. *Sustainable Energy Technologies and Assessments, 36*, 100533.
7. El Hajjaji, A., & Khamlichi, A. (2017). Analysis of a RBF neural network based controller for pitch angle of variable-speed wind turbines. *Procedia Engineering, 181*, 552–559.
8. Assareh, E., & Biglari, M. (2015). A novel approach to capture the maximum power from variable speed wind turbines using PI controller, RBF neural network and GSA evolutionary algorithm. *Renewable and Sustainable Energy Reviews, 51*, 1023–1037.
9. Ramasamy, S. (2017). Single stage energy conversion through an RBFN controller based boost type Vienna rectifier in the wind turbine system. *Gazi University Journal of Science, 30*(4), 253–266.
10. Ndirangu, J. G., Nderu, J. N., Maina, C. M., & Muhia, A. M. (2016). Power output maximization of a PMSG based standalone wind energy conversion system using fuzzy logic. *IOSR Journal of Electrical and Electronics Engineering, 11*(1), 58–66.
11. Khaing, T. Z., & Kyin, L. Z. (2015). Control scheme of stand-alone power supply system with battery energy storage system. *International Journal of Electrical, Electronics and Data Communication, 3*(6), 19–25.
12. Hussein, M., Senjyu, T., Orabi, M., Wahab, M., & Hamada, M. (2013). Control of a stand-alone variable speed wind energy supply system. *Applied Sciences Open Access, 3*(2), 437–456.
13. Poultangari, I., Shahnazi, R., & Sheikhan, M. (2012). RBF neural network based PI pitch controller for a class of 5-MW wind turbines using particle swarm optimization algorithm. *ISA Transactions, 51*(5), 641–648.
14. Hayati. (2013). Application of radial basis function network for the modeling and simulation of turbogenerator. *Journal of Advances in Information Technology, 4*(2), 76–79.
15. Tiwari, R., & Rameshbabu, N. (2017). Comparative analysis of pitch angle controller strategies for PMSG based wind energy conversion system. *I.J. Intelligent Systems and Applications, 5*, 62–73.
16. Hong, C.-M., Chen, C.-H., & Tu, C.-S. (2013). Maximum power point tracking-based control algorithm for PMSG wind generation system without mechanical sensors. *Energy Conversion and Management, 69*, 58–67.

Simulation Optimum Performance All-Wheels Plug-In Hybrid Electric Vehicle

Salem Al-Assadi

1 Introduction

The rising gas prices starting around 2004, concerns around air quality, and the *Environmental Protection Agency (EPA)* regulations have increased interest in renewable forms of energy using *hybrid electric vehicles (HEVs)* and other less polluting alternatives such as *battery electric vehicles (BEVs)* [1, 2].

HEVs combine at least two energy converters from *internal combustion engine (ICE)* and *electric motor (E-motor)* to meet the power demand and to provide mileage range and safety similar to conventional *ICE* vehicle with a reduction in lifetime fuel consumption and harmful emissions of fossil fuel by 25–30% [3]. The *ICE* converter used in *HEVs* allows a wider driving range and provides additional torque when higher torque is required during fast vehicle acceleration or steep hill climbing. The *hybrid electric vehicles with plug-in capability (PHEVs)* are even more effective in reducing emissions by 30–50% compared to conventional *ICE* vehicles [3], since they are mostly operated in all-electric mode that doesn't emit harmful tailpipe pollutants. When low carbon intensity electricity is used to charge the vehicle, *PHEVs* can be 30–47% more energy efficient than conventional *HEVs* and 51–63% more efficient than conventional *ICE* vehicles [3]. *PHEVs* can be even more efficient than conventional *HEVs* due to the limited use of the *ICE* which allows the engine to operate closer to its maximum efficiency [4]. The large battery in the *PHEV* is more efficient, and charging from a renewable source may

S. Al-Assadi (✉)
MAHLE Powertrain LLC, Plymouth, MI, USA

cost less (e.g., wind power, solar energy, or hydroelectricity) in addition to being largely emission-free as compared to the on-board generator [4]. It often has a more powerful electric output capable of longer and more frequent electric mode driving, which helps lower the operating cost, saving around 40–60% in energy costs, compared to conventional *HEVs and ICE* vehicles, respectively [5]. Several studies published by the Belfer Center [6] and the US National Research Council [7, 8] have concluded that *PHEVs* with larger and heavier batteries cost more, but they expected that the cost will continue to decline in the future while gasoline prices will increase.

The *AWD-PHEV* configuration considered in this article offers optimum vehicle performance in three different driving modes (EV, Series, and Parallel). The 60 kW NiMH battery pack powered a rear traction motor connected directly to the rear axle and can provide power of up to 50 kW to drive the rear wheels. A *B*elt *S*tater *G*enerator (*BSG*) powertrain having 60 kW generator linked mechanically through the accessory belt to drive the *2.5L 6-cylinders I*nternal *C*ombustion *E*ngine (*ICE*), which provides extra power to the front axle through a hydraulic separation clutch coupled to the six speeds transmission gearbox. In EV mode, the rear traction motor can run to provide power to the rear wheels to meet the driver power demand. In Series hybrid mode, when the battery capacity *s*tate *o*f *c*harge (*SOC*) level is low and not enough to drive the traction motor, the *i*nternal *c*ombustion *e*ngine (*ICE*) drives a generator *(BSG)* within its maximum efficiency at constant speed and constant torque to provide the requested electric energy to the rear traction motor and/or to charge the 60 kW NiMH battery pack. At higher vehicle speeds when the power demand is higher than the power provided from the rear traction motor and/or the battery capacity *SOC* is low and not enough to drive the traction motor, the separation hydraulic clutch is locked, and the Parallel hybrid mode is entered. In Parallel mode with "power-assist operation" activated, when battery *SOC* is high and the power from the rear traction motor is not enough to drive the vehicle, the *ICE* runs at optimal torque adding the extra power required directly to the front axle. In Parallel mode, when the driver needs a high torque especially during fast acceleration or steep hill climbing and the battery capacity is high, the "boost operation" is activated to deliver the requested higher torque. The *ICE* operates under full load with the maximum available *ICE* torque. The difference between the requested torque from the driver and the available maximum *ICE* torque is used as the requested torque to the rear traction motor. In Parallel mode with "power-assist and charge low operation" activated, when the battery *SOC* is low, the *ICE* can run at different speeds, adding power to the front axle in addition to driving the generator *(BSG)* to charge the high-voltage battery pack. The requested *ICE* torque varied and depended on the sum of available requested torque of the rear traction motor and the requested torque from driver command. In addition, when the vehicle speed drops during braking, the regenerative braking power provided from the mechanical friction brakes is recovered from the rear traction motor functioning in regeneration mode to supply the "electricity" power to charge the high-voltage battery pack.

The article starts with a brief highlight of the main powertrain components of the *AWD-PHEV* plant model and the top level methodology of the control strategies
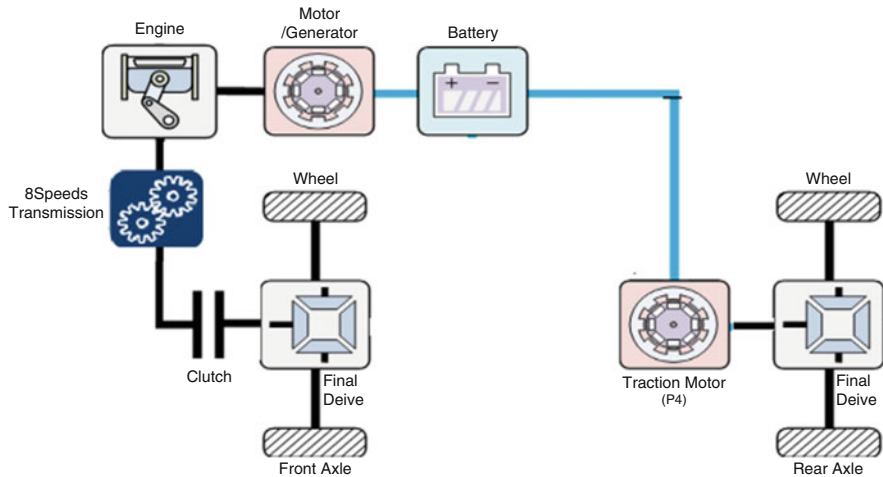
Fig. 1 Powertrain components of AWD-PHEV

design used for driving the *AWD-PHEV*, followed by a brief description of the complete simulation model and simulation results, and finally, we present our conclusions.

2 Plug-In Hybrid Electric Vehicle Components

The top-level configuration (Fig. 1) of the *AWD-PHEV* plant model with the main powertrains is considered in this article, which has a mechanical connection to the front and rear axles. The *ICE/generator* (*BSG*) is directly connected to the front axle through a hydraulic separation clutch coupled to the six-speed transmission gearbox. The rear traction motor (*E-motor*) is coupled directly to the rear axle. This configuration of the *AWD-PHEV* offers optimum vehicle performance in three different driving modes (EV, Series, and Parallel).

3 Plug-In Hybrid Electric Control Methodology

All control strategy points designed inside the supervisor *hybrid controller unit* (*HCU*) are summarized in the stateflow chart (Fig. 2). This chart shows how to evaluate a state variable called *hybrid states*, transition from one state to another, and how the current driving state of the vehicle provides the correct torque distributions based on the driver torque demand. It switches between the 16 different operating *hybrid states* depending on many conditions. When a selected hybrid state is
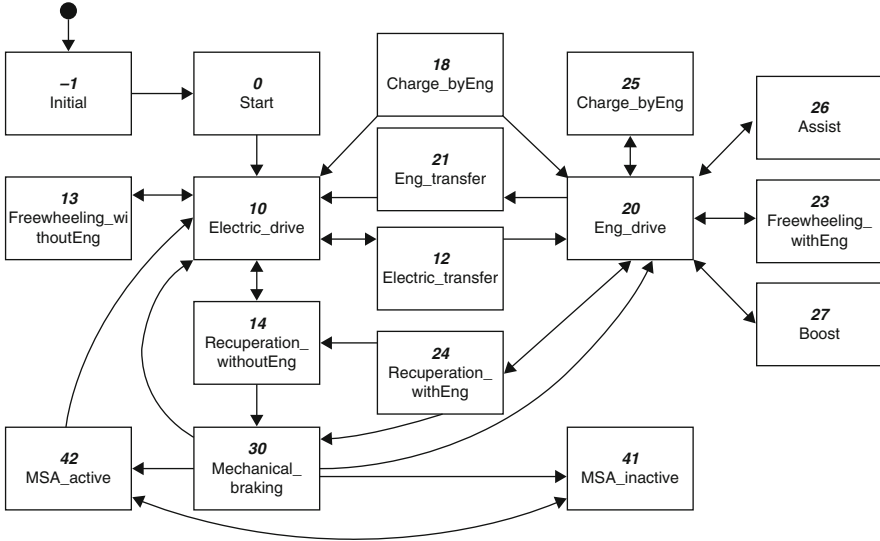
Fig. 2 Control strategies (HCU) stateflow chart

activated, it provides the control signals to all controller units of the vehicle powertrain subsystems including the generator, commanded ignition, and requested torque to the *ICE*, requested torque to the rear traction motor, requested mechanical torque of the vehicle wheel brake, and clutch status (open/closed) coupled to the six-speed transmission gearbox. Furthermore, the *HCU* calculates a requested brake torque, which depends on the brake pedal position of the driver subsystem. When the selected *hybrid state* is activated, it separates the requested brake torque of the recuperating motor torque and a requested torque of the mechanic brake with wheel vehicle brakes.

3.1   EV Mode

The EV mode provides the driver torque demand to the rear traction motor for pure electric drive. In this mode, the state (*Electric-drive, State-10*) is activated, when the battery capacity *SOC* is higher than the lower limit and the rear traction motor is capable of providing the requested driver torque. The driver torque demand depends on the acceleration pedal, which is used as the requested torque for running the traction motor to provide the torque to the rear wheels.

3.2   Series Mode

When the battery power capacity *SOC* is close to the lower limit value and the available power provided from the rear traction motor is enough to drive train, the Series mode is entered.

In Series mode, the state (*Charge-byEng, State-18*) is activated, commanded ignition, and requested torque to the *ICE*. The *ICE* drives a *Generator (BSG)* within its maximum efficiency at constant speed and constant torque to provide the requested electric energy from the generator to the rear traction motor and/or to the storage system when it needs to be charged. In this mode, the rear traction motor is only in use and connected to the rear wheels to drive the vehicle, and the *ICE/generator (BSG)* is decoupled from the vehicle wheels.

3.3   Parallel Mode

At higher vehicle speeds, when the driver power demand is higher than the power provided from the rear traction motor and/or battery *SOC* capacity is low to power the rear traction motor, the Parallel hybrid mode is entered. In this mode, the separation clutch is locked, and the state (*Eng_drive, State-20*) is activated to connect both the rear traction motor and the *ICE/generator (BSG)* to drive train.

In Parallel mode, the state (*power assist, State-26*) is activated, and when the battery capacity *SOC* is high and the power from the rear traction motor is limited and not enough to drive the vehicle, it uses the optimal *ICE* torque as the requested *ICE* torque to add the extra power required directly to the front axle. The difference between the optimal *ICE* torque and the requested torque from the driver is used as a requested torque to the rear traction motor. This state is used especially for better efficiency drive of the Parallel hybrid mode operation.

In Parallel mode, when the driver needs a high torque especially during fast acceleration or steep hill climbing that requires maximum driving torque and the battery capacity is high, the state (*Boost, State-27*) is activated. This state is mainly used to achieve the higher torque request; the *ICE* operates under full load, and the maximum available *ICE* torque is used as the requested *ICE* torque. The difference between the requested torque from the driver and the available maximum *ICE* torque is used as requested torque to the rear traction motor.

In Parallel mode, with low battery *SOC*, the state "power assist and charge low" (*Charge_byEng, State 25*) is activated. In this state, the *ICE* can run at different speeds, adding power to the front axle as well as drive the *generator (BSG)* to charge the high-voltage battery pack. The requested *ICE* torque varies depending on the sum of available requested torque of the rear traction motor and requested torque from the driver command.

3.4   Recuperation Brake Energy Mode

The states for "Recuperation Brake Energy" mode are used to simulate the recuperation of the brake energy. When the vehicle speed drops during braking, the regenerative braking power provided from the mechanical friction brakes recovered from the rear traction motor functional in regenerating mode is converted into "electricity" power to charge the high-voltage battery pack. When braking occurs during EV mode, the state (*Recuperation-withoutEng*, *State-14*) is activated, the rear traction motor used in generator drive mode to supply the "electricity" power to charge the high-voltage battery pack. When braking occurs during Parallel mode, the state (*Recuperation-withEng, State-24*) is activated, the separation clutches open, the requested torque of the engine is set to 0 NM, and all requested brake torque is recovered from the rear traction motor.

3.5   Motor Start/Stop Automatic (MSA) Mode

The *MSA* states (*Active/Inactive, States-42 and 41*) are used to simulate the automatic start/stop function and only used at vehicle standstill. In (*MSA-Active, State-42*), the *ICE* shuts down to reduce the fuel consumption and disconnects from the drive train, and the rear traction motor is not in use. In ("*MSA-Inactive", State-41)*, the *ICE* requested a 40 Nm (*ICE Friction*) starting torque to the generator that functional in motoring drive mode and the requested torque of the rear traction motor is set to – 40 Nm.

3.6   Freewheeling Mode

The (*Freewheeling-with/without_Eng, States-23 and 13*) are used to simulate a freewheeling driving mode. When the state (*Freewheeling withEng, State-23*) is activated, both *ICE* and rear traction motor are connected to the drive train. The ignition signal is turned on, the *ICE* torque is set to 0 Nm, and the requested torque to rear traction motor is set to 0 Nm. When the state (*Freewheeling without_Eng, State-13*) is activated, the ignition signal is turned off, the *ICE* requested torque is set to −50 Nm, and the requested torque to rear traction motor is set to 0 Nm.

3.7   Mechanical Braking Mode

The (*Mechanical braking, State-30*) provides the brake torque for pure mechanical brake with wheel vehicle brakes. When activated, the *ICE* is connected to the drive

train, but the requested torque is set 0 Nm. The requested brake torque from the driver command leaded as the requested torque for the mechanic of the wheels brake system.

4   AWD-PHEV Plant Model

In this article, the simulation of the complete *AWD-PHEV* plant model (Fig. 3) was created using the *Velodyn* tool [9]. This *AWD-PHEV* plant model simulates all subsystems of the powertrain components including their controller units, all accessories, and cooling systems for the vehicle.

5   Application

All vehicle dynamic specifications and the main powertrain components parameters (Table 1) are used to simulate this *AWD-PHEV* plant model (Fig. 3).

The supervisor *hybrid controller unit* (*HCU*) controls all powertrain components operation using the control strategies illustrated in the stateflow chart (Fig. 2). It acts as a master controller during a drive cycle for all powertrain slave controller units such as *ICE/generator (BSG)*, rear traction motor (*E-motor)*, battery pack, clutch status (open/closed), and the six-speed transmission gearbox.

5.1   Simulation Results

The three modes of operation (EV, Series, and Parallel) with most of the transition *hybrid state* (Fig. 2) activities during *US06* drive cycle simulation of this *PHE*V model can be covered by setting the battery starting capacity value to $SOC = 58\%$ and the lower limit allowed value to 30%.

Figures 4, 5, 6, 7, 8, 9, 10, and 11 shows the transition to *hybrid states* during the drive cycle with the three modes of operation, performances of the vehicle dynamic, battery pack condition, all powertrain components (*ICE/generator, E-motor, clutch, and transmission gears*), and the regenerative braking torque when the vehicle speed drops while braking.

It was observed (Fig. 4) that the EV mode (*State-10*) and Series hybrid mode (*State-18*) are the dominant modes of operation to achieve the best drive torque demand during this drive cycle. The transition from EV mode to Series hybrid mode occurred when the battery capacity (*SOC*) level (Fig. 7) was close to the lower limit value (*SOC = 33%*).

In Series hybrid mode, the state (*Charge_byEng, State-18*) is activated, and the *ICE* starts (Fig. 9) to drive a *generator (BSG)* (Fig. 8) within its maximum efficiency

Table 1 Vehicle specification parameters

Vehicle specifications	
Vehicle platform	Passenger car
Vehicle mass (kg)	1234
Dynamic wheel radius (m)	0.25
Aero drag coefficient	0.32
Air mass density (Kg/m^3)	1.202
Vehicle drag coefficient (Nh^2/km^2)	0.33/0.0033
Wheel drag coefficient constant	0.014
Front area (m^2)	1.83
Distance from COG to front axle (m)	1.6851
Height COG over ground (m)	0.5
Engine (ICE) specifications	
Engine size (cc)	2500
Max speed (rpm)	5500
Max torque (Nm)	260
Inertia (kg*m^2)	0.12
Rear traction E-motor/generator specifications	
E-motor type	Traction motor
Motor power (KW)	50
Max. speed (rpm)	5500
Continuous torque (Nm)	225
Peak torque (Nm)	450
Mass (kg)	50
HV battery specifications	
HV type	NiMH
#Serial/parallel cells	240/1
Capacity each cell (Ah)	5.5
Max. capacity power (KW)	60
(Min/max) cell (volt)	0.8/1.68
Mass each cell (kg)	0.2
Front/rear axle specifications	
Vehicle drive	FWD/AWD
Gear ratios	[3.1 2.13 1.48 1.14 0.95 0.82]
Inertia of each input shaft (kg*m^2)	0.0064
Inertia of output shaft (kg*m^2)	0.012

at constant speed and constant torque to provide an "electrical" power to the rear traction motor (Fig. 10) and/or to charge the high-voltage battery pack (Fig. 7). However, during fast acceleration, when propulsion power demand is higher than the power provided from the rear traction motor and/or battery *SOC* capacity is low to power the rear traction motor, the transition from Series hybrid mode to Parallel hybrid mode occurs.
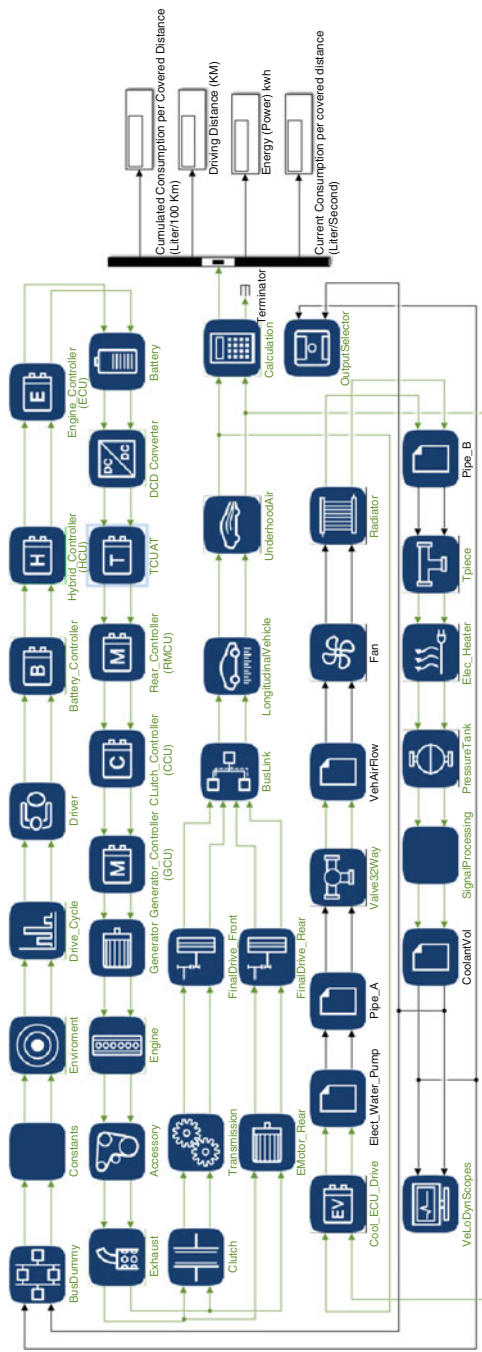
Fig. 3 AWD-PHEV plant model
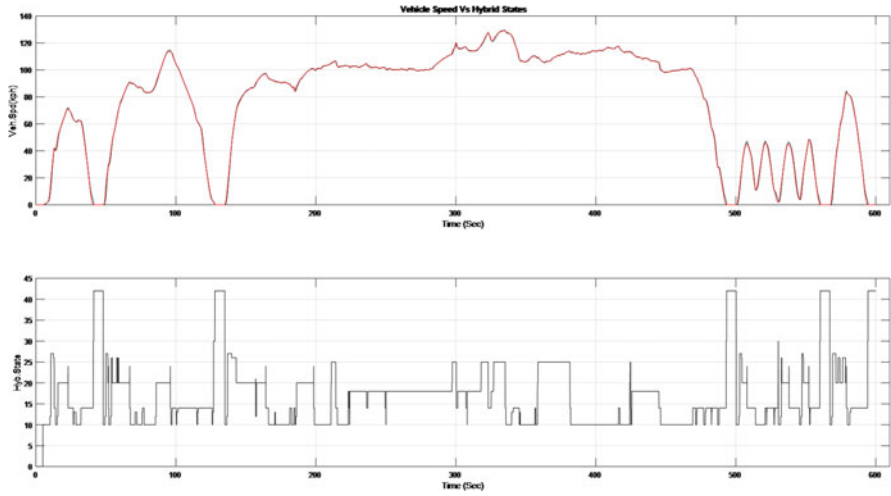
Fig. 4 Hybrid control states
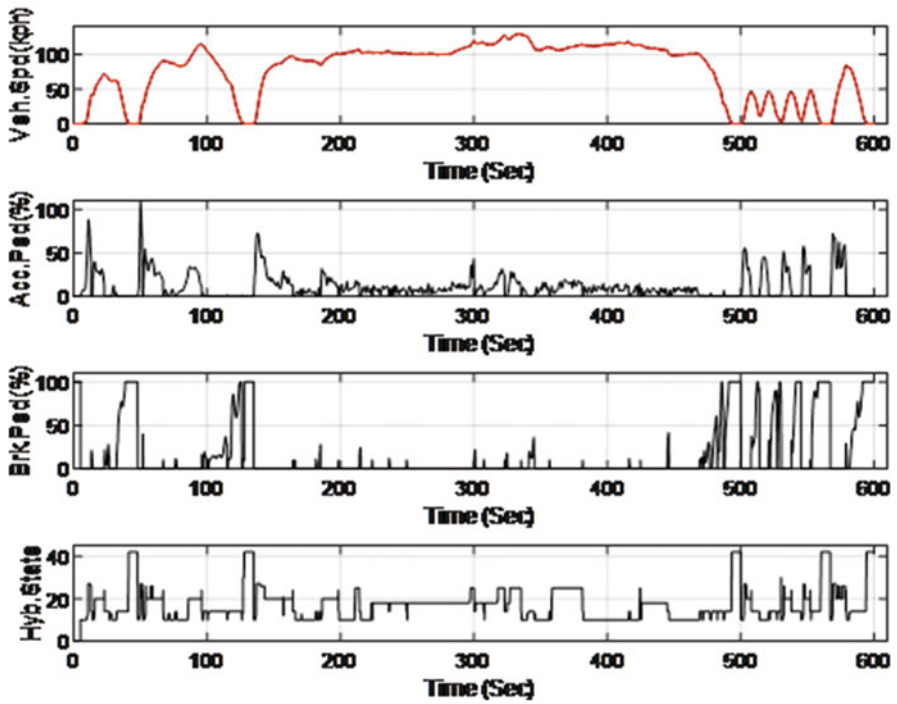
Fig. 5 Vehicle performance
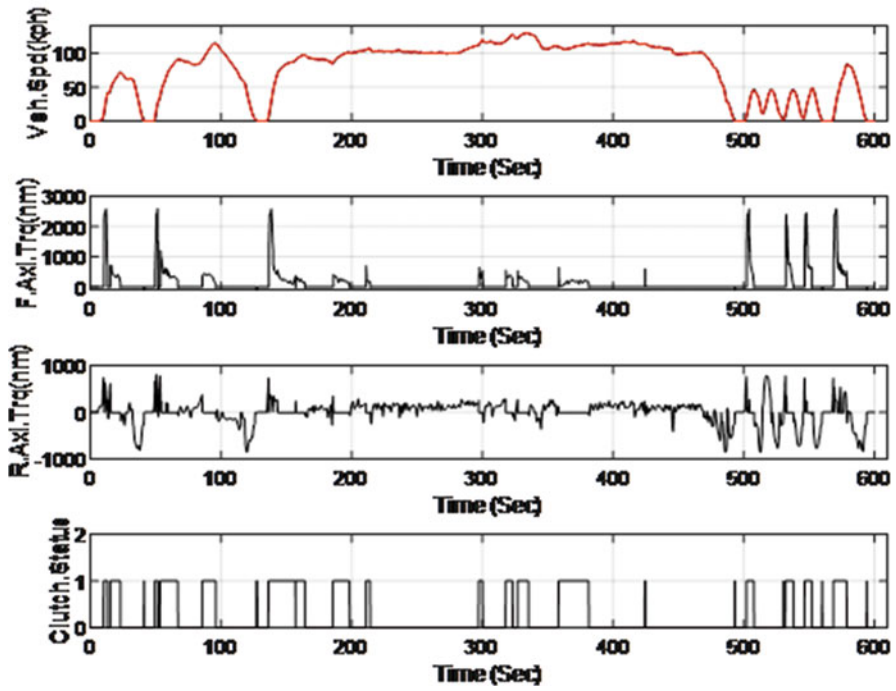
Fig. 6 Axles/clutch performances
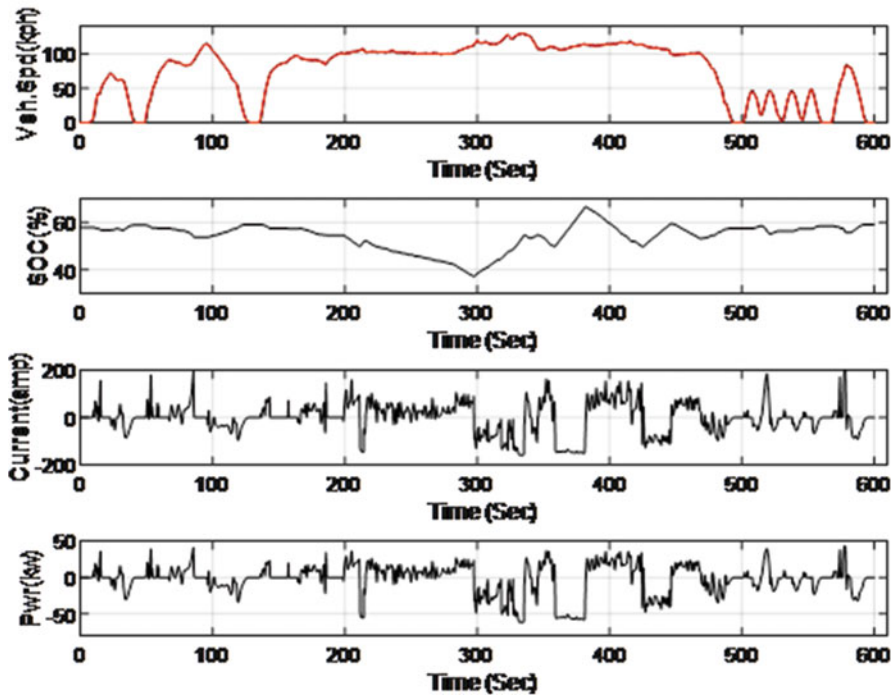
Fig. 7 Battery pack performance
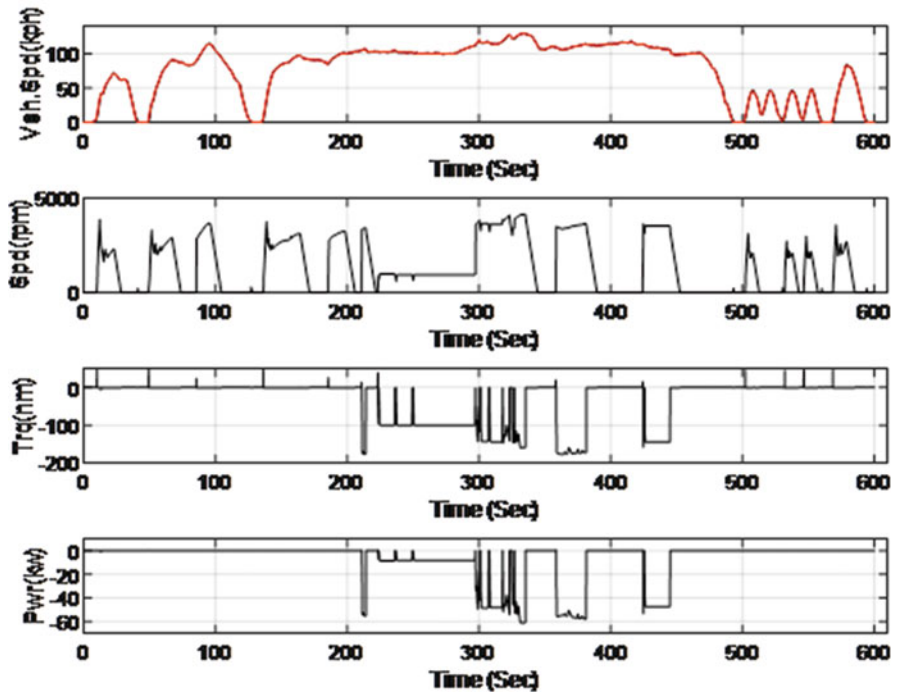
Fig. 8 Generator performance
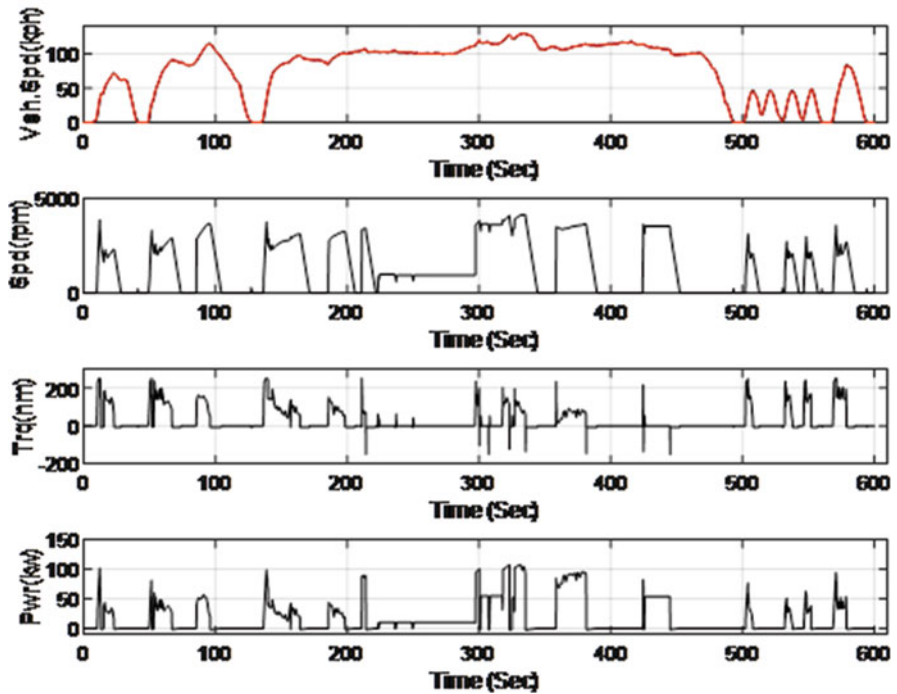
Fig. 9 Engine performance
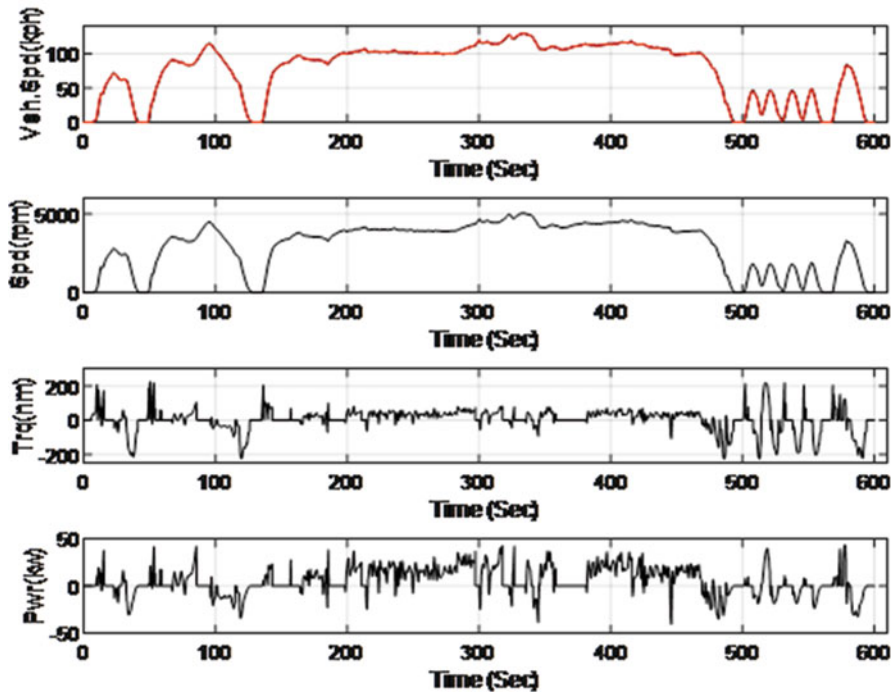
Fig. 10 Rear E-motor performance
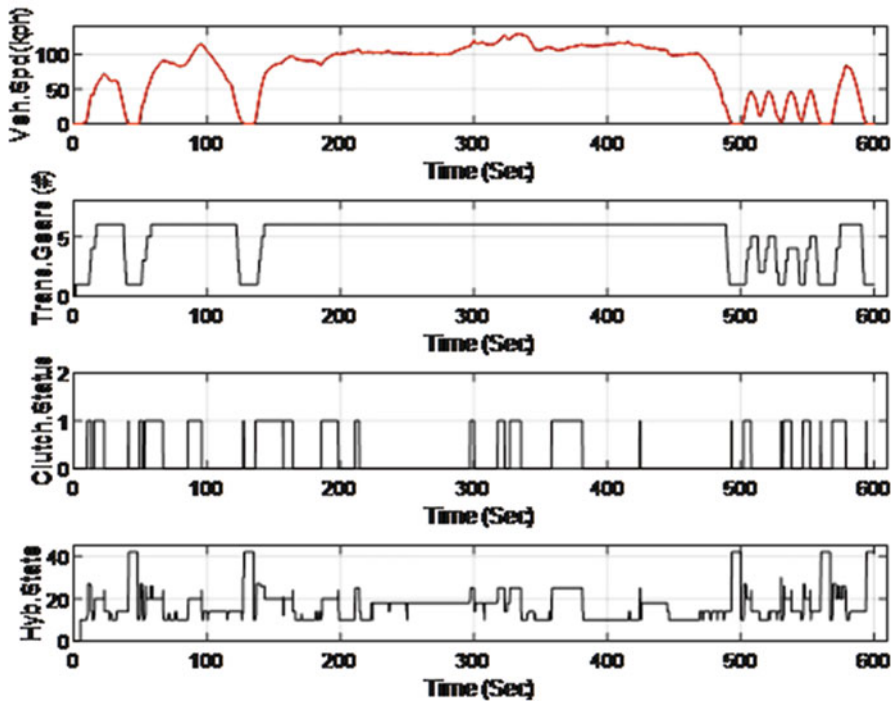
Fig. 11 Transmission/clutch performance

In Parallel mode, the separation clutch is locked (Fig. 11), and the (*Eng_drive, State-20*) is activated; the rear traction motor and the *ICE* are both connected to the drive train (Fig. 6). In Parallel mode, when battery capacity (*SOC*) is higher than the limit value and the power from the rear traction motor is not enough to drive the vehicle, the state "power assist" (*Assist, State-26*) is activated, and the *ICE* runs at optimal torque adding the extra power required directly to the front axle. The difference between the optimal *ICE* torque and the requested torque from the driver is used as a requested torque to the rear traction motor. In Parallel mode, with low battery capacity (*SOC*), the state "power assist and charge low" (*Charge_byEng, State-25*) is activated, and the *ICE* adds the power to the front axle and charges the high-voltage battery pack. In Parallel mode, if the driver needs a high torque especially during fast acceleration, the state (*Boost, Stat-27*) is activated, and the *ICE* operates under full load to use the maximum *ICE* available torque. The difference between the requested torque from the driver and the available maximum *ICE* torque is used as the requested torque to the rear traction motor.

It was also noticed from these figures how the "Recuperation Brake Energy" *is* used to recuperate the brake energy (Fig. 5) when the vehicle speed drops while braking. The regenerative braking power provided from the mechanical friction brakes recovered from the rear traction motor functional in regenerating mode supplies the "electricity" power to charge the high-voltage battery pack.

6   Conclusions

This article presents the simulation results of a typical passenger *AWD-Plug h*ybrid *e*lectric *v*ehicle (*PHEV*). It illustrates how the control strategies designed inside the supervisor *hybrid controller unit* (*HCU*) manage the best distribution of the driver torque demand for all powertrain drive components, *ICE/generator (BSG)*, and rear traction motor (*E-motor*). The three different modes of operation (EV, Series, and Parallel) offer optimum vehicle performance during *US06* drive cycle. In addition, when the vehicle speed drops during braking, the regenerative braking power provided from the mechanical friction brakes recovered from the rear traction motor functional in regenerating mode supplies the "electricity" power to charge the high-voltage battery pack.

References

1. Anderson, D. C., & Anderson, J. (2010). *Electric and hybrid cars-a history* (2nd ed.). McFarland & Company Inc.
2. Al-Assadi, S., & McConnell, J. (2019). *Pure electric vehicle simulation using powertrain estimation*. SAE WCX-2019, 01-0367.
3. Bowyer, J., Pepke, E., & Groot, H.. (2019). *Environmental assessment of ConVentional vs hybrid vs battery electric vehicles*. Dovetail Partners Consuming Report No. 6.

4. Kneipping, E., & Duvall, M. (2014). *Environmental assessment of plug-in hybrid electric vehicles* (Vol. 2). Air Quality Analysis Based on AEO-2006 Assumptions for 2030 Electric Power Research Institute and Natural Resources Defense Council.
5. Wu, X., Dong, J., & Lin, Z. (2013). Cost analysis of plug-in hybrid electric vehicles using GPS-based Longitudinal travel data. *Energy Policy, 68*.
6. Lee, H., & Lovellette, G. (2011). *Will electric cars transform the U.S. market?* Belfer Center for Science and International Affairs, Harvard Kennedy School of Government, HKS Faculty Research Working Paper Series RWP11-032.
7. National Research Council. (2010). *Plug-in hybrid vehicle costs likely to remain high, benefits modest for decades*. National Academy of Sciences.
8. National Research Council. (2011). *Transitions to alternative transportation technologies-plug-in hybrid electric vehicles*. The National Academies Press.
9. IAV Vehicle Longitudinal Dynamics Simulation Tool. (2016). *User manual-Velodyn library documentation-BOSCH automotive handbook* (6th ed.).

Artificial Intelligence Application to Flexibility Provision in Energy Management System: A Survey

Oludamilare Bode Adewuyi, Komla A. Folly, David T. O. Oyedokun, and Yanxia Sun

1 Introduction

Energy remains an integral part of the human sustainability drive. Thus, the global call for clean, affordable, and reliable energy supply through the United Nations Sustainable Energy for All (SE4ALL) initiatives has become a crucial component of the energy transition efforts of different countries. However, the interaction between modern energy needs and energy production is becoming complex. Moreover, the economic implications of energy investments and the environmental impacts of energy projects are taking a new dimension due to the changing nature of energy production and some governance (i.e., socio-political) issues. Hence, in most cases, inadequate planning of the energy sector has led to poor return on investment in supply quality and reliability, especially in developing countries. In recent years, national and international energy planning policies have focused on developing models and tools that consider the several interlinking goals of modern energy supply systems. Crucial aspects of these goals include building resilience in energy systems toward achieving increased energy access. Achieving these goals will come with good economic benefits for both the suppliers and the consumers by improving supply quality, reducing negative socio-environmental impacts of energy production, increasing diversification of energy supply mix, etc., as indicated in Fig. 1 [1]. Therefore, research efforts on energy issues are

O. B. Adewuyi (✉) · K. A. Folly · D. T. O. Oyedokun
Department of Electrical Engineering, University of Cape Town, Rondebosch, South Africa
e-mail: adewuyiobode@gmail.com; komla.folly@uct.ac.za; david.oyedokun@uct.ac.za

Y. Sun
Department of Electrical & Electronic Engineering Science, University of Johannesburg, Johannesburg, South Africa
e-mail: ysun@uct.ac.za
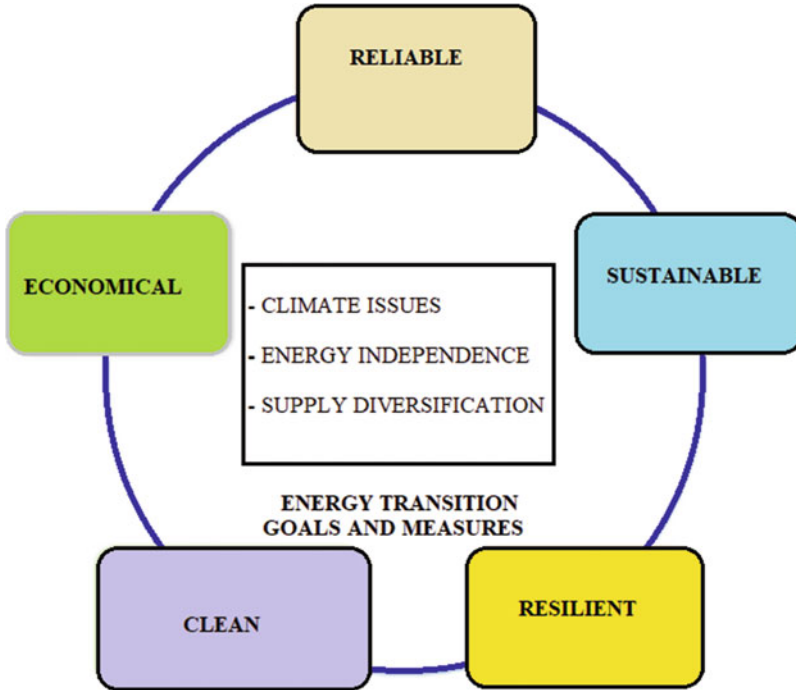
Fig. 1 Conceptual model of sustainable energy transition targets (SDG7)

becoming transdisciplinary and involve integrated interaction of different energy planning tools and operation goals toward achieving more effective sustainable energy transition for different regions of the world.

Providing a clean, reliable, and affordable electricity supply has been one of the aspirations of many countries. For this purpose, most countries are setting up reforms and committees to formulate and charter strategic policies toward attaining 100% green energy transition within the shortest possible time [2]. Renewable energy-based microgrid can provide the necessary support for consumer loads with reduced stress on the existing grid infrastructure since they are closer to the consumer ends. The efforts of the United States toward efficient sustainable energy transition have been well emphasized by the US Presidency. The United State has set a goal of achieving a 100% clean energy power sector by 2035 toward making the energy sector sustainable and cutting down emission of greenhouse gases in the environment [3–5]. Many European countries are also working conscientiously toward achieving their set goals on sustainable energy and environment. Specifically, Germany, UK, France, Netherlands, and Sweden are among the leading European nations that have embarked on developing different sustainable energy pathways aimed toward attaining 100% renewable energy by 2050 [6–8]. Quite several countries in Africa are also taking the initiatives in terms of commitment

and efforts toward introducing a significant amount of renewable energy resources into their sustainable energy roadmap. The efforts of the following countries are worth mentioning: Kenya [9], Nigeria [10], Ghana [11], Mauritius [12], Egypt, and South Africa [13].

The call from the United Nations environment and energy division for the increase in the deployment of clean technologies for power generation using the renewable energy resources is getting stronger. However, the flexibility requirements of contemporary energy systems are becoming enormous as the amount of power from intermittent energy resources increases [14]. As a result, the modalities for meeting the requirements for techno-economic viability of energy systems are tending to be more complicated in recent times. For instance, researchers in South Africa conducted a detailed research on the economic cost of electricity supply interruptions in the face of increase integration of variable renewable energy resources. One of the key observations is that a full day of national blackout costs $3.4b to the economy. This finding highlights the cost of unmet energy need and the importance of maintaining high levels of reliability through appropriate flexibility measure [15]. Thence, to meet up with the minimum obligations for reliability, dynamic and robust schemes need to be devised to ensure real-time matching of load demand and available supply [16, 17]. Consequently, meeting the operational flexibility needs of power systems remains an essential yardstick for analyzing the strength and robustness of the grid to accommodate a shift from fossil fuel-based power injection to renewable energy resources-based [18, 19]. A grid infrastructure that is designed with adequate flexibility provision is capable of mitigating the effects of disturbances that can result from the inevitable fluctuations in the supply and load demand dynamics [20]. Thus, sufficient operational flexibility management mechanisms are a precondition for planning substantial injection of power from variable VREs [10, 21]. By general definition, power system operational flexibility is often depicted as the measure of the capability of grid infrastructure to techno-economically manage the variability and inherent uncertainties of demand and supply across all important schedules [22]; and this can be achieved by active deployment of adaptable power system equipment known as flexibility providers [23]. The remaining part of this book chapter is organized thus: section two provides insight on the conventional approaches to managing the flexibility management. A concise review of artificial intelligence and its deployment for flexibility management in energy system is presented in section three. In section four, a planning framework for integrated flexibility management using artificial intelligence concept is discussed, and the work is concluded in section five.

2 Conventional Approach to Flexibility Management

The conventional approach to energy supply system planning and design involves three disjointed stages: component capacity optimization, optimal operation scheduling using unit commitment, and evaluation of the energy market strategies
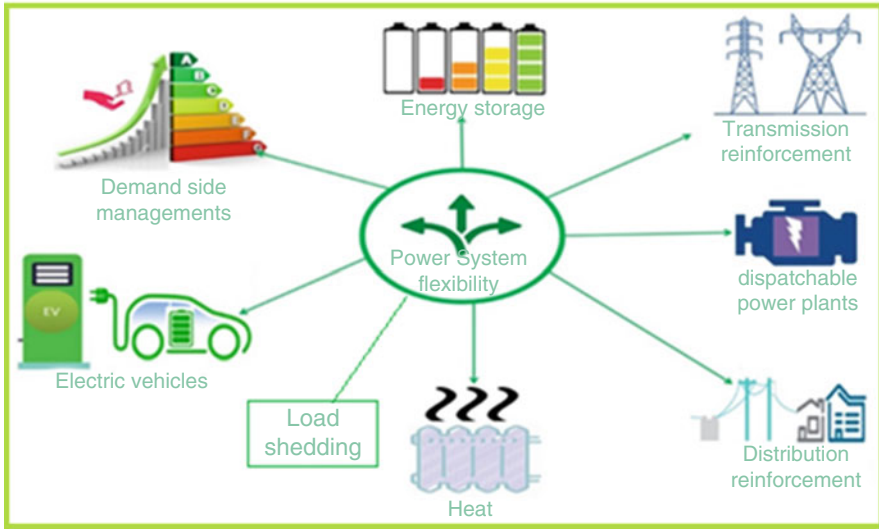
Fig. 2 Conventional power system flexibility management approaches [22]

for economic service exchange [24]. Segregating these three important components when designing an energy system often leads to redundancy in terms of component oversizing and inefficient flexibility management provision. Essentially, the efficiency of the power systems operation is mainly a function of the dispatchability and efficiency of control of the system generators whose capacity is determined at the first stage of design. Furthermore, as the share of power production from the VREs increases, the ability to control the outputs of energy supply systems and ensure techno-economic dispatch of the generators comes with significant level of complexities and at an additional cost, as discussed [25, 26]. The cost of flexibility is estimated as the extra cost to be considered while integrating adaptable flexibility mechanisms for checkmating the proliferated consequences of intermittency due to massive integration of VREs [10, 27]. Common techniques for energy system flexibility management, especially from the load side, are shown in Fig. 2 [28], etc. Flexibility management can also be initialized from the supply end by controlling generators' ramping power and cycles, as well as controlling the generation limits. Other flexibility management practices from the supply end include increasing the cycles of generators shutdowns and start-ups in multi-generators configuration as outlined in [29].

The concept of hybrid energy systems, which involves the combinations of multiple renewable and non-renewable generators as well as backups, has evolved as a cost-effective tool for achieving flexibility management in energy systems with high uptake of VREs [30]. The significance of optimally planned hybrid energy supply technologies with energy storage system (ESS) toward achieving essential flexibility management was enunciated in [31]. In the same vein, in

ref. [26], a concise structure for analyzing the most cost-effective and technically appropriate flexibility requirements of energy supply system using complementarity of generators and storages was presented. It is however essential to note that the robustness of the hybrid energy supply system depends greatly on the accuracy and reliability of the forecasting tool for VREs, available generation, load demand projections, and real-time market dynamics [32, 33]. With improved accuracy of prediction, crucial information about the energy management system (EMS) set up in terms of possible periods of power deficits and surpluses can be anticipated and prepared for before the eventual occurrence. The authors in [34] investigated and provide a direct illustration of the importance of ensuring accuracy in the prediction of renewable energy resources toward achieving a cost-effective design of EMS and avoiding generators' oversizing, as well as reducing curtailment. With the adaptation of different power market scenarios, exhaustive models are developed for accurate prediction of power output from wind generators in [35], and a similar work was reported in [36]. Some practical flexibility provision mechanisms reported in the literature are discussed as follows:

2.1 Demand-Side (Load) Management

Load management involves the set of optimal real-time techno-economic actions taken by system operators toward achieving a stable match of the system instantaneous load demand and power generation [37, 38]. The specific goal of load management is to ensure that the most suitable and economically viable operating conditions are achieved based on the information of the supply (generating) capacity and the demand (load) conditions of the power system per time. In this regard, load management is one of the techniques for flexibility management, which can be influenced at both the supply and demand ends in response to the operational interests of the system operator and credible economic signals from the energy market. Electrical loads are categorized into either flexible/responsive loads (flexible demand resources, FDRs) or static/rigid loads (limited demand resources) for load management purposes. For the FDRs, the time of use can be changed from time to time in response to the system load and available generation dynamics. Common FDRs include heating and ventilation systems, refrigerators, washing machines, *etc*. Most often, their operation time can be rescheduled from the peak demand period and supply shortages to later when the available supply is sufficient and surplus/in excess. On the other hand, appliances such as security lights, illumination loads, alarm systems, and home entertainment are often regarded as non-shiftable loads; their usage is not usually subjected to varying time conditions, except if necessary.

In recent times, the innovative grid concept has injected more intelligence into load management practices, especially in the face of the changing load patterns and proliferation of energy supply from renewable energy injection. Existing grid infrastructures are equipped with information and communication technologies for real-time monitoring and prompt control of power system equipment. As a result,

the smart grid can make intelligent decisions on the appropriate flexibility actions toward meeting the operational needs of the EMS while smoothly executing actions, such as load-shifting or load-shedding, toward achieving stable system operating conditions. Another significant switch in EMS operations since the incorporation of smartness to grid infrastructures is the invitation for electricity users' participation in determining the dynamics of the electricity market using the concept of demand-side management (DSM) [39]. In recent years, research on DSM as a tool for flexibility management in EMS through appropriate FDRs for controlling the load demand patterns of electricity consumers has intensified [40, 41]. Thus, the imbalance between load demand and available system generation per time can be easily mitigated for high-renewable energy-based EMS [42, 43]. Furthermore, in [44], an FRDR-controlled approach for providing effective flexibility measures based on integrated DSM for buildings was developed and implemented. While DSM is a broad concept, demand response programs (DRP) are the underlying energy market strategies by which consumers' electricity consumption behaviors are tactically altered in terms of the time of demand for using their FDRs.

The change in customers' electricity usage patterns is achieved by utility companies making available some incentivization tariff packages such as flexible payments and lucrative prices for consumed electricity units [45]. DRP, as an integral branch of load management, is a conscious way of influencing the electricity consumption patterns of energy users' by way of motivations through incentivized benefits from energy suppliers [46]. With an appropriately designed DR scheme, the flexibility needs of the grid through the additional generation and transmission capacity expansion can be grossly reduced [47, 48]. Consequently, most of the available information in the literature on the concepts of DRP is focused more on creating an ideal market for electricity transactions and service delivery. Thus, the most adopted types of DRPs are: namely, day-ahead pricing (DHP), critical peak pricing (CPP), time of use (TOU), real-time pricing (RTP), interrupted curtailable and direct load control, and so on [49, 50]. However, for implementing DRP effectively, real-time supply and future power system status in terms of the changing load and generation dynamics should be considered to exploit the energy market fully [51, 52] while capturing the VREs' output uncertainties [34, 53]. Therefore, in [54–57], several arrangements were made to strategically incorporate DSM and energy storage systems (ESSs) in the capacity sizing optimization of EMS components. With these strategies of incorporating DSM and ESS into optimal planning of EMS, it is observed that the flexibility of the energy systems increases, and the overall cost of EMS design is comparatively reduced.

2.2 Energy Storage Systems (ESSs)

The supporting roles of energy storage systems (ESSs) for upscaling the VREs integration into power systems are significant for so many applications [58]. Some of the essential functions of ESSs make them an ideal tool for facilitating optimal

restraining of the nasty effects of VREs intermittency on the supply outputs [59]. Depending on the techno-economic specifications and design technologies, several energy storage technologies have been designed and reported in works of literature [60]. Considerable research works have investigated and provided insights on the financial values (in terms of cost saving) of proper selection, planning, and design of appropriate energy storage facilities for different power system configurations. Available ESSs technologies include the most deployed battery energy storage (BESS) [61], pumped hydro storage (PHESS) [62], hydrogen storage [63], compressed air energy storage (CAES) [64], flywheel technologies [65], etc. In reference [66], a hybrid energy system model that included flexibility constraints for managing flexibility in a smart home environment was developed using a PV system and different ESSs. To accommodate the flexibility constraint, the authors increased the effective hours for operating the ESSs to limit the amount of power procured from the utilities.

Analyses of potential benefits of large-scale energy storage facilities as viable options for providing techno-economically efficient flexibility support for wind energy integration are reported in [67]. The report analyzed the feasibility of pumped hydro storage systems (PHESS). Furthermore, the economic shrewdness of adding CAES is qualitatively assessed, and the authors also proposed possible strategies for motivating investors' interest in financing additional projects on ESSs development. In [68], a metric is developed based on the response of the energy supply system to additional power injection from VREs toward evaluating the flexibility performance with the inclusion of sufficient energy storage capacity. It is generally observed that the deployment of ESSs can significantly influence the effective scheduling of the system generators using the day-ahead dispatch strategies. It can also improve the economic operation of the power system. In [69], a generator scheduling strategy based on a day-ahead dispatch approach was designed for an integrated natural gas and power system using DSM and ESSs integration under a high injection of power from wind turbines.

Moreover, a general model for assessing the flexibility needs in an integrated EMS that consists of combined heat and power (CHP) systems and heat-based ESS is discussed in [70]. The authors observed that when the ESS is centrally located, more flexibility provisions are gained than when several ESS units are designed. In a similar work, the authors in [71] developed a multiple steps structure for assessing the potential benefits of incorporating BESS in high VREs-dependent power systems. At the initial step, the authors considered a stochastic UC approach for the derivation of the adaptable scheduling of the BESS using an appropriate economic dispatch environment. In addition, the forecast uncertainty from wind power within a limited prediction horizon was also considered in the design procedure. Furthermore, the significant benefits of incorporating ESSs, especially BESS and PHES, for providing grid flexibility measures toward supporting significant uptake of renewable energy sources have been evaluated using different approaches, as provided in several works of literature on flexibility management [72–78].

2.3   Electric Vehicles: V2G and G2V Technologies

In the face of the massive integration of fluctuating inverter-based generators, battery energy storage (BESS) technology has developed to be one of the most applicable technologies for power system flexibility management [79]. Due to the consistent success recorded with BESS, electric vehicle (EV) technologies are developing daily as technically effective, economically efficient, and environmentally friendly means of transportation. EV technology depends majorly on the fidelity of the BESS technology for performance and operationality. Encouraged by the dual benefits of energy storage and cost-effective mobility, more research efforts have been devoted to EV interactions with electricity grids in recent times [80, 81]. The technologies responsible for the interaction of EVs with the grids are technically known as the grid-to-vehicle (G2V) and vehicle-to-grid (V2G) technologies [82]. Combining these two technologies achieves bidirectional power flow for providing supplementary services to the grid, including flexibility management. The introduction of electric vehicles as a tool for power system flexibility management has been verified in several research studies carried out on the concept of vehicle-to-grid, V2G, and grid-to-vehicle, G2V, technology [83].

In reference [84], the random behavior of electric vehicle mobility (EVM) was modeled as a flexibility provider for energy transfer in a smart grid environment considering wind energy uncertainty using the optimal grid reconfiguration (OGR) mechanism. To effectively measure the impact of EVM on grid performance, the authors developed a novel method to evaluate the system flexibility in the presence of thermal generators and EVs. The authors in reference [85] explore using a fleet of plug-in hybrid EVs (PHEVs) as a mechanism for regularizing energy imbalances that may result from the massive integration of wind energy resources in the generation expansion plan of the north-eastern Brazil power system. In the study, an optimization tool was deployed to verify the most efficient dispatch modality for variable output of the wind farms without compromising the grid stability and flexibility needs. Similar studies on EVs' use to ensure adequate provision of flexibility requirements for power systems for different regions are reported in [86–91], etc. Generally, the contribution of EVs, i.e., G2V and V2G technologies as flexibility providers, is increasing daily. In the face of the continuously changing nature of power systems, flexibility needs are expected to increase. Thus, EV applications have shown huge prospects for cross-border interactions in highly interconnected systems [92, 93].

2.4   Grid Reinforcement

Grid reinforcement is one of the earlier strategies for managing the inherent flexibility needs of the power systems [94]. However, population growth and the continuously changing face of technology often cause an extreme increase in the

load demand beyond the grid's existing capacity, and this causes deterioration in the power systems' performance. Hence, commissioning new facilities and introducing supporting equipment, such as distributed generators, energy storage, and EVs, at crucial sections of the power system for network enhancement and congestion management are found to be inevitable [95, 96]. However, introducing VRE-based generators and ancillary facilities can contribute to additional technical challenges, leading to the deterioration of the grid flexibility performance index [97, 98]. Thus, grid reinforcement has been widely achieved through generation, and transmission capacity expansion planning using unit commitment and economic dispatch algorithms when introducing additional generation from VREs technologies [99–105].

As the amount of renewable energy integration into the power systems increases with the decommissioning of synchronous generators, the inherent inertia of power systems has significantly reduced. The lack of adequate inertia support in modern power systems has negatively affected the flexibility capability. In recent times, grid-forming inverters (GFIs) are currently being positioned as one of the solutions to managing grid inertia moving forward [106]. This is based on the way the inverter responds to change in grid conditions (in particular, the grid voltage). "Grid forming inverter" is an umbrella term that includes the concept of virtual synchronous machines (VSM), power synchronization loop, voltage-controlled inverter, etc. The swing equation is somewhat involved in some instances [107]. Authors in [108] proposed a framework for reinforcing the transmission and distribution network with inverter-based DGs, through increase efficiency in power delivery and extraction. The framework includes multi-agent control low-voltage-based DGs enabled by phase estimated Thevenin equivalent impedance and efficient power delivery. This model promotes increased participation of DGs to advance grid flexibility requirements while maintaining the required level of power quality and reduction in losses.

In reference [76], transmission system flexibility enhancement and transmission congestion mitigation were achieved using a network-constraint unit commitment (NCUC) model in the presence of battery energy storage and transmission switching. The objective of the NCUC model is to minimize the overall energy supply system operating cost while exploring the mobility of the battery storage system for enhancing the transmission network performance and achieving network congestion management. However, managing the flexibility requirements of interconnected power systems by network reinforcement is often encountered with the problem of data privacy preservation between neighboring utilities. Thus, an equivalent economic dispatch model that considers hidden flexibility information alongside other power systems' constraints is proposed in [109]. The equivalent flexibility model for network enhancement involves a multiperiod economic dispatch problem involving interconnected power networks using mixed-integer linear programming (MILP) approach.

3 Review of Artificial Intelligence and Its Application to Flexibility Management in Energy System

The foundational unit of AI is the artificial neural networks (ANNs) that mimic the biological neural network, i.e., human nervous system. The motivation behind this is connected to the understanding of the fact that the ability of humans (and other animals) to learn skills, such as visual, auditory, reading and writing, kinesthetic, and so on, is achieved experientially or iteratively using the trial and error rule [110]. Thus, it is not just the number of attempts but also the volume/magnitude and clarity of provided instructions that have been found crucial to increasing the human ability to learn and learn well. Generally, human structure for learning, reasoning, and perception of stimulus/signals is a function of the numerous electrical linkages between principal actors within the neural network such as the neurons, dendrites, soma, axon, synapses, etc., via the nerve[111]. All these components of BNN are arranged in layers, and the brain coordinates all the activities. Thus, in the same vein, the ANN models were developed by Warren McCulloch and Walter Pitts in 1943 with several mathematical/analytical/logical operands, operators, and operations arranged in layers to be coordinated by the processing capacity of computers in response to the supply of relevant data [112].

The main corridor for AI implementation is machine learning (ML), and its improved version is known as deep learning (DL) [113, 114]. There are different variants and improved variants of ML and DL algorithms that are in existence as developed by researchers over time. However, the basic units of ML and DL algorithms, irrespective of their level of complexity, are the ANNs. The conceptual development of ANN for ML and DL applications within the scientific knowledge domain is widely regarded as a point of synergy between the frontline fields of information/computational science and statistics [115]. As evident in the ANN operating procedures, the computer used the knowledge of statistics to ascertain the preciseness of the ANN model in creating patterns and recognizing trends/dynamics within the given set of complete data. Once the relationship that describes the input–output dynamics of the provided data set has been established, a complete description (output values) can be obtained from a new incomplete set of data (input sets only) supplied to the computer. The processing of teaching the computers through the provision of a complete set of data is generally known as "training," and the process of ascertaining the accuracy of the generated patterns/input–output relationship using a different set of data is known as "testing" [116]. A simple illustration of the progression and interactions between ANN, AI, ML, and DL is shown in Fig. 3.

In terms of structure, the ANN model for ML is considered to have a few hidden layers, while that of DL is commonly expected to have several hidden/processing layers [118]. Regarding the complexity of processing layers, the structures of simple and deep neural network models are shown in Fig. 4. Deep learning can identify patterns and correlations between unstructured data with multiple hidden layers. Thus, DL has a significant advantage over ML algorithms in predictive analytics.

Mimicking the intelligence or behavioural pattern of humans or any other living entity.

A technique by which a computer can "learn" from data, without using a complex set of different rules. This approach is mainly based on training a model from datasets.

Deep Learning:
A technique to perform machine learning inspired by our brain's own network of neurons.
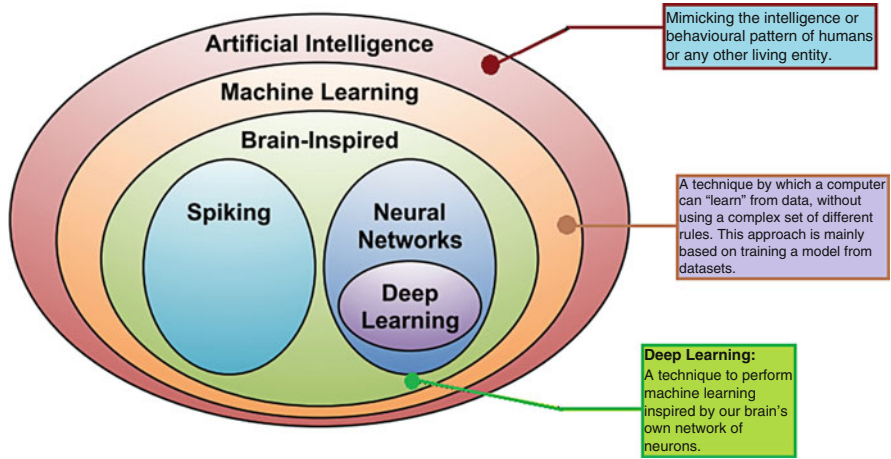
Fig. 3 Progression of AI from ML to DP [117]

(a). SIMPLE NEURAL NETWORK

One input layer   Multiple hidden layers   The output layer

(b). DEEP NEURAL NETWORK
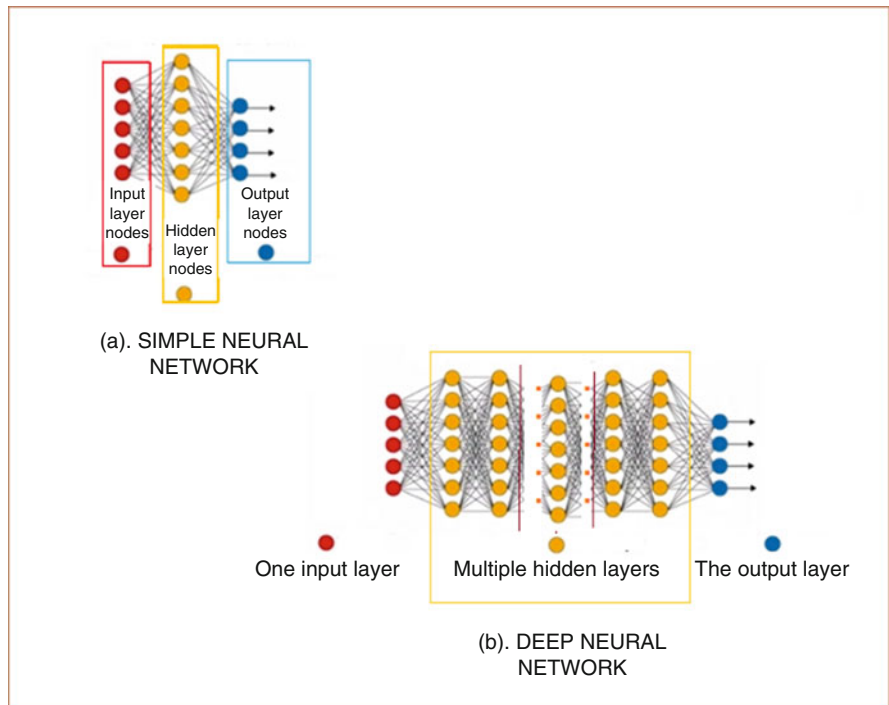
Fig. 4 Artificial neural network models, (**a**) simple NN; (**b**) deep NN[117]

Some of these advantages are its better self-learning capabilities; it can test its accuracy in terms of its predictions/outputs and updates itself as a necessity toward achieving better outputs with minimal human inputs [119]. Integrating AI into

existing flexibility management approaches offers myriad benefits, which are both technical and economic compliant. Some of the most recent works on deploying AI to energy management systems are presented in Table 1.

The scope of the reviews summarized in the table above is based on the authors' contribution in line with the type of the AI tool deployed, and whether or not flexibility provisions are considered in the problem formulation. Thus, the summary presented in Table 1 shows that most of the existing works on the adoption of AI in energy management systems are limited to resource prediction and energy market forecast. Deep learning algorithms that offer vital solutions to some important requirements of modern energy systems such as big-data handling [140] and data/information privacy have not been explored [141].

4   Planning Integrated Flexibility Management with Artificial Intelligence

Secure and economical operation of power systems is becoming difficult to achieve at the transmission and sub-transmission levels due to the increasingly dynamic nature of electricity networks [142, 143]. The complexity of grid operation is increased further by the liberal and competitive structure of the modern electricity markets [144]. Moreover, factoring in the flexibility requirements of the energy system into the design process to increase system reliability makes the decision-making procedure more complicated. Thus, introducing modern intelligent decision-making/control agents is essential for precise flexibility needs identification and deployment of appropriate flexibility providers at different instances. The advent of artificial intelligence (AI) is reshaping the methods of providing solutions to current severe developmental issues. Common AI applications involve deploying intelligent-based learning for accurate prediction and solution preferment to issues that are too puzzling for the crude human ability to handle. As a branch of information science and engineering, AI can be deployed to develop and design intelligent agents that can perceive the specific flexibility needs in an innovative microgrid environment. These intelligent agents can take necessary actions toward making the most efficient decision on the suitable flexibility provider toward maximizing the VREs uptake while limiting the use of fossil-based backups. In this context, AI-enabled integrated flexibility management refers to a method of providing readily adaptable mechanisms based on AI to accommodate the effects of uncertainty and variability in energy demand and the availability of resources in an intelligent energy supply system. AI-enabled flexibility management approach can make automatic self-decision for optimal load-shifting and ancillary device deployment based on the real-time situation of the energy system.

The AI flexibility manager can combine forecasted data using a relevant machine learning and deep learning approach and actual data from intelligent devices strategically placed at the supply and demand side with appropriate Internet of

Table 1 Summary of recent artificial intelligence application to energy management systems

Reference	Year	Key features/contribution	Adopted AI model	Merit	Included flexibility?
[120]	2022	Forecasting of solar energy resource	ANN—Support vector machine and random forest	Improve solar resource prediction	✗
[121]	2019	Forecast energy usage requirement; energy consumption control and management	Polak–Ribiére gradient backpropagation neural networks (PRGBNNs); gradient with descent adaptive learning rate and momentum backpropagation (GDALBNNs)	Prominent improvement in load forecasting and precise tracking of energy consumption level	✓
[122]	2019	Optimal control of energy supply and energy demand dynamics; load prediction and renewable energy potential forecast	Backpropagation ANN, model predictive control (MPC), genetic algorithm (GA)	Combined supply- and demand-side optimization improves profit by exploring thermal flexibility	✓
[123]	2019	Forecasting of renewable energy resources; optimal scheduling of energy usage based on the availability of renewable energy; maximization of demand-side flexibility	ANN -, MPC	Regulation of on-site energy generation, grid consumption, and grid feed-in to achieve greater demand flexibility	✓
[124]	2019	Renewable energy resource potential verification; optimal control of the energy market/electricity market design	AI-based platform model for energy trading*	Improve the operating efficiency, reliability, and intelligent control of the energy trading system	✗
[125]	2019	Predicting uncertainty in future prices in the energy market; adaptive real-time decisions for effective demand response scheduling	ANN and multi-agent reinforcement learning	Handles energy management for multiple appliances, minimizes user energy bills and dissatisfaction costs, significant reduction of electricity cost	✓
[126]	2018	Load monitoring and forecast, load disaggregation	ANN, Monte Carlo simulation	Handles real-time or/and forecasting load management applications	✓
[127]	2020	Load demand prediction	Supervised learning using backpropagation neural network, multi-linear regression, SVM	Improved accuracy of demand prediction with high efficiency and advanced demand-side control for the enhancement of energy flexibility	✓

Table 1 (continued)

Reference	Year	Key features/contribution	Adopted AI model	Merit	Included flexibility?
[128]	2020	Real-time autonomous energy management strategy; energy resource prediction; uncertainty management	Model-free deep reinforcement learning	Reduced end user's energy cost	✓
[129]	2017	Deterministic solar PV power forecast	Deep convolutional neural network (DCNN) with wavelet transforms (WTs), quantile regression (QR)	Improved forecasting accuracies over varying seasons and several prediction horizons	✗
[130]	2018	Prediction of solar power generation	Artificial neural networks (ANNs) -feedforward backpropagation algorithm; adaptive neuro-fuzzy inference system (ANFIS)	Improved forecast performance when compared to ANFIS only	✗
[131]	2019	Photovoltaic power forecasting	Two variants of deep convolutional neural networks (CNNs), i.e., residual network (ResNet) and dense convolutional network (DenseNet) with meta learning model	Reduction of training difficulties in deep network; improved forecasting accuracy and reliability of predictions	✗
[132]	2020	Power forecasting for solar PV systems	Recurrent neural network with long short-term memory (RNN-LSTM) model	Improved capability to recognize temporal patterns in the time series data of solar PV	✗
[133]	2019	Pattern recognition of residential customer loads for forecasting flexibility needs	Machine-learning-based regression models—generalized linear mixed effects (GLME).	With better precision of flexibility forecast, there is reduced cost and improved reliability of operation; *Not as efficient as the recurrent NN and deep reinforcement learning approach	✓

[134]	2020	Energy consumption pattern/load prediction	Hybrid machine-learning-based approach—multilayer perceptron (MLP), support vector regression (SVR), and CatBoost (decision trees)	Better accuracy of prediction compared to other approaches using different error analyses	×
[135]	2021	Day-ahead forecast of available distributed generation, energy demand planning and resource scheduling with demand-side management	Support vector regression technique and K-means clustering technique	Significant cost reduction	×
[136]	2021	Estimating the charging demand of hybrid electric vehicles (HEVs)	Advanced support vector machine combined with dragonfly optimizer	Intelligent charging achieved a 2.5% reduction in the total operation cost of the microgrid compared to coordinated scheme	×
[137]	2021	Load level computation, optimal energy trading with grid, battery scheduling	Convolutional neural networks with sliding window training technique	Improvements in prediction accuracy and significant decrease in electricity bill and carbon dioxide emission	×
[138]	2021	Electricity price forecasting	Feedforward ANFIS and space vector regression (SVR) combined with time series and auto-regression (AR) algorithms	Increase accuracy of prediction leads to reduced cost of electricity; computational complexity and time is significantly reduced.	×
[139]	2022	Improved electricity price forecasting	Optimal kernel-based extreme machine learning with non-dominated sorting genetic algorithm II (NSGA-II)	Developed an effective electricity price forecasting technique for the real electricity market	×

Things (IoT) edge devices [145, 146]. Such an AI-based flexibility management framework can efficiently integrate real-time power system flexibility requirements into capacity planning. It can also combine operation scheduling to increase the share of renewable energy uptake while reducing the use of fossil fuel-based thermal generators for backups and curtailing redundancy [147]. Another emerging research area in this direction is the concept of peer-to-peer (P2P) energy trading, which has significantly changed how energy is generated and consumed within a neighborhood. In this situation, excess energy produced by a household can either be sold to the grid or to neighbors that need energy. Depending on the load condition and weather, the selling neighbor, i.e., the energy producer at a particular time, can be an energy buyer (consumer) at another time leading to each neighbor being called prosumers [148, 149]. This new concept is gaining prominence and is significantly an outflow of Internet of Things (IoT) technology. However, the efficiency of this arrangement depends greatly on consistent and precise weather data and information on the prosumers' load demand and energy consumption[150]. Thus, P2P can be enhanced with the deep learning capability of artificial intelligence technology for big-data analysis and enhanced prediction handling.

5   Conclusions

Due to the complicated load and supply balance dynamics, the massive amounts of renewable energy introduced into the energy mix poses significant challenges for utilities and their customers. The renewable energy generators' outputs are intermittent and thus create an imbalance between the instantaneous load demand and available supply at different instances of time. Besides, the inertia in power systems is becoming lesser due to the displacement of the rotating mass of conventional generators with inverter-based generators. Thus, the challenge of meeting the flexibility needs of modern power systems is becoming significantly high in recent times. Because of this, existing traditional methods of meeting the flexibility needs of power systems are becoming insufficient; this calls for developing new intelligent approaches that can handle complex situations. Different Artificial Intelligence (AI) concepts are deployed as a solution provider to numerous complex power systems operational problems, especially in resource forecasting, electricity market dynamics prediction, intelligent decision-making for generator scheduling, and more. Hence, this book chapter reviews existing flexibility management techniques and some crucial areas of AI deployment in energy management systems toward meeting the flexibility needs of modern energy supply systems. It also provides insights into the research direction for the effective adoption of AI to achieve better performance. As observed from the survey, deficient deployment of deep learning approaches for big data handling for accurate prediction and preserving information privacy are some of the more obvious areas for further research into flexibility needs management in interconnected energy systems.

References

1. Gasser, P., Lustenberger, P., Cinelli, M., Kim, W., Spada, M., Burgherr, P., Hirschberg, S., Stojadinovic, B., & Sun, T. Y. (2021). A review on resilience assessment of energy systems. *Sustainable and Resilient Infrastructure, 6*(5), 273–299.
2. Senshaw, D. A., & Kim, J. W. (2018). Meeting conditional targets in nationally determined contributions of developing countries: Renewable energy targets and required investment of GGGI member and partner countries. *Energy Policy, 116*, 433–443.
3. Chlela, S., Selosse, S., & Maïzi, N. (2022). Pathways to decarbonization of European islands: Ensuring the integration of high renewable energy and power system flexibility. In *IAEE energy forum* (pp. 16–19).
4. Borland, J., & Tanaka, T. (2018). Overcoming barriers to 100% clean energy for Hawaii starts at the bottom of the energy food chain with residential island nano-grid and everyday lifestyle behavioral changes. In *2018 IEEE 7th World Conference on Photovoltaic Energy Conversion (WCPEC) (A Joint Conference of 45th IEEE PVSC, 28th PVSEC 34th EU PVSEC)* (pp. 3829–3834).
5. Horowitz, R., Binsted, M., Browning, M., Fawcett, A., Henly, C., Hultman, N., McFarland, J., & McJeon, H. (2022). The energy system transformation needed to achieve the US long-term strategy. *Joule, 6*(7), 1357–1362.
6. Hansen, K., Mathiesen, B. V., & Skov, I. R. (2019). Full energy system transition towards 100% renewable energy in Germany in 2050. *Renewable and Sustainable Energy Reviews, 102*, 1–13.
7. Bramstoft, R., & Skytte, K. (2017). Decarbonizing Sweden's energy and transportation system by 2050. *International Journal of Sustainable Energy Planning and Management, 14*, 3–20.
8. Kiptoo, M. K., Adewuyi, O. B., Lotfy, M. E., Amara, T., Konneh, K. V., & Senjyu, T. (2019). Assessing the techno-economic benefits of flexible demand resources scheduling for renewable energy–based smart microgrid planning. *Future Internet, 11*(10), 219.
9. Mollenhauer, E., Christidis, A., & Tsatsaronis, G. (2018). Increasing the flexibility of combined heat and power plants with heat pumps and thermal energy storage. *Journal of Energy Resources Technology, 140*(2), 020907.
10. Adewuyi, O. B., Lotfy, M. E., Akinloye, B. O., Howlader, H. O. R., Senjyu, T., & Narayanan, K. (2019). Security-constrained optimal utility-scale solar PV investment planning for weak grids: Short reviews and techno-economic analysis. *Applied Energy, 245*, 16–30.
11. Sakah, M., Diawuo, F. A., Katzenbach, R., & Gyamfi, S. (2017). Towards a sustainable electrification in Ghana: A review of renewable energy deployment policies. *Renewable and Sustainable Energy Reviews, 79*, 544–557.
12. Khoodaruth, A., Oree, V., Elahee, M., & Clark, W. W. (2017). Exploring options for a 100% renewable energy system in Mauritius by 2050. *Utilities Policy, 44*, 38–49.
13. Aliyu, A. K., Modu, B., & Tan, C. W. (2018). A review of renewable energy development in Africa: A focus in south Africa, Egypt and Nigeria. *Renewable and Sustainable Energy Reviews, 81*, 2502–2518.
14. Bolwig, S., Bazbauers, G., Klitkou, A., Lund, P. D., Blumberga, A., Gravelsins, A., & Blumberga, D. (2019). Review of modelling energy transitions pathways with application to energy system flexibility. *Renewable and Sustainable Energy Reviews, 101*, 440–452.
15. Akpeji, K. O., Olasoji, A. O., Gaunt, C., Oyedokun, D. T., Awodele, K. O., & Folly, K. A. (2020). Economic impact of electricity supply interruptions in South Africa. *SAIEE Africa Research Journal, 111*(2), 73–87.
16. Huang, Y. W., Kittner, N., & Kammen, D. M. (2019). ASEAN grid flexibility: Preparedness for grid integration of renewable energy. *Energy Policy, 128*, 711–726.
17. Conteh, A., Lotfy, M. E., Adewuyi, O. B., Mandal, P., Takahashi, H., & Senjyu, T. (2020). Demand response economic assessment with the integration of renewable energy for developing electricity markets. *Sustainability, 12*(7), 2653.

18. Ulbig, A., & Andersson, G. (2015). Analyzing operational flexibility of electric power systems. *International Journal of Electrical Power & Energy Systems, 72*, 155–164.
19. Brouwer, A. S., van den Broek, M., Seebregts, A., & Faaij, A. (2015). Operational flexibility and economics of power plants in future low-carbon power systems. *Applied Energy, 156*, 107–128.
20. Koltsaklis, N. E., Dagoumas, A. S., & Panapakidis, I. P. (2017). Impact of the penetration of renewables on flexibility needs. *Energy Policy, 109*, 360–369.
21. Belderbos, A., & Delarue, E. (2015). Accounting for flexibility in power system planning with renewables. *International Journal of Electrical Power & Energy Systems, 71*, 33–41.
22. Babatunde, O. M., Munda, J. L., & Hamam, Y. (2020). Power system flexibility: A review. *Energy Reports, 6*, 101–106.
23. Papaefthymiou, G., & Dragoon, K. (2016). Towards 100% renewable energy systems: Uncapping power system flexibility. *Energy Policy, 92*, 69–82.
24. Hussain, M., & Gao, Y. (2018). A review of demand response in an efficient smart grid environment. *The Electricity Journal, 31*(5), 55–63.
25. Gong, H., & Wang, H. (2016). Day-ahead generation scheduling for variable energy resources considering demand response. In *2016 IEEE PES Asia-Pacific Power and Energy Engineering Conference (APPEEC)* (pp. 2076–2080).
26. Ding, Y., Shao, C., Yan, J., Song, Y., Zhang, C., & Guo, C. (2018). Economical flexibility options for integrating fluctuating wind energy in power systems: The case of China. *Applied Energy, 228*, 426–436.
27. Lund, P. D., Lindgren, J., Mikkola, J., & Salpakari, J. (2015). Review of energy system flexibility measures to enable high levels of variable renewable electricity. *Renewable and Sustainable Energy Reviews, 45*, 785–807.
28. Taibi, E., Nikolakakis, T., Gutierrez, L., Fernandez, C., Kiviluoma, J., Rissanen, S., & Lindroos, T. J. (2018). Power system flexibility for the energy transition: Part 1, overview for policy makers.
29. Ma, J., Silva, V., Belhomme, R., Kirschen, D. S., & Ochoa, L. F. (2013). Evaluating and planning flexibility in sustainable power systems. In *2013 IEEE power & energy society general meeting* (pp. 1–11). IEEE.
30. Impram, S., Nese, S. V., & Oral, B. (2020). Challenges of renewable energy penetration on power system flexibility: A survey. *Energy Strategy Reviews, 31*, 100539.
31. Zhou, B., Xu, D., Li, C., Chung, C. Y., Cao, Y., Chan, K. W., & Wu, Q. (2018). Optimal scheduling of biogas–solar–wind renewable portfolio for multicarrier energy supplies. *IEEE Transactions on Power Systems, 33*(6), 6229–6239.
32. Notton, G., Nivet, M.-L., Voyant, C., Paoli, C., Darras, C., Motte, F., & Fouilloy, A. (2018). Intermittent and stochastic character of renewable energy sources: Consequences, cost of intermittence and benefit of forecasting. *Renewable and Sustainable Energy Reviews, 87*, 96–105.
33. Gürtler, M., & Paulsen, T. (2018). The effect of wind and solar power forecasts on day-ahead and intraday electricity prices in Germany. *Energy Economics, 75*, 150–162.
34. Martinez-Anido, C. B., Botor, B., Florita, A. R., Draxl, C., Lu, S., Hamann, H. F., & Hodge, B.-M. (2016). The value of day-ahead solar power forecasting improvement. *Solar Energy, 129*, 192–203.
35. Wang, Q., Wu, H., Florita, A. R., Martinez-Anido, C. B., & Hodge, B.-M. (2016). The value of improved wind power forecasting: Grid flexibility quantification, ramp capability analysis, and impacts of electricity market operation timescales. *Applied Energy, 184*, 696–713.
36. Xydas, E., Qadrdan, M., Marmaras, C., Cipcigan, L., Jenkins, N., & Ameli, H. (2017). Probabilistic wind power forecasting and its application in the scheduling of gas-fired generators. *Applied Energy, 192*, 382–394.
37. Kostková, K., Omelina, L., Kyčina, P., & Jamrich, P. (2013). An introduction to load management. *Electric Power Systems Research, 95*, 184–191.

38. Bellarmine, G. T. (2000). Load management techniques. In *Proceedings of the IEEE SoutheastCon 2000. 'Preparing for The New Millennium' (Cat. No. 00CH37105)* (pp. 139–145). IEEE.

39. Zhang, Q., & Li, J. (2012). Demand response in electricity markets: A review. In *2012 9th International Conference on the European Energy Market* (pp. 1–8). IEEE.

40. Jabir, H., Teh, J., Ishak, D., & Abunima, H. (2018). Impacts of demand-side management on electrical power systems: A review. *Energies, 11*(5), 1050.

41. Niu, J., Tian, Z., Zhu, J., & Yue, L. (2020). Implementation of a price-driven demand response in a distributed energy system with multi-energy flexibility measures. *Energy Conversion and Management, 208*, 112575.

42. Söder, L., Lund, P. D., Koduvere, H., Bolkesjø, T. F., Rossebø, G. H., Rosenlund-Soysal, E., Skytte, K., Katz, J., & Blumberga, D. (2018). A review of demand side flexibility potential in northern Europe. *Renewable and Sustainable Energy Reviews, 91*, 654–664.

43. Pastore, L. M., Basso, G. L., Sforzini, M., & de Santoli, L. (2020). Heading towards 100% of renewable energy sources fraction: a critical overview on smart energy systems planning and flexibility measures. In *E3S Web of Conferences* (Vol. 197, p. 01003). EDP Sciences.

44. Chen, Y., Xu, P., Gu, J., Schmidt, F., & Li, W. (2018). Measures to improve energy demand flexibility in buildings for demand response (DR): A review. *Energy and Buildings, 177*, 125–139.

45. Siano, P. (2014). Demand response and smart grids—a survey. *Renewable and Sustainable Energy Reviews, 30*, 461–478.

46. Jin, M., Feng, W., Marnay, C., & Spanos, C. (2018). Microgrid to enable optimal distributed energy retail and end-user demand response. *Applied Energy, 210*, 1321–1335.

47. Shigenobu, R., Adewuyi, O. B., Yona, A., & Senjyu, T. (2017). Demand response strategy management with active and reactive power incentive in the smart grid: A two-level optimization approach. *AIMS Energy, 5*, 482–505.

48. Moghaddam, M. P., Abdollahi, A., & Rashidinejad, M. (2011). Flexible demand response programs modeling in competitive electricity markets. *Applied Energy, 88*(9), 3257–3269.

49. Hussain, I., Mohsin, S., Basit, A., Khan, Z. A., Qasim, U., & Javaid, N. (2015). A review on demand response: Pricing, optimization, and appliance scheduling. *Procedia Computer Science, 52*, 843–850.

50. Chauhan, A., Khan, M. T., Srivastava, A., Tripathi, A., Hussain, S. S., & Ustun, T. S. (2022). Techno-economic assessment and environmental analysis of an optimal hybrid system under novel demand response scheme for a remote region of India. *Energy Reports, 8*, 284–291.

51. Neupane, B., Pedersen, T. B., & Thiesson, B. (2018, June). Utilizing device-level demand forecasting for flexibility markets. In Proceedings of the Ninth International Conference on Future Energy Systems (pp. 108–118).

52. Ferreira, P., Almeida, D., Dionísio, A., Bouri, E., & Quintino, D. (2022). Energy markets—Who are the influencers?. Energy, 239, 121962.

53. González-Aparicio, I. and Zucker, A. (2015). Impact of wind power uncertainty forecasting on the market integration of wind energy in Spain. *Applied Energy, 159*, 334–349.

54. Amrollahi, M. H., & Bathaee, S. M. T. (2017). Techno-economic optimization of hybrid photovoltaic/wind generation together with energy storage system in a stand-alone micro-grid subjected to demand response. *Applied Energy, 202*, 66–77.

55. Naderipour, A., Ramtin, A. R., Abdullah, A., Marzbali, M. H., Nowdeh, S. A., & Kamyab, H. (2022). Hybrid energy system optimization with battery storage for remote area application considering loss of energy probability and economic analysis. *Energy, 239*, 122303.

56. Das, B. K., Hassan, R., Islam, M. S., & Rezaei, M. (2022). Influence of energy management strategies and storage devices on the techno-enviro-economic optimization of hybrid energy systems: A case study in Western Australia. *Journal of Energy Storage, 51*, 104239.

57. Wang, Y., Zhang, Y., Xue, L., Liu, C., Song, F., Sun, Y., Liu, Y., & Che, B. (2022). Research on planning optimization of integrated energy system based on the differential features of hybrid energy storage system. *Journal of Energy Storage, 55*, 105368.

58. Taibi, E., Nikolakakis, T., Gutierrez, L., Fernandez, C., Kiviluoma, J., Rissanen, S., & Lindroos, T. J. (2018). Power system flexibility for the energy transition: Part 2, IRENA FlexTool methodology.

59. Stinner, S., Huchtemann, K., & Müller, D. (2016). Quantifying the operational flexibility of building energy systems with thermal energy storages. *Applied Energy, 181*, 140–154.

60. Ralon, P., Taylor, M., Ilas, A., Diaz-Bone, H., & Kairies, K. (2017). Electricity storage and renewables: Costs and markets to 2030. In *International renewable energy agency*. Abu Dhabi.

61. Khiareddine, A., Salah, C. B., Rekioua, D., & Mimouni, M. F. (2018). Sizing methodology for hybrid photovoltaic /wind/ hydrogen/battery integrated to energy management strategy for pumping system. *Energy, 153*, 743–762.

62. Awan, A. B., Zubair, M., Sidhu, G. A. S., Bhatti, A. R., & Abo-Khalil, A. G. (2019). Performance analysis of various hybrid renewable energy systems using battery, hydrogen, and pumped hydro-based storage units. *International Journal of Energy Research, 43*(12), 6296–6321.

63. Zhang, W., Maleki, A., Rosen, M. A., & Liu, J. (2018). Optimization with a simulated annealing algorithm of a hybrid system for renewable energy including battery and hydrogen storage. *Energy, 163*, 191–207.

64. Huang, Y., Keatley, P., Chen, H., Zhang, X., Rolfe, A., & Hewitt, N. (2018). Techno-economic study of compressed air energy storage systems for the grid integration of wind power. *International Journal of Energy Research, 42*(2), 559–569.

65. Li, X., & Palazzolo, A. (2022). A review of flywheel energy storage systems: state of the art and opportunities. *Journal of Energy Storage, 46*, 103576.

66. Bahramara, S. (2021). Robust optimization of the flexibility-constrained energy management problem for a smart home with rooftop photovoltaic and an energy storage. *Journal of Energy Storage, 36*, 102358.

67. Loisel, R. (2012). Power system flexibility with electricity storage technologies: A technical–economic assessment of a large-scale storage facility. *International Journal of Electrical Power & Energy Systems, 42*(1), 542–552.

68. Yang, J., Zhang, L., Han, X., & Wang, M. (2016). Evaluation of operational flexibility for power system with energy storage. In *2016 International Conference on Smart Grid and Clean Energy Technologies (ICSGCE)* (pp. 187–191).

69. Li, Y., Wang, J., Han, Y., Zhao, Q., Fang, X., & Cao, Z. (2020). Robust and opportunistic scheduling of district integrated natural gas and power system with high wind power penetration considering demand flexibility and compressed air energy storage. *Journal of Cleaner Production, 256*, 120456.

70. Nuytten, T., Claessens, B., Paredis, K., Van Bael, J., & Six, D. (2013). Flexibility of a combined heat and power system with thermal energy storage for district heating. *Applied Energy, 104*, 583–591.

71. Li, N., Uckun, C., Constantinescu, E. M., Birge, J. R., Hedman, K. W., & Botterud, A. (2015). Flexible operation of batteries in power system scheduling with renewable energy. *IEEE Transactions on Sustainable Energy, 7*(2), 685–696.

72. Seward, W., Qadrdan, M., & Jenkins, N. (2022). Quantifying the value of distributed battery storage to the operation of a low carbon power system. *Applied Energy, 305*, 117684.

73. Efremov, C., Leu, V., & Sanduleac, M. (2021). Increasing system flexibility through a combination of pumped-hydro and battery-storage systems. An overview of possible developments. In *2021 International Conference on Electromechanical and Energy Systems (SIELMEN)* (pp. 237–242). IEEE.

74. Teng, Y., Wang, Z., Li, Y., Ma, Q., Hui, Q., & Li, S. (2019). Multi-energy storage system model based on electricity heat and hydrogen coordinated optimization for power grid flexibility. *CSEE Journal of Power and Energy Systems, 5*(2), 266–274.

75. Garcia-Torres, F., Bordons, C., Tobajas, J., Real-Calvo, R., Santiago, I., & Grieu, S. (2021). Stochastic optimization of microgrids with hybrid energy storage systems for grid flexibility services considering energy forecast uncertainties. *IEEE Transactions on Power Systems, 36*(6), 5537–5547.

76. He, H., Du, E., Zhang, N., Kang, C., & Wang, X. (2021). Enhancing the power grid flexibility with battery energy storage transportation and transmission switching. *Applied Energy, 290*, 116692.

77. Mohler, D., & Sowder, D. (2017). Energy storage and the need for flexibility on the grid. In *Renewable energy integration* (pp. 309–316). Elsevier.

78. Denholm, P., & Hand, M. (2011). Grid flexibility and storage required to achieve very high penetration of variable renewable electricity. *Energy Policy, 39*(3), 1817–1830.

79. Divya, K., & Østergaard, J. (2009). Battery energy storage technology for power systems—an overview. *Electric Power Systems Research, 79*(4), 511–520.

80. Gago, R. G., Pinto, S. F., & Silva, J. F. (2016). G2V and V2G electric vehicle charger for smart grids. In *2016 IEEE International Smart Cities Conference (ISC2)* (pp. 1–6).

81. Zhang, B., & Kezunovic, M. (2015). Impact on power system flexibility by electric vehicle participation in ramp market. *IEEE Transactions on Smart Grid, 7*(3), 1285–1294.

82. Salvatti, G. A., Carati, E. G., Cardoso, R., da Costa, J. P., & Stein, C. M. D. O. (2020). Electric vehicles energy management with V2G/G2V multifactor optimization of smart grids. *Energies, 13*(5), 1191.

83. Han, S., & Acquah, M. A. (2021). *Grid-to-vehicle (G2V) and vehicle-to-grid (V2G) technologies*. MDPI.

84. Nikoobakht, A., Aghaei, J., Niknam, T., Farahmand, H., & Korpås, M. (2019). Electric vehicle mobility and optimal grid reconfiguration as flexibility tools in wind integrated power systems. *International Journal of Electrical Power & Energy Systems, 110*, 83–94.

85. Borba, B. S. M., Szklo, A., & Schaeffer, R. (2012). Plug-in hybrid electric vehicles as a way to maximize the integration of variable renewable energy in power systems: The case of wind generation in northeastern Brazil. *Energy, 37*(1), 469–481.

86. Wen, C.-K., Chen, J.-C., Teng, J.-H., & Ting, P. (2012). Decentralized plug-in electric vehicle charging selection algorithm in power systems. *IEEE Transactions on Smart Grid, 3*(4), 1779–1789.

87. Šare, A., Krajačić, G., Pukšec, T., & Duić, N. (2015). The integration of renewable energy sources and electric vehicles into the power system of the Dubrovnik region. *Energy, Sustainability and Society, 5*(1), 1–16.

88. Wang, B., Zhao, D., Dehghanian, P., Tian, Y., & Hong, T. (2020). Aggregated electric vehicle load modeling in large-scale electric power systems. *IEEE Transactions on Industry Applications, 56*(5), 5796–5810.

89. Backe, S., Korpås, M., & Tomasgard, A. (2021). Heat and electric vehicle flexibility in the European power system: A case study of Norwegian energy communities. *International Journal of Electrical Power & Energy Systems, 125*, 106479.

90. Cañigueral, M. and Meléndez, J. (2021). Flexibility management of electric vehicles based on user profiles: The Arnhem case study. *International Journal of Electrical Power & Energy Systems, 133*, 107195.

91. Zhang, P., Qian, K., Zhou, C., Stewart, B. G., & Hepburn, D. M. (2012). A methodology for optimization of power systems demand due to electric vehicle charging load. *IEEE Transactions on Power Systems, 27*(3), 1628–1636.

92. Yang, Z., Li, K., & Foley, A. (2015). Computational scheduling methods for integrating plug-in electric vehicles with power systems: A review. *Renewable and Sustainable Energy Reviews, 51*, 396–416.

93. Heggarty, T., Bourmaud, J.-Y., Girard, R., & Kariniotakis, G. (2020). Quantifying power system flexibility provision. *Applied Energy, 279*, 115852.

94. You, L., Ma, H., Saha, T. K., & Liu, G. (2022). Security-constrained economic dispatch exploiting the operational flexibility of transmission networks. *International Journal of Electrical Power & Energy Systems, 138*, 107914.

95. Moeller, C., Kotthaus, K., Zdrallek, M., & Schweiger, F. (2021). Comparison of incentive models for grid-supporting flexibility usage of private charging infrastructure. In *ETG congress 2021* (pp. 1–6). VDE.

96. Kazemi-Razi, S. M., Abyaneh, H. A., Nafisi, H., Ali, Z., & Marzband, M. (2021). Enhancement of flexibility in multi-energy microgrids considering voltage and congestion

improvement: Robust thermal comfort against reserve calls. *Sustainable Cities and Society, 74*, 103160.

97. Billinton, R., & Wangdee, W. (2007). Reliability-based transmission reinforcement planning associated with large-scale wind farms. *IEEE Transactions on Power Systems, 22*(1), 34–41.

98. Brown, T., Schlachtberger, D., Kies, A., Schramm, S., & Greiner, M. (2018). Synergies of sector coupling and transmission reinforcement in a cost-optimised, highly renewable European energy system. *Energy, 160*, 720–739.

99. Conejo, A. J., & Baringo, L. (2018). Unit commitment and economic dispatch. In *Power system operations* (pp. 197–232). Springer.

100. Shahbazitabar, M., & Abdi, H. (2018). A novel priority-based stochastic unit commitment considering renewable energy sources and parking lot cooperation. *Energy, 161*, 308–324.

101. Nosair, H., & Bouffard, F. (2017). Economic dispatch under uncertainty: The probabilistic envelopes approach. *IEEE Transactions on Power Systems, 32*(3), 1701–1710.

102. Kornrumpf, T., Meese, J., Zdrallek, M., Neusel-Lange, N., & Roch, M. (2016). Economic dispatch of flexibility options for grid services on distribution level. In *2016 Power Systems Computation Conference (PSCC)* (pp. 1–7). IEEE.

103. Thatte, A. A., & Xie, L. (2016). A metric and market construct of inter-temporal flexibility in time-coupled economic dispatch. *IEEE Transactions on Power Systems, 31*(5), 3437–3446.

104. Chondrogiannis, S., Poncela-Blanco, M., Marinopoulos, A., Marneris, I., Ntomaris, A., Biskas, P., & Bakirtzis, A. (2021). Chapter 8—power system flexibility: A methodological analytical framework based on unit commitment and economic dispatch modelling. In A. Dagoumas (Ed.), *Mathematical modelling of contemporary electricity markets* (pp. 127–156). Academic Press.

105. Papaemmanouil, A., Andersson, G., Bertling, L., Johnsson, F., et al. (2010). A cost-benefit analysis of transmission network reinforcement driven by generation capacity expansion. In *IEEE PES general meeting* (pp. 1–8). IEEE.

106. Li, Z., Cheng, Z., Li, S., Si, J., Gao, J., Dong, W., & Das, H. S. (2021). Virtual synchronous generator and SMC based cascaded control for voltage-source grid-supporting inverters. *IEEE Journal of Emerging and Selected Topics in Power Electronics, 10*(3), 2722–2736.

107. Unruh, P., Nuschke, M., Strauß, P., & Welck, F. (2020). Overview on grid-forming inverter control methods. *Energies, 13*(10), 2589.

108. Gabriels, G. H., Windapo, M. O., Oyedokun, D. T., & Ruggeri, S. (2020). Proposed framework for integration of optimal current injection and multi-agent control of the LV distribution network. In *2020 6th IEEE International Energy Conference (ENERGYCon)* (pp. 521–526). IEEE.

109. Dai, W., Yang, Z., Yu, J., Cui, W., Li, W., Li, J., & Liu, H. (2021). Economic dispatch of interconnected networks considering hidden flexibility. *Energy, 223*, 120054.

110. Leite, W. L., Svinicki, M., & Shi, Y. (2010). Attempted validation of the scores of the VARK: Learning styles inventory with multitrait–multimethod confirmatory factor analysis models. *Educational and Psychological Measurement, 70*(2), 323–339.

111. Rameshkumar, G., & Samundeswari, S. (2014). Neural network, artificial neural network (ANN) and biological neural network (BNN) in soft computing. *Volume, 30*(3), 3.

112. Levy, S. (1992). *Artificial life: The quest for a new creation*. Random House Inc.

113. Mohammed, M., Khan, M. B., & Bashier, E. B. M. (2016). *Machine learning: Algorithms and applications*. CRC Press.

114. Balas, V. E., Roy, S. S., Sharma, D., & Samui, P. (2019). *Handbook of deep learning applications* (Vol. 136). Springer.

115. Ongsulee, P. (2017). Artificial intelligence, machine learning and deep learning. In *2017 15th International Conference on ICT and Knowledge Engineering (ICT&KE)* (pp. 1–6). IEEE.

116. Ingre, B., & Yadav, A. (2015). Performance analysis of NSL-KDD dataset using ANN. In *2015 International Conference on Signal Processing and Communication Engineering Systems* (pp. 92–96). IEEE.

117. Sze, V., Chen, Y.-H., Yang, T.-J., & Emer, J. S. (2017). Efficient processing of deep neural networks: A tutorial and survey. *Proceedings of the IEEE, 105*(12), 2295–2329.
118. Shinde, P. P., & Shah, S. (2018). A review of machine learning and deep learning applications. In *2018 Fourth International Conference on Computing Communication Control and Automation (ICCUBEA)* (pp. 1–6). IEEE.
119. Janiesch, C., Zschech, P., & Heinrich, K. (2021). Machine learning and deep learning. *Electronic Markets, 31*(3), 685–695.
120. Alassery, F., Alzahrani, A., Khan, A., Irshad, K., & Kshirsagar, S. R. (2022). An artificial intelligence-based solar radiation prophesy model for green energy utilization in energy management system. *Sustainable Energy Technologies and Assessments, 52*, 102060.
121. Ahmad, T., Chen, H., & Shah, W. A. (2019). Effective bulk energy consumption control and management for power utilities using artificial intelligence techniques under conventional and renewable energy resources. *International Journal of Electrical Power & Energy Systems, 109*, 242–258.
122. Reynolds, J., Ahmad, M. W., Rezgui, Y., & Hippolyte, J.-L. (2019). Operational supply and demand optimisation of a multi-vector district energy system using artificial neural networks and a genetic algorithm. *Applied Energy, 235*, 699–713.
123. Finck, C., Li, R., & Zeiler, W. (2019). Economic model predictive control for demand flexibility of a residential building. *Energy, 176*, 365–379.
124. Xu, Y., Ahokangas, P., Louis, J.-N., & Pongrácz, E. (2019). Electricity market empowered by artificial intelligence: A platform approach. *Energies, 12*(21), 4128.
125. Lu, R., Hong, S. H., & Yu, M. (2019). Demand response for home energy management using reinforcement learning and artificial neural network. *IEEE Transactions on Smart Grid, 10*(6), 6629–6639.
126. Ponoćko, J., & Milanović, J. V. (2018). Forecasting demand flexibility of aggregated residential load using smart meter data. *IEEE Transactions on Power Systems, 33*(5), 5446–5455.
127. Zhou, Y., & Zheng, S. (2020). Machine-learning based hybrid demand-side controller for high-rise office buildings with high energy flexibilities. *Applied Energy, 262*, 114416.
128. Ye, Y., Qiu, D., Wu, X., Strbac, G., & Ward, J. (2020). Model-free real-time autonomous control for a residential multi-energy system using deep reinforcement learning. *IEEE Transactions on Smart Grid, 11*(4), 3068–3082.
129. Wang, H., Yi, H., Peng, J., Wang, G., Liu, Y., Jiang, H., & Liu, W. (2017). Deterministic and probabilistic forecasting of photovoltaic power based on deep convolutional neural network. *Energy Conversion and Management, 153*, 409–422.
130. Kumar, K. R., & Kalavathi, M. S. (2018). Artificial intelligence based forecast models for predicting solar power generation. *Materials Today: Proceedings, 5*(1), 796–802.
131. Zang, H., Cheng, L., Ding, T., Cheung, K. W., Wei, Z., & Sun, G. (2020). Day-ahead photovoltaic power forecasting approach based on deep convolutional neural networks and meta learning. *International Journal of Electrical Power & Energy Systems, 118*, 105790.
132. Jung, Y., Jung, J., Kim, B., & Han, S. (2020). Long short-term memory recurrent neural network for modeling temporal patterns in long-term power forecasting for solar PV facilities: Case study of South Korea. *Journal of Cleaner Production, 250*, 119476.
133. Ahmadiahangar, R., Häring, T., Rosin, A., Korõtko, T., & Martins, J. (2019). Residential load forecasting for flexibility prediction using machine learning-based regression model. In *2019 IEEE International Conference on Environment and Electrical Engineering and 2019 IEEE Industrial and Commercial Power Systems Europe (EEEIC/I&CPS Europe)* (pp. 1–4). IEEE.
134. Khan, P. W., Byun, Y.-C., Lee, S.-J., Kang, D.-H., Kang, J.-Y., & Park, H.-S. (2020). Machine learning-based approach to predict energy consumption of renewable and nonrenewable power sources. *Energies, 13*(18), 4870.
135. Rocha, H. R., Honorato, I. H., Fiorotti, R., Celeste, W. C., Silvestre, L. J., & Silva, J. A. (2021). An artificial intelligence based scheduling algorithm for demand-side energy management in smart homes. *Applied Energy, 282*, 116145.

136. Lan, T., Jermsittiparsert, K., T Alrashood, S., Rezaei, M., Al-Ghussain, L., & A Mohamed, M. (2021). An advanced machine learning based energy management of renewable microgrids considering hybrid electric vehicles' charging demand. *Energies, 14*(3), 569.
137. Shivam, K., Tzou, J.-C., & Wu, S.-C. (2021). A multi-objective predictive energy management strategy for residential grid-connected PV-battery hybrid systems based on machine learning technique. *Energy Conversion and Management, 237*, 114103.
138. Yousaf, A., Asif, R. M., Shakir, M., Rehman, A. U., Alassery, F., Hamam, H., & Cheikhrouhou, O. (2021). A novel machine learning-based price forecasting for energy management systems. *Sustainability, 13*(22), 12693.
139. Yang, W., Sun, S., Hao, Y., & Wang, S. (2022). A novel machine learning-based electricity price forecasting model based on optimal model selection strategy. *Energy, 238*, 121989.
140. Najafabadi, M. M., Villanustre, F., Khoshgoftaar, T. M., Seliya, N., Wald, R., & Muharemagic, E. (2015). Deep learning applications and challenges in big data analytics. *Journal of Big Data, 2*(1), 1–21.
141. Boulemtafes, A., Derhab, A., & Challal, Y. (2020). A review of privacy-preserving techniques for deep learning. *Neurocomputing, 384*, 21–45.
142. Monti, A., & Ponci, F. (2015). Electric power systems. In E. Kyriakides & M. Polycarpou (Eds.), *Intelligent monitoring, control, and security of critical infrastructure systems* (1st ed.). Springer.
143. Adewuyi, O. B., Danish, M. S. S., Howlader, A. M., Senjyu, T., Lotfy, M. E., et al. (2018). Network structure-based critical bus identification for power system considering line voltage stability margin. *Journal of Power and Energy Engineering, 6*(9), 97.
144. Wu, Y.-K. (2007). A novel algorithm for ATC calculations and applications in deregulated electricity markets. *International Journal of Electrical Power and Energy Systems, 29*(10), 810–821.
145. Sarker, I. H. (2021). Machine learning: Algorithms, real-world applications and research directions. *SN Computer Science, 2*(3), 1–21.
146. Bae, H., Jang, J., Jung, D., Jang, H., Ha, H., Lee, H., & Yoon, S. (2018). Security and privacy issues in deep learning. arXiv preprint arXiv:1807.11655.
147. Kiptoo, M. K., Lotfy, M. E., Adewuyi, O. B., Conteh, A., Howlader, A. M., & Senjyu, T. (2020). Integrated approach for optimal techno-economic planning for high renewable energy-based isolated microgrid considering cost of energy storage and demand response strategies. *Energy Conversion and Management, 215*, 112917.
148. Soto, E. A., Bosman, L. B., Wollega, E., & Leon-Salas, W. D. (2021). Peer-to-peer energy trading: A review of the literature. *Applied Energy, 283*, 116268.
149. Park, C., & Yong, T. (2017). Comparative review and discussion on P2P electricity trading. *Energy Procedia, 128*, 3–9.
150. Jogunola, O., Ikpehai, A., Anoh, K., Adebisi, B., Hammoudeh, M., Son, S.-Y., & Harris, G. (2017). State-of-the-art and prospects for peer-to-peer transaction-based energy system. *Energies, 10*(12), 2106.

Machine Learning Applications for Renewable Energy Systems

Yasir Saleem Afridi, Laiq Hassan, and Kashif Ahmad

1 Introduction

In the modern world, our dependency on technology and modern machines has increased resulting in a significant increase in energy consumption. The World Bank indicators show a strong link between the consumption of energy and the development of a country in different aspects of life, such as economy, infrastructure, health, education, etc. [1]. Fossil fuels, which include crude oil, natural gas, and coal, mainly remained a primary source of energy. However, in the current era, where global warming and climate change are considered to be among the biggest threats to mankind, the focus has been shifted toward renewable sources of energy, such as hydropower, geothermal heat, solar, and wind energy. Compared to fossil fuels, renewable sources of energy bring several advantages. For instance, it is a source of energy that never runs out. More importantly, its zero carbon emission characteristic makes it more environmentally friendly by ensuring cleaner air and water.

While speaking about renewable sources of energy, hydropower has always been the leading source of energy. However, over the past decade, wind power and solar power have also gained a lot of attention [2]. The extensive research in the area has led to the development of technologically advanced and highly complex power generation machines. On one hand, where this development has increased the efficiency and performance of the equipment, it has also generated the need

Y. S. Afridi (✉) · L. Hassan
Department of Computer Systems Engineering, University of Engineering and Technology, Peshawar, Pakistan
e-mail: Yasirsaleem@uetpeshawar.edu.pk

K. Ahmad
Department of Computer Science, Munster Technological University, Cork, Ireland

for artificially intelligent energy forecasting, planning, and plant operation and maintenance models/solutions. These models/solutions also make use of state-of-the-art machine learning (ML) algorithms for a diversified set of tasks in the domain.

The current fast-paced advancements in the fields of artificial intelligence (AI) and ML have reduced the need for human intervention in carrying out different complex operations in the power sector to a minimum level. These developments have also enabled us to adopt a proactive approach to the challenges faced while managing such intricate renewable energy systems. The industry experts and analysts foresee a pivotal role being played by AI and ML in the future of renewable energy systems. Investments pertinent to AI in the renewable energy sector are expected to cross USD 7.78 billion by 2024, as per a market intelligence report published by BIS Research [3]. The extensive opportunities for growth offered by AI and ML have forced the major market players to incorporate them into their strategies. The applications of AI and ML in addressing the problems faced by energy companies are plentiful. This chapter provides an overview of AI and ML applications for renewable energy systems. The key applications covered in the chapter include: (i) weather prediction/forecasting using ML algorithms, (ii) forecasting energy supply and demand through AI, (iii) integration of AI with smart grids, and (iv) AI-based condition monitoring and prognostics maintenance systems. An overview of available resources, such as datasets and ML algorithms, for the researchers in the domain is also provided. Moreover, the chapter highlights the key challenges associated with the successful deployment of ML algorithms and potential future research directions in the domain.

The rest of the chapter is organized as follows. Section 2 provides an overview of the existing literature on the topic. Section 3 provides an overview of some key applications of ML for renewable energy systems. Section 5 highlights the key challenges and potential opportunities in the domain. Finally, Sect. 6 concludes the chapter by providing key insights and lessons learned.

2   Related Work

The literature reports outstanding generalization capabilities for ML algorithms in different application domains, such image classification [4], speech recognition [5], and text processing [6]. ML algorithms allow the identification of hidden patterns in a large collection of data and extract meaningful insights. Similar to other application domains, where ML algorithms have been proved very effective, the energy sector also provides a huge amount of data on different aspects of energy systems [2, 7]. To extract meaningful insights from the data, several interesting ML solutions, exploring different aspects of the energy sector, have been proposed in the literature.

Most of the recent efforts in the domain focus on renewable energy systems. For instance, Lai et al. [8] provide a detailed survey of ML models for the prediction tasks in renewable energy systems. The authors discussed different aspects of the

domain, such as the performance of existing ML models, pre-processing techniques, and parameter selection approaches adopted in the literature. Gu et al. [9], on the other hand, discuss the use of ML algorithms for renewable energy materials. The authors explored the potential of ML in key renewable energy technologies including catalysis, batteries, solar cells, and crystal discovery. Daniel et al. [10] provide an overview of ML applications in harnessing of renewable energy, such as wind, solar, and thermal energy.

The literature also reports interesting works on certain aspects of ML-based solutions for renewable energy applications. For instance, Salcedo et al. [11] provide an overview of feature selection approaches adopted in ML-based predictive solutions for renewable energy applications. The authors also highlight the challenges, potential, and key aspects of the feature selection process, such as the impact of certain features on the predictive capabilities of ML models in renewable energy applications. Several studies focus on applications of certain types of ML algorithms for renewable energy. For example, Perera et al. [12] explored the potential of reinforcement learning, which represents a sub-category of ML algorithms, in renewable energy applications. In total, seven different applications of renewable energy relying on reinforcement learning algorithms, namely *building energy management system*, *dispatch*, *vehicle energy systems*, *energy devices*, *grids*, *energy markets prediction*, are discussed.

The rich literature on the topic shows the potential of ML in renewable energy applications. However, there are several challenges associated with the successful deployment of ML algorithms in different applications of renewable energy. In this chapter, we highlight such challenges by exploring different aspects of ML applications in renewable energy. We also highlight the potential opportunities, existing resources, and future research directions in the domain.

3   Key Applications

The list of ML applications for renewable energy is very diverse as shown in Fig. 1. In this section, we provide an overview of some of the key applications with a reasonable amount of existing literature, such as weather and energy consumption forecasting, prognostic maintenance, and ML applications in smart grids.

3.1   Forecasting

The process of estimating future events, states, and processes by deploying various conceptual models is known as forecasting. Forecasting is an important aspect of renewable energy systems, specifically solar and wind power, keeping in view their variable energy generation nature. The wind and solar power systems are therefore known as variable renewable energy (VRE) systems because their generation output
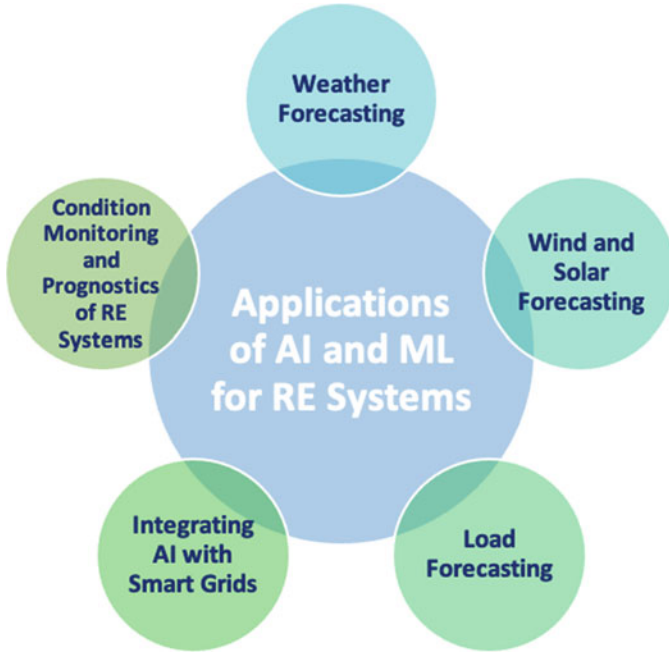
Fig. 1 Some key applications of AI and ML for renewable energy

varies in time, based on the intensity of their sources (i.e., the wind and the Sun). Consequently, an aspect of uncertainty gets associated with them as the power generation by these sources cannot be predicted with perfect accuracy [13]. This is where ML comes into play and is extensively used to carry out forecasts of wind speeds and solar irradiance. In the renewable energy sector, ML algorithms are used for the prediction/forecasting of the future events and states of different elements associated with renewable energy. Irrespective of several forecasting systems being adopted, the model errors continue to exist. However, with the increased use of advanced statistics, ML and AI, the accuracy of these forecasting models has been improved significantly. In the following subsections, we discuss some of the key forecasting applications in the domain.

3.1.1 Weather Forecasting

Weather forecasting plays a vital role in integrating solar and wind power generations into the grid, especially in cases where the penetration levels are high. The most crucial scheduling input for VRE generators that are weather dependent is obtained from weather forecasting data. Therefore, the forecast for power generations is a combination of regional weather forecasts and plant availability.

In the literature, several interesting solutions for weather forecasting have been proposed. These methods can be broadly classified into two categories, namely physical methods and statistical methods [13]. In the physical methods, weather data including temperature, pressure, humidity, surface roughness, and obstacles are fed into a numerical weather predictor (NWP) model. The model in return generates weather conditions using physical and mathematical laws that are specific to terrain and can be converted into energy production. The statistical methods used alongside the NWP models aim to increase the correctness of the results generated by employing historic and real-time generation data. Persistence forecasting, for instance, is used as a benchmark for evaluating the advanced forecasting methods as it is the simplest statistical method based on an assumption that the current generation levels will remain constant in the near future [14]. Advanced forecasting methods make use of AI and big data to carry out the predictions by analyzing live as well as historical weather data. Since advanced forecasting facilitates and improves VRE integration, it is one of the main applications of AI in weather forecasting. With continual advancements in computing power and ML algorithms, these forecasts have become more and more accurate over the past few years.

Moreover, the VRE forecasting approaches could also be categorized into centralized and decentralized methods. Centralized VRE forecasting is the cumulative system-wide forecast of all the VRE generators within a specific balancing area. The centralized forecasts are normally administered by the system operators and are considered to be one of the best approaches for economic dispatch. On the other hand, decentralized VRE forecasting is carried out by individual power generators. It facilitates the system operator in making efficient decisions pertinent to potential transmission congestion by providing plant-level information. The centralized VRE forecasting is more effective as it incorporates a single methodology of forecasting across all distributed power generators [15]. Therefore, it lowers the uncertainties at the system operator level and reduces the financial burden of carrying out individual forecasts on the distributed power generator level. However, relying on a single methodology in the case of centralized forecasting increases the risk of systematic bias. This issue can be addressed by incorporating the ensemble forecasting method, where an aggregate of the results generated by multiple forecast models is taken rather than relying on a single forecasting model [16].

3.1.2 Wind and Solar Power Production Forecasting

In the areas with moderate to high wind power generation, the operators make use of wind energy forecasting to predict the power generation. Likewise, the solar irradiance data are used to forecast solar power forecasting. Given the stochastic nature of wind and solar power generations, ML algorithms have been extensively used for carrying out short-term forecasts of these entities. The current trends in solar and wind power estimation use disaggregation of power generation as well as innovative features and structural information for carrying out short-term forecasts. For instance, based on the video recordings of the sky, convolutional

neural networks (CNNs) have been trained to predict near-real-time solar power generation [17]. The solar and wind power output is directly and closely related to the prevailing weather conditions. Recent research, therefore, aims to seamlessly integrate weather forecasting and power generation prediction. Efforts are being made to improve the efficiency of the weather forecasting models to effectively use them as an input for predicting VRE power generation. Numerous physics-based NWP models have been developed to estimate solar irradiance from 0 to 72 h ahead [18]. The output of these multi-timescale NWP models is then used as an input to ML algorithms for carrying out probabilistic power predictions. Similarly, various techniques take the NWP data as features to carry out supervised wind power forecasts. However, the supervised power prediction techniques have a limitation when dealing with distributed energy sources, where the size, location, panel orientation, and hardware data are not always available to the system operators for all the interconnected systems [19]. In such scenarios, satellite and aerial imagery data can be fed into ML models for effectively predicting power outputs [2].

There are several benefits of wind and solar power forecasting. On one hand, it enables the power system operators to maintain lesser reserves. On the other hand, it helps them in handling the supply-side uncertainties. Moreover, efficient predictions can also help in tackling the extreme changes in wind and solar generation that cause a sudden change in the power output. Wind and solar power predictions also enable the grid operators to schedule and dispatch generating plants efficiently. Thereby, the power system operators can make smart and profitable choices on power purchasing by relying more on VRE sources. Furthermore, the wind and solar power prediction also facilitates the power generators by allowing them to carry out plant maintenance during the low production period. Based on the power prediction data, project financers can make better decisions by assessing the plant output data and thus arranging the necessary finance, accordingly.

Nevertheless, the prospects for future research studies to deeply integrate weather and power prediction are quite bright. More studies need to be carried out to develop hybrid physical models where NWP physics-based models are directly incorporated into ML power prediction models.

3.1.3   Load Forecasting

The very fact that electricity cannot be stored in large quantities has given rise to a principle in the power industry known as "the balancing rule." This rule suggests that a consistent balance must always be maintained between the amount of electricity demanded and the amount of electricity supplied. This is important because in both excessive generation and undersupply of electric power, monetary losses are faced by power operators. Hence, to maintain an ideal balancing situation, load forecasting has become an important phenomenon of the current power market. Load forecasting is a technique used by power operators to predict the energy demand to balance it with the anticipated energy supply. Load forecasting also plays a pivotal role in effective decision-making during power system capacity planning to

meet the current load requirements and power system expansion to cater the future anticipated load requirements.

Load forecasting can be broadly classified into three groups based on the time horizons of the planning strategies. These categories include: (i) long-term load forecasting (LTLF), (ii) medium-term load forecasting (MTLF), and (iii) short-term load forecasting (STLF). LTLF ranges from 1 year to 20 years and is mainly used for carrying out economic planning of new generation capacity and transmission network. It also facilitates in predicting the future needs for expansion and infrastructure development. MTLF normally predicts the load for a period ranging from 1 week to 1 year. MTLF plays an important role in making decisions pertinent to the scheduling of fuel supplies, carrying out the maintenance activities, financial planning, and tariffs formulation. STLF, on the other hand, ranges from 1 h to 1 week and provides the basis for taking profitable decisions regarding generation units start-up and shutdown. STLFs are used to maintain the demand–supply balance that are important to avoid undersupply and excessive supply of energy. It also provides the information regarding the daily operations and unit commitment to the system operators. STLF is also used to overcome the transmission constraints by providing approximate load flow. STLF also facilitates in economic load dispatching and security assessment.

Load forecasting is a stochastic problem rather than deterministic. Hence, there is no certainty in forecasting. The reason being load forecasting depends upon numerous factors that need to be taken into account while designing a forecasting model. Some of the factors include load density, population growth, historical data, alternative energy sources, and other geo-graphical factors.

Among all the aforementioned load forecasting types, STLF is mostly utilized. One of the potential reasons for more focus on STLF is that it plays a vital role in managing energy transfer schedules based on the estimated load for periods ranging from thirty minutes to an entire day. Therefore, an efficient STLF reduces the expenses incurred by the system operators and enhances the efficiency of the transmission network [20]. In recent years, various techniques have been applied for enhancing the accuracy and efficiency of the load forecasting for VRE systems, including AI and fuzzy logic. Based on their explainability, flexibility to use, and symbolic reasoning, AI has gained more importance and is now being widely used. A technique based on fuzzy logic to carry STLF by incorporating historic weather data has been used by [21]. A detailed review on AI-based load forecasting for smart grids and buildings has been carried out by [22]. ANNs have been used to carry out next day load forecasting [23]. Similarly, an ANN-based STLF for distribution systems [24] and a non-linear autoregressive ANN with exogenous vector inputs to carry out STLF has been developed [25]. Since STLF is based on non-stationary data having forecasting horizon dependencies, LSTM has been used in lieu of its unprecedented ability to handle long-term data dependencies [26]. Atef et al. [27] proposed a deep-stacked LSTM model to forecast the load demand. The results showed that bidirectional LSTM (Bi-LSTM) outperformed the simple LSTM models in terms of forecasting accuracy. Similarly, hybrid ANN models with fuzzy logic have also been developed for accurately predicting the load demand

by classifying a large input load dataset. A forecasting model that takes into account the effect of weather and holidays data on the load forecast has been developed using fuzzy logic and ANN [28]. Fuzzy logic has also been used to construct temperature and holiday factor rule bases, an ANN model is then used to predict the hourly load demand. The forecast results showed that the hybrid model produced better results as compared to a standalone ANN model. Also, an enhanced convolutional neural network (CNN) has been proposed to forecast electricity price and load [29]. Numerous AI techniques have been used to carry out load forecasting, and the research show that they have achieved promising results as compared to the conventional techniques. The non-parametric AI-based techniques can clearly overcome the limited capabilities of traditional parametric (statistical) models such as linear regression, stochastic modeling of time series, and general exponential techniques [30]. However, adequate and suitable training data, an appropriate learning algorithm, and an optimized network structure help increasing the overall performance and accuracy of the models, thus reducing the network complexities.

3.2   Integrating AI with Smart Grids

In the past decade, a global paradigm shift from the conventional centralized energy generation to the distributed renewable energy generation has been observed. This has given rise to the need of replacing the traditional transmission and distribution systems with more resilient and smart power distribution and transmission systems. Since, the current grids cannot efficiently cater the fluctuating generation from multiple distributed renewable energy sources and have become obsolete. Therefore, the current grids are now being replaced with the "smart grids." A smart grid is a network that allows two-way flow of data and electricity by effectively integrating digital communication technology with energy distribution, thus, enabling the system operators to optimize the generation, transmission, and distribution of energy on one end and consumers to make cost-effective decisions regarding energy consumption on the other end. Although it is an important factor, but smart grids do not rely on power delivery only, rather the main aspect of a smart grid is a two-way connection of energy and information. Therefore, a smart grid generates an extensive amount of data that is also necessary for its successful operation. Hence, the conventional computational techniques do not have the ability to process such huge amount of data. This is where AI comes into play, capable enough to take into account millions of variables and data points that include but are not limited to weather, location, generation, infrastructure, demand, and assets. AI helps every household and system operator in making proactive decisions regarding the energy generation and supply and the associated energy cost. For instance, if we know ahead of time that it is going to rain for a week, the loss in the solar generation can be catered by proactively upscaling the other generation sources for that specific week. This is what makes AI so appealing for the implementation and

management of smart grids. Since the modern power systems are revolutionizing at a fast pace, more and more distributed and diversified smart grid components, such as smart metering systems, digital communication infrastructure, distributed energy sources, and electric vehicles, are getting integrated into the power network along with an underlying communication system. This enables the customers and grid to be directly connected with the help of AI. Thus, homeowners can comprehensively monitor their consumption through smart metering systems and hence take profitable decisions by smartly consuming electricity during low-cost hours. Furthermore, a massive amount of data generated by these smart grid components help automate and enhance the performance of smart grids by supporting vast applications such as forecasting the system state, distributed energy management, fault diagnosis, and grid security against cyberattacks.

3.2.1 Applications of AI in Smart Grids

In smart grids, AI and ML algorithms are used for a diversified set of tasks. In this section, we provide an overview of some of the key applications of AI and ML for smart grids. These applications include:

- **Assessment of Power Grid Stability:** The assessment of the stability of power grids is vital for ensuring the reliability and security of power systems. The power system stability ensures that the system maintains an equilibrium operation state or promptly reaches a new equilibrium state when a small change is induced [31]. The traditional models require extensive computing resources because of their dependence on dynamic power system models. Therefore, data-driven AI-based models are applied to carry out power grid stability analysis because of their efficient performance. The smart grid stability assessment mainly comprises transient stability assessments, small-signal stability, frequency stability, and voltage stability assessment [32]. Transient stability assessment is the ability to determine whether a system will remain synchronized when a huge change in the normal operating state takes place. The small-signal stability assessment, on the other hand, represents the ability of the system to maintain the state of synchronization during small disturbances. The frequency stability assessment is the ability of the system to maintain a steady frequency during the generation and load imbalances, while the voltage stability assessment is the ability of the system to evaluate and maintain voltage stability during a voltage collapse.
- **Faults Diagnosis:** The increased complexity of smart grids has introduced numerous sensitive equipment and components into the system. Protection of such equipment against faults is very important for carrying out smooth operations. Fault diagnosis in smart grids, therefore, provides a defense mechanism for the safety of the sensitive equipment and helps to quickly isolate the faults. With the increased integration of VRE resources in smart grids, effective fault diagnosis has become a great challenge. AI and ML, therefore, play an important

role in carrying out efficient predictive, preventive, and corrective maintenance activities for smart grids.

The literature reports several interesting fault detection techniques. For instance, Fazai et al. [33] proposed an extreme learning machine (ELM) model for fault location detection based on wavelet transform. Similarly, an ensemble framework consisting of five ML algorithms is developed to analyze the power grid frequency disturbances that detected faults with three levels of severity [34]. In [35], a semi-supervised ML model based on KNN and decision tree algorithms are used for fault diagnosis of the transmission and distribution system of microgrids. Extensive research has been carried out in this area that reflects the effectiveness of AI and ML models for carrying out fault diagnosis in smart grids.

- **Security of Smart Grids:** The inherent vulnerability of communication technology and the complexity of smart grids have exposed the communication layers to various security issues. A probable cyberattack on the system can result in operational failures, loss of synchronization, interruption in the power supply, cascading failures, and complete blackouts. Having lethal and vital economic and social consequences, power grids have become a lucrative target for cyberattacks [36]. The most common attacks carried out on smart grids include false data injection attacks (FDIA) and distributed denial of service (DDoS) attacks. In FDIA, the system data are being altered to mislead the power operators, while in DDoS attacks the attackers attempt to make a service unavailable for its intended users. In recent years, various state-of-the-art AI-based approaches have been proposed to ensure the overall security of smart grids. For instance, a neural network model based on stacked denoising autoencoder (SDAE) has been proposed that identifies four different attacks on smart grids [37]. Kosek et al. [38], on the other hand, used an ANN model to identify malicious actions for controlling voltage in the low-voltage distribution grids. Similarly, a semi-supervised ML framework with a domain-adversarial training of known attacks has been used to detect anomalies and patterns for identifying the returning threats at distinct loads and hours [39]. Although sophisticated techniques have been proposed for ensuring the security of the smart grids, however, interdisciplinary research to develop a holistic and methodical solution can further help to tackle the security threats prone to smart grids, effectively.

3.3 Condition Monitoring and Fault Prognostics of Renewable Energy Systems

The continual advancements in the renewable energy sector have led to the development of more complex generation units. Such intricate generation units require more effective and efficient operation and maintenance (O&M) techniques. Furthermore, a delay in diagnosing a fault increases the cost of its rectification. Also, fault can propagate and damage other equipment that can further add to plant shutdown and uncalled-for outages, whereas, with the exponential increase

in demand and increased dependency on energy globally, power outages and plant downtimes are highly unfavorable. For ensuring efficient and cost-effective O&M, the current reactive approaches toward fault diagnosis are being replaced with more advanced proactive approaches where the system faults are being predicted. Hence, condition-based monitoring (CBM) and fault prognostics have become the need of the day. To meet these challenges, state-of-the-art AI and ML models have been developed to predict the faults in renewable energy systems, including hydropower, wind power, and solar power projects. In the following subsections, we provide an overview of hydro, wind, and solar projects.

3.3.1   Hydropower Projects

Hydropower plants (HPPs) being one of the first renewable sources of energy are mostly relied upon to cater to the baseload demands of grids. Therefore, plant availability and reduced downtimes are very important while carrying O&M of HPPs. Consequently, the current preventive and corrective maintenance procedures are being replaced with more advanced diagnostic and prognostic maintenance systems. Hence, several efforts are being made for O&M. For instance, a graphical software-based condition monitoring system using wavelet analysis has been developed for a Francis turbine [40]. The research shows that the vast majority of predictive maintenance solutions for HPPs are data-driven. Several data-driven predictive maintenance models for HPPs are being analyzed and classified into three categories: a) physical models, b) stochastic models, and c) ML-based data mining models [41]. Likewise, support vector machine (SVM)-based CBM and fault diagnostic technique for HPPs have been developed [42]. Although SVM outperformed other classification methods, it required higher computational time. Deep learning models have also been used to carry out the CBM and predictive maintenance of HPPs. For instance, a deep neural network-based anomaly detection model in multivariate time-series data has been used [43]. The patterns in the data were captured using long short-term memory (LSTM) because of its unprecedented performance while dealing with time-series data. Similarly, the remaining useful life (RUL) of hydropower turbine bearings has also been determined using the bearing vibrations data acquired from run-to-failure experiments [44]. Although a lot of research have been carried out on the CBM of HPPs; however, variations in the operating conditions of the HPPs make the adaptability (i.e., a model trained on data obtained at one plant could be used for the prediction of data obtained at a plant at a different location with different operating environments) of these models a very complex process.

3.3.2   Wind Power Projects

Among all the renewable energy sources, CBM and fault prognostics for wind turbines (WTs) have always been in the limelight because of the following reasons:

- WTs have got a very high capital cost; therefore, for an effective payback period, plant availability should be maximized.
- WTs normally operate under stressful conditions because of the extreme weather conditions and a constantly variable load; therefore, they have got a higher failure probability.
- Large offshore WTs have got a higher failure downtime because of the access difficulties.

Therefore, an improved CBM and fault prognostics system for WTs can avoid its subassemblies from getting damaged, hence minimizing the plant downtime. Various fascinating and distinct solutions pertinent to the CBM of WTs are reflected in the literature. One of the key components of a WT that transfers the power between the turbine and the generator shaft is the gearbox. Being one of the most critical components, it contributes maximum to the capital cost of the WTs. Consequently, the associated maintenance and repair cost of gearboxes is also very high. Being an important aspect of renewable wind projects, several interesting solutions have been proposed for fault prognostics of wind turbines. For instance, a data-driven framework based on ANN is developed for carrying out the fault prognostics of WT gearbox [45]. The mechanical fault diagnosis of WTs can be further improved by analyzing the vibration signals acquired from the accelerometers along with the power signals. A similar fault diagnostic system based on data mining techniques using multi-sensor data has been proposed [46]. Likewise, models for the estimation of RUL of WTs main bearing have been presented using the likelihood functions [47]. With the advancements in computational resources and the development of new AI algorithms, the search for the development of the most optimal fault diagnostic system for WTs continues.

3.3.3 Solar Power Projects

As compared to wind and hydropower projects, solar power projects are purely electrical and are therefore less susceptible to degradation and faults. Therefore, CBM and fault diagnostics in solar power projects are mostly related to the photovoltaic (PV) modules' health analysis, monitoring the power loss, and the performance monitoring of energy storage systems. For instance, a framework based on ANN is used to carry out the PV health monitoring and analyze the degradation to make effective maintenance decisions accordingly [48]. The performance ratio (PR) of a PV module is the ratio of the actual generation against the rated generation capacity of that module. PR is a key indicator when assessing the reliability of a solar PV system. Various ML techniques have been used to predict the PR of solar power plants to improve the energy reliability [49]. Likewise, performance evaluation of several deep learning techniques including LSTM, ANN, and RNN has been assessed for carrying out the prognosis of solar power projects. The results indicated that LSTM outperformed the other algorithms in terms of accuracy especially while predicting temperature sequences [50]. The research pertinent to

CBM and fault prognostics in solar power projects is still at an inchoate stage and requires further studies to be conducted.

4 Resources (ML Algorithms and Datasets)

4.1 AI/ML Algorithms

In this section, we provide an overview of some of the most commonly used AI/ML algorithms for different applications in renewable energy. For better arrangement, the algorithms are categorized into four categories, namely fuzzy logic, hidden Markov models (HMMs), classical ML algorithms, and neural networks (NNs). In the following subsections, we provide a detailed overview of each of the categories. Moreover, a summary of some of the recent methods from each category is provided in Table 1.

Table 1 Sample works based on each type of ML algorithm discussed in this section

Ref.	ML Model	Application	Description of the method
[54]	FL & NNs	Solar forecasting	It is a hybrid solution combining FL and NNs for solar forecasting. FL is mainly used for pre-processing to correlate key features including cloud cover, wind speed, and temperature
[55]	FL	Fault detection	Relies on FL for comparing electrical parameters against the theoretical parameters to identify faulty PV components
[58]	HMMs	Fault detection	It is a two-step solution where initially PCA is used to extract and select relevant features. An HMM is then trained on the extracted features for the detection and classification of faults
[57]	HMMs	Energy consumption forecasting	Relies on HMMs to deal with the heterogeneous data collected from different sensors for forecasting a day-ahead load
[46]	SVMs	Fault detection	An SVMs classifier, under three different experimental setups, is trained on multi-modal features obtained through different sensors for fault detection in wind turbines
[60]	RF	Energy consumption	Relies on an ensemble of RF classifiers that are trained on features extracted through fast Fourier transform
[66]	CNN & LSTM	Energy state prediction	Relies on a hybrid CNN-LSTM-based framework for energy state prediction from sequences of battery's state of energy and other observable parameters of the mobile edge computing systems
[67]	Power forecasting	CNN & LSTM	Relies on two different hybrid models including a CNN-LSTM and a ConvLSTM trained on uni-variate and multivariate datasets for forecasting power production of a self-consumption PV plant

4.1.1 Fuzzy Logic

Fuzzy logic (FL) represents a subset of AI algorithms that are inspired by the reasoning capabilities of a human. Similar to humans, FL techniques take into account various intermediate possibilities (i.e., degrees of truth) between 0 and 1 [51]. An FL architecture is mainly composed of four components: namely: (i) rules, (ii) fuzzification, (iii) inference engine, and (iv) defuzzification. The first component (i.e., rules) contains a list of rules and conditions (if-then) provided by domain experts. The second component converts inputs (sensor data) into fuzzy sets. The inference engine then determines/decides rules and actions to be performed based on the degree of match between fuzzy input and the rules. Finally, fuzzy sets are converted back into crisp values in the defuzzification process.

FL techniques have been adopted in several types of AI systems in different application domains, such as medicine, autonomous cars/vehicle intelligence, bio-informatics, consumer electronics, and aerospace [52]. FL techniques have also been widely exploited for different applications of AI for renewable energy [2, 53]. Some key applications of FL in the renewable energy sector include prognostics maintenance, site selection for solar power, solar forecasting, and forecasting energy consumption. For instance, Sivaneasan et al. [54] proposed an NNs and FL-based framework for solar forecasting. The FL-based techniques are mainly used to find a correlation of key features, such as cloud cover, temperature, wind speed, and wind direction, with irradiance value. Similarly, Zaki et al. [55] proposed a fault detection framework for solar power systems relying on FL to detect and differentiate eight different types of faults in solar systems. Lau et al. [56], on the other hand, utilize FL for forecasting energy consumption in a manufacturing system. The framework mainly monitors and analyzes the consumption of energy by the manufacturing plant when the functionality/operations of certain production units vary.

4.1.2 Hidden Markov Models (HMMs)

HMMs are state-space models that model the evolution of observable events depending on some non-observable internal factors (hidden states). The observed event is known as a "symbol," while the non-observable factors are called "states." We note that HMMs could be used in applications with an observable event "Y" and the non-observable factor/event "X" where the outcome of "Y" is influenced by the outcome of "X" in a known way. In such situations, the goal is to explore the outcome of "X" by observing "Y." Moreover, the outcome of "Y" at $t = t_0$ must only depend on the outcome/value of "X" at time $t = t_0$, and the outcome of both "Y" and "X" at time $t < t_i$ should not have any impact on the outcome of "Y" at $t = t_0$. This implies that the value of "Y" should not depend on the historical values of "X" at any stage.

The literature reports several variations of HMMs, such as profile-HMMs, maximum entropy Markov models (MEMM), pair-HMMs, and context-sensitive HMMs. HMMs and their variations have been proved very effective in different

application domains, such as speech analysis, text recognition, machine translation, and activity recognition. These types of AI algorithms are more effective in applications with sequential and time-series data.

There are several applications of AI in renewable energy that involve analysis of sequential and time-series data, such as predictive maintenance (predicting the remaining useful life of machines), forecasting energy consumption, and load monitoring. The literature already reports several interesting works in this direction. For instance, Bajracharya et al. [57] proposed a HMMs-based energy forecasting framework for predicting a day-ahead load of a data center. The basic motivation behind the proposed solution is to take advantage of HMMs' capabilities of dealing with heterogeneous data in a better way. Kouadri et al. [58], on the other hand, employ HMMs for fault detection in wind energy converter systems. As a first step, the authors use principal component analysis (PCA) to extract and select relevant features. Subsequently, an HMM is trained on the extracted features for the detection and classification of faults.

4.1.3 Conventional ML Algorithms

Conventional ML algorithms, which are also called traditional ML algorithms, represent a subset of ML algorithms that work on features generally extracted by human experts of a domain. These algorithms can be used for several tasks including classification, regression, clustering, and dimensionality reduction. The literature reports a diversified set of traditional ML algorithms, such as support vector machines (SVMs), decision trees, random forest (RF), nearest neighbors, K-means, and Bayes algorithms. Traditional ML algorithms possess several key characteristics that make them a preferable choice for different applications. These characteristics include simplicity in terms of concepts/understanding and implementation. More importantly, these algorithms are interpretable/explainable that bring several advantages to critical and human-centric applications [7]. For instance, interpretable ML models not only result in better failure analysis but also allow an opportunity to further improve the models' performance by tuning them [59].

Most of the initial efforts on intelligent analysis via AI/ML in the energy sector are based on classical ML algorithms [2]. In this regard, the traditional classification algorithms, such as SVMs, RF, and Bayes classifiers, and clustering techniques, such as K-means, self-organizing map (SOM), and Gaussian mixture model (GMM) clustering algorithms, are widely exploited for different tasks in the domain. The key applications of renewable energy where traditional ML algorithms have been shown very effective include prognostic maintenance, energy consumption forecasting, weather forecasting, and other smart grid applications. For instance, Santos et al. [46] employed an SVMs classifier under three different experimental setups for fault detection in wind turbines. The classifier is trained on multi-model features including data from different types of sensors. Similarly, Li et al. [60] rely on RF for forecasting energy consumption.

4.1.4   Artificial Neural Networks (ANNs)

Artificial neural networks (ANNs), which are also called neural networks, represent one of the most commonly used families of AI/ML algorithms. ANNs are mainly inspired by the biological neural system where different algorithms are used to identify hidden patterns in data. Similar to a human brain, ANNs are composed of connected units namely "neurons," which are also known as "nodes" and are based on a mathematical function (i.e., activation function) that collects input data, performs mathematical operations, and produces output according to specific criteria. These neurons are arranged in layers. A typical ANN (i.e., feed-forward NN) generally consists of three types of layers, namely: (i) input, (ii) hidden, and (iii) output layers. ANNs with a single hidden layer are called single-layer perceptrons, while the ANNs with multiple hidden layers are called multi-layer perceptrons.

There are different types of NNs, such as convolutional neural networks (CNNs), recurrent neural networks (RNNs), and feed-forward NNs, each with a specific set of characteristics. For instance, CNNs are more useful for image analysis. Similarly, RNNs have been proved more effective for sequential and time-series data [4].

In the renewable energy sector, due to the nature of the data, RNNs are most commonly used for different tasks. Among RNNs, long short-term memory (LSTM) and bidirectional LSTM (bi-LSTM) are widely exploited for different tasks in AI applications for renewable energy. Some key applications where LSTM and bi-LSTM have been very effective include prognostic maintenance [2], forecasting energy consumption [61], the impact of climate change on renewable energy resources, risks assessment of renewable resources [62], and forecasting solar power [63]. CNNs are also widely utilized for different applications in the renewable energy sector. CNNs are most used for image-based solutions in the domain. Some key applications of AI for renewable energy where CNNs could be useful include image-based prognostic maintenance of renewable energy systems [2] and power load forecasting [64]. The literature also reports several hybrid solutions combining CNNs and RNNs (LSTM) for different tasks in the domain. These hybrid solutions allow to extract spatio-temporal features that result in better classification performances [65]. For instance, Ku et al. [66] proposed a CNN-LSTM-based solution for predicting the state of energy to avoid battery overcharging and discharging. Similarly, a CNN-LSTM model is proposed by Agga et al. [67] for the prediction of power production of a self-consumption PV plant.

4.2   Datasets

The applicability of ML algorithms in a domain largely depends on the availability of quality data. It is therefore important to provide the readers with a list of publicly available datasets for each application of ML in the renewable energy sector. The

literature reports several datasets; however, most of them are not publicly available. Thus, in this section, only publicly available datasets are covered.

4.2.1   Forecasting Energy Supply, Demand, and Weather

Forecasting energy supply and demand is one of the key applications of renewable energy that benefited from ML algorithms. It generally involves processing a huge amount of weather data for meaningful insights, such as weather forecasting, mainly due to the dependency of renewable energy sources on climate changes [68]. Due to this connection, weather data are considered along with other factors for forecasting energy supply and demand. In this section, we discuss some of the publicly available datasets containing energy consumption and weather data for forecasting energy demand and supply via ML algorithms:

- **ENTSOE Dataset [69]**: The dataset provides statistics on electrical consumption, generation, pricing, and weather data for Spain collected from different sources for 4 years. The consumption and energy generation data are obtained from ENTSOE, which is a public portal for transmission service operator (TSO) data. The pricing and weather data, on the other hand, are obtained from the Spanish TSO Red Electric Espana and an open weather API, respectively. One of the key characteristics of the dataset is the hourly consumption data and the corresponding forecasts by the TSO for consumption and pricing, which can be used as a baseline for the underlying ML solutions. Moreover, the objectives of the dataset are multi-fold. For instance, it could be used for: (i) visualization of load and supply data, (ii) analyzing the impact of weather and major cities on the energy supply, demand, and price, and (iii) forecasting hourly and daily energy supply, demand, and price, etc. The dataset is provided in two separate files namely the energy dataset and weather features.
- **Daily Electricity Price and Demand Dataset [70]**: The dataset provides statistics on the daily electricity price and demand in Victoria, Australia. The dataset provides prices and demands for a total of 2016 days from January 1, 2015 to October 6, 2020. The feature set is composed of 14 different features including date/day entries, price, demand, temperature, solar exposure, and rainfall information. For price and demand, it provides values of daily, negative, and positive recommended retail price (RRP). For temperature, both max and min values are provided.
- **Half-hourly Electricity Demand Dataset [71]**: This dataset is also based on the data collected in Victoria, Australia; however, it aims at operational demands. The operational demand represents the demand for energy met by local and semi-scheduled generating units having an aggregated energy higher than 30 MW as well as by energy sources/energy imported to the region. The dataset provides a total of 52,608 data samples/records each containing five different fields of information (i.e., features). These fields include the date, time, electricity

demand in megawatts, temperature, and a binary field indicating public holidays and working days.

- **Building Data Genome 2 (BDG2) Dataset** [72]: It is an open dataset containing data samples (readings) from 3053 different energy meters installed in 1636 different buildings. The data are collected over two years by measuring meter readings on an hourly basis. The dataset provides measurements of electricity consumption, heating, and cooling water, steam, and irrigation meters. The dataset is also used for great energy predictor III (GEPIII) organized by ASHRAE (American Society of Heating and Air-Conditioning Engineers). The dataset also provides weather and other additional information in the form of meta-data. The meta-data file is comprised of 30 different features including key information, such as building ID, site ID, timezone, latitude, longitude, and the number of floors and occupants in the buildings.

- **ISHRAE Weather Dataset** [73]: The dataset covers weather data from 62 different locations in India. The dataset is developed by White Box Technologies by collecting weather data from multiple sources, including the Indian Bureau of Meteorology (IBM), the US National Center for Environmental Data (NCEI), and satellite-derived solar radiation data.

- **Hourly Energy Demand Generation and Weather** [74]: The dataset provides electrical consumption, generation, pricing, and weather data for Spain recorded for 4 years. The data are collected from different sources including ENTSOE (a public portal for Transmission Service Operator (TSO)) and Spanish TSO Red Electric España. The former provides consumption and generation data, while the latter is the source of settlement prices. The weather data, on the other hand, are obtained from the Open Weather API for the 5 largest cities in Spain.

- **Household Electric Power Consumption** [75]: The dataset provides readings of electric power consumption in one household for 4 years. The readings are collected at a sample rate of a one-per minute. It includes readings of different electrical quantities as well as sub-metering values. The feature set includes date, time, global active power, global reactive power, voltage, global intensity, sub-metering (includes readings of kitchen containing a dishwasher, an oven, and a microwave), sub-metering 2 (includes laundry room containing a washing machine, a tumble drier, a refrigerator, and a light), and sub-metering 3 (includes an electric water heater and an air conditioner).

4.2.2 Smart Grids

The literature also provides several datasets to train and evaluate ML algorithms for a diversified set of operations in smart grids. Some of the publicly available datasets in the domain include:

- **Electrical Grid Stability Simulated Dataset** [76, 77]: This is a simulated dataset for local stability analysis of the 4-node star system. The system represents a decentralized smart grid control unit implementing demand response without significant changes to the infrastructure. The dataset provides a total of

10,000 data instances each covering 14 attributes including 11 predictive, 1 non-predictive, and a couple of goal attributes. These attributes include reaction time of energy producers and consumers, power balance (producers and consumers), and price elasticity coefficient (gamma) of energy producers and consumers.

- **SustDataED2 Dataset [78]**: The dataset provides smart meter data, which could be useful to train and evaluate ML algorithms for several applications in smart grids. The dataset provides energy consumption data of individual appliances as well as aggregated consumption of one household in Portugal for 96 days. The data are collected through plug-wise sensors installed at 18 different appliances at 0.5 Hz. Moreover, the data are annotated in a semi-automatic way where first event detection algorithms are used to identify each appliance's events. The events are then manually inspected to verify the labels. The ground truths are provided for both individual appliance consumption and aggregated energy consumption for the house in separate CSV files.

4.2.3 Condition Monitoring and Prognostics Maintenance

Predictive maintenance is one of the key applications of ML for renewable energy systems. In this application, both accelerometer data and endoscopic images can be used. Some publicly available datasets for the application are:

- **Vibration Signal Dataset [79]**: The dataset provides a large collection of data samples (approximately 16,384 instances), generated at a sample rate of 12.8 K samples per second, from six different wind turbines. Although all the samples are generated with the same specification of the wind turbines, the data are organized into six different files each containing data samples generated by a separate turbine. Moreover, the signals are segmented to obtain uniform segments each 1.28 s long. The dataset also provides additional information along with the signal segments. This includes key features, such as the duration for which the data are recorded and the turbine's speed.
- **Wind Generator Dataset [80]**: The dataset is used for the predictive maintenance of wind turbine generators. The dataset provides a diversified set of features covering different aspects of wind turbine generators. In total, each data sample is composed of 101 different features and a single label field with two possible values representing the status of the component either *faulty* or *normal* [80]. The feature set can be roughly divided into environmental conditions (e.g., operational time and wind speed), measurements for wind turbine components (e.g., average rotations per minute), and electrical variables (e.g., voltage, current, and frequency).
- **Gearbox Raw and Elaborated Data [81]:** The dataset is provided in two different forms including a collection of raw gearbox signals and a set of computed features, which is also called elaborated data. Both types of data could be used for predictive maintenance depending on the nature of ML algorithms. The elaborated dataset contains statistical features, such as the standard deviation of accelerations computed at different intervals/frequencies. In the current form,

the elaborated dataset provides data samples at the frequencies of 10, 100, and 1000 consecutive data points. Each data sample is annotated as either a healthy or broken component. We note that the data are generated in a simulated environment through a simulator, namely SpectraQuest by placing four sensors placed at different points. Moreover, the dataset also provides data with different loads ranging from 0 to 90%.

- **Wind Turbine Failure Detection [82]:** The dataset is meant for early-stage failure detection in wind turbines. The dataset provides data on five different components of wind turbines including gearbox, generator, generator bearing, transformer, and hydraulic group. The data are collected through different sensors placed at five different wind turbines for two years at a time interval of 10 min. The resultant dataset is composed of 81 different features including different environmental factors. Moreover, the data are provided in separate training and test set.
- **Grid-connected PV System Faults (GPVS-Faults) Dataset [83]:** This data is also generated in a simulated environment under sixteen different simulation/experimental settings. The data samples generated in each experimental setup are provided in a separate file. Moreover, the dataset provides a deeper annotation hierarchy including: (i) faulty and non-faulty classes (i.e., containing fault-free samples), (ii) types of faults (a total of seven types are covered), and (ii) operational modes, namely limited and maximum power modes. Moreover, the feature set is composed of eleven features including time and various types of current and voltage measurements.

5   Challenges and Open Research Issues

In this section, some of the key open research issues and challenges associated with the successful deployment of ML algorithms for renewable energy applications have been discussed.

- **Availability of Data for Training and Evaluation**: The energy sector is one of the application domains that lack quality annotated data for the training and evaluation of ML algorithms for different tasks. To overcome this issue, the literature reports some efforts for synthesized datasets where data samples are generated in a simulated environment. Though these datasets have been proved effective in training ML models for different tasks, it is very hard to replicate real-life scenarios in a simulated dataset that may affect the performances of the models in real-life applications. Moreover, the generation of these datasets in a simulated environment is also very expensive and requires a lot of effort.
- **Feature Engineering**: In the energy sector, multi-modal data are usually collected through different types of sensors. The selection of the most appropriate and informative features from the heterogeneous data is a challenging and time-consuming job. Moreover, it requires deep knowledge of the domain and a

complete understanding of the data collection process and environmental factors. Though deep-learning-based solutions generally do not involve a feature selection process, it is a critical process for classical ML algorithms. Moreover, the recent shift toward explainable AI solutions has further increased the importance of the feature engineering/selection process [2].

- **Adversarial Attacks**: In the modern world, adversarial attacks, which involve crafting a receivable input sample to misguide or disturb the predictive capabilities of an ML model, are one of the biggest threats to ML-based solutions in critical applications [7, 84]. Renewable energy is one of the critical applications of ML where risks associated with a wrong prediction of an ML model are generally very high. Since most ML models including classical and deep learning models are prone to adversarial attacks, the development of robust ML models for renewable energy applications is the way forward.

- **Integration of Traditional Power Systems in Smart Grids**: The fast-paced development of distributed renewable generation sources and microgrids has resulted in the increased development of smart grids, whereas the traditional power systems still use the old infrastructure for energy distribution. Integration of these traditional power systems in the smart grids has given rise to more uncertainties and complexities for the modern smart grids. This means that smart grids now have to handle an even larger quantity of data, which is still a challenge for them [85]. More research needs to be done to increase the adaptiveness, robustness, and online processing capabilities of the AI algorithms to effectively handle such a large volume of diversified data.

- **Cyberattacks**: As compared to the traditional grids, smart grids opt a two-way communication with multiple integrated devices, which is a lucrative target for cyber attackers. Significant research has been done to develop AI models that can effectively identify the cyber risks; however, smart grids are still prone to a wide variety of attacks [86]. A trade-off is therefore to be made between the performance of AI algorithms and the security of the smart grids.

- **Power Curtailment**: As compared to other sources of energy, VRE such as solar and wind power projects has got relatively low-capacity factor. To meet the demand during peak hours, these projects are over-built in terms of capacity. At times usage or storage of the excess energy is not possible. Therefore, access to energy is being reduced or curtailed. This is not only a monetary wastage but also a wastage of energy. Effective utilization of curtailed energy is still a big challenge for the VRE systems.

- **Load Control**: Currently, the power system operates in a fashion where the load is being adjusted according to the demand of the energy. This limits the dependence on VRE because it is a variable generation. Therefore, the need for curtailment and reduced generation is also there. This challenge can be addressed if the power systems are designed in a way that instead of matching the load, energy shall be utilized only when there is a VRE generation in the grid. A paradigm shift from load control to demand control is therefore needed. Hence, controllable and responsive loads being one of the most underutilized reliability resources can balance the demand and supply over all time frames ranging from seconds to seasons.

6 Conclusions

This chapter discusses the key applications of ML and AI for renewable energy by providing a detailed overview of challenges, available resources in the form of datasets and ML algorithms, and potential future research directions. The chapter discusses how AI and ML algorithms can help in forecasting future events, states, and processes associated with renewable energy. Moreover, an overview of some of the key applications of AI and ML in smart grids and prognostic maintenance is also provided. The literature shows that AI and ML can play a vital role in further enhancing the productivity and management of renewable energy resources. Despite being widely explored over the last few years, several aspects need to be considered to fully explore the potential of AI and ML in the renewable energy sector.

References

1. Lloyd, P. J. (2017). The role of energy in development. *Journal of Energy in Southern Africa, 28*(1), 54–62.
2. Afridi, Y. S., Ahmad, K., & Hassan, L. (2021). Artificial intelligence based prognostic maintenance of renewable energy systems: A review of techniques, challenges, and future research directions. *International Journal of Energy Research*.
3. Global artificial intelligence (AI) in energy market. https://bisresearch.com/industry-report/artificial-intelligence-energy-market.html
4. Ahmad, K., & Conci, N. (2019). How deep features have improved event recognition in multimedia: A survey. *ACM Transactions on Multimedia Computing, Communications, and Applications (TOMM), 15*(2), 1–27.
5. Bianco, M. J., Gerstoft, P., Traer, J., Ozanich, E., Roch, M. A., Gannot, S., & Deledalle, C.-A. (2019). Machine learning in acoustics: Theory and applications. *The Journal of the Acoustical Society of America, 146*(5), 3590–3628.
6. Kadhim, A. I. (2019). Survey on supervised machine learning techniques for automatic text classification. *Artificial Intelligence Review, 52*(1), 273–292.
7. Ahmad, K., Maabreh, M., Ghaly, M., Khan, K., Qadir, J., & Al-Fuqaha, A. (2022). Developing future human-centered smart cities: Critical analysis of smart city security, data management, and ethical challenges. *Computer Science Review, 43*, 100452.
8. Lai, J.-P., Chang, Y.-M., Chen, C.-H., & Pai, P.-F. (2020). A survey of machine learning models in renewable energy predictions. *Applied Sciences, 10*(17), 5975.
9. Gu, G. H., Noh, J., Kim, I., & Jung, Y. (2019). Machine learning for renewable energy materials. *Journal of Materials Chemistry A, 7*(29), 17096–17117.
10. Daniel, C., Shukla, A. K., & Sharma, M. (2021). Applications of machine learning in harnessing of renewable energy. In *Advances in clean energy technologies* (pp. 177–187). Springer.
11. Salcedo-Sanz, S., Cornejo-Bueno, L., Prieto, L., Paredes, D., & Garcia-Herrera, R. (2018). Feature selection in machine learning prediction systems for renewable energy applications. *Renewable and Sustainable Energy Reviews, 90*, 728–741.
12. Perera, A., & Kamalaruban, P. (2021). Applications of reinforcement learning in energy systems. *Renewable and Sustainable Energy Reviews, 137*, 110618.
13. Meenal, R., Binu, D., Ramya, K., Michael, P. A., Vinoth Kumar, K., Rajasekaran, E., & Sangeetha, B. (2022). Weather forecasting for renewable energy system: A review. *Archives of Computational Methods in Engineering, 29*(5), 2875–2891.

14. Monteiro, C., Keko, H., Bessa, R., Miranda, V., Botterud, A., Wang, J., & Conzelmann, G. (2009). A quick guide to wind power forecasting: state-of-the-art 2009. Technical report, Argonne National Lab. (ANL), Argonne, IL (United States).

15. Katz, J. (2015). Grid integration studies: Data requirements, greening the grid. Technical report, National Renewable Energy Lab. (NREL), Golden, CO (United States).

16. Chernyakhovskiy, I., et al. (2016). Forecasting wind and solar generation: Improving system operations, greening the grid. Technical report, National Renewable Energy Lab. (NREL), Golden, CO (United States).

17. Sun, Y., Szűcs, G., & Brandt, A. R. (2018). Solar PV output prediction from video streams using convolutional neural networks. *Energy & Environmental Science, 11*(7), 1811–1818.

18. Yang, D. (2019). On post-processing day-ahead NWP forecasts using Kalman filtering. *Solar Energy, 182*, 179–181.

19. Foley, A. M., Leahy, P. G., Marvuglia, A., & McKeogh, E. J. (2012). Current methods and advances in forecasting of wind power generation. *Renewable Energy, 37*(1), 1–8.

20. Sadaei, H. J., e Silva, P. C. d. L., Guimarães, F. G., & Lee, M. H. (2019). Short-term load forecasting by using a combined method of convolutional neural networks and fuzzy time series. *Energy, 175*, 365–377.

21. Ranaweera, D., Hubele, N., & Karady, G. (1996). Fuzzy logic for short term load forecasting. *International Journal of Electrical Power & Energy Systems, 18*(4), 215–222.

22. Raza, M. Q., & Khosravi, A. (2015). A review on artificial intelligence based load demand forecasting techniques for smart grid and buildings. *Renewable and Sustainable Energy Reviews, 50*, 1352–1372.

23. Velasco, L. C. P., Villezas, C. R., Palahang, P. N. C., & Dagaang, J. A. A. (2015). Next day electric load forecasting using artificial neural networks. In *2015 International Conference on Humanoid, Nanotechnology, Information Technology, Communication and Control, Environment and Management (HNICEM)* (pp. 1–6). IEEE.

24. Hernández, L., Baladrón, C., Aguiar, J. M., Calavia, L., Carro, B., Sánchez-Esguevillas, A., Pérez, F., Fernández, Á., & Lloret, J. (2014). Artificial neural network for short-term load forecasting in distribution systems. *Energies, 7*(3), 1576–1598.

25. Buitrago, J., & Asfour, S. (2017). Short-term forecasting of electric loads using nonlinear autoregressive artificial neural networks with exogenous vector inputs. *Energies, 10*(1), 40.

26. Rafi, S. H., et al. (2020). Highly efficient short term load forecasting scheme using long short term memory network. In *2020 8th International Electrical Engineering Congress (iEECON)* (pp. 1–4). IEEE.

27. Atef, S., & Eltawil, A. B. (2020). Assessment of stacked unidirectional and bidirectional long short-term memory networks for electricity load forecasting. *Electric Power Systems Research, 187*, 106489.

28. Yang, K., & Zhao, L. (2009). Application of Mamdani fuzzy system amendment on load forecasting model. In *2009 Symposium on Photonics and Optoelectronics* (pp. 1–4). IEEE.

29. Zahid, M., Ahmed, F., Javaid, N., Abbasi, R. A., Zainab Kazmi, H. S., Javaid, A., Bilal, M., Akbar, M., & Ilahi, M. (2019). Electricity price and load forecasting using enhanced convolutional neural network and enhanced support vector regression in smart grids. *Electronics, 8*(2), 122.

30. Baliyan, A., Gaurav, K., & Mishra, S. K. (2015). A review of short term load forecasting using artificial neural network models. *Procedia Computer Science, 48*, 121–125.

31. Baltas, N. G., Mazidi, P., Ma, J., de Asis Fernandez, F., & Rodriguez, P. (2018). A comparative analysis of decision trees, support vector machines and artificial neural networks for on-line transient stability assessment. In *2018 International Conference on Smart Energy Systems and Technologies (SEST)* (pp. 1–6). IEEE.

32. You, S., Zhao, Y., Mandich, M., Cui, Y., Li, H., Xiao, H., Fabus, S., Su, Y., Liu, Y., Yuan, H., et al. (2020). A review on artificial intelligence for grid stability assessment. In *2020 IEEE International Conference on Communications, Control, and Computing Technologies for Smart Grids (SmartGridComm)* (pp. 1–6). IEEE.

33. Fazai, R., Abodayeh, K., Mansouri, M., Trabelsi, M., Nounou, H., Nounou, M., & Georghiou, G. E. (2019). Machine learning-based statistical testing hypothesis for fault detection in photovoltaic systems. *Solar Energy, 190,* 405–413.

34. Niu, H., Omitaomu, O. A., & Cao, Q. C. (2020). Machine committee framework for power grid disturbances analysis using synchrophasors data. *Smart Cities, 4*(1), 1–16.

35. Abdelgayed, T. S., Morsi, W. G., & Sidhu, T. S. (2017). Fault detection and classification based on co-training of semisupervised machine learning. *IEEE Transactions on Industrial Electronics, 65*(2), 1595–1605.

36. Tufail, S., Parvez, I., Batool, S., & Sarwat, A. (2021). A survey on cybersecurity challenges, detection, and mitigation techniques for the smart grid. *Energies, 14*(18), 5894.

37. Zhou, L., Ouyang, X., Ying, H., Han, L., Cheng, Y., & Zhang, T. (2018). Cyber-attack classification in smart grid via deep neural network. In *Proceedings of the 2nd International Conference on Computer Science and Application Engineering* (pp. 1–5).

38. Kosek, A. M. (2016). Contextual anomaly detection for cyber-physical security in smart grids based on an artificial neural network model. In *2016 Joint Workshop on Cyber-Physical Security and Resilience in Smart Grids (CPSR-SG)* (pp. 1–6). IEEE.

39. Zhang, Y., & Yan, J. (2020). Semi-supervised domain-adversarial training for intrusion detection against false data injection in the smart grid. In *2020 International Joint Conference on Neural Networks (IJCNN)* (pp. 1–7). IEEE.

40. Liu, Z., Zou, S., & Zhou, L. (2012). Condition monitoring system for hydro turbines based on LabVIEW. In *2012 Asia-Pacific Power and Energy Engineering Conference* (pp. 1–4). IEEE.

41. Wang, S., Wang, K., & Li, Z. (2016). A review on data-driven predictive maintenance approach for hydro turbines/generators. In *6th International Workshop of Advanced Manufacturing and Automation* (pp. 30–35). Atlantis Press.

42. Selak, L., Butala, P., & Sluga, A. (2014). Condition monitoring and fault diagnostics for hydropower plants. *Computers in Industry, 65*(6), 924–936.

43. Zhang, C., Song, D., Chen, Y., Feng, X., Lumezanu, C., Cheng, W., Ni, J., Zong, B., Chen, H., & Chawla, N. V. (2019). A deep neural network for unsupervised anomaly detection and diagnosis in multivariate time series data. In *Proceedings of the AAAI Conference on Artificial Intelligence* (Vol. 33, pp. 1409–1416).

44. Wang, D., Tsui, K.-L., & Miao, Q. (2017). Prognostics and health management: A review of vibration based bearing and gear health indicators. *IEEE Access, 6,* 665–676.

45. Verma, A., Zappalá, D., Sheng, S., & Watson, S. J. (2022). Wind turbine gearbox fault prognosis using high-frequency SCADA data. In *Journal of Physics: Conference Series* (Vol. 2265, p. 032067). IOP Publishing.

46. Santos, P., Villa, L. F., Reñones, A., Bustillo, A., & Maudes, J. (2015). An SVM-based solution for fault detection in wind turbines. *Sensors, 15*(3), 5627–5648.

47. Herp, J., Pedersen, N. L., & Nadimi, E. S. (2019). Assessment of early stopping through statistical health prognostic models for empirical RUL estimation in wind turbine main bearing failure monitoring. *Energies, 13*(1), 83.

48. Riley, D., & Johnson, J. (2012). Photovoltaic prognostics and heath management using learning algorithms. In *2012 38th IEEE Photovoltaic Specialists Conference* (pp. 001535–001539). IEEE.

49. Bandong, S., Leksono, E., Purwarianti, A., & Joelianto, E. (2019). Performance ratio estimation and prediction of solar power plants using machine learning to improve energy reliability. In *2019 6th International Conference on Instrumentation, Control, and Automation (ICA)* (pp. 36–41). IEEE.

50. Correa-Jullian, C., Cardemil, J. M., Droguett, E. L., & Behzad, M. (2020). Assessment of deep learning techniques for prognosis of solar thermal systems. *Renewable Energy, 145,* 2178–2191.

51. Dernoncourt, F., & Sander, E. (2011). Fuzzy logic: between human reasoning and artificial intelligence. *Project Report Paris*.

52. Abduljabbar, R., Dia, H., Liyanage, S., & Bagloee, S. A. (2019). Applications of artificial intelligence in transport: An overview. *Sustainability, 11*(1), 189.

53. Suganthi, L., Iniyan, S., & Samuel, A. A. (2015). Applications of fuzzy logic in renewable energy systems—a review. *Renewable and Sustainable Energy Reviews, 48*, 585–607.
54. Sivaneasan, B., Yu, C., & Goh, K. (2017). Solar forecasting using ANN with fuzzy logic pre-processing. *Energy Procedia, 143*, 727–732.
55. Zaki, S. A., Zhu, H., & Yao, J. (2019). Fault detection and diagnosis of photovoltaic system using fuzzy logic control. In *E3S Web of Conferences* (Vol. 107, p. 02001). EDP Sciences.
56. Lau, H. C., Cheng, E., Lee, C. K., & Ho, G. T. (2008). A fuzzy logic approach to forecast energy consumption change in a manufacturing system. *Expert Systems with Applications, 34*(3), 1813–1824.
57. Bajracharya, A., Khan, M. R. A., Michael, S., & Tonkoski, R. (2018). Forecasting data center load using hidden Markov model. In *2018 North American Power Symposium (NAPS)* (pp. 1–5). IEEE.
58. Kouadri, A., Hajji, M., Harkat, M.-F., Abodayeh, K., Mansouri, M., Nounou, H., & Nounou, M. (2020). Hidden Markov model based principal component analysis for intelligent fault diagnosis of wind energy converter systems. *Renewable Energy, 150*, 598–606.
59. Khan, T., Ahmad, K., Khan, J., Khan, I., & Ahmad, N. (2022). An explainable regression framework for predicting remaining useful life of machines. arXiv preprint arXiv:2204.13574.
60. Li, C., Tao, Y., Ao, W., Yang, S., & Bai, Y. (2018). Improving forecasting accuracy of daily enterprise electricity consumption using a random forest based on ensemble empirical mode decomposition. *Energy, 165*, 1220–1227.
61. Yan, K., Li, W., Ji, Z., Qi, M., & Du, Y. (2019). A hybrid LSTM neural network for energy consumption forecasting of individual households. *IEEE Access, 7*, 157633–157642.
62. Liu, B., Chen, J., Wang, H., & Wang, Q. (2020). Renewable energy and material supply risks: A predictive analysis based on an LSTM model. *Frontiers in Energy Research, 8*, 163.
63. Gensler, A., Henze, J., Sick, B., & Raabe, N. (2016). Deep learning for solar power forecasting—an approach using autoencoder and LSTM neural networks. In *2016 IEEE International Conference on Systems, Man, and Cybernetics (SMC)* (pp. 002858–002865). IEEE.
64. Aurangzeb, K., Alhussein, M., Javaid, K., & Haider, S. I. (2021). A pyramid-CNN based deep learning model for power load forecasting of similar-profile energy customers based on clustering. *IEEE Access, 9*, 14992–15003.
65. Kumari, P., & Toshniwal, D. (2021). Long short term memory–convolutional neural network based deep hybrid approach for solar irradiance forecasting. *Applied Energy, 295*, 117061.
66. Ku, Y.-J., Sapra, S., Baidya, S., & Dey, S. (2020). State of energy prediction in renewable energy-driven mobile edge computing using CNN-LSTM networks. In *2020 IEEE Green Energy and Smart Systems Conference (IGESSC)* (pp. 1–7). IEEE.
67. Agga, A., Abbou, A., Labbadi, M., & El Houm, Y. (2021). Short-term self consumption PV plant power production forecasts based on hybrid CNN-LSTM, ConvLSTM models. *Renewable Energy, 177*, 101–112.
68. Rolnick, D., Donti, P. L., Kaack, L. H., Kochanski, K., Lacoste, A., Sankaran, K., Ross, A. S., Milojevic-Dupont, N., Jaques, N., Waldman-Brown, A., et al. (2022). Tackling climate change with machine learning. *ACM Computing Surveys (CSUR), 55*(2), 1–96.
69. Hourly energy demand generation and weather. https://www.kaggle.com/datasets/nicholasjhana/energy-consumption-generation-prices-and-weather
70. Daily electricity price and demand data. https://www.kaggle.com/datasets/aramacus/electricity-demand-in-victoria-australia
71. Half-hourly electricity demand for Victoria, Australia. https://tsibbledata.tidyverts.org/reference/vic_elec.html
72. Miller, C., Kathirgamanathan, A., Picchetti, B., Arjunan, P., Park, J. Y., Nagy, Z., Raftery, P., Hobson, B. W., Shi, Z., & Meggers, F. (2020). The Building Data Genome Project 2, energy meter data from the ASHRAE great energy predictor III competition. *Scientific Data, 7*, 368.
73. ISHAREA dataset. http://weather.whiteboxtechnologies.com/ISHRAE
74. Hourly energy demand generation and weather dataset. https://www.kaggle.com/datasets/nicholasjhana/energy-consumption-generation-prices-and-weather

75. Household electric power consumption dataset. https://www.kaggle.com/datasets/uciml/electric-power-consumption-data-set
76. Smard grid stability dataset. https://tinyurl.com/2t2ddhm8
77. Arzamasov, V., Bohm, K., & Jochem, P. (2018). Towards concise models of grid stability. In *2018 IEEE International Conference on Communications, Control, and Computing Technologies for Smart Grids (SmartGridComm)* (pp. 1–6). IEEE.
78. Pereira, L., Costa, D., & Ribeiro, M. (2022). A residential labeled dataset for smart meter data analytics. *Scientific Data, 9*(1), 1–11.
79. Martin del Campo Barraza, S., Sandin, F., & Strömbergsson, D. (2018). Dataset concerning the vibration signals from wind turbines in northern Sweden.
80. Mammadov, E. E. O. (2019). Predictive maintenance of wind generators based on AI techniques. Master's thesis, University of Waterloo.
81. Gearbox fault diagnosis: elaborated datasets. https://tinyurl.com/mbu5cv8w
82. The EDP dataset. https://tinyurl.com/2nva3ta5
83. GPVS-faults: Experimental data for fault scenarios in grid-connected PV systems under MPPT and IPPT modes. https://tinyurl.com/nw2aha8
84. Al-Maliki, S., El Bouanani, F., Ahmad, K., Abdallah, M., Hoang, D., Niyato, D., & Al-Fuqaha, A. (2021). Opportunistic use of crowdsourced workers for online relabeling of potential adversarial examples.
85. Kazmi, S. A. A., Hasan, S. F., & Shin, D.-R. (2015). Analyzing the integration of distributed generation into smart grids. In *2015 IEEE 10th Conference on Industrial Electronics and Applications (ICIEA)* (pp. 762–766). IEEE.
86. Gunduz, M. Z., & Das, R. (2018). Analysis of cyber-attacks on smart grid applications. In *2018 International Conference on Artificial Intelligence and Data Processing (IDAP)* (pp. 1–5). IEEE.

New Technologies and Equipment for Smelting Technical Silicon

Mirtemir Kurbanov (iD), **B. M. Abdurakhmanov** (iD), **Mukhsindjan Ashurov** (iD), and **Valeriy Kharchenko** (iD)

1 Introduction

The classical method of obtaining technical silicon (TSi) [1, 2] includes operations for preparing the charge, that is, grinding a silicon-containing component (SCC), for example, silica (SiO_2) in the form of vein quartz and carbonaceous reducing agent (CRA), which uses charcoal, coke, and petroleum coke, to a given size, their mixing in a given stoichiometric ratio, feeding the resulting charge into an electric arc furnace (EAF) and smelting the TSi by its carbothermic reduction from SCC in one way or another. According to [1–3], the technological process is carried out in EAF, the device of which is also described in detail in the same place.

Both the main and secondary operations of the technology and, respectively, the equipment for smelting TSi have been modernized repeatedly and various useful improvements described in [1–11]. For example, a graphite electrode was made with a central hole for the passage of an inert gas as a carrier gas for part or all of the SCC in a fine fraction. The main purpose of the improvements were attempts to changes in the method of supplying the charge or its individual components into the EAF [12, 13], since with the classical portion loading of furnace charge to the electrodes, the smelting of TSi proceeds in an intermittent mode and under suboptimal conditions, since different areas of the furnace charge are at different temperatures and where it is less, SiO_2 is restored up to SiO, which is carried away from the EAF with waste gases.

M. Kurbanov (✉) · B. M. Abdurakhmanov · M. Ashurov (✉)
Institute of Ion-Plasma and Laser Technologies of the Academy of Sciences of the Republic of Uzbekistan, Tashkent, Uzbekistan

V. Kharchenko
Federal Scientific Agroengineering Center VIM, Moscow, Russia

In [13], the CRA was crushed to a size of 0÷1 mm, which is comparable to the size of quartz sand particles (QS), and then CRA was divided into two parts; one part of the CRA was mixed with SiO2 in a powdered state, and the resulting furnace charge was supplied into the arc combustion zone through a hollow graphite electrode using a carrier inert gas with simultaneous running, taking into account a given stoichiometric ratio between SiO_2 and CRA, of another CRA part the into the furnace by a portion loading to the electrodes.

This technology is one of the first, albeit partial, but successful attempts to solve the long overdue need in practice to modernize the carbothermic process, aimed at improving its environmental and economic indicators. The disadvantage of the described technology is that it is focused on a two-stage process; at the first stage of which, SiC is obtained by low-temperature carbonization of silica, and only at the second stage, TSi is smelted, during which SiC extracted from the EAF and ground to a particle size of 0÷1 mm is used as one of the CRA parts.

Despite numerous studies, the technology of silicon smelting has not yet been perfected, and currently a number of challenges remain unresolved. The main of them are:

 (i) Silicon production is an energy-intensive process that consumes 11–17 MW per 1 ton of product. In the structure of the cost of technical silicon, the cost of electricity is 30–35% of the total production costs.
 (ii) The silica-containing raw materials used for the standard silicon production technology – high-quality quartzite, vein quartz, and CRA – charcoal, petroleum coke, and coal coke are scarce and expensive materials.
(iii) Fine-grained and fine-dispersed silicon production waste, the volume of which exceeds the volume of the target product itself, is not used in charge preparation.
(iv) The process of silicon smelting is not perfect, requiring improvement of technological operations (charge loading mode, smelting, etc.).

The present study is devoted to finding solutions to the abovementioned problems obstructing the efficiency of TSi production by modernizing the process of TSi smelting and increasing its controllability. Such an integrated approach to solving the problem of silicon smelting technology, unlike other studies in this direction, contributes to increasing the profitability of silicon smelting as a whole, because existing problems and their solutions are closely related to each other.

2 Materials, Equipment, and Methods

2.1 Materials

The silica-containing raw materials (quartz, quartzite, and quartz sands), carbonaceous reducing agents (wood and coal, petroleum coke), and production waste,

which is a fine-dispersed screening of small quartzite and carbonaceous reducing agent formed during the preparation of raw materials for smelting, as well as technogenic dust waste from the production of silicon and ferrosilicon – microsilica (MS) – were used as initial the materials. The MS contained up to ~95 mass. % SiO_2, with the sizes of amorphous globule particles from ~10–20 nm to 250 nm. One of the solid types of CRA was petroleum coke with a solid carbon content of more than 90.0%; ash, no more than 0.7%; and moisture, 1.5–2.0%. When briquetting fine solid waste of silicon production, technical carbon (soot) of the K-354 brand with particle sizes of 10–200 microns and carbon content of 95.0%, which is a product of natural gas combustion at thermal power plants, was also used as a hydrocarbon.

As an alternative CRA, we proposed using a relatively cheap natural gas compared to charcoal, consisting of 94% methane (CH_4) [14–17, 37]. The method of methane supplying to the EAF will be described below.

2.2 Methods

The analysis of the chemical composition of the SCC, CRA, MS, TSi, and other materials was carried out using the ICP mass spectrometer MS 7700 (Agilent Technologies International Japan, Ltd., Japan). To study the morphology and particle sizes, a transmission electron microscope (TEM, LEO–912 AB Zeiss Germany) was used. The phase composition of the materials was determined using an automated XRD-6100 X-ray diffractometer (Shimadzu, Japan).

2.3 Experimental Equipment

It is known that DC arc furnaces are used for the smelting of TSi in recent years instead of AC arc furnaces, having a number of advantages and allowing to reduce (i) the consumption of graphite electrodes up to 2 kg per 1 ton of liquid metal; (ii) electricity consumption up to 20%; metal-carbon monoxide by 2–4%; and the amount of dust emissions by 6–7 ounce. The DC arc is highly stable, but at the same time, DC furnaces are more expensive than AC furnaces by 10–25% due to the cost of a DC power source.

For the synthesis of silicon carbide, a resistance furnace of the GAN-150 × 130 brand was used/1500/2500-S (Linn High Therm, Germany).

For experiments on the use of gaseous CRA, we made a choice in favor of a direct current (DC) EAF. The device was designed in the form of a DC furnace with a conductive base and a closed cooled vault. The circuit diagram of the device is shown in Fig. 1. It consists of an EAF, a transformer, and a DC rectifier unit, water cooling systems, ventilation, and a gas distribution unit for natural gas supply.

The proposed technology provides for the supply of methane not just together with the charge, as a gas atmosphere, but directly into the furnace to the combustion
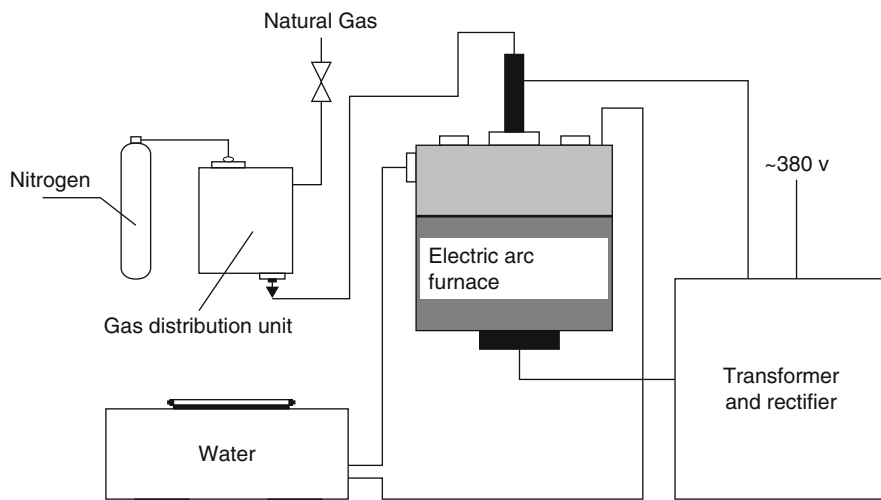
Fig. 1 Circuit diagram of the technological section devices [17]

zone of the electric arc. At the same time, it was necessary to solve a number of fundamentally new technological and engineering tasks. Among the latter is the methane supply system. In order to ensure the reaction of silica and methane in the furnace, it is necessary to ensure that the latter enters the zone with the highest temperature in the furnace. Based on this, the supplying through the upper hollow graphite electrode was chosen. However, there are a number of obstacles. Thus, at the initial stage of charge melting, the hole in the electrode is sealed and clogged with fine charge particles, as well as a result of the reaction between methane and these particles in the electrode cavity itself. Therefore, at this stage of smelting, before the furnace charge is heated and methane is supplied into the furnace, nitrogen gas is supplied through the central hole in the electrode, which, being chemically inert relative to silicon and other components of the furnace charge, prevents the hole from slagging before the start of the main operation.

An important innovation targeted at increasing the efficiency of the interaction of methane with silica is the provision of dissociation and partial ionization of the atoms of the substances that make up methane on the path of its supply to the furnace [14, 18]. This technique was based on the physical effect of the methane molecule decomposition into active carbon and atomic hydrogen upon contact of this gas with the heated surface of the catalyst, which was used as a metallic nickel. The catalyst housing 6 was made of nickel (see Fig. 2), which is a hollow cylinder with a massive blind bottom and many small holes with a diameter of ~0.1 mm on the side surface. The cylinder was suspended on a wire rope 7 with the possibility of vertical movement in the cavity of the central longitudinal hole in the graphite electrode 3. By approaching or distancing the nickel cylinder from the arc burning zones, its surface temperature can be adjusted and maintained in the optimal range

Fig. 2 The EAF scheme demonstrating the method of supplying natural gas to the combustion zone of the furnace arc according to the patent of the Uzbekistan Republic №: 05440 [14]: (1) furnace body; (2) furnace lid; (3) hollow graphite electrode with a diameter of 76 mm; (4) charge (briquettes); (5) combustion zone of electric arc; (6) nickel ionizer in the form of a hollow cylinder; (7) wire rope
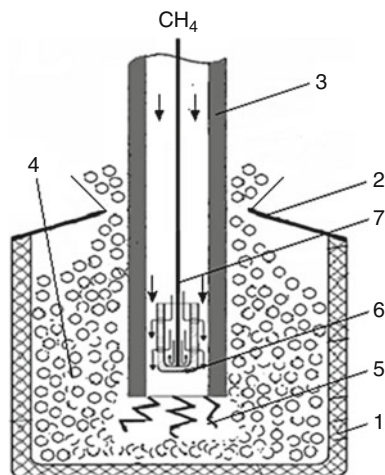
for nickel catalytic properties, lying between 400 and 600 °C. The physical effect of the methane decomposition on the catalyst makes it possible to increase the reactivity of the methane components, hydrogen, and carbon. Carbon and hydrogen, supplying into the furnace directly, interact actively with the main components of the furnace charge (SiO_2, SiO, SiC), which is accompanied by the effective release of elemental silicon. Note that carbon and hydrogen also interact with any oxygen-containing complexes that are formed during the electric arc process. In comparison with known technical solutions related to the use of gaseous reducing agents in silicon smelting, one of which is CO, used in the process of plasma TSi production [19], it follows that with the same mass supply of CO and CH_4 to the furnace, the technology we propose is more efficient than, for example, in [19–21], where there is a dissociation of the molecule of the used CO, and one carbon atom can enter into the reaction. Whereas in the variant we propose, four hydrogen atoms participate in the decomposition of the methane molecule in addition to the carbon atom. It is precise because of the high reactivity of dissociated and partially ionized methane components that it is possible to simplify the requirements for solid CRA and use a wider range of carbon-containing substances in the proposed technology than in classical technology, since there is insufficient reactivity of brown or hard coal, oil pitches, cokes, or their mixtures, as well as fine waste; the mentioned materials are easily compensated by the extremely high activity of the above methane components. Therefore, the suggested technology expanding the range of used hydrocarbons allows us to solve the issue of import substitution of charcoal and coke.

When assessing the reducing activity of methane, it is necessary to pay attention to its ability to ionize and dissociate. As is known, the CH_4 molecule has a tetrahedral structure, which is due to the *sp3* hybridization of the carbon atom and the tetrahedral direction of the four hybrid electron clouds of the carbon atom. Moreover, the C − H bonds in the CH molecule are the same in all directions and

are located at an angle of 109° 28′. Each of the four *sp3*-hybrid carbon atomic orbitals participates in axial (σ-) overlap with s-atomic orbitals of hydrogen or with *sp3*-atomic orbitals of another carbon atom, forming σ-bonds C–H or C–C.

The peculiar structure of the CH_4 molecule affects the interaction with electrons and leads to a wide variety of possible reactions that may take place, including the formation of different combinations of both neutral and ionized components, for example:

$$e + CH_4 \rightarrow H_3^+ + C + H + 2e \tag{1}$$

$$e + CH_4 \rightarrow H^+ + C + 3H + 2e \tag{2}$$
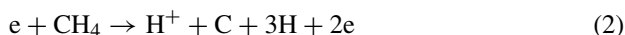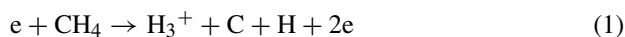
Since the H_3^+ ion is not stable and dissociates according to the scheme: $H_3^+ \rightarrow H_2^+ + H^+$, with the appearance of atomic hydrogen, this makes an additional contribution to the reduction process. It is not difficult to see that under the influence of ionization, characteristic of a burning electric arc, the formation of numerous combinations of neutral and ionized components of methane is possible, and therefore its sufficiently high activity should be expected even in the usual reduction process. In our case, already dissociated components of CH_4 enter the combustion zone of the electric arc, which in itself increases its reactivity and, moreover, facilitates their ionization. Note that the supply of dissociated CH_4 goes directly into the combustion zone of the electric arc, where the temperature obviously exceeds the temperature of formation of SiO, which is at least 1700°C.

Therefore, the process of obtaining silicon with methane using in the furnace, according to [20], can be written as the following generalized reaction:

$$SiO + CH_4 \rightarrow Si + CO + 2H_2 \tag{3}$$
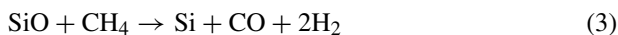
Note that at the middle levels of the furnace, where the silica gasification degree is not high, it is possible to obtain silicon by the reaction:

$$SiO_2 + CO + H_2 \rightarrow Si + CO + H_2O \tag{4}$$
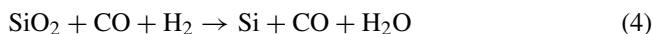
which was observed in a plasma reactor according to [20], and moreover, it was adopted as the basis for the plasma smelting of TSi developed.

In our case, in the presence of dissociated methane in the furnace and the appearance of atomic hydrogen, the role of the latter increases significantly, and, in our opinion, the reaction involving CO, molten silica, and hydrogen becomes decisive, which manifests itself in the decrease in the specific energy intensity of the EAF when methane is supplied as CRA. At the same time, the fundamental point is that we propose to partially dissociate methane molecules on the feed path to the EAF directly [14, 18].

3 Results and Discussion

Smelting into the DC furnace has shown various combinations of CH_4 with other local CRA and various local SCC showed that the methane usage of makes it possible to obtain high-quality TC grades Kr0 and Kr00, in the case of the use of vein quartz (CRA) from the Zargar (a) and Akbuyrin (b) deposits (Table 1).

Experiments have shown that it is advisable to limit the replacement of solid CRA with methane by ~80%. The optimal range of the combination of solid and gaseous CRA is set in the ratio 50/50 to 20/80, within which the minimum number of current surges and gas fistulas is noted. This technology makes it possible to ensure high quality of the target product, replace imported coke with local raw materials, and significantly reduce the specific energy intensity of the smelting of TSi up to 8% [3, 7, 22].

One of the physical reasons for this is the supply of CH_4 only after partial dissociation of methane molecules on the heated surface of the nickel catalyst. The other one is that both methane and the carbon and hydrogen atoms obtained from it are subjected to ionization in the combustion zone of the electric arc, which naturally leads to an even greater increase in the reactivity of this CRA. Another fundamental difference is the adjustment [14, 18] of the mentioned methane reactivity, which is the most important characteristic of CRA. To this end, we propose to regulate the content of H_2O vapors in methane in a controlled manner and, thereby, to change the ratio of hydrogen and oxygen atoms and ions directly in the combustion zone of the electric arc, that is, to influence the process of melting TSi by methods of physical electronics. It is known that the electric field of the EAF consists of two parallel branches. The first branch is "electrode-voltaic arc-under," and the second branch is "electrode-charge-under." Voltage ratio V (arc)/V (charge) varies according to various estimates [1, 3, 22], within very wide limits: from 15/85% to 85/15% that cannot be unambiguously explained by the difference in the equipment used in the research. Thus, experts not only do not have a common opinion about the role of these two branches of the current flow, but it is generally believed that it is possible to control the energy release and to estimate the amount of energy accurately that is released directly into the electric arc area.

Actually, in order to control the process, it is necessary to first determine the signal, by the magnitude of which it would be possible to judge the speed of the process and (or) its performance, and only then look for means of influencing this

Table 1 The chemical composition of the TSi used as the CRA is up to 80% CH_4

Si	Fe	Al	K	Ca	Na	Ti	Mg	Ni	Mn
(a) Smelting of TSi from SCC in the form of the Zargar deposit									
98.85	0.44	0.22	0.20	0.07	0.099	0.043	0.007	0.009	0.069
(b) Smelting of TSi from SCC in the form of CRA of the Akbuyrin deposit									
99.3	0.29	0.20	0.027	0.072	0.087	0.022	0.006	0.008	0.006

Fig. 3 Temperature vs resistivity of various hydrocarbons: (1) birch retort charcoal; (2) semi-coke "Baysunsky"; (3) charcoal; (4) a mixture of soot from the combustion of natural gas with quartz sand 50/50% with the addition of binder; (5) crushed vein quartz; (6–7) mixtures of soot with QS 35% and 70%
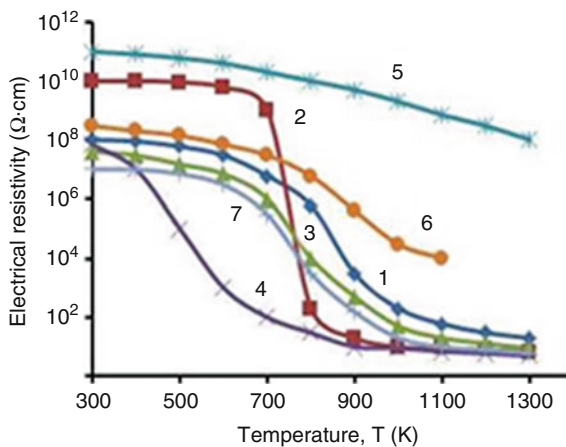
parameter. As such a signal, we propose to use the amount of current flowing in an electric arc. Therefore, the task of ensuring maximum energy release is in the arc burning area, and hence the maximum concentration of the course of reduction reactions near this area is one of the main ones. It is not difficult to notice that this is exactly our suggestion for supplying CRA in a gaseous state directly to the combustion zone of the electric arc.

Figure 3 shows the temperature change in the resistivity of various CRA (curves 1–3), soot obtained as a result of burning natural gas 4, crushed CRA 5, and mixtures of said soot with QS 6–7, in which the soot content is, respectively, 35% and 70%. It follows from the analysis of the curves (Fig. 3) that the resistivity of the furnace charge depends on the resistivity of the carbonaceous materials added to it and the ratio of the volumes of ore (SiO_2) and carbon (2C) parts. Despite the similar nature of the temperature change, the absolute values of the resistivity of the "Baysunsky" semi-coke 2 imported to the Republic Uzbekistan, charcoal 3, and birch retort coal 1 in the low temperatures (up to ~850 K) differ by almost two orders of magnitude, and only at temperatures near 1000 K, their values become comparable. Special interest causes the area of high temperatures. The resistance of all solid CRA with an increase in temperature reaches a plateau and no tends to zero. Based on these data, it can be concluded that the semi-coke made from "Baysun coal" has acceptable electrical conductivity, and if the required ash content and reactivity are provided, then this local CRA can be used in the production of ordinary TSi brands, as well as FeSi instead of imported charcoal.

The revealed fact of a strong dependence of the resistivity of the furnace charge on the CRA content in the form of fine soot is also important because it was used as the basis for additional studies, the result of which was the discovery of the "dimensional effect." Namely, a significant effect on the conductivity of the furnace charge is not only the CRA content in it but also the particle sizes of SCC and CRA brought into contact. At the same time, it is necessary to note the uniformity of this parameter for the entire array of equally prepared CRA and SCC powders. Thus,

Table 2 The electrons interaction with a methane molecule and its constituent hydrogen and carbon atoms [12]

Reaction number	Interaction reaction	
1	$e + CH_4$	$CH_4^+ + 2e$
2a		$CH_3^+ + H + 2e$
2b		$CH_3^+ + H^- + e$
3		$CH_2^+ + H_2 + 2e$
4a		$CH^+ + H + H_2 + 2e$
4b		$CH^+ + H^- + H_2 + e$
5		$C^+ + 2H_2 + 2e$
6		$H^+ + CH_3 + 2e$
7		$H_2^+ + CH_2 + 2e$
8		$H_3^+ + C + H + 2e$
8a		$H_3^+ + CH^- + e$
9a		$H + H_2 + CH + 2e$
9b		$H^+ + H + CH_2 + 2e$
9c		$H^+ + C + 3H + 2e$
10a		$H_2^+ + C + H_2 + 2e$
10b		$H_2^+ + C + 2H + 2e$

briquetting of finely dispersed smelting components is not only expedient, from the point of view of technology stability, reproducibility of the conditions of TSi smelting, and reduction of specific energy consumption, but can also be optimized, both by taking into account the particle sizes of the furnace charge and by deliberate grinding of its components to specified size. As for the electrical conductivity of the furnace charge, based on the monotonous course of curves 6 and 7 at high temperatures, its sharp increase by heating is unlikely. Therefore, in the case of supplying SCC (methane) or a charge in bulk to the electrodes and supplying most of the hydrocarbons to the burning zone of the electric arc, the process of smelting TC can be controlled only by changing the amount of methane supply and (or) adjusting its reactivity. This conclusion is based on experimental facts obtained in terms of the ionization of methane molecules by physical electronics methods [12], namely, as a result of exposure to molecular methane of an electron beam in the energy range 5–90 eV, as well as data from works [23, 24] in which the electron impact method was used for CH_4 ionization (see Table 2).

It should be noticed that in the combustion zone of an electric arc characterized by a high temperature of ~6000 K at a voltage between the graphite electrode and the EAF hearth in the range from 50 to 500 V, electrons can have energies that overlap the range specified in [12].

Then, according to [12], as a result of the action of an electron beam, due to the peculiarities of the structure of the methane molecule, it is possible to obtain a whole set of various ions (Table 2). The table shows that reaction 1 illustrates a single ionization with the formation of a molecular ion and reactions 2a, 3, 4a, 5, 6, 7, and 8 describe the processes of so-called dissociative ionization with the formation of fragmentary ions and neutrals, whereas reactions 2b, 4b, and 8a correspond to the occurrence of even ion pairs, that is, positive and negative ions, for example,

according to the reaction 4b (CH^+) and (H^-). In [12, 23], the multivariance of reactions 6 and 7 is noted, which, as can be seen from the table, can lead to the formation of various combinations of ions and neutral components, the general characteristic of which is a higher reactivity compared to that of the initial CH_4.

It is important to note that the ionized components are concentrated in the area of the electric arc combustion and their concentration affects the amount of current in the arc. That is, in addition to the main traditional method of the current regulation in the arc by moving up and down the graphite electrode, not to mention such techniques as regulating the voltage between the electrode and the hearth, which cannot be carried out in a wide range or an extremely inertial method consisting in drawing a charge to the electrodes with a large or, conversely, a lower content of CRA, we have proposed a new technique based on a controlled change in the furnace charge resistance in the arc burning area by regulating the supply of methane to this combustion zone; it is subjected to dissociation with subsequent ionization of hydrogen and carbon.

The analysis of the smelting course of TSi with methane showed a decrease in the number of current surges and their amplitudes, as well as the number of gas fistulas in the processes with an increase in productivity and a decrease in energy intensity. The physical reason for this is a decrease in the residence time of gaseous silicon monoxide in the free state, which is responsible, among other things, for the fistula's formation, due to the greater likelihood of its reacting with hydrogen and carbon ions with the release of silicon.

As an additional regulator of the ratio between the concentration of gaseous reducing agents and, conversely, oxidants in the combustion zone of the electric arc, we proposed to use H_2O vapors supplied together with methane. The useful application of water vapor in silicon technologies is known, including the regulation with its help of the intensity of high-temperature oxidative and reducing reactions involving silicon in the medium of hydrogen and other gases [25, 26]. We proceeded [18] from the fact that in the zone of electric arc gorenje, the water molecule breaks down into H_2, H, and OH, which are active reagents with high reactivity, and also no less active hydrogen and oxygen ions arise, which react in the furnace of the EAF with gaseous silicon monoxide and carbon monoxide formed there, reducing the latter to Si and C, respectively, or, conversely, oxidizing to SiO_2 and CO_2, depending on the local excess of the concentration of these substances relative to the equilibrium state determined by temperature and stoichiometric ratio between CRA and SiO_2. This assumption has been confirmed in practice. Thus, we have suggested continuous monitoring of the current in the arc as an indicator of the smelting progress, and as its operational regulator — changing the supply of gaseous CRA to the arc combustion zone with the use of natural gas for extinguishing fistulas and associated current surges, humidification supplied to the furnace EAF. Let us illustrate the possibilities of controlling the smelting process through regulating the methane supply and changing its reactivity by humidification [37]. According to our proposed regulations for conducting the process of TSi smelting with partial replacement of solid CRA with methane, the optimal ratio

for each specific case of gaseous and solid CRA is determined, firstly, from a given stoichiometric ratio between SCC and CRA. To do this, during the ignition operation of the EAF, when its operating temperature is reached, the operating current in the electric arc is measured, and, by the absence of its throws, that is, the smooth arc combustion, the optimal range of the ratio between CH_4 and applied solid CRA is determined. That is, we additionally assign a fundamentally new responsible role to the EAF ignition operation, which consists in determining the optimal ratio between gaseous (methane) and solid CRA specifically used for this smelting. It has been experimentally proven that the permissible amount of CH_4 in the composition of CRA is from 50% to 80%, but the optimal value of the supply of CH_4, of course, depends on the specific solid CRA used (coke, charcoal, sawdust, petroleum coke, etc.) Since most (up to 80%) of the CRA is supplied to the furnace in gaseous, then it response to melting progress failures caused by either a violation of the stoichiometric ratio of the components or a sharp local change in the amount of one of them caused by the combustion of hydrocarbons, gas fistulas, or, provided for by the regulations of the process, periodic injection of a new batch of charge in a solid state, objectively manifested in throws, operating current, and, indirectly, in a change in the hum of the furnace, can be quickly stopped by changing the supply of CH_4. This can be done at a constant value of the applied voltage, and by a smooth change in the operating current, it is possible to judge the real consumption of raw materials during melting, and with certain experience, and a change in the real ratio between CRA and SCC in the electric arc zone and an increase or decrease in the supply of methane to stabilize this most important technological parameter, directly related to the melting speed in the period between regular, routine injections into the furnace of a new batch of charge. Of exceptional importance is the fact that the natural gas supplied to the combustion zone of the electric arc, to compensate for the current surges caused by the periodic injection of new portions of the charge, is intentionally controlled by humidification. This is provided by passing part of the methane stream through a bubbler with distillate and regulating the humidification degree by diluting the humidified methane with the main flow of this gas and (or) controlled changes in the flow of methane passed through the bubbler, as well as by regulating the temperature of distilled water in the bubbler. The introduction of water vapor directly into the combustion zone of an electric arc together with methane is accompanied first by the dissociation of its molecule and then by the ionization of oxygen, hydrogen, and carbon atoms, which increases the reactivity of the CRA. In this case, there is a change in the electrical resistance of the substances in the discharge gap and, accordingly, the magnitude of the current in the electric arc at the same applied voltage and the same distance between the graphite electrode and the furnace hearth. This circumstance is the basis for increasing the flexibility and speed of controlling the technological process of smelting TSi.

So, the typical regulations for the smelting of TSi using CH4 and charcoal on an experimental DC EAF are reduced to the installation of an EAF for this solid CRA ignition operation, and with its optimal ratio with CH_4 being 50–50%, the operating current in the arc is ~2200 A with permissible fluctuations within 50 A. Current fluctuations above 50 A are stopped by the supply of moistened CRA [18].

This proposal testing has shown that with its help, it is possible to reduce the specific power consumption by 8% while ensuring high controllability of the smelting process and obtaining the TSi of the Kr00 brand [28, 29].

The obtained results also demonstrated that in order to more fully solve the problem of increasing the controllability of the process of TSi smelting, it is necessary to radically change the method of feeding the charge, namely, to organize the supply of SCC to the arc burning area, similar to how we did it in terms of the supply of CRA and as we tried to do earlier in a two-stage process [13, 27]. The elaboration of options for changing the method of feeding the charge into the furnace of the EAF led to the need to assess the possibility of using the charge in a fundamentally different state than that usually used in the lump fraction or in the briquettes form.

Two points should be noted. In our opinion, a higher degree of controllability and stability of processes should be expected when using a DC for EAF. In an alternating current EAF, by definition, the movement direction of not only electrons but also ions, including ions of the product of the TSi melting, is constantly changing. The second remark concerns the influence of impurities that are present in the initial materials of the charge on its electrical conductivity value. In our opinion, the electrical conductivity of the charge is determined primarily by the ratio of SCC and solid CRA and then by the charge temperature, as well as the particle sizes of CRA and SCC in the briquettes with a mechanical contact in them. The impurities of the SCC at about 2–3% and the CRA purity indicators close to this do not affect the electrical conductivity of the charge, do not determine the amount of current in the arc, and can locally, but vanishingly little, affect the rate of a number of reactions of silica reduction by carbon. Impurities also do not determine the conductivity of the target smelting product, into which they pass, being restored, like Si, from their oxides, by carbon and begin to influence the conductivity of TSi during its solidification, although the influence of any impurity is instrumentally difficult to measure due to the actual compensation of different types of impurities with each other and the fine-grained structure of TSi. Table 3 shows the data of the transition coefficients of impurities – the ratio between their content in the TSi and in the initial charge, that is, in CRA and SCC in percentage.

The fundamental difference between the presented data and known in the literature [1–3, 8, 9, 30, 31] is that TSi is obtained by the "cold container" method [32] using microwave heating, in which contamination of the target product with impurities from the furnace walls and from the graphite electrode, that always occurs during standard electric arc smelting, is completely excluded.

Based on the literature analysis devoted to the problems of TSi smelting, it can be concluded that the main purpose of the most radical changes in the TSi smelting

Table 3 Transition coefficients of the impurities (wt.%)

Fe	Ca	Al	P	Ti	Mg	Mn	Cr	Ni	K
93	82	87	48	90	56	47	59	50	47

technology described there were attempts to improve the methods of feeding the charge into the EP, an operation extremely difficult to automate. This is precisely what new technical solutions were aimed at, for example, [11, 13] also the most perfect of them [27]. Thus, according to [27], the regulation of the technological process of TSi smelting includes operations of preparing the charge by crushing the CRA to the size of 0÷1 mm, which is comparable to the particle sizes of the quartz sand that is also used as a silicon-containing component. This process also includes separating the CRA into two parts, and mixing the silicon-containing component with a part of the CRA as powder, and the resulting charge is fed directly into the combustion zone of the electric arc through a hollow graphite electrode with simultaneous feeding, taking into account a given stoichiometric ratio between the silicon-containing component and the CRA, of another part of the CRA into the furnace and the actual TSi smelting. This technology makes it possible to increase the yield of the product by 1–12%, depending on the TSi used in each specific case of smelting, the mass ratio of the ground solid CRA, as which SiC is used to the QS mass. This technology is one of the first but successful attempts to solve the long overdue need in practice to modernize the process of TSi smelting aimed at improving its ecological and economic indicators.

The described innovations complicate the technological process. Firstly, the technology [27] is focused on the so-called two-stage process, at the first stage of which SiC is obtained in a separate EAF, for example, by low-temperature carbidization of the initial silica. At the second stage, using separate technological equipment and using the second EAF, TSi is smelted, during which SiC ground to a particle size of 0÷1 mm (i.e., comparable to the particle size of the QS) is used as one of the parts of CRA. The other part of the HC is fed into the EAF in the same way as in [1, 3] and other, close to classical, options for implementing the process of TSi smelting [8] by manual or mechanically automated periodic ripple around graphite electrodes.

The described two-stage technology is undoubtedly cumbersome and more energy-intensive, since per unit of the final product produced requires the use of almost twice the amount of equipment, additional production space, and, of course, additional electricity consumption.

It should be noticed that the periodic feed of the charge into the furnace known from the classical method [1] by an outline to the electrodes or, as in [27], an outline to them of a CRA part is an uneven process. This is accompanied by changes in the operating current in the electric arc, which changes sharply after each successive injection of the charge into the furnace. This circumstance reduces the possibility of operational control over the course of melting by the magnitude of the operating current in the electric arc and tightens the requirements for the qualification of personnel. In addition, the introduction through the central axial hole in the graphite electrode directly into the combustion zone of the electric arc of a mixture of QS with ground SiC supplied to the upper part of the electrode by screw dispensers, and then by a flow of inert carrier gas, is accompanied by active combustion, that is, destruction of the opposite extremity of the graphite electrode located in the EAF in the combustion zone arcs [27]. This disadvantage is inherent not only in [27] but

also occurs, for example, in [11, 36], not only for the smelting of TSi but also high silicon grades of FeSi.

We propose a radically modernized method of smelting. Firstly, it is proposed to supply CRA in two aggregate states, gaseous and solid, which the expediency was shown earlier in [17]. Secondly, during the charge preparation, this is suggested to mix the solid part of the CRA subjected to pre-grinding with the CRA with the addition of a binder to the paste-like state of the charge, when briquettes are usually formed from the charge. This technology is described in [17, 33–35]. Then the resulting freshly prepared charge in a pasty state, continuously supplied directly to the combustion zone of the electric arc through a hollow electrode, and the gaseous part of the CRA (methane), taking into account the stoichiometric ratio between the CSi and CRA, to be fed into the furnace through a separate channel, coaxial with the feed channel of the charge [18]. It is also proposed to supply methane continuously and directly to the combustion zone of the electric arc, and the feed rate of the charge and CRA is adjusted according to the magnitude of the current flowing. That is, to use the process control technique described in [14, 29, 37]. This innovation radically changes the equipment for TSi smelting, and its implementation is a rather complex engineering task.

Therefore, it was decided to gradually check the operability of its new distinctive features, including the main one, in terms of supplying the furnace charge in a pasty state (CPS). Furthermore, we considered the issue of the possibility of simultaneous feeding of charge to the EAF in any combination of its three states or types (solid lump fraction, pasty state, briquettes) with the CRA supply in various states – methane gas – and in the solid lump state as coke or charcoal, as well as both of these components in the composition of briquettes as soot and fine silica waste and charcoal or coke, screened out for batch operations. To do this, relying on the regulations of the TSi smelting according to [29], which includes preparing the charge in a paste-like state by mixing the lumped SCC or QS ground to a given size, with the addition of a part of solid CRA crushed to a given size using a binder, feeding freshly prepared CPS in continuous mode directly into the furnace of the EAF into the burning zone of electric arc, the supply of another part of the CRA to the combustion zone of the electric arc of methane, only part of the charge is intentionally transferred to a paste-like state, and the rest of the charge is fed in a lump fraction or in the briquettes with an outline to the electrode. At the same time, the supply of CPS and CRA and in the gaseous state is carried out in the directions towards each other, respectively, from below and above relative to the furnace of the EAF with the mixing of these melting components directly in the combustion zone of the electric arc under the charge layer in the lump fraction. Figure 4 illustrates the design of the EAF, in which the option of feeding the furnace charge of three types, including CPS, is implemented.

As can be seen from Fig. 4, the EAF (1) with an internal, graphitized wall 2 with a hollow graphite electrode 3, equipped with a central hole used as a means of supplying a part of the CRA (methane), the CPS supplying to the furnace is carried out through a separate channel from the CRA supply channel, starting at the loading hopper 4, where first, the finished CPS 5 arrives, which is then pushed through using
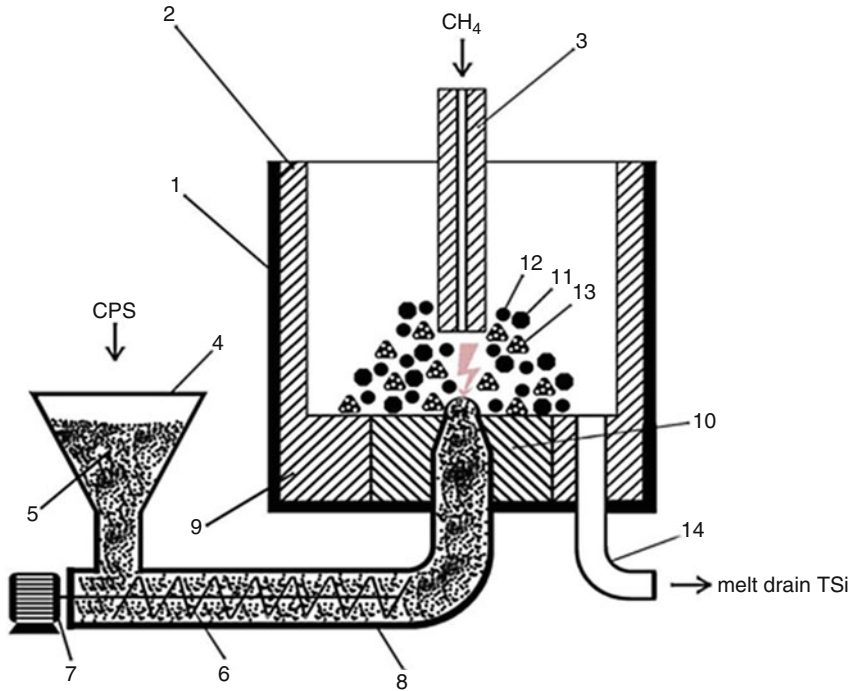
Fig. 4 Scheme of the EAF variant according to Patent IAP UZ 06836 [37], which is a simplified version of Patent UZ IAP 05986 [29], with the supply of the charge in a pasty state in combination with the supply in the lump fraction and briquettes and with the supply of parts of the CRA in the form of CH_4 (shown by the arrow)

a screw dispenser 6 with an electromechanical drive 7 through a channel-pipeline 8, made in the lower part of the EAF 1 directly under the tip of the hollow graphite electrode 3 through the graphite neck 10, that has a shape tapering from the inside to a cone. An outline of the charge in a lump fraction consisting of SCC in a lump fraction 11 and CRA also in a lump in the form of, for example, charcoal or coke in pieces 12 or in the form of briquettes 13 containing soot and waste trifles from the charging operation is carried out in a standard way [1, 3] through the grate from above around the electrode 3. The drain channel 14 of the TSi smelt is shown by an arrow.

The TSi melting was carried out using the described technology and device as follows: first, CPS was made by mixing, ground in a ball mill to the same size ~0.2–0.4 mm., lumpy CRA with CRA with, crushed to the same size, 1/3 of the solid CRA in the form of coke, using a binder based on sodium CRA with a module 2.5÷3.0. Part of the same mixture of components was sent to the manufacture of briquettes. In parallel, they were preparing the SCC and the CRA, which were supposed to be sent to the EAF in a lump fraction.

Table 4 The impurity composition of the TSi obtained on the EAF with a combined feed of the furnace charge in a lump fraction (~30%) and in a pasty state in combination with the supply of CRA in a lump fraction (~65%) and in the form of CH_4 [29]

Si	Al	Fe	Ca	Mg	Ba	P	V
98.97	0.34	0.33	0.32	0.0085	0.0055	0.007	0.0050

For this aim, coke of the KO-3-5 brand (GOST 89-35-77) and pieces with dimensions of ~20 mm were used to supply the furnace with a draft to the electrode, and the trifle was sent to the grinding mentioned above. Similarly, CRA with a SiO_2 content of ~98% was sorted, and pieces of ~20 mm were selected for direct use of the sketch to the electrode, and the CRA trifle was also crushed using a ball mill, until particles with a size comparable to the size of the QS particles were obtained. QS with an initial SiO_2 content of $97 \div 98\%$ was washed with water, dried, and then thoroughly mixed with grinding of small CRA and with grinding of coke fines with the addition of a binder based on sodium liquid glass with a module (SiO_2/Na_2O) from 2.5 to 3.0.

So, the resulting mass, that is, the charge in a paste-like state, is partially used directly and partially goes to the manufacture of briquettes, that is, pellets of ~30 mm in size, which, after molding, were dried at ~400 K and then fed manually into the EAF by a sketch around the electrode together with silica (SiO_2) in the form of CRA and coke in a lump fraction; the resulting CPS was fed into a filling funnel, and with the help of an auger, it was pushed through a steel pipe, analogous to the pipeline 8 in Fig. 4 welded to the bottom of the EAF casing. In the graphite plate of the EAF, a hole with a diameter of 40 mm was made directly under the tip of the hollow graphite electrode, that is, into the burning zone of the electric arc, which is shown in Fig. 4 with a zigzag arrow. The fundamental difference of this method is that in the opposite direction, directly under the graphite electrode, under a layer of lump charge and briquettes, a CPS is fed, which is controllably pushed into the combustion zone of the electric arc at a given speed through the hole (Fig. 4) depicted with a narrowing, conical along the course of the CPS. Thus, CPS and CH_4 and the charge in the lump fraction and briquettes are fed into the EAF through separate channels, spatially separated with mixing directly in the combustion zone of the electric arc. The feed rate of CPS, as well as the frequency of sketching briquettes, CRA, and CRA to the electrode in a lump fraction, as well as the consumption of natural gas CH_4 supplied through a hollow electrode is regulated according to the standard method, that is, the smooth "course of the furnace" [1], and, in parallel, according to the method we proposed [18], that is, tracking the amount of current flowing in an electric arc. The chemical composition of the obtained TSi is given in Table 4.

It was shown that the EAF with these alterations, in principle, work in the modes of implementation of the new technology, both in full and in partial implementation, for example, with the supply of CRA to the furnace in the form of methane and coke, but only in ground form as part of briquettes or only in a lump fraction, or predominantly, that is, up to ~80% [15] in the form of natural gas. And SCC

in the furnace can be served not only by a combination of CPS, CRA in a lump fraction, and briquettes but also by independent use of each or any pair of these three components of SCC.

The limiting case is when, for one reason or another, the hole in the graphite plate of the EAF is closed with a graphite plug and the TSi smelting is carried out within the framework of the regulations [1, 3, 8] according to the classical scheme. Experiments have shown that the best option is the TSi smelting with a combined supply of SCC in the initial period of the process. Then, when the first portions of the melt appear, it is advisable to recharge the bath by feeding the furnace charge in a pasty state, and sintered silica and CRA in a lump fraction and (or) briquettes are used mainly as a kind of "vault" over the bath.

The application of silicon production waste in concrete and building mixes. Electric arc smelting of TSi and siliceous alloys, the most popular of which is FeSi [4], based on the carbothermic Si reduction process, from silica and, accordingly, iron, manganese, chromium, and calcium from their oxides, is accompanied, as was reported above, by the appearance of dust waste consisting mainly of microsilica particles (MS), the daily volume of which is comparable to the amount of the target product, and, for example, on a 9600 KVA electric arc furnace used for smelting FSi of the running grades FSi45, FSi65 is more than 8 tons. MS is thoroughly, at least 95%, captured by gas purification means, since it is dangerous to the environment [38]. The most primitive are the well-known ways of disposing of MS as unclaimed waste, the simplest but far from the best of which is its storage in slag fields with subsequent mixing with soil.

MS, as shown in [39] and confirmed by instrumental estimates [33–35, 42] of its particle size distribution, is globules of amorphous SiO_2 with sizes from 50 nm to a few micrometers, and the smaller the particle sizes, the more often they aggregate into conglomerates of tens and hundreds of pieces. It should be noted that the capture of MS is carried out using filters with different cell sizes, and in the production of TSi or FeSi, it is possible to divide MS into groups of globule sizes without any additional costs, but this is simply not done.

If the total granulometric composition of the particles of MS arising in various industries is approximately the same, then its chemical composition, on the contrary, strongly depends on the type of target product produced, its brand, and, of course, the raw materials used, which determines the variety of ways to use MS as a secondary raw material.

To illustrate this, Table 5 compares the chemical composition of the MS that occurs at a number of enterprises in Russia and Uzbekistan during the TSi smelting and siliceous alloys [4, 34, 35, 39].

It can be seen that the content of SiO_2 in the MS of different enterprises varies within very wide range, and even if we limit our consideration only to waste from the production of TSi and high silicon grades of FeSi (pos. 1, 2, 4, 8, 9 Table.5), then the content of silicon dioxide in the MS is in the range from 89% to 95%.

As it was noted, briquetting is one of the advanced methods that make it possible to dispose of MS in the same technological processes where it is formed. However,

Table 5 The chemical composition of the MS for different enterprises during the production of TSi and siliceous alloys of various types and grades

№ n/n	Metallurgical enterprise	Alloy grades	Oxides proportion (wt.%)					
			SiO_2	Fe_2O_3	Al_2O_3	CaO	MgO	K_2O+Na_2O
1	Kuznetsk ferroalloys	FeSi 90, FeSi 75	90.1	2.0	1.7	2.3	0.8	1.9
2	Chelyabinsk electrometallurgical plant	FeSi 75, FeSi 65	89.2	0.4	1.7	2.1	1.7	1.4
3	Ermakovsky ferroalloy plant	FeSi 65, FeSi 45	70.1	3.4	2.0	11.4	0.1	0.9
4	Bratsk aluminum plant	TSi Kr1, TSi Kr2	91.7	0.4	0.5	1.2	–	–
5	Aktobe ferroalloy plant	FSiCr 40	66.1	2.2	1.3	0.4	14.6	–
6	Aktobe ferroalloy plant	FCr 800	16.6	1.8	6.6	0.5	38.6	–
7	Zestafoni ferroalloy plant	SiMn20	33.8	2.3	3.9	4.6	4.0	2.4
8	Angren ferrosilicon plant	FeSi 75	92.77	1.37	1.79	1.54	0.74	1.64
		FeSi 65	90.79	2.28	1.41	1.91	0.94	2.42
		FeSi 65	94.23	1.17	1.36	1.58	0.41	1.15
		FeSi 45	70.07	2.61	3.30	3.3	0.68	0.84
9	Bekabad metallurgical plant	FeSi 65	95.8	0.8	0.4	0.4	0.4	1.0
10	Bekabad metallurgical plant	FeSi 65	97.85	0.17	1.11	0.32	0.03	0.51

based on the fact of the increased content of such impurities harmful to the TSi as Fe and considering that silica in the form of CRA or quartzite with a SiO_2 content of at least 97% is used for smelting even its ordinary grades [1–5], it is clear that the MS obtained as the waste from the smelting of FeSi [4] and other siliceous alloys are generally unacceptable for the TSi production. In general, the waste from the production of siliceous alloys due to the deliberate implementation of specific metals into them should be processed at the same enterprises and to obtain the same target products, during the smelting of which they are formed. As for the waste from the smelting of the TSi, in addition to the trifles of silica and CRA, in general, it is impractical to return them to the production of silicon in the form of briquettes directly, while the introduction of MS from the processes of TSi melting into briquettes used for the FeSi smelting or other siliceous alloys, on the contrary, is possible and useful.

To optimize this technology, it was shown that the amount of MS introduced into the composition of the silica part of the briquettes for the smelting of FSi should not be chosen randomly, but taking into account the average particle sizes of other silicon-containing substances used in briquetting, which is convenient to estimate by their bulk density [18, 40–42]. Such a technique allows to increase the share of MS in briquettes for the smelting of FSi up to 40% without losing their strength characteristics and at the same time reduce by 5–15% the specific energy

Table 6 Compressive strength of concrete containing cement, QS, and MS in various combinations at different maturation periods

Physical and mechanical characteristics	Compressive strength, kgs/cm^2			
	3 days	14 days	21 days	28 days
Cement PPC 400	22.23 ÷ 25.05	40.54 ÷ 41.01	45.19 ÷ 45.23	50.86 ÷ 51.22
5% MS + cement	27.11 ÷ 30.62	45.19 ÷ 46.05	50.12 ÷ 50.93	55.19 ÷ 55.20
10% MS + cement	35.40 ÷ 35.85	57.23 ÷ 58.02	60.03 ÷ 62.89	65.82 ÷ 65.70
15% MS + cement	45.22 ÷ 55.41	60.12 ÷ 61.00	65.82 ÷ 65.70	70.08 ÷ 71.34
20% MS + cement	55.06 ÷ 55.21	70.36 ÷ 70.61	77.28 ÷ 87.40	100.23 ÷ 100.05

consumption for the smelting of the target product, which is important for such an energy-intensive process, what is the electric arc melting of FSi.

The MS usage as an additive in the production of concrete is great interest [39]. From the numerous literature and patents on this subject, it follows that the addition of MS to cements of any brands, naturally, with the correct dosage, invariably increases the strength characteristics of concrete, which is especially valuable when creating dams, foundations, arched bridge, and other concrete, load-bearing structures, including especially responsible, complex shapes, and also operated in conditions of high humidity, frost, alternating temperature changes, etc. The use of this experience is useful for the Uzbekistan Republic and other Central Asian republics located in a seismically active region, which is currently undergoing rapid housing and special construction. The Table 6 presents data on the compressive strength of concrete samples, the sealing of which was carried out by mixing PPC-400 cement with a constant amount of quartz sand from the May deposit with a humidity of 0.43% and with the addition of MS to the mixture, obtained as waste during the smelting of FSi 65 at the Bekabad Metallurgical Combine and having a humidity of 0.24%. The proportion of the MS substituting cement in the mixture varied from 5% to 25%.

It can be seen from Table 6 that the MS addition to cement mixtures, even without the introduction of a plasticizer into them, increases the compressive strength of concrete by 1.5–2 times, estimated according to the methodology regulated by GOST 310.4–81, and this parameter depends on the amount of the additive and the age of concrete in a complex way. In particular, the dependence of strength on the value of the additive MS has the form of a curve with a maximum of ~20% content in the initial cement mixture of MS, while the dependence of strength on age has a maximum in the region of 20 days. The data obtained by us, in general, are similar to those given in [44–49], where there is also the existence of complex relationships between the strength characteristics, the age of concrete, the content of MS in the cement mixture, as well as the brand of cement and, of course, contradictions existing among different authors regarding the optimal ratios of these components of the cement mixture.

The maximum increase in the flexural strength of concrete is observed when cement is replaced by 15% of the MS, consisting of silicon dioxide particles having

the shape of "globules" with dimensions regulated by TU 00186200–12:2019 ranging from a few micrometers to tens of nanometers. The sizes of microsilica particles the value of which can change in wide range effect significantly on the strength characteristics of concrete. Therefore, we propose to conduct a separate selection of MS with a different characteristic size, which can be achieved by its organization in various places of the evacuation and purification system of gases departing from the EP, that is, in fact, it is proposed, by no means, to mix the dusty waste poured out in various places of the gas purification system but, on the contrary, sort MS by the size of dust particles and purposefully use them in order to achieve maximum efficiency, not only in the production of concrete and building mixes but, as will be shown below, also in the synthesis of adhesive compositions such as alkaline "liquid glass" (LG).

The greatest effect from the use of intentionally selected, taking into account the size, and then mixed fine components can be obtained when creating finishing building mixes, since they provide not only increased strength but also smoothness of the surface when solidified. No less important, in our opinion, is the selection of MS by the size of globules and when it is used in the manufacture of ceramic products of various [40, 43], including technical [44] purposes.

MS is a raw material for the manufacture of silicate glue. Less studied is the field of application of MS instead of or in mixtures with QS in the manufacture of adhesives of the LG type, which are widely used in everyday life, in various industries, and in construction [39]. mentions a method [50] according to which LG is made by mixing MS, sodium hydrate, and ordinary water and then cooking the mixture for an hour at atmospheric pressure at a temperature in the range of 85–95 °C, and the cooking time is determined by the LG module. The achievement of a useful effect in the method [50], which consists in shortening the duration and simplifying the technology, is ensured by the fact that an MS containing from 6% to 16% by weight of carbonaceous impurities in the form of graphite and SiC dust particles with high thermal conductivity is selected.

Leaving without discussion the arguments of the authors [50] regarding the physicochemical processes of the interaction of alkali with SiO2 in the presence of heat-conducting impurities C and SiC, we point out the fact that the mass spectral analysis of the MS obtained in various processes and from different enterprises (Table 6) does not show the presence of these impurities in it, especially in such a large amount. SiC and free carbon are certainly present in the smelting process of TSi and siliceous alloys, but SiC is formed in the middle part of the EP in the charge descending to the furnace and actively interacts as a reducing agent with the gaseous silicon monoxide rising up and is completely consumed. As for the free carbon entering the furnace with a charge, it is also always consumed completely. To ensure the normal "course of the furnace", the CRA amount added to the charge is always chosen more than is required by the stoichiometric ratio of the carbothermic reduction reaction of silica.

In order to implement a relatively simple technology for producing LG using microsilicon, in contrast to [50], we propose to use technogenic carbon dust, formed,

of course, not in the furnace but during the charge operation, as well as finely dispersed waste intentionally crushed by additional grinding, in mixtures with MS fed into a container for reaction with an aqueous NaOH solution. UV is also formed on the mentioned operation. Only in this case, the content of the carbonaceous component in the mixture with the MS can be adjusted within wide limits, including, to overlap the optimal range of their content specified in [50]. Such close attention paid by us to the production of LG is due to the fact that this ingredient is used as a binder in the manufacture of briquettes during the smelting of FS [4, 17, 33–35] in quantities of 3–6 kg per 100 kg of crushed silica charge materials, including MS, the amount of which in this part of the charge, for example, for the smelting of FSi with a low silicon content, can be up to ~40%. Therefore, the optimization of the binder production process from the point of view of simplifying its production and reducing the cost of this ingredient, the annual consumption of which, for example, on a 9600 KVA furnace can be ~500 tons when organizing smelting only on briquetted charge, seems to be an urgent and economically justified task.

The development of the proposed technology and its localization at the metallurgical enterprise contributes to the creation of a specialized briquetting area of the charge, which includes aggregates for the preparation and mixing of sand, quartzite fines, MS, and binder, which is manufactured on site, followed by the molding of briquettes from this mixture and their processing. In this regard, we propose the application a new optimized version of technology subscribed in [51–53], the essence of which is reduced to the separate use of certain fractions of MS. This allows to significantly reduce the role of carbon particles, while simultaneously using for the synthesis reaction of liquid glass the heat of gases escaping from the electric arc furnace, by analogy with the use of geothermal heat for these purposes [54].

The new technical solution developed by us [54] for the synthesis of LG consists of the following steps: i) preparation of a MS suspension in the sodium hydroxide solution and subsequent hydrothermal treatment at 80–85°C and atmospheric pressure; ii) addition to the MS the dust and fine-dispersed waste from the operation of grinding the waste of the mentioned target products, arising during the rejection of products before sending to the consumer, that is, fine-dispersed waste of TSi or FSi in the amount of 5÷6 wt.%.

The physicochemical essence of our proposal [54] consists in the fact that the pre-crushed or already sufficiently fine and dust particles of the target products introduced into the suspension instead of carbon and carborundum, that is, TSi or FSi, unlike C and SiC, enter into a chemical reaction with a solution of sodium hydroxide and completely, without sediment, dissolve in suspension. At the same time, such a suspension is a one-component system, the thermal conductivity of which is always higher than that of the starting substance and directly depends on the amount of dissolved dust particles TSi or FSi, and not two-component, as in the case of introducing insoluble particles C or SiC into it [51–53], the amount of which must be adjusted to the same acceptable values in order to achieve an increase in thermal conductivity up to 6÷16 wt. % or 6÷8 wt. %, respectively.

Our proposal [54] is focused on the use of waste from modern production of both TSi and FSi, which makes it useful to dispose not only MS but also dust and fine-dispersed waste from the production of TSi and FSi, which inevitably arise when the castings of these products are broken into pieces with dimensions regulated by GOST 2169-69 and GOST 1415-93, respectively, and then it ensures the achievement of all the tasks set, including the replacement of carbon and carborundum in the LG technology, which are absent in the waste of modern TC or FS productions, on the dust and fine-dispersed waste of these target products always available in it.

The new method of using MS proposed by us in the manufacture of briquettes for the smelting of siliceous alloys involves a set of measures consisting of:

(i) Organization of the manufacture of the binder directly on site from the MS by selecting its small fractions with the sizes of amorphous particles of silicon dioxide from tens of nanometers to 200 nanometers, which are combined with an aqueous solution of sodium hydrate to ensure mixing and heating using the heat of gases leaving the EP.

(ii) Pulling out the resulting mixture with constant stirring at a temperature of 80–90 °C for 30–40 minutes until the formation, in fact, of the desired binder in a jelly-like state.

(iii) Mixing the resulting heated mass of a jelly-like binder with a pre-washed QP with water and with the remaining part of the MS, taken in equal parts by weight.

(iv) Adding the specified, continuously mixed mixture of fine and dusty waste of LG or quartzite, as well as HC from the charge operation at the rate of 9 kg of binder for every 100 kg of total silicon and carbon-containing raw materials.

(v) Forming pressed briquettes and drying them using a stream of air heated by heat, gases escaping from the EP.

The physicochemical and technical essence of the new method we propose is, firstly, that the various fractions of the MS are proposed to be used separately.

To do this, MS, poured out in different places of the purification system (after different filters), exhaust gases from the EP and differing in geometric dimensions, is not mixed, as is generally accepted, but is used separately, and the finest fraction containing SiO_2 particles 50–200 nm in size is used for on-site preparation of a binder for briquettes. The rest of the microsilica, that is, the fraction of SiO_2 particles with sizes greater than 200 nm but less than 2–3 μm, is sent for processing as part of mixtures for the briquettes themselves, that is, in a mixture with QS, as well as with other fine and dust waste silicon and carbonaceous components.

The selection and use of the smallest fractions of MS for the preparation of a binder accelerate the process of interaction between an aqueous solution of sodium hydrate and silicon dioxide SiO_2, which constitutes ~98÷95% of the selected nanosized particles of MS. In this case, the so-called size effect plays a role, according to which the smaller the particles of a substance, the easier and at lower energy costs they enter into a chemical reaction. That is, in our case, SiO_2 and alkali react in an aqueous solution of Na_2O at temperatures lower than usual, which

reduces the duration and energy intensity of obtaining a binder. It is important to note that the selection of the MS fraction necessary for this with dimensions of 50–200 nm is carried out without any special equipment and additional costs, only by its selection where it is screened out precisely with such dimensions, that is, after a certain number of filters of the standard used in industry systems for cleaning gases from the EAF.

The remaining part of the MS with larger SiO_2 particles enters the mixture, as already mentioned, together with the QS preliminarily washed with water. Such a simple flotation makes it possible to remove clay spreads from the surface of sand particles and increase the SiO2 content from 97% to 98%, for example, in the QS of the Dzheroyskoe deposit, to 99–99.5 wt.%.

It is advisable to stipulate that MS and washed QS enter the mixture for briquettes in equal proportions. This refinement proposed by us provides a guarantee of the overall high content of SiO_2 in the briquettes, since the content of SiO_2 in the MS usually ranges from 89% to 95%. In mixtures with high-purity QS with a SiO_2 content of 99–99.5%, taken in equal proportions with MS, the SiO_2 content is quite consistent with the purity of QS or quartzite, which is usually used in the smelting of FeSi or quartzite, the fines of which are also added to briquettes, which means that the addition of MS cannot worsen the quality of the target product in terms of the content of impurities.

MS as a Raw Material for the Synthesis of Micro- and Nanosized Powders of Silicon Carbide (SiC). It is also necessary to point out the great prospects for the use of MS in SiC technology [55] and, in particular, nanosized powders of this material, the production of which is currently based on plasma metallurgical technology (PMT) [58] and furnace synthesis (FS) [55].

A probable mechanism for the FS of SiC from mixtures of MS and CRA was proposed in [55], according to which the process of carbothermal reduction of MS proceeds with the active participation of gaseous silicon oxides. As in the case of the formation of MS, the mechanism of SiC synthesis is multichannel, and, which is of particular interest, as a result of the studies, the role of the size effect, that is, the real sizes of MC and CRA particles entering into chemical interaction, was identified and evaluated, which we also drew attention to in the development of optimized technologies for concrete, briquetting of MS and the creation of "LG" on its basis. The size effect in the "gas-dispersed crystalline phase" system manifests itself in a change in the saturated vapor pressure above the surface of crystalline particles depending on the degree of dispersion of the solid phase, and, accordingly, an increase in the interaction rate is due to an increase in the evaporation surface of SiO_2 and a high adsorption capacity of the developed surface of the applied finely dispersed hydrocarbon. That is, when using fine and well-mixed materials, which are mixtures of MS and, for example, soot, especially obtained by burning natural gas, the primary interaction is the solid-phase contact interaction $SiO_2(t) + C(t)$, which, at temperatures ~1500 K, gaseous silicon and carbon monoxides are formed and, at temperatures above 1800 K, oxygen-deficient silicon-oxygen melt is also formed. The formation of silicon-oxygen melt films in the contact zone between

silica and carbon increases the contact surface and intensifies the reduction process. Another channel for the formation of SiC is based on the interaction of gaseous SiO with solid carbon, and the completeness of the transition of silicon from MS to SiC depends on its manifestation. Thus, according to [55, 56], reduction of SiO_2 to SiC proceeds predominantly through the formation of a silicon-oxygen melt, which is processed without significant accumulation at high rates of chemical reactions. The resulting SiC then interacts with the said silicon-oxygen melt until it completely disappears.

In contrast to PS, the process of SiC formation in a plasma-metallurgical reactor, in which MS, natural gas-methane, and nitrogen plasma flow are used as initial reagents, can be considered as a "single-channel" process [55], proceeding with the participation of silicon vapor and hydrogen cyanide according to the "steam-crystal."

PMT, unlike FS, makes it possible to obtain a product in the form of nanopowders with a particle size of 60–70 nm with a minimum number of surface defects and also makes it possible to control the synthesis process, for example, by controlling the composition of the gas phase, introducing certain additives into it, which ensures the production of SiC with specified electrical properties. At the same time, with the help of FS, SiC based on MS can be obtained in the form of a micropowder with a particle size of 200–900 nm and higher, which is also in demand in various fields of technology. It should be noted that the synthesis temperature when using MS can be significantly reduced compared to the traditional version of the PS of this material, as well as the duration of the process, which makes it possible to reduce the specific power consumption by almost two times compared to the traditional SiC production technology.

We have carried out a series of studies aimed at developing the processes of furnace synthesis of SiC using MS and different types of CRA. MS, which is a technogenic waste from the production of TSi and FeSi, was used as a silica raw material, and carbon black and methane were used as hydrocarbons.

It follows from the obtained experimental data that the particle size of SiC powders and their granulometric composition depends on the particle size of the used hydrocarbons. The size ratio of silica and CRA particles affect the reaction rate of carbon with SiO_2.

The resulting powder with a particle size of hexagonal 4H and 6H SiC types from 30 to 400 nm belongs to the class of mixtures of nano- and micropowders, which are in demand in various fields of practical application and, in terms of their cost indicators, exceed the prices for TSi and FeSi, the production waste of which is not used in as a raw material for their production. This circumstance indicates the expediency of combining the smelting of TSi and FeSi with the furnace synthesis of silicon carbide at one enterprise. It should be noted that substandard products of SiC furnace synthesis, in turn, can be successfully used in electric arc smelting of elite grades of TSi with a guaranteed reduction in specific energy consumption.

The results obtained, based on standard equipment and methods of furnace synthesis of SiC, allowed us to proceed to the development of a new method for obtaining powders of this substance.

We propose to modernize the process of furnace synthesis of micro- and nanosized SiC powders, which includes batch preparation operations by mixing CRA particles in the form of charcoal, petroleum coke, or their mixtures, specially ground to a given particle size, and a silicon-containing component in the form of MS, which is a dusty waste from carbothermal processes of electric arc smelting TSi or FeSi, placing the resulting mixture in a resistance furnace and carrying out the synthesis of silicon carbide. For this, a part of the solid CRA in the form of ground petroleum coke or charcoal or mixtures thereof is proposed to be replaced with gaseous CRA in the form of natural gas, taking into account the stoichiometric ratio between silicon and carbon, and the SiC synthesis operation is carried out with the provision of its flow; the natural gas is preliminarily subjected to dissociation into carbon and hydrogen, by contact with the heated surface of the catalyst; the completeness of the synthesis process is judged by the change in the color of the flame ignited at the outlet of the resistance furnace, reaction gases; and the heat from their combustion is useful to use to heat the catalyst.

New equipment was created to implement the new process. Synthesis of SiC was carried out with a gradual and gradual increase in temperature from 700 to 1900 °C [57].

The scheme of the experimental apparatus is shown in Fig. 5. It is shows a section of the setup containing a resistance furnace 1, equipped with a tubular flow system 2, with a heating zone "A" and a cooling zone "B," with front 3 and rear 4 flanges, and equipped with nozzles 5 and 6, respectively, for supplying a portion of the carbonaceous reducing agent supplied as methane (shown by an arrow labeled "CH_4") and withdrawing the reaction gases.

The charge prepared in advance consisted of finely dispersed wastes of petroleum coke and microsilica. The ratio of the mixed components of the charge was deliberately reduced to 50% the amount of solid carbonaceous reducing agent – petroleum coke, determined by stoichiometric ratio of the reaction of silicon with carbon. The missing part of the carbonaceous reducing agent was replenished with natural gas containing the reducing agent in the form of carbon and hydrogen, since natural gas is 94% CH_4. The mixture, consisting of waste petroleum coke and microsilica, was poured without any compaction on the tiers of a multi-tiered boat 15 made of refractory ceramics and then, using a rod 16, was pushed inside the tubular flow system 2 of the resistance furnace 1, namely, into the heating zone "A." Then the front flange 3 was installed, equipped with a prechamber 7, the system was purged with an inert gas – nitrogen, the heating was turned on, and upon reaching the set temperature in zone "A," methane was let into the tubular flow system 2. The consumption of methane was chosen taking into account the missing part of the carbonaceous reducing agent, according to the stoichiometric ratio between silica and carbon, and it was monitored by the position of the rotameter float.

The silicon carbide synthesis was carried out, as it was already noted above, with the preliminary dissociation of methane supplied through pipe 5 to flow system 2. To do this, methane was passed through prechamber 7, which is a flow container with built-in catalyst 8. The catalyst 8 was a hollow body made of nickel with fine mesh partitions 9 installed inside. Nickel was chosen due to its experimentally
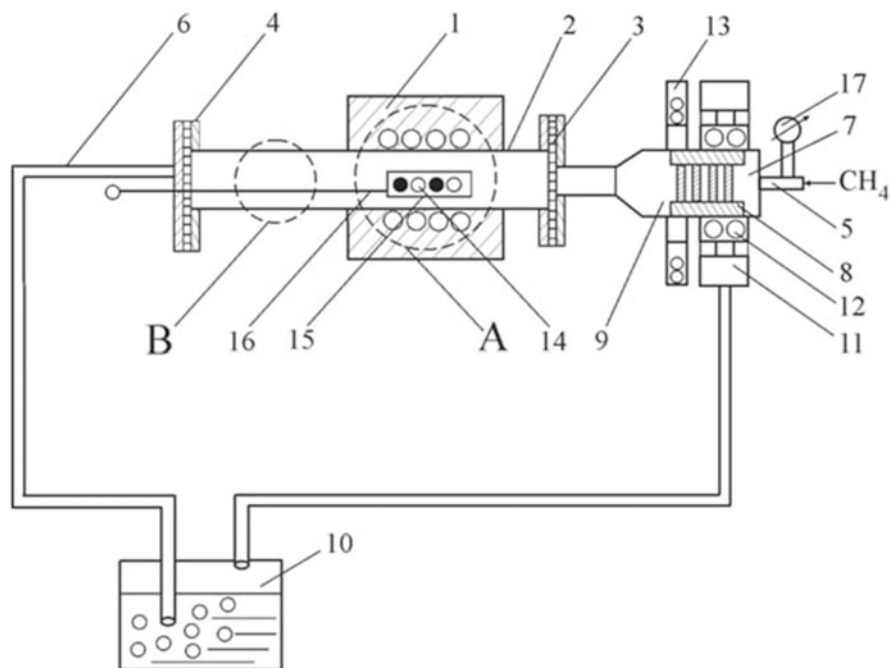
Fig. 5 Scheme of the experimental apparatus for the silicon carbide synthesis using methane: (1) resistance furnace; (2) tubular flow system of the resistance furnace; ("A") furnace heating zone; ("B") furnace cooling zone; (3 and 4) front and rear flanges; (5) CH_4 supply pipe; (6) reaction gas outlet; (7) front chamber; (8) nickel catalyst; (9) partition in the form of fine mesh nickel meshes; (10) shutter; (11) burner; (12) reaction gas flame; (13) adjustable nickel catalyst electric heater; (14) methane dissociation products; (15) multi-tiered boat; (16) rod for moving the boat; (17) pressure gauge

proven catalytic properties with respect to methane. The outer walls of the catalyst 8 are in contact with the inner walls of the prechamber to provide thermal contact. Outside, prechamber 7 was heated to ~600–800 °C using two heaters – burner 11 and adjustable electric heater 13. As a result of methane contact with the heated catalyst surface, it dissociates into hydrogen and carbon, which contributes to an increase in the reactivity of methane in silica reduction reactions.

To determine the optimal synthesis conditions and achieve the maximum yield of SiC, experiments were carried out by varying the proportion of methane in the composition of the total carbonaceous reducing agent: petroleum coke, $C_{pc}(s)$, and gaseous methane, $CH_4(g)$. While maintaining the total amount of carbonaceous reducing agent required by the stoichiometric ratio to reduce silicon with carbon, the proportion of $CH_4(g)$ varied from 0.15 to 0.60 of the total amounts of carbon, and $C_{pc}(s)$ decreased from 0.85 to 0.40, respectively.

The test results of the proposed method and the developed device for its implementation have shown the operability, efficiency, and usefulness of the

proposed technology. SiC powders with a predominant particle size of less than 100 nanometers were synthesized. The analysis of the powder X-ray indicates the production of SiC cubic 3C and hexagonal 4H and 6H polytypes of interest for use in modern technology.

Similar positive results were obtained in the case when K-354 carbon black was used as 85% of solid HC, which is a soot product of natural gas combustion when generating electricity at thermal power plants, with particle sizes of 10–200 μ and with a solid carbon content of ~95%. In the synthesis of silicon carbide powders, 15% of the bulk of the hydrocarbon in the form of soot was also natural gas, also intentionally, according to the invention, subjected to dissociation resistance to carbon and hydrogen at the entrance to the flow furnace. As a source of silicon, an MS was also used, which is an environmentally hazardous, dusty waste produced by FSi and TSi with a content of amorphous particles-SiO_2 globules of 95–97% by weight and having dimensions from 10–20 to 250 nm.

The obtained SiC powders are dominated by particles having an irregular, "fragmentary" shape with a smooth surface on which there are no manifestations of "roughness," that is, pits, cracks, protrusions, and other growth defects. X-ray analysis of these micro and nanopowders also clearly indicates the production of SiC cubic 3C and hexagonal 4H and 6H polytypes, which are in demand in the production of both abrasives and high-temperature ceramics.

4 Conclusion

Based on the study of the process of melting technical silicon in electric arc furnaces: a new method for smelting silicon and silicon alloys has been proposed and implemented, which provides for the supply of methane to the combustion zone of the electric arc of the furnace and the use of briquetted charge, which makes it possible to replace traditional carbon reducing agents in the form of charcoal and coke by 80% with natural gas (methane) and obtain technical silicon with a purity not less than 98.5%, as well as ferrosilicon of any grades.

Expediency is shown when replacing a part (50–80%) of a solid carbonaceous reducing agent with a gaseous one in the form of methane to ensure its dissociation into hydrogen and carbon by contact with a nickel catalyst heated to ~800 K directly on the methane supply path to the electric arc burning area and also control the process by the magnitude of the current flowing in the electric arc and quickly stop its spontaneous and regular surges by adding water vapor to methane.

For the first time, the use of a furnace charge in a pasty state was proposed, and a new method for its supply to an electric arc furnace was developed, and a variant of this new technology was experimentally tested, which consists in supplying a gaseous carbonaceous reducing agent and a charge in a pasty state in opposite directions directly into the burning area of an electric arc and allowing simultaneous use traditional supply of charge in lumpy fraction and briquettes.

The possibilities of increasing the profitability of silicon production by returning the waste of this production to the technological cycle in the form of briquettes, as well as using them for the synthesis of silicon carbide, glue "liquid glass," and in the construction industry for strengthening concrete, are shown.

References

1. Vengin, S., & Chistjakov, A. (1972). *Tehnicheskij kremnij*. Metallurgija. (in Russian).
2. Katkov, O. (1999). *Vyplavka Tehnicheskogo Kremnija*. IrGTU. (in Russian).
3. Jolkin, K., Zelberg, B., Barancev, A., Jasevich, O., Krjuchkov, V., Jolkin, D., Jakovlev, S., & Balakirev, S. (2013). *Proizvodstvo kremnija*. MANEB. (in Russian).
4. Ryss, M. (1985). *Proizvodstvo ferrosplavov*. Metallurgija. (in Russian).
5. Evseev, N., Radchenko, N., Men'shikov, P., & Begunov, A. (1988). Utilizacija pylevyh othodov pri proizvodstve kremnija. *Tsvetnye metalli, 11*, 64–65. (in Russian).
6. Tolstoguzov, N. (1992). *Shema karbotermicheskogo vosstanovlenija kremnija. Tsvetnaya metallurgiya* (5th ed.). Izvestija vuzov. (in Russian).
7. Nemchinova, N. (2013). *Termodinamicheskoe modelirovanie pri izuchenii karbotermicheskogo processa poluchenija kremnija*. IrGTU. (in Russian).
8. Ragulina, R., & Emlin, B. (1972). *Jelektrotermiya kremniya i silumina*. Metallurgiya. (in Russian).
9. Katkov, O. (1994). Izvlechenie kremnija pri vyplavke kvarcitov v dugovyh elektropechah Cvetnaja metallurgiya. *Izv.Vuzov*. (in Russian).
10. Abdurakhmanov, B., Ashurov, H., Kurbanov, M., & Nuraliev, U. (2014). Modernization of the technology for obtaining technical silicon for solar energy. *Applied Solar Energy, 50*, 282–286.
11. Tolstoguzov, N., et al. (1996). *Sposob vyplavki vysokokremnistogo ferrosilicija i tehnicheskogo kremniya*. Patent RU 2068008.
12. Zavilopulo, A., Mikita, M., Mylymko, A., & Shpenik, O. (2013). Ionizacija i dissociativnaja ionizacija molekul metana. *Zhurnal tehnichesko fiziki, 9*, 8–14. (in Russian).
13. Sposob poluchenija kremnija. *Avtorskoye svidetelstvo*. USSR, 1579014, kl. S01 B 33/02.
14. Abdurahmanov, B., Ashurov, H., Kurbanov, M., & Salihov, S. (2017). *Sposob poluchenija tehnicheskogo kremnija*. Patent UZ IAP 05440. (in Russian).
15. Ashurov, M., Ashurov, K., Kurbanov, M., & Abdurahmanov, B. (2013). Optimizatsiya karbotermicheskogo protsessa vyplavki tehnicheskogo kremniya. *Reports of the Academy of Sciences of Uzbekistan, 3*, 26–29. (in Russian).
16. Abdurahmonov, B., Ashurov, H., Kurbonov, M., & Salihov, S. (2015). *Sposob poluchenija ferrosilicija*. Patent UZ IAP 05557. (in Russian).
17. Kurbanov, M. (2018). Abstract of Doctoral Dissertation (DSc) on Technical Sciences "*Perfection of the technology of smelting of technical silicon and siliceous alloys*". Tashkent .
18. Abdurahmanov, B. (2021). Abstract of dissertation of the doctor of philosophy (Phd) on technical sciences "*Modernization of the electric arc process of silicon reduction and creation of electronic devices based on it*". Tashkent.
19. Monsenm, B., Kolbeinsen, L., Prytz, S., Myrvagnes, V., & Tang, K. (2014). Possible use of natural gas for Silicon or Ferrosilicon production CONFERENCE 2013. In *Proceeding of the thirteenth International Ferroalloys Congress, Efficient technologies in ferroalloy industry* (pp. 467–478).
20. Chernjahovskij, L. (2014). Metallurgicheskiy kremniy iz shihtovih briketov. In *CONFERENCE Kremniy– 2014, Aktualniye problemi fiziki, materialovedeniya, tehnologii kremnija, nanometrovyh struktur i priborov na ego osnove* (Vol. 1, pp. 27–30) (in Russian).
21. Chernjahovskij, L. (2001). *Rol vodoroda v karbotermicheskom vosstanovlenii metallov* (4th ed.). Tsvetnye metally. (in Russian).

22. Gasik, M., Ljakishev, N., & Emlin, B. (1988). *Teorija i tehnologija proizvodstva ferrosplavov*. Metallurgija. (in Russian).

23. Zavilopulo, A., et al. (2013). Ionizastiya i dissotsiativnaya ionizatsiya molekul metana. *J. technicheskoy fiziki, 83*(9), 8–14. (in Russian).

24. Zavilopulo, A., et al. (2012). Osobennosti dissoziativnoy ionizatsii molekul metana. *Technicheskoy fiziki, 38*(20), 69–77. (in Russian).

25. Harchenko, V. (1976). *Voprosy jepitaksialnogo osazhdenija kremnija*. Fan. (in Russian).

26. Abdurahmanov, B., Pashkudenko, V., & Harchenko, V. (1976). *Kinetika rosta jepitaksialnyh sloev kremnija v uvlazhnennom vodorode*. Izvestija AN USSR. (in Russian).

27. Zadde, V., Stenin, V., & Strebkov, D. (2008). Patent RU 2385291. (in Russian).

28. Ashurov, M., Ashurov, K., Kurbanov, M., & Abdurahmanov, B. (2013). Optimizacija karbotermicheskogo processa vyplavki tehnicheskogo kremnija. *Reports of the Academy of Sciences of Uzbekistan, 1*(3), 26–29. (in Russian).

29. Abdurahmanov, B., Ashurov, H., & Kurbanov, M. (2019). *Sposob poluchenija tehnicheskogo kremnija i ustrojstvo dlja ego osushhestvlenija*. Patent UZ IAP 05986, Rasmij ahborotnoma. (in Russian).

30. Wei, L. (2016). Research on smelting process and submerged arc furnace for silico-calcium alloy. In *Proceedings of the 2nd 2016 International Conference on Sustainable Development (ICSD)* (Vol. 94, pp. 78–80). Atlantis Press. CONFERENCE 2016. (in Russian).

31. Afanas'ev, V., Gorohov, A., Gribov, B., Evdokimov, B., Zinov'ev, K., & Krasnikov, G. (2009). *Sposob poluchenija kremnija vysokoj chistoty*. Patent RU 2008114420/15 (in Russian).

32. Ashurov, M., Abdurahmanov, B., & Uskenbaev, D. (2009). Vosstanovlenie kremnija iz kremnezemnyh mineralov metodom prjamogo vysokochastotnogo plavlenija v holodnom kontejnere. *Reports of the Academy of Sciences of Uzbekistan, 5*(3), 32–34. (in Russian).

33. Kurbanov, M., Abdurahmanov, B., Ashurov, H., & Kim, E. (2016). Vozvrat melkodispersnyh othodov proizvodstva tehnicheskogo kremnija i ferrosilicija v tehnologicheskij process. In *Sbornik Tezisov XI Konferencii po aktualnom problemam fiziki, materialovedenija, tehnologii i diagnostiki kremnija, nanometrovyh struktur i priborov na ego osnove.*, "Kremnij – 2016", Conference 2016 (p. 87) (in Russian).

34. Abdurahmanov, B., Ashurov, M., Ashurov, H., Kurbanov, M., & Nuraliev, U. (2017). Povyshenie rentabel'nosti i jekologicheskoj chistoty proizvodstva tehnicheskogo kremnija i ferrosilicija. *Uzbekskij fizicheskij zhurnal, 19*(5), 314–322. (in Russian).

35. Abdurahmanov, B., Adilov, M., Ashurov, M., Ashurov, H., Kadyrov, A., Kurbanov, M., & Nuraliev, U. (2017). Puti povyshenija jekonomicheskih i jekologicheskih pokazatelej tehnologicheskih processov vyplavki tehnicheskogo kremnija i ferrosilicija. *Uchenye zapiski, 3*(42), 86–101. (in Russian).

36. Abdurahmanov, B., Ashurov, H., & Kurbanov, M. (2018). *Himiko-metallurgicheskiy peredel kremnezema v monosilanovoe syr'e dlja solnechnoj jenergetiki i nanoelektroniki*. Tashkent. (in Russian).

37. Abdurahmanov, B., Ashurov, H., Kurbanov, M., Ashurov, M., & Tuljaganov, S. *Sposob poluchenija tehnicheskogo kremnija*. Patent UZ. IAP 06836. (in Russian).

38. Pavlov, S., Snitko, J., & Pljuhin, S. (2001). Othody i vybrosy pri proizvodstve ferrosilicija. *Jelektrometallurgija, 4*(1), 22–28. (in Russian).

39. Lohova, N., Makarova, I., & Patramanskaja, S. (2002). *Obzhigovye materialy na osnove mikrokremnezema*. Bratsk. (in Russian).

40. Kurbanov, M., Nuraliev, U., & Kurbanov, S. (2018). Ispol'zovanie mikrokremnezema v tehnologii poluchenija kremnija i ferrosilicija. *Himija i himicheskie tehnologii, 1*(1), 8–12.

41. Ashurov, M., Abdurahmanov, B., Ashurov, H., & Kurbanov, M. (2017). Ispol'zovanie mikrokremnezema v tehnologicheskih processah vyplavki tehnicheskogo kremnija i ferrosilicija. *Reports of the Academy of Sciences of Uzbekistan, 2*(1), 24–27. (in Russian).

42. Abdurahmanov, B., Ashurov, H., & Kurbonov, M. (2017). *Sposob opredelenija optimal'nogo kolichestva mikrokremnezema v kremnezemnoj chasti briketiruemoj shihty dlja vyplavki tehnicheskogo kremnija ili ferrosilicija*. Patent UZ IAP 05998. (in Russian).

43. Shitikov, E., Strockij, V., & Gordeeva, E. (2008). Issledovaniye fiziko-mekhanicheskikh svoystv vysokoprochnogo betona s dobavkoy mikrokremnezema. *Tsniis, 3*(1), 41–48. (in Russian).
44. Abdurahmanov, B., & Kurbanov, M. (2021). (in Russian)). Karbotermichekij sintez nanoporoshkov karbida kremnija s ispol'zovaniem mikrokremnezema. *Uzbekskij fizicheskij zhurnal, 23*(1), 57–64. https://doi.org/10.52304/.v23i1.225
45. Kaprielov, S., Shejnfel'd, A., Gazizulin, V., & Voronov, J. (1992). Effektivniy put utilizasti ultradispersnikh produktov gazoochistki pechi. *Stal, 5*(1), 83–85. (in Russian).
46. Batrakov, V., Kaprielov, S., & Shejnfel'd, A. (1999). Modifizirovannie betony novogo pokoleniya. *Beton i zhelezobeton, 2*, 24–25. (in Russian).
47. Kaprielov, S., Shejnfel'd, A., Tverdostupov, A., & Telkov, J. (1990). Ispolzovanie otkhodov proizvodstva ferrosplavov. *Shahtnoe stroitel'stvo, 9*, 26–28. (in Russian).
48. Shikirjanskij, A., Fomin, G., Pogorelov, M., Ryss, M., & Kosachev, E. (1990). *Stroitel'niy rastvor. Avtorskoe svidetelstvo*. USSR 1323545C. (in Russian).
49. Milovanova, R., Semenova, V., & Chupina, A. (1991). *Stroitel'nyj rastvor. Avtorskoe svidetel-stvo*. USSR 637358C. (in Russian).
50. Karnauhov, J, & Sharova, V. (2002). *Syrevaya smes dlya izgotovleniya penobetona*. Patent RU 2056353. (in Russian).
51. Kashura, V., & Potapov, V. (2006). *Sposob polucheniya vodnikh silikatov*. Patent RU2320538 (in Russian).
52. Karnauhov, J., & Sharova, V. (1997). *Sposob polucheniya zhidkogo stekla*. Patent RU 2085489. (in Russian).
53. Rusina, V., & Tarasova, N. (2011). *Sposob polucheniya zhidkogo stekla*. Patent RU 2333890. (in Russian).
54. Abdurahmanov, B., Ashurov, M., Ashurov, H., Kurbanov, M., Nijazov, A., & Nuraliev U. (2019). *Sposob polucheniya zhidkogo stekla*. Patent UZ IAP 20190266. (in Russian).
55. Galevskij, G., Protopopov, E., & Temljancev, M. (2014). Ispol'zovaniye tekhnogennykh metallurgicheskikh otkhodov v tekhnologii karbida kremniya.Vestnik Kuzbasskogo GTU. *Metallurgija, 4*(104), 103–110. (in Russian).
56. Polyakh, O. (2014). Primenenie texnogennikh otxodov metallurgichesskich predpriytiy dlya proizvodstva karbida kremniya. *Izvestiya vuzov, Chernaya metallurgiya, 57*(8), 23–29. (in Russian).
57. Abdurahmanov, B., Nuraliev, U., Kurbanov, M., & Ashurov, H. (2021). *Sposob polucheniya mikro i nanorazmernyh poroshkov karbida kremnija i ustrojstvo dlja ego osushhestvlenija*. Patent UZ IAP 20210226. (in Russian).
58. Polyakh, O., & Rudneva, V. (2007). *Mikrokremnezem v proizvodstve karbida kremnija*. Nauka. (in Russian).

Reconfiguration of Distribution Network Considering Photovoltaic System Placement Based on Metaheuristic Algorithms

Thuan Thanh Nguyen , **Thang Trung Nguyen** , **and Cuong Viet Vo**

1 Introduction

Distribution network (DN) accounts for a large proportion of the power system. However, power loss on the DN also accounts for a high part of the total loss of the power system. This situation occurs because the DN is operated at low voltage level. Therefore, reducing power loss in order to improve the operational efficiency of the DN is always a matter of concern in the operation of the DN.

In order to reduce power loss, several techniques can be implemented such as raising operating voltage, increasing line cross section, compensating reactive power, installing distributed generation (DG), and transferring loads among lines. In which, the last technique mentioned above is one of the most effective solutions for reducing power loss on the DN without any costs. This technique is implemented by varying the power flow on the lines through opening and closing of the existing switches located on the lines to form radial operating structures. This process is often called reconfiguration of the DN (RDN). Although it is not expensive to invest

T. T. Nguyen (✉)
Faculty of Electrical Engineering Technology, Industrial University of Ho Chi Minh City, Ho Chi Minh City, Vietnam
e-mail: nguyenthanhthuan@iuh.edu.vn

T. T. Nguyen
Power System Optimization Research Group, Faculty of Electrical and Electronics Engineering, Ton Duc Thang University, Ho Chi Minh City, Vietnam
e-mail: nguyentrungtrang@tdtu.edu.vn

C. Viet Vo
Faculty of Electrical and Electronics Engineering, Ho Chi Minh City University of Technology and Education, Ho Chi Minh City, Vietnam
e-mail: cuongvv@hcmute.edu.vn

in equipment, the opening and closing of switches to find the optimal radial network structure is a complex problem with possible solutions of up to two powers of *n* for the DN with *n* switches. Therefore, finding an effective solving method to the RDN problem also attracted the attention of researchers and DN operators.

In addition, as aforementioned, installing DG is also an effective solution to improve the efficiency operation of the DN. Compared to RDN, installing DG is more expensive, but in the context of the depletion of fossil energy sources and the strong development of renewable energy sources. The appearance of DG on the DN is increasingly popular. Therefore, implementing RDN should consider the influence of DG location and capacity. In particular, the solution of combining RDN and optimal DG placement is one of the effective solutions to maximize the effectiveness of both solutions in improving the efficiency of the DN. However, this combination makes the problem even more complicated due to the variety of variables to be determined.

Merlin and Back were the first to propose the RDN problem and solve it by the discrete branch-and-bound method [1]. Civanlar et al. [2] used the switch exchange technique to determine the optimal radial network configuration for power loss reduction. Both the discrete branch-and-bound and switch exchange techniques are based on the heuristic technique that is relied on knowledge and experience in operation of the DN. These methods often face many challenges in finding the globally optimal solution and dealing with constraints. Meanwhile, these limitations can be overcome by using metaheuristic methods for RDN problem. Therefore, in recent years, many methods based on metaheuristic algorithms have been applied to the RDN problem such as genetic algorithm (GA) [3–5], particle swarm optimization (PSO) [6–9], improved harmony search (IHS) [10], enhanced sine–cosine algorithm (ESCA) [11], improved whale optimization approach (IWOA) [12], coyote optimization algorithm (COA) [13], group search optimization (GSO) [14], modified marine predators optimizer (MMPO) [15], modified symbiotic organisms search (MSOS) [16], and the combination of the exchange market algorithm and wild goats algorithm (EMA-WGA) [17].

For the combined problem of RDN and DG placement, it is mainly solved by the metaheuristic-based methods because of the simplicity in description and constraints. There are a number of recent works that have solved the combined problem of RDN and DG placement by metaheuristic-based approaches such as salp swarm algorithm (SSA) [18], fireworks algorithm [19], intersect mutation differential evolution [20], and sine–cosine algorithm [21].

In this chapter, the details of applying the recent metaheuristic algorithm namely golden jackal optimization (GJO) and the well-known algorithm namely PSO for the simultaneous RDN and photovoltaic system placement (RDN-PVSP) problem are presented. GJO is developed based on the idea of the hunting behavior of the golden jackals, wherein the search phases of GJO are relied on prey searching, enclosing, and pouncing behaviors [22]. PSO is one of the most popular optimization algorithms based on swarm intelligence that takes the idea from food searching behavior of birds [23]. GJO and PSO are applied to search the optimal open switches as well

as optimal location and peak power of PV system (PVS) to minimize power loss of two test DNs.

The structure of this study can be organized as follows: Section 1 reviews the RDN-PVSP problem and existing approaches. Section 2 mentions the output power of PVS, the main goal, and the related constraints of the RDN-PVSP problem. Section 3 describes how the GJO and PSO methods are applied for the RDN-PVSP problem. Section 4 analyzes and discusses the results in different test systems. Finally, the conclusion is presented in Sect. 5.

2 Model of the RDN-PVSP Problem

2.1 Power Generation of PVS

The solar irradiance affects the output power of PVS. The irradiance distribution at time t can be described by the beta PDF as follows [24–26]:

$$f_{\text{PDF}}\left(S^t\right) = \begin{cases} \frac{\Gamma\left(a^t+b^t\right)}{\Gamma(a^t)\Gamma(b^t)}\left(S^t\right)^{\left(a^t-1\right)}\left(1-S^t\right)^{\left(b^t-1\right)}; 0 \leq S^t \leq 1, a^t, b^t \geq 0 \\ 0 \qquad\qquad\qquad\qquad\qquad\qquad ; \text{otherwise} \end{cases}$$

(1)

where S^t is the solar irradiance in kw/m^2 at time t, $f_{\text{PDF}}(S^t)$ is the distribution of the irradiance at time t, and a^t and b^t are defined by the mean (ρ^t) and standard deviation (ϑ^t) of irradiance at time t as follows:

$$b^t = \left(1-\rho^t\right)\left(\frac{\rho^t\left(1+\rho^t\right)}{\left(\vartheta^t\right)^2}-1\right)$$

(2)

$$a^t = \frac{\rho^t b^t}{1-\rho^t}$$

(3)

The continuous PDF at time t is divided into sub-states to find the PVS output power (P_{PVS}). The P_{PVS} is determined by the probability of all possible sub-states as follows:

$$P_{\text{PVS}} = \sum_{i=1}^{K} \mu_i\left(S_i^t\right) P_{\text{PVS}p} S_{m,i}^t$$

(4)

where K is the number of possible irradiance states, $S_{m,i}^t$ is the mean irradiance of the state i at time t, $P_{\text{PVS}p}$ is the peak power of PVS that is defined as (5), and $\mu_i\left(S_i^t\right)$ is the probability of irradiance that belongs to the range of $\left[S_{1,i}^t, S_{2,i}^t\right]$ that is defined as (6).

$$P_{\mathrm{PVS}p} = \eta_{\mathrm{PVS}}.F_{\mathrm{PVS}} \tag{5}$$

$$\mu_i\left(S_i^t\right) = \int_{S_{1,i}^t}^{S_{2,i}^t} f_{\mathrm{PDF}}\left(S_i^t\right) d\left(S_i^t\right) \tag{6}$$

where η_{PVS} and F_{PVS} are the efficiency and area of the PVS, respectively.

2.2 The Main Objective of the RDN-PVSP

Power loss reduction is considered as one of main objectives in operating the DN due to its high portion in the total loss of the power system [27]. Thus, the objective function of the RDN-PVSP is to reduce power loss. It is defined as follows:

$$\Delta P = 3\sum_{i}^{n_l} |I_i|^2 R_i \tag{7}$$

where ΔP is the total loss of the DN, n_l is the number of branches, I_i is the current through branch i, and R_i is the resistor of branch i.

2.3 The Constraints of the RDN-PVSP Problem

Radial topology: The RDN process has to maintain the radial topology of the DN. It is formulated as follows [28, 29]:

$$|\mathrm{determinant}(C)| = 1 \tag{8}$$

where C is a matrix that represents the connection of the DN.

Power balance:

$$\begin{cases} P_G + \sum_{i=1}^{n_{\mathrm{PVS}}} P_{\mathrm{PVS},i} = P_{\mathrm{LOAD}} + \Delta P \\ Q_G + \sum_{i=1}^{n_{\mathrm{PVS}}} Q_{\mathrm{PVS},i} = Q_{\mathrm{LOAD}} + \Delta Q \end{cases} \tag{9}$$

where $P_G + jQ_G$ is the complex power of the grid, $P_{\mathrm{PVS},i} + jQ_{\mathrm{PVS},i}$ is the complex ouput power of the PVS i, and $P_{\mathrm{LOAD}} + jQ_{\mathrm{LOAD}}$ and $\Delta P + j\Delta Q$ are the load and power loss of the DN.

Voltage and current limits: The bus voltage and branch current of the DN have to be in the allowed ranges:

$$\begin{cases} V_D \leq V_j \leq V_U \\ I_i \leq I_{U,i} \end{cases} \tag{10}$$

where V_j is the voltage amplitude of bus j with $j = 1, 2, \ldots, n_b$, n_b is the number of buses, $[V_D, V_U]$ is the allowed boundary of the voltage, and I_i and $I_{U,i}$ are the current and the allowed values of branch i.

Furthermore, in order to ensure that the installation of PVS does not affect other DNs, total output power of PVSs does not exceed the total load and losses of the DN. This is mathematically formulated as follows:

$$\sum_{i=1}^{n_{PVS}} P_{PVS,i} \leq P_{LOAD} + \Delta P \tag{11}$$

3 Optimal Solution Searching Method for the RDN-PVSP Problem

3.1 Application of GJO for the RDN-PVSP Problem

Step 1. Generating the Current Population of RDN-PVSP Candidates In GJO, each solution is considered as a prey. Similar to other metaheuristic algorithms, to search the optimal solution, the initial prey population is generated randomly as follows:

$$R_{i,j} = R_{\min,j} + \theta_1 \left(R_{\max,j} - R_{\min,j} \right) \tag{12}$$

where $R_{i,j}$ is the variable j with $j = 1, 2, \ldots, D$ of prey i with $i = 1, 2, \ldots, N$; $[R_{\min,j}, R_{\max,j}]$ is the boundary of variable j; D and N are the number of variables of each prey and the population size, respectively; and θ_1 is the random number in [0,1].

Each solution of the RDN-PVSP problem includes three variable types consisting of open switch, PVS placement location, and its peak power. The variables indicating the open switch and PVS placement location are represented by integer numbers, while the variables indicating the PVS peak power are represented by real numbers. Thus, to map the RDN-PVSP problem, the current prey population needs to be modified as follows:

$$R_{i,j} = \begin{cases} f_r \left(R_{i,j} \right); j \leq n_{sw} \\ f_r \left(R_{i,j} \right); n_{sw} + 1 \leq j \leq n_{sw} + n_{PVS} \\ R_{i,j} \qquad ; \text{otherwise} \end{cases} \tag{13}$$

where n_{sw} is number of open switches to form the radial topology of the DN and f_r is the round function.

To evaluate the fitness of each prey, the parameter of the DN is updated. The open switch variables are used to remove the corresponding branches from the branch data. The PVS peak power variables are used to estimate the PVS output power as (4). Then, the PVS placement location and the PVS output power are used to update the bus data of the DN. If the radial topology constraint in (8) is satisfied, the power flow using the Newton method integrated in MATPOWER [30] is used to calculate the load flow. If the power balance is ensured, the objective function, voltage, and current limits as well as total output power limit of PVSs are integrated to the fitness function as follows:

$$
F_i = \Delta P_i + k_p \left(\sum_{j=1}^{n_b} \max\left(V_j - V_U, 0\right) + \sum_{j=1}^{n_b} \max\left(V_D - V_j, 0\right) \right.
$$
$$
\left. + \sum_{i=1}^{n_l} \max\left(K_{I,i} - 1, 0\right) + \max\left(\sum_{i=1}^{n_{PVS}} P_{PVS,i} - P_{LOAD} - \Delta P_i, 0\right) \right)
$$
$$
(14)
$$

where F_i is the fitness value of prey i, $K_{I,i}$ is the load-carrying factor of branch i, and k_p is the penalty constant.

After calculating the fitness value of each prey, the two best preys in the population are considered to position the male and female jackals, wherein the male one stands in front of the female one.

The hunting process of jackals can be divided into two stages including searching and enclosing prey. In searching the prey, the male jackal usually leads and the female one follows. Other individuals move to these two individuals. While enclosing prey, jackals often harass and make the prey weak before they pounce. In JGO, based on these behaviors, the exploration mechanism based on searching for prey and the exploitation mechanism based on enclosing prey are equipped to find the optimal solution. The choice of either mechanism is based on the escaping energy level of the prey, which is defined as follows:

$$
E = 1.5\,(2\theta_2 - 1)\left(1 - {}^t\!/_T\right) \tag{15}
$$

where E is the escaping energy of prey, θ_2 is the random number in [0,1], and t and T are the current and maximum number of iterations.

The value of the escaping energy of the prey in Fig. 1 shows that in the earlier iterations, the prey has a high escaping energy level, and this value decreases in the later iterations. When the prey has a high escaping energy level, jackals will have to search for them, and when the prey has a low energy escaping level, they will be surrounded and destroyed. The details of the prey searching and enclosing process are presented as the below steps.
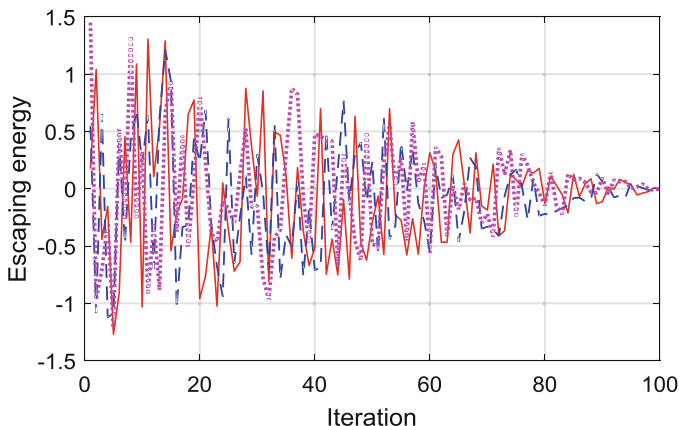
Fig. 1 Escaping energy of the prey over 100 iterations in three runs

Step 2. Searching the Prey If the prey has a high escaping energy level, jackals will have to search for them. In nature, the male jackal leads the hunting process, and it is followed by the female one. Furthermore, jackals can smell and follow the prey. Based on this metaphor, the exploration of GJO is formed as follows:

$$R_{1,i}^t = R_M^t - E\left|R_M^t - \alpha L\left(\beta\right) R_i^t\right| \tag{16}$$

$$R_{2,i}^t = R_{FM}^t - E\left|R_{FM}^t - \alpha L\left(\beta\right) R_i^t\right| \tag{17}$$

where $R_{1,i}^t$ and $R_{2,i}^t$ are the male and female jackal positions compared to the current prey R_i^t; R_M^t and R_{FM}^t are the male and female jackal positions, respectively, at the current iteration; L is the levy distribution coefficient that is used to formulate the movement of the prey; α is the scale factor that is often set to 0.05; β is the constant that is selected to 1.5; and R_i^t is the prey i.

Step 3. Enclosing the Prey Jackals harass the prey to reduce the prey's escaping energy. Then, jackals enclose and pounce on the prey. This action of jackals is modeled as follows:

$$R_{1,i}^t = R_M^t - E\left|\alpha L\left(\beta\right) R_M^t - R_i^t\right| \tag{18}$$

$$R_{2,i}^t = R_{FM}^t - E\left|\alpha L\left(\beta\right) R_{FM}^t - R_i^t\right| \tag{19}$$

In the above equations, the term $\alpha L(\beta)$ prevents jackals from moving rapidly toward the prey. This helps GJO to exploit the search space.

Step 4. Update New Position of the Prey The prey positions are updated based on the new positions of the male and female jackals as follows:
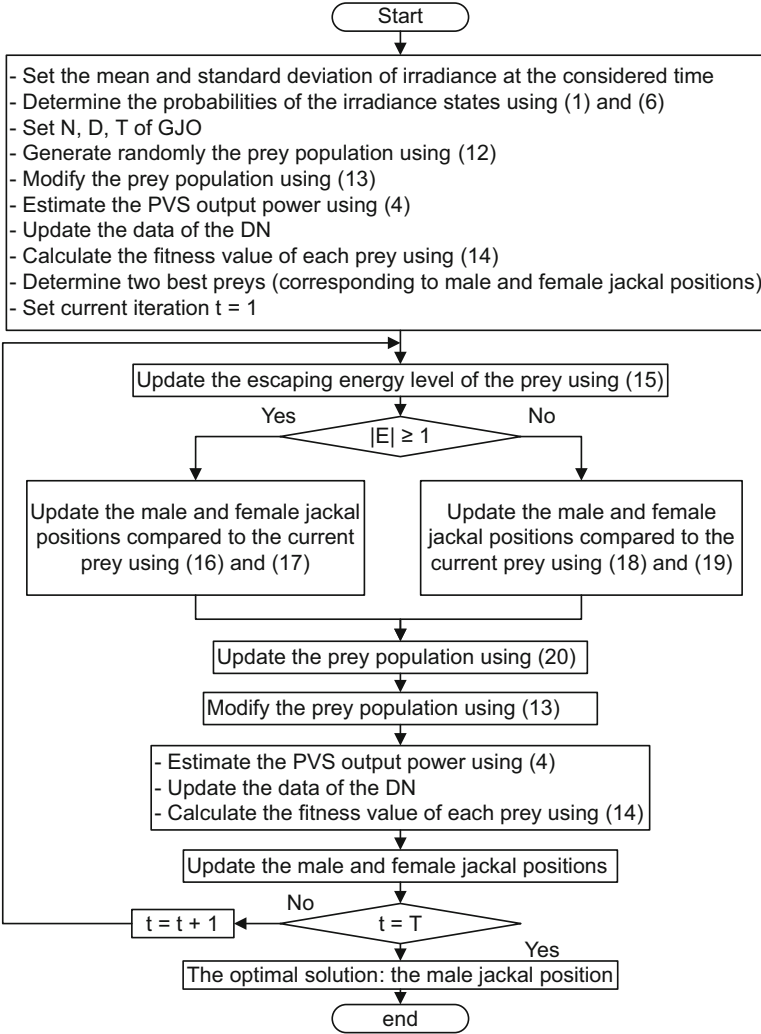
Fig. 2 Flowchart of the RDN-PVSP method based on GJO

$$R_i^{t+1} = \left(R_1^t + R_2^t \right) / 2 \tag{20}$$

After the updated position, the prey population is modified to map with the RDN-PVSP problem by using (13). Then each solution validated the fitness value by using (14). Finally, the two best solutions for the current population are used to update the male and female jackal positions. The steps for solving the RDN-PVSP problem based on GJO are presented in Fig. 2.

3.2 The RDN-PVSP Method Based on PSO

Based on GJO's search mechanisms, it can be seen that GJO's search process relies on information of the leading individuals. This idea is similar to that of PSO. PSO is one of the most popular optimization algorithms based on swarm intelligence that takes the idea from food searching behavior of birds [23]. While PSO updates the warm position relying on the current positions and the leader of the whole population, GJO relies on the current positions and two leaders of the population. Therefore, in this chapter the performance of GJO for the RDN-PVSP problem will be compared with that of PSO. In PSO, the position of each particle is considered as a candidate solution to the optimization problem. Details of PSO for the RDN-PVSP problem are implemented as follows:

Step 1. Generating the Current Population of RDN-PVSP Candidates The generation of the initial population of PSO for the RDN-PVSP problem is similar to that of GJO. Firstly, the population is generated and modified using (12) and (13). Then the fitness value of each solution is evaluated using (14). Finally, the best solution for population (R_{gbest}) is determined.

Step 2. Update the Current Population The moving velocity of each particle depends on the best position of the population and the best experience itself. It is mathematically modeled as follows:

$$V_i^{t+1} = wV_i^t + C_1\theta_3\left(R_{\text{best},i}^t - R_i^t\right) + C_2\theta_4\left(R_{\text{gbest}}^t - R_i^t\right) \tag{21}$$

where V_i^{t+1} and V_i^t are the velocity of the next and current iterations; C_1 and C_2 are, respectively, the cognitive and social factors which are selected to 2; θ_3 and θ_4 are the random numbers in [0, 1]; $R_{\text{best},i}^t$ and R_{gbest}^t are the best position of each particle and the warm; and w is the initial weight that is defined as follows:

$$w = w_{\max} - (w_{\max} - w_{\min})^t\big/T \tag{22}$$

where $w_{\max}$ and $w_{\min}$ are the highest and lowest weights, respectively.

The new position of the population is updated as follows:

$$R_i^{t+1} = R_i^t + V_i^{t+1} \tag{23}$$

After the updated positions, the particle population is modified to map with the RDN-PVSP problem using (13). Then each solution validated the fitness value using (14). Then, the best position of each particle is updated as follows:

$$R_{\text{best},i}^{t+1} = \begin{cases} R_i^{t+1}; \text{if } F_i < F_{\text{best},i}^t \\ R_{\text{best},i}^t; \text{otherwise} \end{cases} \tag{24}$$

```
                              ( Start )
                                  │
  ┌───────────────────────────────────────────────────────────────────────┐
  │ - Set the mean and standard deviation of irradiance at the considered time │
  │ - Determine the probabilities of the irradiance states using (1) and (6)  │
  │ - Set N, D, T of PSO                                                       │
  │ - Generate randomly initial particle population using (12)                │
  │ - Modify the particle population using (13)                               │
  │ - Estimate the PVS output power using (4)                                  │
  │ - Update the data of the DN                                               │
  │ - Calculate the fitness value of each particle using (14)                 │
  │ - Determine the best particle                                             │
  │ - Assign initial particle position to the current best position of each particle │
  │ - Set current iteration t = 1                                             │
  └───────────────────────────────────────────────────────────────────────┘
                                  │
      ┌───────────────────────────┴─────────────────────────────┐
      │  ┌──────────────────────────────────────────────────┐    │
      │  │ Update the velocity of each particle using (21)   │    │
      │  └──────────────────────────────────────────────────┘    │
      │                         │                                 │
      │    ┌─────────────────────────────────────────────────┐   │
      │    │ Update the position of each particle using (23)  │   │
      │    └─────────────────────────────────────────────────┘   │
      │                         │                                 │
      │      ┌──────────────────────────────────────────┐        │
      │      │ Modify the population using (13)          │        │
      │      └──────────────────────────────────────────┘        │
      │                         │                                 │
      │  ┌──────────────────────────────────────────────────┐    │
      │  │ - Estimate the PVS output power using (4)         │    │
      │  │ - Update the data of the DN                       │    │
      │  │ - Calculate the fitness value of each particle using (14) │
      │  └──────────────────────────────────────────────────┘    │
      │                         │                                 │
      │  ┌──────────────────────────────────────────────────┐    │
      │  │ Update the current best particle position using (24) and (25) │
      │  └──────────────────────────────────────────────────┘    │
      │                         │                                 │
      │  ┌──────────────────────────────────────────────────┐    │
      │  │ Update the best particle position of the whole population │
      │  └──────────────────────────────────────────────────┘    │
      │                         │                                 │
      │                        No                                 │
  ┌─────────┐          ◇───────────────◇                         │
  │ t = t+1 │◄─────────│    t = T      │                         │
  └─────────┘          ◇───────────────◇                         │
      └────────────────────────│                                 
                              Yes                                
              ┌──────────────────────────────────────┐          
              │ The optimal solution: the best particle │        
              │ position of the whole population       │          
              └──────────────────────────────────────┘          
                                  │
                              ( end )
```

Fig. 3 Flowchart of the RDN-PVSP method based on PSO

$$F_{\text{best},i}^{t+1} = \begin{cases} F_i; & \text{if } F_i < F_{\text{best},i}^t \\ F_{\text{best},i}^t; & \text{otherwise} \end{cases} \tag{25}$$

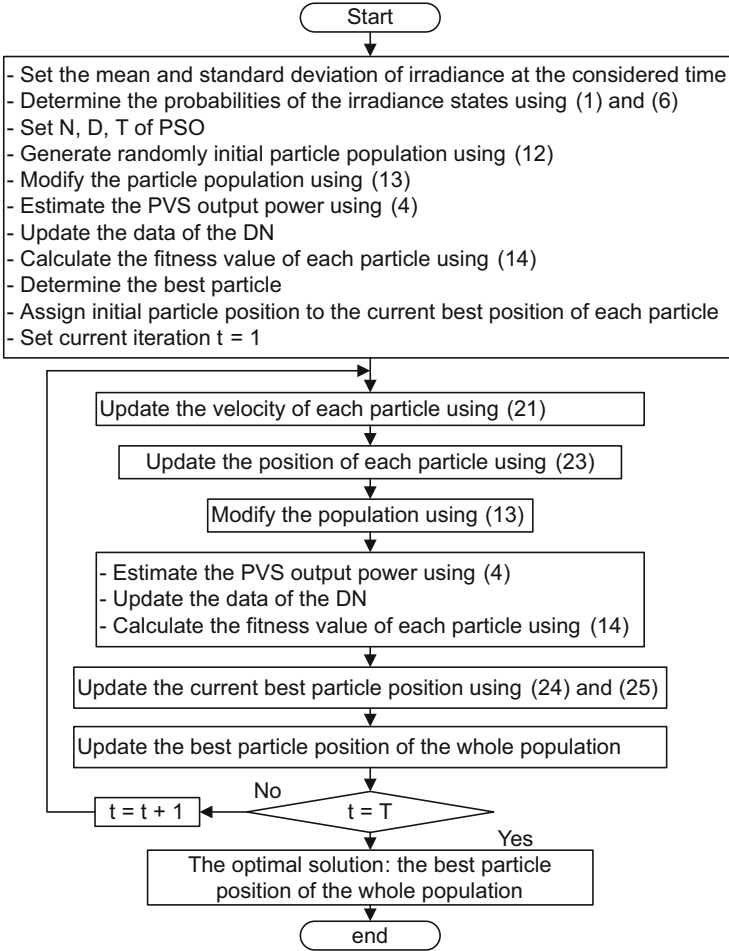Finally, the best position of the population is updated. The steps for solving the RDN-PVSP problem based on PSO are presented in Fig. 3.

4 Simulation Results and Discussion

In this section, in order to validate the performance of GJO and PSO for the RDN-PVSP problem, the standard 33-buses and 69-buses DNs are used to search the optimal open switches, PVS location, and PVS power. Both GJO and PSO are coded in the MATLAB software. For each DN, three cases are considered in terms of power loss, voltage, and current profiles as follows:

Case 1: Initial status
Case 2: Reconfiguration of DN (RDN)
Case 3: Reconfiguration of DN and PVS placement (RDN-PVSP)

For the three cases, case 1 shows the current radial status of the DN, and case 2 presents that the DN is only reconfigured and is applied for determining the optimal radial DN without PVS placement, while case 3 is applied for searching for the optimal radial DN and optimal PVS placement. For case 2, the control parameters of GJO and PSO consisting of population size, dimension, and maximum number of iterations are chosen to be 20, 5, and 100, respectively. For case 3, they are respectively set to 30, 11, and 1000. The lower V_D and upper V_U voltage amplitudes are chosen to be 0.95 and 1.05 pu, respectively.

In order to determine the output power of PVSs, it is assumed that the irradiance at the PVS installation area is split into states consisting of 0–0.2, 0.2–0.4, 0.4–0.6, 0.6–0.8, 0.8–1.0 kW/m^2 and the mean irradiance at this area at the considered time is 0.610 kW/m^2 with standard deviation of 0.273 kW/m^2. The probabilities of the irradiance states relying on the beta PDF according to (1) and (6) are shown in Fig. 4. The efficiency of PVS is chosen to be 0.186. The number of PVS is limited to three for each DN. The installed area for each PVS is in the range of [1000, 20,000] m^2 corresponding to the peak power of each PVS obtained by (5) in the range of [0.186, 3.72] MW.
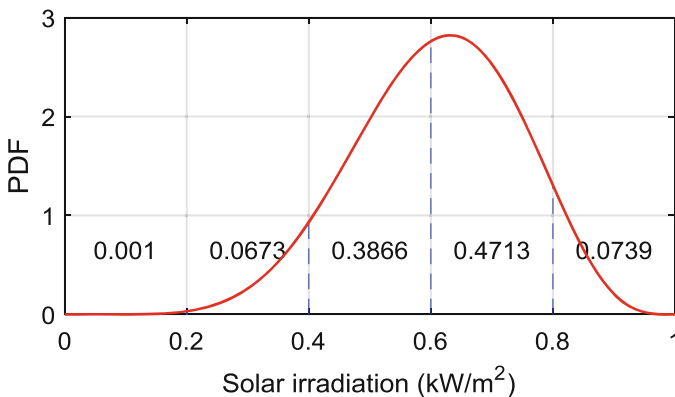

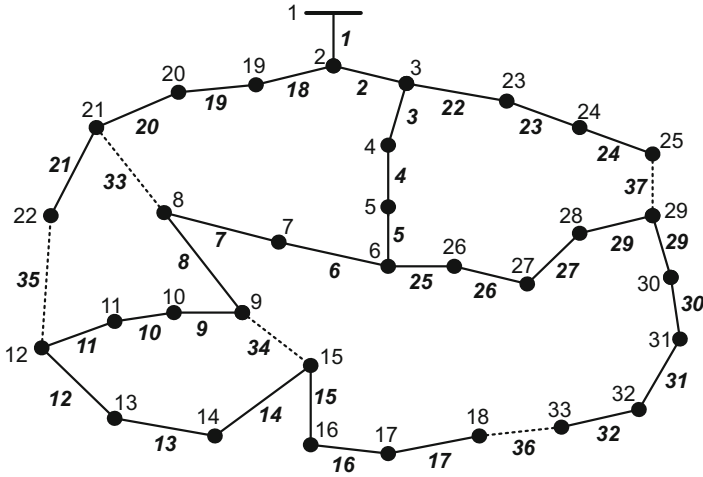**Fig. 4** The beta PDF corresponding to solar irradiance states

Fig. 5 The 33-buses DN

4.1 The 33-Buses DN

The 33-buses DN with a single-line diagram in Fig. 5 has a voltage level of 12.66 kV, 37 branches, and 5 open switches. The DN's parameters are taken from [31].

Table 1 presents the calculated results of GJO and PSO for the 33-buses DN. In the case 1, power loss is 202.6863 kW, and the minimum voltage amplitude (V_{min}) is 0.9131 pu that is 0.0369 lower than the allowed lower voltage limit. In addition, the maximum current-carrying factor (K_{Imax}) is also 0.0518 higher than the allowed value.

The performance of RDN in case 2 has helped to reduce significantly power loss. The power loss has been reduced to 62.704 kW from 202.6863 to 139.9823 kW that corresponds to a reduction of 30.94%. Furthermore, V_{min} and K_{Imax} are also improved compared to those of the case 1. The K_{Imax} value has been reduced from 1.0518 to 1.0361 pu corresponding to a reduction of 1.49% compared to that of case 1. The V_{min} is increased to 3.08% compared to that of case 1, and it is only 0.0088 pu lower than the allowed lower voltage limit.

By performing the optimal RDN-PVSP using GJO, the power loss is reduced from 202.6863 to 50.7745 kW. Thus, the power loss is reduced by 151.9118 kW, corresponding to a reduction of about 74.95% of the original power loss. The maximum load-carrying factor is also significantly reduced from 1.0518 to 0.5643 pu corresponding to a reduction of 46.35% compared to that of case 1. In addition, the lowest node voltage amplitude has also improved by 6.79% compared to that of case 1. The optimal solution obtained by GJO in case 2 is exactly the same with that of GSO [14] and MSOS [16]. Compared to IHS [10], ESCA [11], and EMA-WGA [17], although the power loss obtained by GJO is higher than 0.4323 kW, the

Table 1 The optimal results of GJO and PSO for the 33-buses DN

Case	Method	Open switches (switch number)	Location of PVS (at node's number)	Peak power of PVS (MW)	Power loss (kW)	Maximum current factor (pu)	Minimum voltage (pu)	Maximum voltage (pu)
Case 1	–	33-34-35-36-37	–	–	202.6863	1.0518	0.9131	1.0
Case 2	GJO	7-14-9-32-28	–	–	139.9823	1.0361	0.9412	1.0
	PSO	7-14-9-32-28	–	–	139.9823	1.0361	0.9412	1.0
	GSO [14]	7-14-9-32-28	–	–	139.9823	–	0.9412	–
	MSOS [16]	7-14-9-32-28	–	–	139.9823	–	0.9412	–
	IHS [10]	7-9-14-32-37	–	–	139.55	–	–	–
	ESCA [11]	7-9-14-32-37	–	–	139.55	–	0.9378	–
	EMA-WGA [17]	7-9-14-32-37	–	–	139.55	–	–	–
Case 3	GJO	33-34-11-31-28	18, 25, 7	1.1860, 2.1046, 1.5561	50.7745	0.5643	0.9751	1.0
	PSO	33-10-8-36-28	15, 7, 25	1.1699, 1.2933, 2.5617	54.8008	0.5574	0.9699	1.0

lowest node voltage amplitude obtained by GJO is 0.0034 pu higher than the above methods.

The comparison between case 2 and case 3 shows that RDN-PVSP brings superior efficiency compared to RDN. The reduction in power loss in case 3 is 44.01% higher than in case 2. The maximum load-carrying factor is 44.86% lower than that of case 2, while the lowest node voltage amplitude is increased by more than 3.71% compared to that of case 2. As shown in Fig. 6, the node's voltage has been significantly improved after implementing RDN and RDN-PVSP, wherein RDN-PVSP gives better efficiency than RDN. Figure 7 shows that the load-carrying coefficients of most branches in the system have been significantly reduced after implementing RDN and RDN-PVSP, wherein RDN-PVSP gives better reduction than RDN. This result shows the effectiveness of RDN-PVSP in improving the capacity of the DN.

The comparison results between GJO and PSO in Tables 1 and 2 show that in case 2, both GJO and PSO have found the optimal configuration of 7-14-9-32-28 as shown in Table 1, but the statistical results obtained in 30 runs presented in Table 2 show the superiority of GJO over PSO. In particular, the maximum, mean,
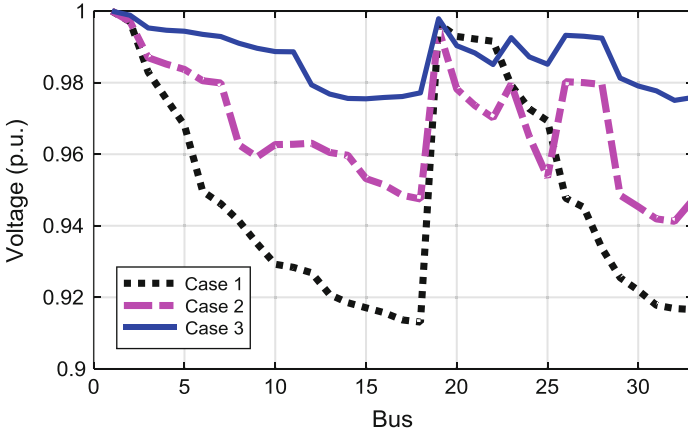
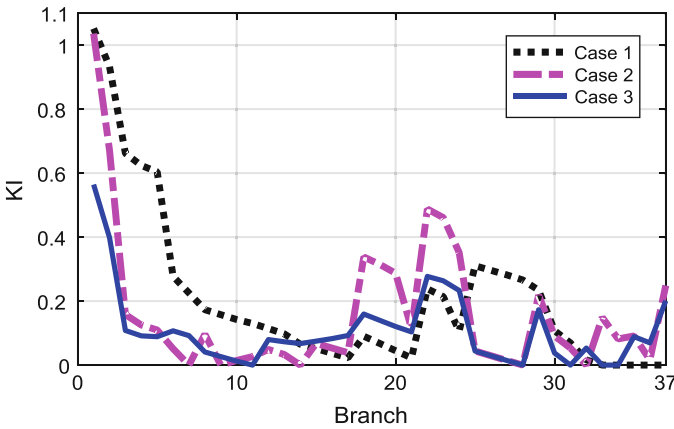**Fig. 6** The voltage amplitude profile of the 33-buses DN

Fig. 7 The current amplitude profile of the 33-buses DN

and standard deviation of the GJO's fitness values are lower than those of PSO. In addition, the execution time of GJO is also lower than that of PSO. In case 3, the obtained results in Table 1 show that the optimal solution obtained by GJO includes open switches of 33-34-11-31-28 and PVSs with peak capacity of 1.1860, 2.1046, and 1.5561 MW installed at the nodes of 18, 25, and 7, respectively. This solution helps to reduce the power loss on the system to 50.7745 kW corresponding to a reduction of 74.95% compared to that of case 1. Meanwhile, the solution obtained by PSO causes a loss of 54.8008 kW corresponding to a reduction of 72.96% compared to that of case 1. This reduction is 1.99% lower than that of GJO. Similar to case 2, the statistical values obtained by GJO in Table 2 for case 3 are lower than those of PSO. In addition, the execution time of GJO is also lower than that of PSO. The average convergence characteristics and fitness values in each run for the

Table 2 The statistical results of GJO and PSO for the 33-buses DN

Case	Method	F_{max}	F_{min}	F_{mean}	STD_F	T_{run} (s)
Case 2	GJO	249.357	205.8525	216.3236	10.2219	5.4536
	PSO	426.2957	205.8525	263.525	46.4197	5.9057
Case 3	GJO	70.9231	50.7745	58.2917	4.5602	73.8417
	PSO	74.23	54.8008	61.1421	4.2983	95.9516
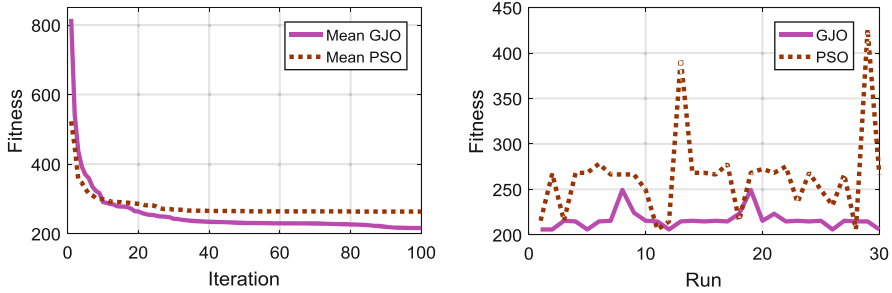
Fig. 8 The convergence characteristic of GJO and PSO for the 33-buses DN in case 2
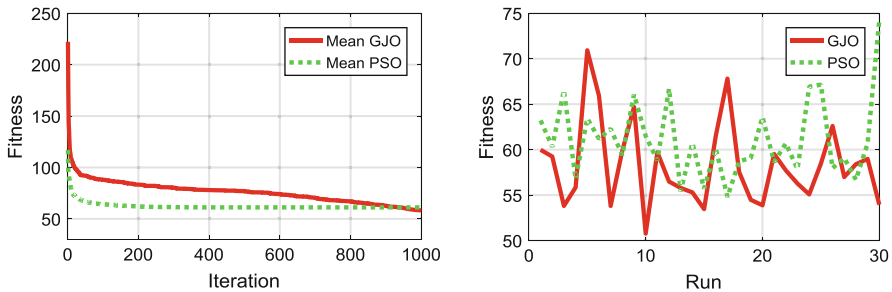
Fig. 9 The convergence characteristic of GJO and PSO for the 33-buses DN in case 3

two cases in Figs. 8 and 9 show that in each iteration GJO usually converges to a better value than PSO and, in each execution, GJO also often finds the better result than PSO. Figure 10 shows that the distribution of fitness values found in 30 runs of GJO is lower than that of PSO and the range of fitness values obtained by GJO is narrower than that of PSO for both cases.

4.2 The 69-Buses DN

The 69-buses DN with a single-line diagram in Fig. 11 has a voltage level of 12.66 kV, 73 branches, and 5 open switches. The DN's parameters are taken from [32].
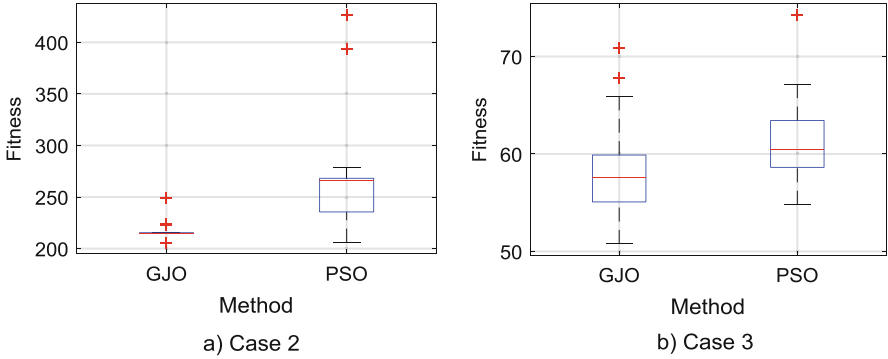
a) Case 2   b) Case 3

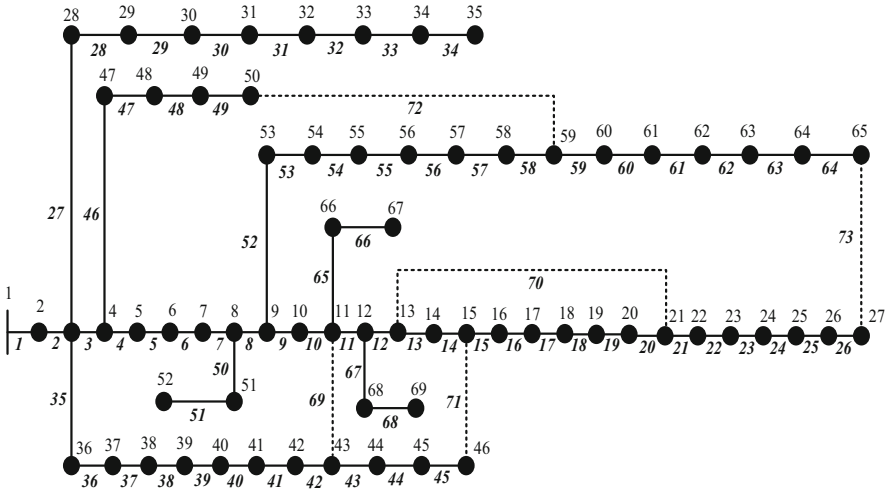**Fig. 10** The box plot of GJO and PSO for the 33-buses DN

Fig. 11 The 69-node distribution network

Table 3 shows the results of GJO and PSO for the 69-buses DN. In case 1, power loss is 224.8871 kW, and V_{min} and K_{Imax} are respectively 0.9092 and 1.2413 pu. Both indexes are out of permitted ranges. After the performance of RDN, power loss has been reduced to 126.2996 kW from 224.8871 to 98.5875 kW that corresponds to a reduction of 56.16%. Furthermore, V_{min} and K_{Imax} are also improved compared to those of the case 1. The K_{Imax} value has been reduced from 1.2413 to 1.2137 pu corresponding to a reduction of 2.22% compared to that of the case 1. The V_{min} is increased to 4.43% from 0.9092 to 0.9495 pu compared to that of case 1.

By performing the optimal RDN-PVSP using GJO, the power loss is reduced from 224.8871 to 35.9526 kW. Thus, the power loss is reduced by 188.9345 kW, corresponding to a reduction of about 84.01% of the original power loss. The maximum load-carrying factor is also significantly reduced from 1.2413 to 0.7514

Table 3 The optimal results of GJO and PSO for the 69-buses DN

Case	Method	Open switches (switch number)	Location of PVS (at node's number)	Peak power of PVS (MW)	Power loss (kW)	Maximum current factor (pu)	Minimum voltage (pu)	Maximum voltage (pu)
Case 1	–	69-70-71-72-73	–	–	224.8871	1.2413	0.9092	1
Case 2	GJO	69-70-14-57-61	–	–	98.5875	1.2137	0.9495	1
	PSO	69-70-14-57-61	–	–	98.5875	1.2137	0.9495	1
	IWOA [12]	14-58-61-69-70	–	–	98.5952	–	–	–
	COA [13]	69-70-14-57-61	–	–	98.5875	–	0.9495	–
	GSO [14]	14-56-61-69-70	–	–	98.59	–	0.9498	–
	ESCA [11]	14-55-61-69-70	–	–	98.6	–	0.9495	–
	MSOS [16]	14-57-61-69-70	–	–	98.5875	–	0.9495	–
	EMA-WGA [17]	14-56-61-69-70	–	–	98.59	–	0.9498	–
Case 3	GJO	69-70-13-57-61	10, 61, 27	1.1216, 2.3544, 0.9036	35.9526	0.7514	0.9814	1
	PSO	69-70-12-55-61	27, 61, 12	0.9393, 2.3512, 0.186	37.499	0.8167	0.9813	1

pu corresponding to a reduction of 39.47% compared to that of case 1. In addition, the lowest node voltage amplitude has also improved by 7.94% compared to that of case 1. The power loss obtained by GJO in case 2 is similar to that of COA [13], MSOS [16], ESCA [11], GSO [14], and EMA-WGA [17] and slightly lower than that of IWOA [12].

Similar to the results of the 33-buses DN, the comparison between case 2 and case 3 shows that RDN-PVSP brings superior efficiency compared to RDN. The reduction in power loss in case 3 is 27.85% higher than in case 2. The maximum load-carrying factor is 37.24% lower than that of case 2, while the lowest node voltage amplitude is increased by more than 3.51% compared to that of case 2. Figure 12 shows that the node's voltage has been improved after implementing RDN and RDN-PVSP, wherein RDN-PVSP gives better improvement than RDN. As shown in Fig. 13, the load-carrying coefficients of the branches gained by RDN-PVSP have been more improvement than that of RDN. This result once again confirms the effectiveness of RDN-PVSP in improving the capacity of the DN.
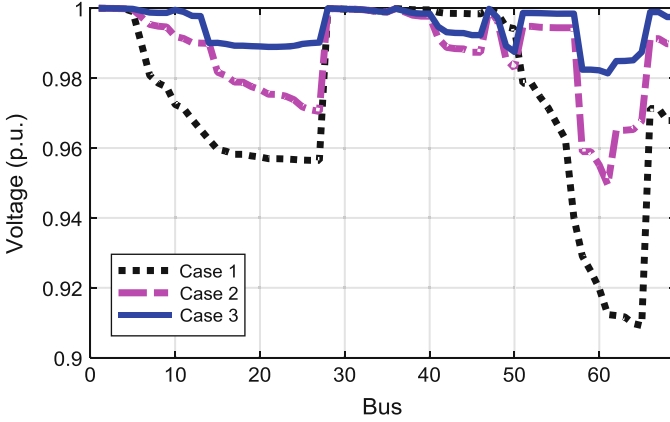
Fig. 12 The voltage amplitude profile of the 69-buses DN
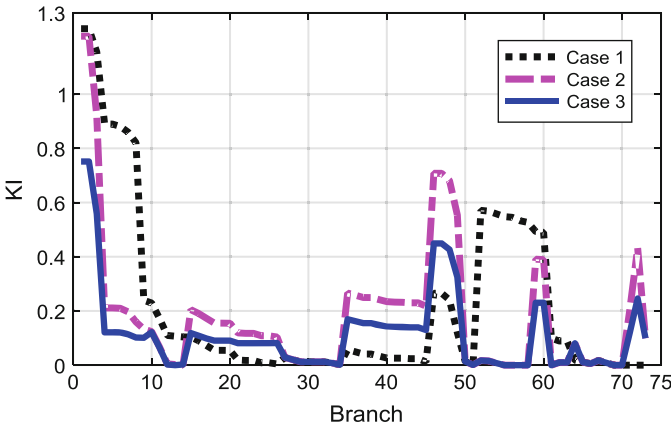

Fig. 13 The current amplitude profile of the 69-buses DN

The comparisons between GJO and PSO for the 69-buses are also shown in Tables 3 and 4. For case 2, the statistical results obtained in 30 runs in Table 4 show the superiority of GJO over PSO, though both GJO and PSO have found the optimal configuration of 69-70-14-57-61 as shown in Table 3. In particular, the maximum, mean, and standard deviation of the GJO's fitness values are lower than those of PSO. For case 3, the obtained results in Table 3 show that the optimal solution obtained by GJO includes open switches of 69-70-13-57-61 and PVSs with peak capacity of 1.1216, 2.35444, and 0.90356 MW installed at the nodes of 10, 61, and 27, respectively. This solution helps to reduce the power loss on the system to 35.9526 kW corresponding to a reduction of 84.01% compared to that of case 1. Meanwhile, the solution obtained by PSO causes a loss of 37.4990 kW corresponding to a reduction of 83.33% compared to that of case 1. This reduction

Table 4 The statistical results of GJO and PSO for the 69-buses DN

Case	Method	F_{max}	F_{min}	F_{mean}	STD_F	T_{run} (s)
Case 2	GJO	556.742	526.4962	541.3005	9.8107	19.0839
	PSO	667.7074	526.4962	595.8009	60.9617	18.9557
Case 3	GJO	72.9126	35.9526	44.4622	6.1116	247.7562
	PSO	76.2899	37.499	47.9712	10.4536	325.0729
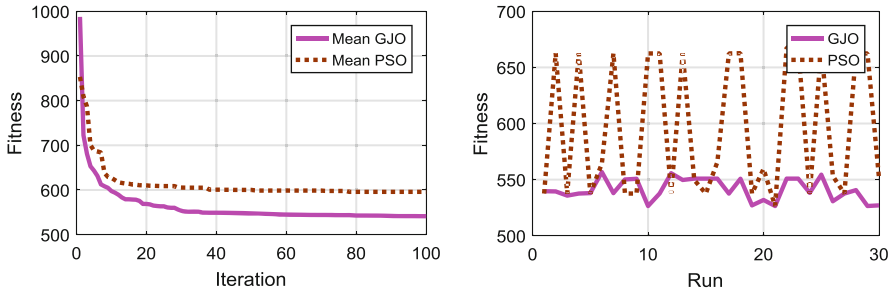
Fig. 14 The convergence characteristic of GJO and PSO for the 69-buses DN in case 2
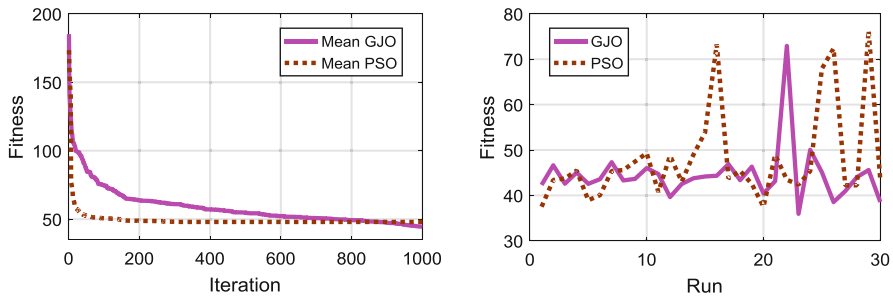
Fig. 15 The convergence characteristic of GJO and PSO for the 69-buses DN in case 3

is 0.69% lower than that of GJO. Similar to case 2, the statistical values obtained by GJO in Table 4 for case 3 are lower than those of PSO. In addition, the execution time of GJO is also lower than that of PSO. The average convergence characteristics and fitness values in each run for the two cases in Figs. 14 and 15 show that in each iteration GJO usually converges to a better value than PSO and, in each execution, GJO also often reaches a better result than PSO. Figure 16 shows that the distribution of fitness values found in 30 runs of GJO for the 69-buses DN is lower than that of PSO and the range of fitness values obtained by GJO is narrower than that of PSO for both cases.
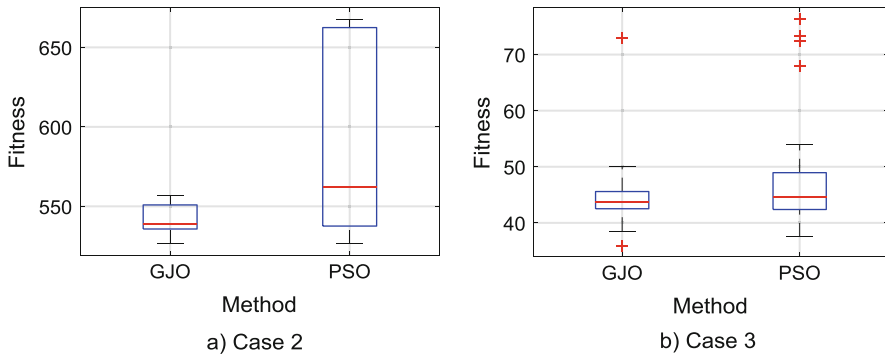
Fig. 16 The box plot of GJO and PSO for the 69-buses DN

5 Conclusion

In this chapter, the application of the recently developed GJO for the RDN-PVSP to minimize power loss of the DN is successfully presented. The efficiency of GJO is compared with the well-known PSO on two test DNs including the 33-buses and 69-buses. For each test DN, three cases consisting of the initial state, RDN only, and RDN-PVSP are considered. The simulated results show that the RDN-PVSP is more powerful than RDN in reducing power loss and improving the voltage and current profiles of the DN. For two test DNs, the power loss reduction of the RDN-PVSP is 44.01% and 27.85%, respectively, higher than that of RDN only. The compared results between GJO and PSO on both of the test DNs show that GJO outperforms PSO for the RDN and RDN-PVSP problem in terms of the final optimal solution and the statistical results. The comparisons with other methods also lead to GJO reaching the optimal solution for the considered problems. Therefore, GJO can be an effective method for the RDN and RDN-PVSP problems.

References

1. Merlin, A., & Back, H. (1975). Search for a minimal loss operating spanning tree configuration in an urban power distribution system. In *Proceeding in 5th power system computation conference (PSCC), Cambridge, UK* (Vol. 1, pp. 1–18).
2. Civanlar, S., Grainger, J. J., Yin, H., & Lee, S. S. H. (1988, July). Distribution feeder reconfiguration for loss reduction. *IEEE Transactions on Power Delivery, 3*(3), 1217–1223.
3. Zhu, J. Z. (2002). Optimal reconfiguration of electrical distribution network using the refined genetic algorithm. *Electric Power Systems Research, 62*(1), 37–42.
4. Ganesh, V., Sivanagaraju, S., & Ramana, T. (2009). Feeder reconfiguration for loss reduction in unbalanced distribution system using genetic algorithm. *International Journal of Electrical and Electronics Engineering, 3*(12), 754–762.
5. Subburaj, P., Ramar, K., Ganesan, L., & Venkatesh, P. (2006). Distribution system reconfiguration for loss reduction using genetic algorithm. *Journal of Electrical Systems, 2*(4), 198–207.

6. Kumar, K. K., Venkata, N., & Kamakshaiah, S. (2012). FDR particle swarm algorithm for network reconfiguration of distribution systems. *Journal of Theoretical and Applied Information Technology, 36*(2), 174–181.

7. Khalil, T. M., & Gorpinich, A. V. (2012). Reconfiguration for loss reduction of distribution systems using selective particle swarm optimization. *International Journal of Multidisciplinary Sciences and Engineering, 3*(6), 16–21.

8. Abdelaziz, A. Y., Mekhamer, S. F., Mohammed, F. M., & Badr, M. A. L. (2009). A modified particle swarm technique for distribution systems reconfiguration. *The Online Journal on Electronics and Electrical Engineering (OJEEE), 1*(1), 121–129.

9. Othman, A. M., El-Fergany, A. A., & Abdelaziz, A. Y. (2015). Optimal reconfiguration comprising voltage stability aspect using enhanced binary particle swarm optimization algorithm. *Electric Power Components and Systems, 43*(14), 1656–1666.

10. dos Santos, M. V., Brigatto, G. A., & Garcés, L. P. (2020). Methodology of solution for the distribution network reconfiguration problem based on improved harmony search algorithm. *IET Generation, Transmission and Distribution, 14*(26), 6526–6533.

11. Raut, U., & Mishra, S. (2021). Enhanced sine–cosine algorithm for optimal planning of distribution network by incorporating network reconfiguration and distributed generation. *Arabian Journal for Science and Engineering, 46*(2), 1029–1051.

12. Abd Elazim, S. M., & Ali, E. S. (2020). Optimal network restructure via improved whale optimization approach. *International Journal of Communication Systems, 34*(1), 1–15.

13. Nguyen, T. T., Nguyen, T. T., Nguyen, N. A., & Duong, T. L. (2020). A novel method based on coyote algorithm for simultaneous network reconfiguration and distribution generation placement. *Ain Shams Engineering Journal, 12*(1), 665–676.

14. Teimourzadeh, H., & Mohammadi-Ivatloo, B. (2020). A three-dimensional group search optimization approach for simultaneous planning of distributed generation units and distribution network reconfiguration. *Applied Soft Computing Journal, 88*, 106012.

15. Shaheen, A. M., Elsayed, A. M., El-Sehiemy, R. A., Kamel, S., & Ghoneim, S. S. M. (2022). A modified marine predators optimization algorithm for simultaneous network reconfiguration and distributed generator allocation in distribution systems under different loading conditions. *Engineering Optimization, 54*(4), 687–708.

16. Thanh Nguyen, T., Ngo, T.-Q., Duong, T. L., & Nguyen, T. T. (2021). Finding radial network configuration of distribution system based on modified symbiotic organisms search. *Complexity, 2021*, 1–23.

17. Jafari, A., Ganjeh Ganjehlou, H., Baghal Darbandi, F., Mohammdi-Ivatloo, B., & Abapour, M. (2020). Dynamic and multi-objective reconfiguration of distribution network using a novel hybrid algorithm with parallel processing capability. *Applied Soft Computing Journal, 90*, 106146.

18. Sambaiah, K. S., & Jayabarathi, T. (2019). Optimal reconfiguration and renewable distributed generation allocation in electric distribution systems. *International Journal of Ambient Energy, 2019*, 1–29.

19. Mohamed Imran, A., Kowsalya, M., & Kothari, D. P. (2014). A novel integration technique for optimal network reconfiguration and distributed generation placement in power distribution networks. *International Journal of Electrical Power and Energy Systems, 63*, 461–472.

20. Khodabakhshian, A., & Andishgar, M. H. (2016). Simultaneous placement and sizing of DGs and shunt capacitors in distribution systems by using IMDE algorithm. *International Journal of Electrical Power and Energy Systems, 82*, 599–607.

21. Raut, U., & Mishra, S. (2020). An improved sine–cosine algorithm for simultaneous network reconfiguration and DG allocation in power distribution systems. *Applied Soft Computing Journal, 92*, 106293.

22. Chopra, N., & Mohsin Ansari, M. (2022, July). Golden jackal optimization: A novel nature-inspired optimizer for engineering applications. *Expert Systems with Applications, 198*, 116924.

23. Kennedy, J., & Eberhart, R. C. (1995). Particle swarm optimization. In *Proceedings of ICNN'95 – international conference on neural networks* (pp. 39–43).

24. Ansari, M. M., et al. (2020). Considering the uncertainty of hydrothermal wind and solar-based DG. *Alexandria Engineering Journal, 59*(6), 4211–4236.
25. Fakharian, A., Sedighizadeh, M., & Khajehvand, M. (2021). Optimal operation of unbalanced microgrid utilizing copula-based stochastic simultaneous unit commitment and distribution feeder reconfiguration approach. *Arabian Journal for Science and Engineering, 46*(2), 1287–1311.
26. Selim, A., Kamel, S., Jurado, F., Lopes, J. A. P., & Matos, M. (2020, September). Optimal setting of PV and battery energy storage in radial distribution systems using multi-objective criteria with fuzzy logic decision-making. In *IET generation, transmission & distribution* (pp. 1–14).
27. Mahesh, K., Nallagownden, P., & Elamvazuthi, I. (2017). Optimal placement and sizing of renewable distributed generations and capacitor banks into radial distribution systems. *Energies, 10*(6), 811.
28. Abdelaziz, A. Y., Mohamed, F. M., Mekhamer, S. F., & Badr, M. A. L. (2010). Distribution system reconfiguration using a modified Tabu search algorithm. *Electric Power Systems Research, 80*(8), 943–953.
29. Thanh Nguyen, T., Nguyen, T. T., & Nguyen, N. A. (2020). Optimal network reconfiguration to reduce power loss using an initial searching point for continuous genetic algorithm. *Complexity, 2020*, 2420171.
30. Zimmerman, R. D., Murillo-Sanchez, C. E., & Thomas, R. J. (2011). MATPOWER: Steady-state operations, planning, and analysis tools for power systems research and education. *IEEE Transactions on Power Systems, 26*(1), 12–19.
31. Baran, M. E., & Wu, F. F. (1989). Network reconfiguration in distribution systems for loss reduction and load balancing. *IEEE Transactions on Power Delivery, 4*(2), 1401–1407.
32. Chiang, H.-D., & Jean-Jumeau, R. (1990). Optimal network reconfigurations in distribution systems: Part 2: Solution algorithms and numerical results. *IEEE Transactions on Power Delivery, 5*(3), 1568–1574.

Technology of Secondary Cast Polycrystalline Silicon and Its Application in the Production of Solar Cells

A. L. Kadirov, B. M. Abdurakhmanov, H. B. Ashurov, and Valeriy Kharchenko (ORCID)

1 Introduction

The low density of solar radiation on the Earth's surface determines the high cost of electricity generated by solar photovoltaic stations (SPVS), since, in order to obtain practically significant capacities, it is necessary to collect and convert solar radiation from large areas, which is associated with both the cost of a large amount of expensive semiconductor materials and the need to develop and maintain high-performance industrial technologies for the manufacture of these materials and solar cells based on monocrystalline silicon (MS). The cost of electricity produced in this way is several times higher than the cost of electricity generated by traditional methods. This is the main reason hindering the development of large-scale silicon-based solar power industry.

In this regard, the attraction and expansion of the use of a non-traditional raw material base for the production of solar cells, including from the waste of raw and metallurgical silicon, such as, for example, the secondary cast polycrystalline silicon (SCPS) considered in this work, are coming to the fore [1, 2].

Attempts to obtain efficient cheap solar cells based on waste silicon production are constantly being made. Thus, solar cells made of polysilicon [3] obtained by the method of directed crystallization in a casting mold (with $\rho \sim 1$–10 Ohm·cm) have an efficiency of only 2–3%. The low efficiency of these solar cells is related to

A. L. Kadirov (✉)
PEI "Khujand State University named after Academician Babajan Gafurov", Khujand, Tajikistan

B. M. Abdurakhmanov · H. B. Ashurov
Institute of Ion-Plasma and Laser Technologies of the Academy of Sciences of the Republic of Uzbekistan, Tashkent, Uzbekistan

V. Kharchenko
Federal Scientific Agroengineering Center VIM, Moscow, Russian

157

the small grain size of polysilicon (~200 μm). Solar cells made of poly-Si, which was obtained by the Stepanov method [4], turn out to be more efficient by growing profiled crystals of p-type conductivity with ~0.8–3.0 Ohm.cm. Their efficiency is in the range of 5–10%.

We note in particular that in the manufacture of solar cells from profiled silicon, preliminary purification of the raw material is required, as a result of which alkali metal impurities are introduced into the substrate material, which increase the rate of carrier recombination. The maximum spectral sensitivity of the solar cells from this material lies in the region of 0.75–0.8 μm while for the solar cells from SCPS, as will be shown below, in the shorter wavelength region of the spectrum ~0.7 μm.

As for tape polycrystalline silicon (PS), although the efficiency of laboratory solar cells made of this material reaches 9% [5, 6], the cost indicators of 1 W of the generated energy turn out to be higher than those of SCPS. This is due to the fact that the tape PS is a super overstressed material that requires an additional operation for normal operation – thermal annealing for 1.5–2 h. Energy costs for this process also affect the cost of photoelectric energy released by such solar cells, and the efficiency of solar cells from strip Si [5], which have not undergone heat treatment, is only 5–6%.

A significant reserve for improving the quality of PS solar cells is the hydrogen passivation of the boundary charge states or the passivation of the recombination activity of the materialby the thermal method [7. Using this method, it is possible to achieve a significant increase in the mobility, lifetime, and diffusion length of charge carriers and, as a consequence, improve the characteristics of the solar cell.

Currently, the following methods of PS passivation are used: thermal annealing [6], thermal annealing in a hydrogen medium [8], acoustic stimulation [9], treatment with hydrogen ions in a hydrogen plasma of a glow discharge, and low-energy H^+ ion implantation, including using the Kaufman source [10].

In the commonwealth of independent states (CIS) countries, the ZTMK silicon laboratory in Zaporozhye was engaged in the manufacture of PS for solar cells on a pilot scale; there is a publication jointly with Rsearch and Poduction Asociation (RPA) Kvant. On a somewhat larger scale, PS for the same purposes, but using the Stepanov method, was carried out by RPA Saturn, Krasnodar. The production of solar cells at RPA Saturn was entirely dependent on the supply of initial silicon, the production of which was concentrated in Ukraine. The rupture of economic ties led to the cessation of these works.

As for the thermoelectric method of converting the thermal component of solar radiation, as well as geothermal heat and the heat of heated bodies, there is a significant gap in this issue in regional research and development, associated primarily with the lack of production facilities producing or processing traditional thermoelectric materials. It is important to note that within the framework of this work, for the first time, the issue of involving various modifications of silicon in the creation of thermal energy converters (TEC) and primarily those produced in the Republic of Tajikistan (RT) is raised.

This paper presents the scientific and practical results of obtaining and a comprehensive study of the electrophysical, photo- and thermal-voltaic properties

of cast PS from silicon production waste, solar cells and TEC based on it and the issuance on this basis of scientifically substantiated modes of manufacturing PS and solar cells, formulated in the form of technological recommendations for implementation at existing production facilities in the region, development of own regional production of technical silicon (TS) based on local raw materials, obtaining PS from the regional TS by analogy with the technology of cast PS, substantiation of the foundations for laying in the RT its own closed production of TS, PS and solar cells and TEC on their basis [1, 2].

2   Smelting, Composition, and Electrophysical Properties of SCPS

The introduction at the beginning of the twenty-first century of reverse technologies for gas phase production of raw Si by hydrogen reduction of trichlorosilane led to a sharp decrease in the cost of silicon and, accordingly, to a decrease in the price of solar electricity with a simultaneous increase in production volume. In this regard, the production of solar cells in the form of SCPS returned to its previous pace. The technology of smelting this material is presented, and variants of its application in the production of solar cells are described, with preference given to the option when SCPS is used as a material for the manufacture of heavily doped silicon substrates, and the base region of the TS is created in films grown on them from the gas phase with using the techniques of the aforementioned reverse technologies.

The task of further reducing the cost of solar cells for ground energy does not lose its relevance and causes the expansion of the use of polycrystalline silicon (PS) for these purposes instead of monocrystalline (MS); however, this transition, given the existing plans to increase the production of photovoltaic products, is in any case associated with the need to increase the production of TS [11, 12] and then raw Si electronic purity. In this regard, the serial production of solar cells based on PS, made from the inevitably proportionally increasing volumes of silicon waste that occurs at all stages of its production, as well as in the production of solar cells and electronic products (EP), is becoming increasingly important. In this case, naturally, there arise the problems of choosing the simplest and most cost-effective technology for the production of blanks for solar cells with an acceptable efficiency from such a raw material. It is known that this indicator for PS TS is somewhat inferior to that for MS TS, which is due to the recombination of charge carriers at the grain boundaries (GB) of PS. In [13], a comparison was made of the passivation efficiency of the recombination activity of impurity and defect centers and electronic states on GBs in PS samples fabricated by various methods, including such a variety of PS as SCPS manufactured by remelting waste raw silicon, MS, and epitaxy, and it was shown that hydrogen ions effectively passivate GBs and dislocation pileups, especially linear dislocations. Transition metal impurities, which are responsible for

reducing the lifetime of charge carriers, can also be passivated both in the volume of grains and at their boundaries.

In [2], based on the problem of increasing the profitability of the production of solar cells based on SCPS, the reasons for the spread in the characteristics of solar cells manufactured in a single cycle based on SCPS were discussed, and the dependence of the photovoltaic (PV) efficiency on the size of the initial plates from this material was established. It was shown that the decrease in the TS efficiency and the spread of its value in a batch are due to the presence in this type of multisilicon of specific structural defects that occur during direct casting, the number of which naturally increases with an increase in the area of a single TS. A number of other parameters and properties of solar cells from the TS PS, including its behavior under illumination with concentrated solar radiation (CSR), were studied in [14], where the first discovered effect of superlinear growth of the short circuit current, observed in the range of CSR 4–5 times at $P_\mathrm{o} = 850$ W/m^2, is reported.

Electrical, photo-, thermal, and thermoelectric, mechanical, and other properties of solar and thermal energy converters made on the basis of PS are explained by the microstructure and morphology of the GBs. A number of studies have been carried out, for example [15–17], where it is shown that the microstructure and morphology strongly depend on the technology for obtaining PS, on the properties of atoms of residual or specially introduced impurities, and also on the processes of their segregation. Therefore, a detailed study of the structure of GBs, the influence of technological factors of impurity atoms, and the determination of ways to control them is currently considered one of the priority tasks of science, which have direct access to the production of semiconductor devices.

The process of obtaining SCPS includes a number of operations similar to the production of silicon according to Czochralski. First of all, this is the preparation and assembly of melts - an operation that boils down to grinding proteins to sizes acceptable for loading into a crucible, and adding dopants, for example, in the case of obtaining secondary silicon for affected elements, the development of silicon doped with small acceptors, namely boron.

The serial production of solar cells based on SCPS can, in principle, be organized by involving the production of the latter, not only waste from the production of raw Si and raw MS but also EP. However, in this case, it is necessary to evaluate the feasibility of metallurgical processing of EP production waste in comparison with the direct use, for example, of substandard silicon single-layer epitaxial structures (SSLES) or substrates freed from the epitaxial layer, which are quite suitable for the manufacture of solar cells of the types p^+-n-n$^+$, n$^+$-p-p$^+$, or n$^+$-p, p$^+$-n [18]. When using n-n$^+$ structures prevailing in the production of SSLES, it is possible to predict the efficiency using a regression model [1, 19] and choose SSLES, on the basis of which to obtain solar cells with the simplest p-n junction and enlightenment with an efficiency of 8–13%, in some cases 15%, quite suitable for a complete set of household photovoltaic devices. Wastes from the production of EP from the operations of manufacturing integrated circuits and discrete semiconductor devices, representing the breakage of plates and structures, of course, should be subjected to metallurgical processing into PS or profiled silicon [2, 18, 20]. In this case, the

main and serious problems are created by waste sorting and chemical-metallurgical processing and processing of raw materials, which exclude the ingress of deep impurities such as Mo, W, Cr, Ag, Au, and Cu, used in integrated circuit technology, into PS. It is here that the experience and developments available in the field of purification of TS by purely metallurgical methods can be successfully applied to a level acceptable for use in photovoltaics, which will be discussed below. As a result of the experiments, we have developed a variant of the technological process for obtaining SCPS going to create solar cells, which includes the operations of preparing raw materials and ligatures, quartz graphite equipment, a mold body, and the process of casting silicon blocks.

The operation of preparing melts includes sampling p-type wastes from raw materials and MS production according to the thermo-electro driving force sign or using the three-probe method, as well as sampling wastes from the production of SSLES p-p$^+$ for doping the charge in order to obtain an ingot of SCPS with a specific resistance of a given nominal value.

Silicon ingots from the indicated raw materials were made by direct casting into graphite molds, followed by directional crystallization of the filled volume in vacuum or in vacuum with a small amount of inert gas flow. The directional crystallization of the melt in the mold was carried out from the bottom up due to the predominant heat removal through the graphite base of the mold and the creation of a thermal backwater to the melt mirror by the upper heating heater. Carrying out directional crystallization ensured the receipt of a columnar structure of manufactured blocks with a fineness of individual grains up to ~2 × 2 mm and without gas shells.

Schematically, the process of obtaining cast polysilicon can be described using the data of Fig. 1 as follows. Melting was carried out in a vacuum of $5 \cdot 10^{-2}$ mm. Hg using graphite directly heated heaters. After holding the melt in melting crucible 1 with heater 2, turning on heater 3 melted silicon plug 4 of sprue 5, and the melt flowed into mold 6 with heater 7. The melt crystallized layer by layer from the bottom of mold 6 to the free surface. The duration of exposure of the melt in the mold, i.e., in fact, the crystallization rate is one of the main technological characteristics of the process, since it determines the size of the polycrystal grains. The experimentally established optimal range of the duration of the melt exposure lies within 1.5–2 h, while the dimensions of individual grains are guaranteed to exceed 2 mm over the entire volume of the ingot [1, 2].

A specially prepared quartz crucible, which is based on a standard quartz crucible, usually used in the processes of obtaining Si according to Czochralski, was used as a container for melting the initial charge – silicon with alloy.

The melt is held until equilibrium crystals appear on the surface in the melting crucible ("frost"). After the appearance of "frost," the power on the "cork" melting heater gradually increases. Heating of the casting mold begins simultaneously with the heating of the loaded silicon raw materials using a heating heater and is carried out until the melt is poured into it while maintaining a rotation speed of ~2–5 rpm. For 2–3 min. Before pouring the melt, the heating heater is set to power corresponding to the mode of crystallization and determined empirically. After

Fig. 1 Scheme of the reactor unit of the melting plant
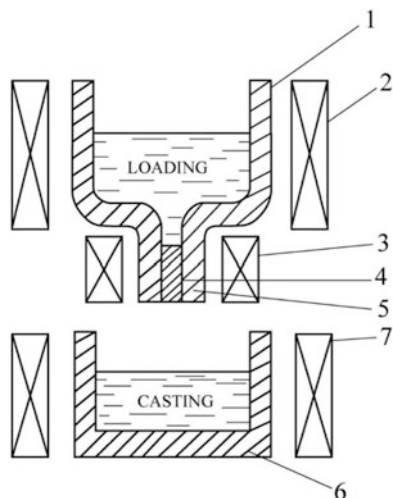
filling the volume of the mold with molten silicon, the power of the heating heater is increased above the power corresponding to the equilibrium state of the solid-liquid system. By controlling the power and visually observing the melt mirror, the poured melt is crystallized for ~2 h. After the end of the crystallization process, the casting is annealed at the same fixed power for at least 90 min.

After cooling, the ingot (Fig. 2) is removed from the mold and inspected to detect cracks and chips. Defective ingots are returned for remelting. Used graphite casting mold parts are cleaned from traces of the melt on the surface and transferred for reuse.

The efficiency of polycrystalline TS, which are also made from SCPS, generally depends on the content of residual impurities in the raw material, impurities transferred from the walls of the melting equipment, and material structure features, in particular, on the size of PS grains. These rather stringent requirements for raw materials limit the volumes of direct processing of waste to those in which, a priori, there are no impurities that give deep energy levels in silicon. In our opinion, the increase in waste processed in SCPS can be increased if we use the experience gained in the field of the conversion of TS by purely metallurgical methods into multisilicon in combination with the purification of such material to an impurity level of at least $10^{-3}\%$ in order to use it in production solar cells.

On Fig. 3 from [21] presents generalized data of various researchers [22–25], clearly showing how the presence of one or another impurity in the base region Si of a solar cell affects the efficiency of the solar cells.

From Fig. 3 follows that the influence of various impurities differs significantly, which is associated with the type and depth of occurrence, the energy levels they create, and in the case of the presence of metals such as tantalum, molybdenum, niobium, zirconium, tungsten or titanium in silicon, their concentration is already at
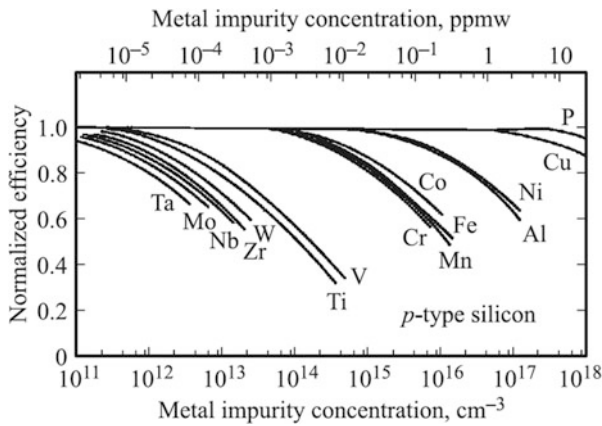
Fig. 2 Ready SCPS ingot in the fault

Fig. 3 Influence of the type and concentration of an impurity of one or another metal in silicon on the efficiency of Si solar cells [22–25]

the level 5.10^{12}–5.10^{14} cm^{-3} catastrophically reduces the efficiency of converting solar radiation into electricity.

There are a number of technologies, as well as scientific schools, that have developed them, offering purification of TS by metallurgical methods [26–30], zone melting of TS [30], remelting in solar furnaces [31], as well as hydrometallurgy methods, that is, by breaking the TS, mainly along GBs and subsequent chemical

etching of impurities from exposed GBs [32], where they were displaced by segregation during TS crystallization.

Thus, the refining of TS is known by release into settling tanks, where the melt is purified by blowing Cl, O_2, and Ar or by treatment with fluxes (Na_3AlF_6, NaCl) [33] by adding fluxes [34]. Numerous, original, and effective technological methods have been developed based on bubbling the FC melt with mixtures of gaseous chemical reagents and, thereby, removing significant amounts of impurities B, P, As, Al, and Ca and a number of other metals due to their entry into high-temperature reactions with the above gases and precipitation of the reaction product into slag or removal from the melt in the form of volatile chemicals [35]. Of great interest is the hydrometallurgical purification of silicon. It is based on the operations of grinding TS to a powder and its purification by etching in HCl. Since the physical phenomenon of segregation of impurities on the surface of grains during the crystallization of the melt is used here, two points are important: ensuring the crystallization of TS with a uniform grain size and ensuring its subsequent grinding mainly along the boundaries of these grains with exposure of the surfaces on which the impurities displaced by segregation are concentrated. If the first condition is difficult to fulfill, then the original TS is crushed to a particle size much smaller than the grain size, in practice up to 50 microns. The method makes it possible to reduce the Al content in TS to $3 \cdot 10^{-6}\%$, that is, to get rid of 75% of this impurity [32]. This method is also effective in the purification of TS from a number of other impurities harmful to solar cells [35], and the purification is facilitated by a decrease in the particle size of the TS powder, an increase in the process temperature, the choice of the optimal pressure and concentration of HCl, and the addition of oxidizing agents ($FeCl_3$ and $(NH_4)2S_2O_8$) [35]. It is possible to get rid of Ca by 66%, from Cr by 92%, by 27% from Fe, by 98% from Cu and Ni, impurities that have an extremely negative effect on the lifetime of charge carriers (CC) in a solar cell, and by 89% from the Zn impurity.

Purification of Ti is carried out [36] by treating the TS powder with a mixture of hydrofluoric (HF) and hydrochloric (HCl) acids, and the efficiency of the operation also increases with a decrease in the particle size of the TS powder, and Ti is removed by 97–99%.

Electrolytic refining of TS with a purity of 99.5% was carried out in an electrolyte of composition, mol.%: $CaCl_2$ (80–81) – NaCl (8–10) – CaO (5.0–8.5) – SiO_2 (2.5–5.0) at a temperature of 1130–1250 K. Si was deposited on the Mo cathode, the content of impurities which turned out to be several times less than in the feedstock, namely: Fe by 6.3 times; Al at 14.8; Ti at 29.7; B by 133; and P by 28 times [37].

The refining of TS is also carried out by the method of partial melting with the removal of the formed liquid phase by centrifugation [38]. At the same time, the Fe content decreases by 37 times; Ti 179 times; and Cu 14 times.

It is also possible to obtain, in a certain way, a mixture of silicon of electronic quality with purified TS (99.95%) [39]. Vacuum treatment of silicon melt TK (99.46%) using arc plasma allows it to be purified to purity (99.93%) [40]. Purification of TS [41] using microwave plasma is promising and productive. In [42], the purification of TS by electron beam melting, vacuum and oxidative refining, and

zone recrystallization is described, which led to an increase in electrical resistivity by a factor of 6, from 0.03 to 0.175 Ohm·cm. Other methods of crystallographic refining are also known.

It was shown in [42] that in one pass of the molten zone, it is possible to increase the purity of TS brand Kr 1 from 98.6% to 99.9%. And zone melting of TS with a purity (99.855%) [43] of an electron-beam furnace after the first pass of the zone led to an increase in the purity of silicon to 99.999%, and after the second pass, it increased by ten times, with a decrease in the content of C and O_2 by three and six times, respectively.

In [44], the distribution of O_2 and C in multisilicon smelted from TS was studied. It is shown that O atoms mainly occupy the interstices of the Si crystal lattice, but up to ~10^{16} cm^3 oxygen is present in the form of precipitates of the second SiO_2 phase. This silicon dioxide is displaced during crystallization at grain boundaries and is also concentrated near dislocations. Carbon sits inside grains up to concentrations determined by the solubility limit and, in the form of SiC, on GBs in complexes of the SiO_4 type and other impurities. O_2 and C worsen the solar cells' efficiency by 1–3% of the absolute value, due to the growth of the series resistance of the solar cells' consistent resistance and the reduction in the lifetime of the CC dissipated on the mentioned complexes. Note that so far we have considered the purification of silicon from impurities that give deep energy levels, the presence of which is most detrimental to solar cells. However, purification from them does not at all indicate the suitability of the obtained material for solar cells, since the most problematic impurity in Si is boron, the maximum content of which should not exceed 10^{17}–10^{18} cm^{-3}, which corresponds to the resistivity of the base of the solar cell ~0.5–1.0 Om.cm. It should be noted that boron was effectively removed from molten TS with moistened Ar or simply with water vapor, as well as with a mixture of Ar and H_2 [45]. A practically important result is achieved by chemical treatment of TS powder with a mixture of weak solutions of HNO_3 and H_2SO_4 acids at $T \sim 400$ K, which makes it possible to purify TS from boron to ~$4 \cdot 10^{-6}$%, as well as from alkali metals [46]. It was shown in [47] that slag (CaO – SiO_2 – LiF), being used in the processing of the TS melt at $T \sim 1720$ K, makes it possible to reduce the B content from $22 \cdot 10^{-6}$ to $1.3 \cdot 10^{-6}$%, i.e., to quite acceptable values for the solar cell base.

In conclusion, we note that after any of the described methods of purification of TS, its additional remelting into ingots, suitable in shape for the manufacture of blank plates for solar cells, is required. At the same time, MS and PS metallurgy wastes are introduced into the mixture, and the given electrophysical properties are imparted to the material by alloying with small impurities [1, 2].

It should also be noted that, unfortunately, the experience of metallurgical purification of TS and multisilicon based on it, which has been accumulated by scientists and specialists, described in this section, may not be in demand in practice. As was emphasized at the beginning of the book, the reason lies in the fact that at the beginning of the twenty-first century, reverse technologies [46, 47] were introduced at the operations of obtaining raw silicon from trichlorosilane, which led to a sharp decrease in prices for raw Si of electronic purity, and many, if not all technologies for purification of TS and multisilicon, turned out to be economically and energetically

uncompetitive. In our opinion, the prospect for these developments can be reopened if efforts are focused on obtaining by metallurgical methods not silicon suitable for creating the base region of a solar cell but silicon heavily doped with small impurities, which should be considered exclusively as a substrate material for solar cells with a deposited film base from the gas phase using reverse technologies. To assess the degree of suitability of the obtained SCPS for the production of solar cells, test structures with p-n transitions performed by diffusion or ion implantation were made from it, followed, on a number of samples, by hydrogen passivation and the deposition of antireflection coatings using standard technologies. Similarly, to illustrate the feasibility of the use of waste-based multisilicon proposed above, we fabricated p-p$^+$ and n-n$^+$ film structures using heavily doped SCPS substrates and gas phase epitaxy, in which p or n regions with a resistivity of ~1 ohm.cm were used as the base of the solar cells, making a p-n junction with a depth of ~1 μm, using the well-known methods indicated above [48].

In this case, when suppressing self-doping using traditional solutions [49] or the technology developed by us [47–50], the layer being grown, which is subsequently used as an n- or p-type TS base, inherits from the multisilicon substrate only the GBs and their orientation, that is, its poly or twin structure, and its electrical characteristics are determined exclusively by special alloying from the gas phase, that is, the influence of substrate impurities on the properties of the TS film base is minimized.

This is illustrated by the data in the table, which shows the characteristics of TSs made from various types of silicon, including SCPS, PS of various grain sizes, SSLES, film structures based on SCPS, and MS. Information is also given on the manifestation of the effect of a superlinear increase in the efficiency of solar cells when they are illuminated by CSR, on the effectiveness of using hydrogen passivation, applying an antireflection coating, and creating pulling electric fields in the body of the solar cell. It can be seen that, as a result of hydrogen passivation, the efficiency of solar cells from SCPS and PS of all types increases. This occurs due to the passivation of recombination centers on the GB by hydrogen. It is important to note that an indicator of the effectiveness of hydrogen passivation is the disappearance of the spectral characteristic, treated with hydrogen ions, solar cells of the region with a change in the polarity of the photocurrent. This section of the solar cells not treated with hydrogen is in the wavelength range of ~1.0–1.1 μm and higher, that is, at the edge of the spectral sensitivity Si solar cells, and is associated with the generation of CC with the participation of energy levels caused by GBs [51, 52]. It can also be seen from the table that the use of PS in the embodiment of the base region of the solar cells from it, firstly, requires deep cleaning of the TS, which is laborious and economically unprofitable, and secondly, such solar cells are always inferior in efficiency to solar cells with an electronic quality silicon base. Therefore, as will be shown again below, we propose to use PS obtained by metallurgical methods from TS, as well as SCPS, exclusively as a heavily doped substrate material, which makes it possible to manufacture TSs with an efficiency equal to that of solar cells based on SSLES from electronic quality Si at those the same electrical parameters of the base (Table 1).

Table 1 Efficiency and some properties of solar cells based on various types of silicon [49, 53]

№	Type of solar cells, electrophysical material characteristics, and manufacturing technology of the base area	Maximum efficiency value at AM 1.5	Presence of the effect of over-linear growth of short current during irradiation of CSR
1	n^+-p, PS base, p-type electronic quality, $\rho \sim 1$ Om cm	10–12	++
2	n^+-p-p$^+$, PS base, p-type electronic quality. The pulling field in the base is made by Al diffusion	11–13	++
3	n^+-p, large block PS base, p-type electronic quality, $\rho \sim 1$ ohm cm. Hydrogen passivation	11–14	–
4	n^+-p, SCPS base, p type, $\rho \sim 1$ Om cm	5–8	+++
5	n^+-p-p$^+$, SCPS base, p-type with back Al alloying	6–8	+++
6	n^+-p, SCPS base, p type, $\rho \sim 1$ ohm cm. Hydrogen passivation	8–9	–
7	n^+-p-p$^+$, p$^+$-SCPS doped to the solubility limit of Al and B, p-film base grown from the gas phase	12–13	+
8	n^+-p-p$^+$, p$^+$-SCPS doped to the solubility limit of Al and B, p-film base grown by gas phase deposition Hydrogen passivation	14	–
9	n^+-p-p$^+$, n^+-multisilicon obtained by repeated remelting of silicon production waste alloyed to the solubility limit of P and Sb, n-film base grown from the gas phase	12	+
10	n^+-p-p$^+$, n^+-multisilicon doped to the solubility limit of P and Sb, n-film base grown from the gas phase. Hydrogen passivation	13–14	–

3 Models for Calculating the Efficiency of Solar Cells in the Conditions of Mass Production

Predictive calculation of the efficiency of such solar cells, under the conditions of their mass production, can be carried out using a regression model, which was confirmed in practice.

$$K/K_o = 0.79 + 0.00026 \ (X_3) \ 2 – 0.03 \ X_1 X_2 X_3 – 0.0003 \ (X_1) \ 3 \tag{1}$$

Model (1) describes changes in efficiency (K) with varying independent variables: X_1 is the specific resistance of the film grown on multisilicon, that is, the solar cell base, the value of which is supposed to vary from 1 to 10 Om·cm; X_2 is the resistivity of the substrate, i.e., the multisilicon itself, which can be varied in

the range from 0.001 to 0.01 ohm·cm; and X_3 is the film base thickness within 20–50 µm. The K/K_o ratio was taken as the output parameter, where K is the efficiency of solar cells fabricated on the basis of film structures with a multisilicon substrate at 300 K before applying an antireflection coating and under illumination with a tungsten lamp with $W_o = 0.1$ W/cm^2, i.e., in standard conditions for testing workpieces Si solar cells in production, and K_o is its minimum allowable value under the specified measurement conditions.

It can also be seen from the table that the hydrogen passivation of the solar cells leads to the disappearance of the section of the superlinear increase in the short current, which occurs during the CSR of medium intensity (5–10 times) due to the effect of the recombination center destruction upon illuminating non-single-crystal TS CSR [14] within which, with active heat removal, the efficiency of solar cells made of poly- and multisilicon can be higher than that of monocrystalline ones.

A comparison of the radiation resistance of various types of solar cells showed that solar cells made of fine-grained polysilicon of electronic purity have the highest resistance to both X-ray radiation and irradiation with fast electrons, but their efficiency, according to the table, is minimal. The radiation resistance of solar cells based on SSLES made in the chlorosilane process on MS substrates of electronic purity is also high, but this is the case for solar cells with a multisilicon base, whether it is SCPS from raw materials pure in terms of impurities or from silicon obtained by remelting metallurgy waste with the addition of TS Kr00 according to Czochralski which is relatively low.

The resistance of solar cell-type n-n$^+$ with a film base with $d = 50$–60 µm, deposited in the chlorosilane process on large-block ($d_{grains} = 500$–1000 µm) substrates from heavily doped with a group of impurities (Sb, P, As) to the solubility limit of each, SCPS turns out to be higher than that of solar cells with a base of KSD-1 silicon widely used in solar cell technology for ground power, as in the case if the p-n junction is created by ion implantation of boron or if the p-n junction is created by thermal diffusion of boron; thus, the use of multisilicon-type SCPS as a substrate material for fabricating film structures for solar cells is much more expedient than using it as a material for fabricating the actual base region of solar cells. At the same time, the technology for obtaining blank structures for solar cells with a film base must be oriented from the very beginning to the use of recycled chlorosilane technologies [54–57], which have shown their highest economic efficiency in the processes of obtaining silicon of raw electronic purity and to methods close to them, developed by us [50] recycling of waste gas-vapor mixtures of epitaxial production.

From a comparison of the radiation resistance of various types of solar cells, it follows that it is the higher, the lower the concentration of boron impurity in the base material of p-type solar cells. But after all, the so-called photon degradation of solar cells with a p-type base manifests itself brighter and faster precisely in such solar cells. And it is caused, apparently, by the same physical reason – the occurrence in the base when exposed to light radiation for a sufficiently long time and when irradiated with charged particles or gamma quanta almost instantly, but depending on the dose of radiation. The question involuntarily arises: Is it possible to use the value of the solar cell radiation resistance, which can be estimated instrumentally

and fairly quickly, as an indicator in predicting the life of the solar cells, for which at present there are no methods other than calculation? The clarification of this question seems to be a very interesting engineering problem.

To control the process of group growth of films for the solar cell base from a computer, it is possible to successfully use the mathematical model of the growth rate, proven in practice, constructed by us by the method of experiment planning [51], which has the form in natural variables:

$$V = 0.5550582 + 0.4924768 \ 10^{-3} X_1 \ (X_2) \ 2 + 0.88611089 \ 10^{-7} X_2 \ (X_3) \ 2 \tag{2}$$

where X_1 is the flow rate of the vapor-gas mixture (VGM) ($H_2 + SiCl_4$) in the range of 60–120/min, covering the range of linear velocities of the VGM over the substrate surface in the range of 26.5–54 cm/s.

X_2-concentration of $SiCl_4$ in hydrogen is in the range of 1.37–2.28 vol.%, and X_3 is the substrate temperature in the range of 1300–1400 K. The proposed model (2) implements the Efroimson algorithm [52] and makes it possible to predict the layer growth rate in the range 0.8–1.2 µm/min while ensuring, according to the nomogram of the predominant occurrence of growth defects [53], the total density of defects arising in the process of growth is not higher than $10–10^2$ cm.

This model can also be used in relation to any technological equipment, provided that the same temperatures of the substrates, the same concentration of the silicon-containing component in the gas-vapor mixture, and the same linear velocity of the VGM flow over the surface of the substrates and exactly the same pressure in the reaction volume for film growth [49, 53] lying at the above flow rates of the gas-vapor mixture in the range of 110–120 kPa.

If it is necessary to grow layers at high rates, one can use the regression mathematical model (2), which describes the kinetics of growth of thick support layers of polycrystalline silicon in the chloride process, with an accuracy of ±15%, used in silicon structures with dielectric insulation.

$$V = -1.077–1.583 \cdot 10^{-7} \ X_1 X_2 X_3 –2.242 –10^{-6} \ X_3 + 3.972 \cdot 10^{-2} \ X_2 + 5.373 \cdot 10^{-4} \ X_3 \tag{3}$$

where X_1 is the deposition temperature 1240–1300 °C; X_2 is the hydrogen flow through the evaporator at a temperature of 20 °C, 60–100 l/min; and X_3 is the hydrogen flow in the main line 20, 60/min.

Model (3)[1] covers the range of $SiCl_4$ concentrations in VGM from 2% to 12% vol and makes it possible to predict the average growth rate of layers in a batch up

---

[1] According to the famous theoretical physicist, Professor A.S. Baltenkov [62], the regression coefficients in models 1 and 2 should be rounded off. In our opinion, this should not be done, since all calculations of the efficiency of a solar cell and the growth rate of its film are fundamental in the chloride process.
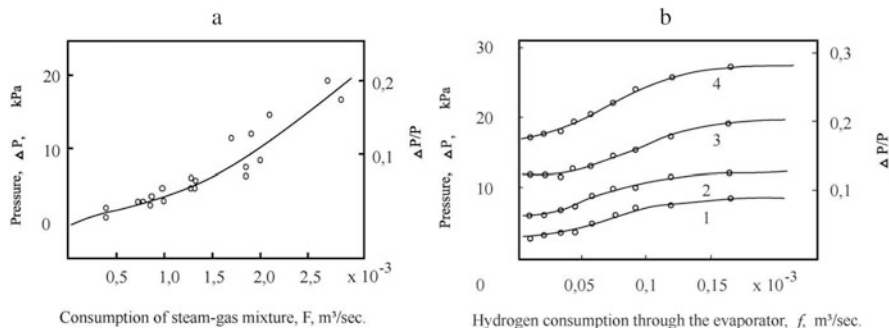
Fig. 4 Influence of H2 and VGM consumption on the overpressure in the reactor (**a**) and evaporator (**b**) with a diluting H2 flow: 1, 0.75; 2, 1.3; 4, 2.83 $m^3/s \times 10^3$; pressure in the room, 98.1 kPa

to 3.2 μm/min. The maximum growth rate is observed at a concentration of $SiCl_4$ in VGM ~5% vol, the maximum of the tested VGM consumption, and a temperature of 1270 °C. The choice of such a range of growth rates is justified if the growth is on multisilicon substrates doped with one or more weakly diffusing and, most importantly, relatively weakly evaporating impurities from the volume and surface of the substrate. In this case, suppression of autodoping can be achieved by simply exceeding the rate of growth over the rates of evaporation and diffusion of substrate impurities.

We experimentally established a very interesting and practically important fact, namely, that one of the most important factors that reduce the growth rate of layers increases the spread of layer parameters between batches and causes an increased level of defects in thickness and surface quality is the excess pressure in the reactor, which increases with an increase in the VGM flow rate from $0.5 \cdot 10^{-3}$ m^3/s to $3 \cdot 10^{-3}$ m^3/s by 20 kPa at a pressure in the process room $P_o = 98.1$ kPa (Fig. 4).

This factor must be taken into account in the operation of growth plants, considering it as one of the main independent process parameters. Moreover, this factor should be taken into account when organizing a group buildup of structures for solar cells.

An important factor affecting the quality of the surface of the layers is also the temperature of the reactor walls in contact with the VGM. For example, the high thermal conductivity of water-cooled metal walls of modern growth equipment designed for processing large diameter substrates leads to a decrease in the VGM temperature near the wall surface and, accordingly, to an increase in the probability of polychloride formation in the VGM due to the residual moisture content of hydrogen even after its purification on palladium filters and being source of defect formation during layer growth. This is accompanied by an increased level of defects in surface quality compared to products made on equipment, for example, with a quartz reactor. Experiments with the introduction of a thermal shield into a metal reactor unambiguously confirm the above. The quality of the structures and the yield

increase, and the growth rate of the layers increases by 20–30%. The results obtained determine ways to improve the design of the reactor unit of installations with a metal reactor, including, along with the use of quartz or graphite heat shields when using serial reactors, the development of reactors with controlled heat removal from the walls, in which conditions can be created that reduce the formation of polychlorides in the deposition zone.

4   Discussion of Results and Conclusions

The use of multisilicon obtained by metallurgical purification of TS, as well as the SCPS type manufactured from wastes of silicon metallurgy and EP as a raw material for solar cells, is advisable to limit its use as a substrate material for film solar cells, the film base region of which is grown by hydrogen reduction of trichlorosilane or silicon tetrachloride. Multisilicone, including SCPS, for these purposes should be a silicon material, deliberately overdoped in the processes of remelting, followed by casting into molds in a vacuum or remelting followed by Czochralski pulling. Re-doping should be carried out by one or a group of small impurities up to the solubility limit and use a charge from a mixture of TS brand Kr00 with waste from the production of silicon raw electronic purity and waste from silicon metallurgy from single crystal pulling and epitaxy operations. The main requirement for such a substrate material is a grain size of at least 300 μm and a resistivity of no more than 0.01 Ohm·cm.

The growth of the film, which will later serve as the base region of the solar cells, must be carried out under conditions of guaranteed suppression of autodoping by known standard methods or original methods based on the entrainment of impurity vapors evaporated from the reverse side of the substrate by a specially created gas flow directed into the cavity of the substrate holder. Naturally, this means, first of all, to prevent the transfer of substrate impurities inherited by its material from the melt of the initial raw material into the growing film. From the very beginning, the buildup of the film base area of the solar cells should be oriented towards the use of reverse technologies, similar to those introduced at the beginning of the twenty-first century for the operations of obtaining raw Si, which led to a tenfold decrease in prices for this product and, accordingly, for TS. The most important condition for the use of advanced technological methods known in the field of gas phase epitaxy in the processes of obtaining film structures on multisilicon substrates, including the use of mathematical regression models to control the process, including those given above, is the provision in, used for film growth, the reaction volume given: the pressure level, the concentration of the silicon-containing component, and the linear velocity of the VGM over the deposition surface.

The value of the results obtained in the development of solar cells with a film base deposited on multisilicon substrates [49, 53], including SCPS, also lies in the fact that the greatest effect can be obtained by using, instead of $SiCl_4$ or $SiHCl_3$, monosilane (SiH_4) [54–56], manufactured according to new technologies [57–59]

of the process which, according to forecasts [60–62], will inevitably replace the chlorosilane process in the 30 s of the twenty-first century. In addition, the use of monosilane will make it possible to reduce the temperature of the substrates by 200–300° at the same film deposition rates, which greatly facilitates the fight against self-alloying. From our data on solar cells, another physically interesting conclusion follows, indicating that the reason for the nonlinearity of the temperature dependences of the parameters of a solar cell made of multisilicon is the generation of charge carriers in it during heating, which occurs with the participation of energy levels due to its inherent structural defects and impurities. As direct evidence, it can be cited that the hydrogen passivation of GBs in multisilicon and SCPS samples is accompanied not only by the disappearance of the effect of the superlinear growth of short current but also by a decrease and even disappearance of the abovementioned nonlinear changes in the solar cell parameters observed during heating.

So, the main conclusions from the foregoing can be formulated as follows:

1. It has been shown that by providing a preliminary sample from p-type silicon waste and high-resistance silicon of any type of conductivity by casting, followed by directional crystallization of the filled volume on the S-3179 installation in a vacuum, it is possible to steadily obtain the initial coarse-grained SCPS with grain sizes of at least 2×2 mm^2 and without gas shells with a specific resistance of 0.5 5 Ohm.cm for the needs of photovoltaics.

2. The maximum efficiency of solar cells based on SCPS, which, under illumination of AM 1 and AM 1.5, is 12.5% and 11.5%, respectively, is observed in solar cells, the substrates for which are previously subjected to grinding, polishing, and chemical etching with further ion implantation phosphorus to a depth of 0.5 μm. Multilayer current-collecting contacts of the titanium-nickel-copper system on the front and back sides of the solar cells are obtained by vacuum deposition in a single technological cycle, which provides the required Ohmic contact with the surface, good adhesion, low current resistance, and corrosion resistance. 1150 nm thick SiOx antireflection coating gives an increase in efficiency by 20–25%.

3. A range has been found within which the dependence of the charge carrier mobility in the SCPS on the concentration of the dopant changes with the formation of a pronounced mobility well, the position of which depends on the size of the SCPS grains. The maximum spectral sensitivity of the obtained solar cells was determined, which falls at ~0.7 μm, which indicates their optimal correspondence to the spectral composition of solar radiation reaching the Earth's surface.

4. It has been shown that hydrogen passivation using a Kaufman source effectively reduces the recombination activity of the charge states of the grain boundary and dislocation clusters, especially linear dislocations, as well as transition metal impurities, which leads to an increase in output parameters; however, this is accompanied by a decrease in the probability of the effect of short-circuit superlinearity closures.

5. The effect of a superlinear increase in the short-circuit current of a solar cell based on SCPS in the range of solar radiation concentration of five to ten times was found, which leads to its increase up to ten times and the efficiency by 20%. A new mechanism is proposed for interpreting the effect of superlinear increase in the lifetime of nonequilibrium carriers with a photoexcitation level due to the appearance of defect-impurity complexes of the negatively charged vacancy-positively charged recombination center type.

6. Obtaining solar silicon based on regional TS [11, 12] is represented either by the traditional technology of chlorosilane processing, raw Si, and mono-Si, the ingots of which do not differ in the residual impurity composition from ordinary Si grades, or by the technology with its metallurgical processing in SCPS, when it was possible to achieve an efficiency of 5–7% without additional technological operations.

7. Initially unsuitable for the photoelectric method of energy conversion, SCPS ingots with arbitrary grain sizes and lifetime can be used in converters of the non-photoactive component of solar radiation and heat of heated bodies. On TEC made of silicon powder and with the concentration of deep levels necessary for the manifestation of the thermovoltaic effect, record high values of the Seebeck coefficient were obtained, an order of magnitude higher than the tabular values for MS.

8. An increase in the efficiency of TEC with minimization of grain sizes on isotype samples from micro-grained SCPS and TS has been established, which makes it possible to predict a sharp increase in the energy characteristics of converters when they are made of silicon with nanosized grains.

9. A TEC made of p-type SCPS with a specific resistance of ~1 Ohm•cm and a grain size of ~300 μm is proposed, in the charge for the smelting of which FC was introduced containing iron impurities with deep energy levels, which ensures the manifestation of an impurity thermal voltaic effect. At the same time, record high values of short circuit current (3 mA) and no-load voltage (60 mV) were obtained at a temperature of 200 °C.

10. It has been established that a necessary and sufficient condition for the manifestation of an impurity thermal voltaic effect on such samples is to provide a threshold concentration of deep levels $>4.10^{18}$ cm^{-3} or obtaining SCPS ingots with a grain size of about 10 μm, that is, to ensure the desired critical concentration of deep levels due to defects at grain boundaries.

11. On the basis of the materials presented in the work, developments, and the existing distribution of productive forces in the region, the task is initiated to assess the possibility of creating in the future in the Republic of Tajikistan an autonomous and complete cycle of production of TS, polycrystalline semiconductor silicon, solar cells, and TEC [63, 64], since Kyrgyzstan, Tajikistan, and Uzbekistan are the owners of the entire chains of production of PS for various purposes, as well as the existing production facilities of EP capable of mastering the manufacture of solar cells and TEC in the shortest possible time.

References

1. Kadyrov, A. L. (2018). *Obtaining and properties of secondary cast polycrystalline silicon* (p. 396). Publishing house "Nuri Marifat".
2. Kadyrov, A. L. (2018). *Electrophysical properties of solar and thermal energy converters based on secondary cast polycrystalline silicon*. Abstract of the dissertation of Dr. f-m. Sciences. Khujand.
3. Berezenko, L. E., Kagan, M. B., Perova, V. I., et al. (1986). Investigation of the characteristics of photoconverters based on polycrystalline silicon. *Geliotekhnika, 6*, 54–57.
4. Bereza, V. P., & Zaks, M. B. (1982). On the issue of the influence of thermoelastic stresses on the growth of wide undeformed silicon tapes by the Stepanov method/Mater. In *IX meeting on obtaining profiled crystals and products by the Stepanov method and their application in the national economy* (p. 360). LIYaF.
5. Kondratieva, L. A., Lozovsky, V. N., et al. (1990). The use of semiconductor silicon waste in the production of ground solar cells. *Geliotekhnika, 2*, 40–43.
6. Kasatkin, V. V., Mikheeva, L. V., Sotnikov, A. M., & Pakseev, Y. B. (1985). Photoconverters based on tape polycrystalline silicon. *Geliotekhnika, 5*, 14.
7. Bilyalov, R. V., & Chirva, V. P. (1988). Influence of thermal passivation on the efficiency of silicon polycrystalline photoconverters. *Geliotekhnika, 1*, 2–6.
8. Iskanderov, A., Kravchuk, V. D., & Muminov, R. A. (1988). Acoustic-stimulated change in the photoresponse of solar cells based on ribbon silicon. *Geliotekhnika, 4*, 25–28.
9. Saidov, M. S., Bilyalov, R. V., Mukhamadiev, V. S., & Chirva, V. P. (1987). Hydrogen passivation of charge states of grain boundaries in film polycrystalline photoconverters. *Geliotekhnika, 6*, 18–20.
10. Muller, J., Barhdafi, A., Courcelle, E., et al. (1986). Passivation of polycrystalline silicon solar cells by low energy hydrogen in implantation. *Solar Cells, 17*(2–3), 201–231.
11. Ashurov, M. K., Abdurakhmanov, B. M., Javkharova, N. I., Kadyrov, A. L., & Kurbonov, M. S. (2020). Some properties of raw materials from various deposits of Central Asia and new technologies for the production of technical silicon. *Scientific Notes of KhSU Named After Academician Bobodzhan Gafurov – Series of Natural and Economic Sciences, 2*(53), 24–29.
12. Ashurov, M. K., Abdurakhmanov, B. M., Javkharova, N. I., & Kadyrov, A. L. (2020). Raw materials and effective technologies for the production of technical silicon. *Reports of the Academy of Sciences of the Republic of Uzbekistan, Mathematics, Technical Sciences, Natural Sciences, 2*, 83–87.
13. Abdurakhmanov, B. M., Bilyalov, R. R., Saidov, M. S., & Chirva, V. P. (1989). Influence of irradiation in hydrogen plasma on the IR absorption spectra of polycrystalline silicon "DAN UzSSR"*, 8*, 24–26.
14. Abdurakhmanov, B. M., Aliev, R., Bilyalov, R. R., Saidov, M. S., & Saidov, A. S. (1996). Features of conversion of concentrated radiation by polycrystalline silicon solar cells. *Heliotechnics, 1*, 38–46.
15. Abdurakhmanov, B. M., Olimov, L. O., & Saidov, M. S. (2008). Electrophysical properties of solar polycrystalline silicon and its n + p structures at elevated temperatures. *Applied Solar Energy, 44*(1), 46–52. ISSN 0003-701X.
16. Abdurakhmanov, B. M., Olimov, L. O., & Abdurazzakov, F. S. (2010). Microstructure of grain boundaries in polycrystalline silicon and its influence on the transport of charge carriers. *Physical Surface Engineering, 8*(1), 72–76.
17. Abdurakhmanov, B. M., Aliev, R., Olimov, L. O., Saidov, M. S., & Chirva, V. P. (1998). Some features of the formation of p-n-structures on polycrystalline silicon by ion implantation of alkali metals. *Geliotekhnika, 5*, 78–83.
18. Abdurakhmanov, B. M., Abdurazzakov, F. S., Aladyina, Z. N., Zainabidinov, S. Z., Kadyrov, A. L., Olimov, L. O., & Sidikov, V. T. (2011, May 24–26). Some properties of planar thermal energy converters based on secondary cast polycrystalline silicon. In *Proceedings of the international scientific symposium "Renewable energy sources: Problems and prospects"*. Khujand, Republic of Tajikistan (pp. 13–18).

19. Bilyalov, R. V., Saidov, M. S., & Chirva, V. P. (1990). Hydrogen passivation of polycrystalline silicon solar cells. *Geliotekhnika, 4*, 36–39.
20. Abdurakhmanov, B. M., Ashurov, H. B., & Kurbanov, M. S. *Patent Ruz No. IAP 05986 Method for obtaining technical silicon and a device for its implementation*.
21. Abdulin, K. A., & Mukashev, B. N. (1995). *FTP, 29*(2).
22. Watrins, G. D., & Troxell, J. R. (1980). *Physical Review Letters, 44*, 593.
23. Kimerling, L. C., Blud, P., & Gibson, W. M. (1979). *Institute of Physics Conference Series, 46*, 273.
24. Bemski, G., Feher, G., & Gere, E. (1958). *Bulletin of American Physical Society, Series II, 3*, 135.
25. Watrins, G. D., & Corbett, J. M. (1964). *Physics Review, 134*, A1359.
26. Abdurakhmanov, B. M., Ashurov, K. B., & Kurbanov, M. S. (2018). *Chemical and metallurgical processing of silica into monosilane raw materials for solar energy and nanoelectronics/monograph* (p. 505). Publishing house "Navroz".
27. Yolkin, K. S., Zelberg, B. I., Barantsev, A. G., Yasevich, O. I., Kryuchkov, V. K., Yolkin, D. K., Yakovlev, S. P., & Balakirev, S. V. (2013). *Silicon production* (p. 364). MANEB.
28. Tolstoguzov, N. V. (1992). *Theoretical foundations and technology of melting silicon and manganese alloys* (p. 239). Metallurgy.
29. Bakhtin, A. A., Chernyakhovsky, L. V., et al. (1992). Influence of the quality of raw materials on the production of high purity silicon. *Non-Ferrous Metals, 1*, 29–32.
30. Nemchinova, N. V. (2010). *Development of the theory and practice of obtaining high-purity silicon by the carbothermic method*. Abstract for the degree of doctor of technical sciences, Irkutsk (p. 40).
31. Kolobov, G. A., Kritskaya, T. V., Moseiko, Y. V., Karpenko, A. V., & Pecheritsa, K. A. (2014). Refining metallurgical silicon to grade purity. *Solnechnaya Metallurgy, 32*(2), 118–126.
32. Yu, Z., Chen, J., Xie, G., et al. (2013). Purification of metallurgical grade silicon from aluminum by autoclave leaching. *Chinese Journal of Rare Metals, 37*(3), 453–460.
33. Sultamurat, G. I., & Gurba, G. R. (2011). Crystalline silicon smelting technology. *Mechanical engineering – Traditions and innovations: A collection of proceedings of the All-Russian Youth Conference* (pp. 445–446). 30.08–01.09.2011, Tomsk, TPU.
34. Nemchinova, N. V., Udalov, Y. P., Klets, V. E., et al. (2010). Tyutrin Study of the process of crystallization of silicon melt. In *Silicon – 2010: abstracts of reports. 7th international conference on topical problems of physics, materials science, technology and diagnostics of silicon, nanometer structures and devices based on it*. N. Novgorod. 06.06–06.09.2010, Nizhny Novgorod, UNN (p. 59).
35. Nemchinova, N. V., & Tyutrin, A. A. (2011). Study of the process of hydrometallurgical refining of silicon. In *Non-ferrous metals – 2011: coll. report 3 International Congress as part of the 16th International Conference on "Aluminium of Siberia", 5 conference on "Metallurgy of non-ferrous and rare metals", 6th symposium "Gold of Siberia"*. Krasnoyarsk, 07–09.09.2011, Krasnoyarsk, Verso (pp. 342–344).
36. Keqiang, X., Yi, M., Wenhui, M., et al. (2013). Extraction of titanium impurity from metallurgical silicon by HF-HCl leaching. *Metallurgist, 7*, 69–73.
37. Cai, J., Luo, X.-T., Haarberg, G. M., et al. (2012). Electrorefining of metallurgical grade silicon in molten CaCl2 based salts. *Journal of the Electrochemical Society, 159*(3), 155–158.
38. Lee, J., Lee, C., & Yoon, W. (2012). Behavior of the impurity-rich phase in metallurgical grade silicon during fractional melting. *Journal of Nanoscience and Nanotechnology, 12*(4), 3473–3477.
39. Shapovalov, B. A., Sheiko, I. V., Nikitenko, Y. A., et al. (2012). Induction melting and refining of silicon in a sectional crystal isotor. *Modern Electrometallurgy, 4*, 25–28.
40. Li, H., & Wan, S. (2010). Vacuum refining metallurgical grade silicon by arc plasma. *Journal of University of Science and Technology of China, 40*(9), 951–956.
41. Wang, J., Li, X., He, Y., et al. (2013). Purification of metallurgical grade silicon by a microwave-assisted plasma process. *Separation and Purification Technology, 102*, 82–85.

42. Loboda, P. I., Sagaydak, Y. P. S., & Bolbut, V. V. (2011). Purification of metallurgical silicon by remelting. *Solid State Physics and Chemistry, 12*(2), 455–459.

43. Mei, P. R., et al. (2012). Purification of metallurgical silicon by horizontal zone melting. *Solar Energy Materials and Solar Cells, 98*, 233–239.

44. Di, S. M., Binetti, S., Libal, J., & et al. (2011). Oxygen distribution on a multicrystalline silicon ingot grown from upgraded metallurgical silicon. *Solar Energy Materials and Solar Cells, 95*(2), 529–533.

45. Ding, Z., Ma, W., Wei, K., et al. (2012). Boron removal from metallurgical-grade silicon using lithium containing slag. *Journal of Non-Crystalline Solids, 358*(18–19), 2708–2712.

46. Tang, P.-P., Chen, Y.-X., Xu, M., et al. (2010). Hydrometallurgical process for the preparation of silicon grade "solar". *Chemical Engineering Journal (China), 38*(11), 68–71.

47. A.S., No. 1163665 USSR. Certificate of authorship No. 1163665 USSR. Substrate holder for gas epitaxy. B. M. Abdurakhmanov, S. R. Boiko, B. T. Pukhov, et al. (USSR) Priority 17.01.81.

48. Abdurakhmanov, B. M., Abrosimova, N. I., Bilyalov, R. R., & Saidov, M. S. (1993). Photoelectric characteristics of solar cells based on cast crystalline silicon. *Geliotekhnika, 1*, 22–24.

49. Abdurakhmanov, B. M. (2021). *Abstract of the dissertation. "Modernization of the electric arc process of silicon reduction and the creation of electronic devices based on it"*, Tashkent.

50. Abdurakhmanov, B. M. *Method for producing silicon*. Author's certificate of the USSR, No. 1464529.

51. Abdurakhmanov, B. M., Abrosimova, N. I., Saidov, M. S., Kustov, I. F., & Kharchenko, V. V. (1982). *UzSSR, 9*, 26–28.

52. Himelblau, D. (1973). *Analysis of processes by static methods* (p. 300). John Wiley & Sons.

53. Kharchenko, V. V. (1976). *Issues of epitaxial silicon deposition* (p. 150). Fan.

54. Iskandarov, S. C., Berdiev, U. F., Turdaliev, T. K., Mamirov, K. A., Ashurov, R. K., & Tulaganov, S. A. *Reactor for the direct synthesis of alkoxysilanes*. Application for invention no. IAP 20160120 dated 03/30/2016.

55. Abdurakhmanov, B. M., Ashurov, M. K., Ashurov, K. B., Kadyrov, A. L., Kurbanov, M. S., & Oksengendler, B. L. (2016). *Problems and prospects of silicon production in Central Asia. Monograph* (p. 420). Nuri Marifat.

56. Ashurov, H. B., Teak Joong, K., et al. *Method for the synthesis of monosilane using trialkoxysilanes*. Ruz patent No. IAP 05179, Rasmiy ahborotnoma, no. 3, dated 31.03.2016.

57. Ashurov, K. B. (2016). *Monosilane technology for the production of polycrystalline silicon and ion-stimulated methods for the creation of silicon structures*. Abstract of a doctoral dissertation. Tashkent.

58. Yang, S. I., Ashurov K., Salikhov, S., et al. *Method for preparing trialkosilane*. South Korea Patent KR 101422080(B1) Date of Patent May 14, 2014.

59. Yang, S. I., Ashurov, K., Salikhov, S., et al. *Method for preparing trialkosilane*. PRC Patent CN104797527, A Date of Patent July 16, 2014.

60. Naumov, A. V. (2007). Once again about the development of solar energy and the market for silicon raw materials in 2007-2010. *Izv. Universities Electron Materials and Techniques, 1*, 15–20.

61. Naumov, A. V., & Plekhanov, S. I. (1991). On the development of the semiconductor polycrystalline silicon market until 2012. *Tsvetnaya Metallurgy. Rare Metals and Semiconductor Materials, 10*, 38–44.

62. Naumov, A. V., & Rynok, A. V. (2015). Polycrystalline silicon market: State and prospects. *Electronics, 9*, 1–8.

63. Decree of the Government of the Republic of Tajikistan dated July 30, 2020, No. 427 "On the Action Plan for 2020–2025 to implement the announcement of 2020–2040 years" Twentieth anniversary of the study and development of natural, exact and mathematical subjects in the field of science and education.

64. Decree of the Government of the Republic of Tajikistan dated June 30, 2021, No. 263 "On the Strategy of the Republic of Tajikistan in the fields of science, technology and innovation for the period up to 2030".

Machine Learning Applications for Renewable-Based Energy Systems

Giorgio Graditi, Amedeo Buonanno, Martina Caliano, Marialaura Di Somma, and Maria Valenti

Abbreviations

AI	Artificial intelligence
ANN	Artificial neural network
ARIMA	Autoregressive integrated moving average
CART	Classification and Regression Tree
CNN	Convolutional neural network
DER	Distributed energy resources
DL	Deep learning
FCM	Fuzzy C-Means
FCNN	Fully connected neural network
FFNN	Feed forward neural network
FL	Fuzzy logic
GAN	Generative adversarial network
GRU	Gated recurrent unit
HME	Hierarchical mixture of experts
HVAC	Heating, ventilation, and air conditioning
LightGBM	Light Gradient Boosting Machine
LSTM	Long short-term memory
LTLF	Long-term load forecast
ML	Machine learning
MLP	Multilayer perceptron

G. Graditi · A. Buonanno (✉) · M. Caliano · M. Di Somma · M. Valenti
ENEA – Italian National Agency for New Technologies, Energy and Sustainable Economic Development, Rome (RM), Italy
e-mail: giorgio.graditi@enea.it; amedeo.buonanno@enea.it; martina.caliano@enea.it; marialaura.disomma@enea.it; maria.valenti@enea.it

177

MTLF	Medium-term load forecast
N-BEATS	Neural basis expansion analysis for interpretable time series
NWP	Numerical weather prediction
PV	Photovoltaic
RES	Renewable energy sources
RNN	Recurrent neural network
STLF	Short-term load forecast
SVM	Support vector machine
SVR	Support Vector Regression
TCN	Temporal convolutional network
XGBoost	eXtreme Gradient Boosting

1 Introduction: Importance of Forecasting in Renewable-Based Energy Systems

The global energy transition is already in place, and this represents the main reply of humanity to safeguard global climate and maintain a sustainable existence on Earth for future generations. The Paris Agreement has an objective of holding the increase in the global average temperature to well below 2 °C above pre-industrial levels and pursuing efforts to limit the temperature increase to 1.5 °C above pre-industrial levels. To achieve this ambitious temperature goal, the Paris Agreement calls for emissions to peak as soon as possible and be reduced rapidly through several measures such as energy efficiency and accelerated adoption of renewables in all energy sectors [29]. As the main consequence of this latter measure, the electricity produced by renewable energy sources (RES) will increase worldwide as already demonstrated by the European Union that can be considered the leader in energy transition and has attended one of the largest growths in the last 5 years especially for electricity produced by photovoltaic and wind.

On the other hand, the growing RES penetration in electricity systems is leading to an increase of reliability and stability issues due to their intermittent nature, thereby defining the compelling need to mitigate the uncertainties related to the production of renewable systems. In such a context, forecasting models and tools play a key role for fostering the transition from the current traditional centralized power systems towards smart grids that are based on advanced control systems for controlling and managing energy provided by distributed energy resources including RES. Managing in a proper way the RES uncertainties has also an important economic impact, since a high forecasting error can increase the overall system costs due to the increase in operating cost and the infrastructure needed. Another problem related to the economic impacts is represented by the RES energy imbalance management due to the difference between the forecasted and real injections of electricity into the grid [32].

In details, RES forecasting affects several parts of power system operation such as scheduling, dispatch, real-time balancing, and reserve requirements. Through proper forecasting tools, system operators can be aware of the up and down
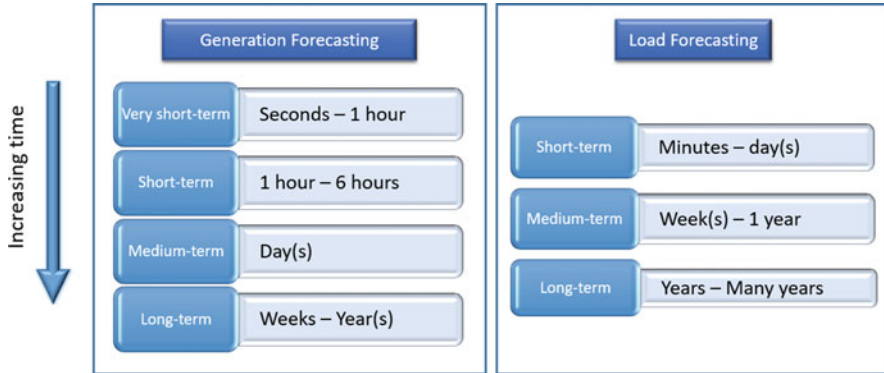
Fig. 1 The different types of generation forecasting (left) and load forecasting (right) based on their time horizon

ramps of RES generation being able to balance load and generation in intraday and day-ahead, thereby obtaining several benefits such as reduction of fuel costs, minimization of RES curtailment, and improvement of power system reliability [121].

The main types of generation forecasts with time horizons (Fig. 1) and key application are listed below [121]:

- The *intra-hour forecasting* (or very short-term forecasting) has a time horizon that goes from seconds to 1 h. It is used for real-time decisions such as dispatch and regulation.
- The *short-term forecasting* has a time horizon that goes from 1 h to 6 h. It is useful for scheduling, grid congestion management, and load following.
- The *medium-term forecasting* has a time horizon of day(s) ahead. It is useful for scheduling, reserve requirement, congestion management, and market trading.
- The *long-term forecasting* has a time horizon of weeks, seasonal, 1 year, or more years. It is used for system and resource planning, contingency analysis, operation management, and maintenance planning.

Along with the rising penetration levels of RES at local level, another major trend that is verified is the evolution of the role of the energy consumer that historically has been a passive user, covering the role of the customer consuming the energy produced at centralized level. Through the advent of distributed generation, the end user has been able to produce and consume their own energy and to store it and sell it back to the grid by exploiting RES availability locally, thereby being called "prosumer" [30]. Ideally, power generation from prosumers will be from RES, and technical solutions as energy storage or demand response can promote self-consumption [130].

However, in order to achieve the benefits deriving from these supportive technologies, it is essential to manage the high uncertainty not only related to RES generation but also related to flexibility of demand. The electricity load profile, given its nonlinearity and stochasticity due to the consumers' behavior, is a signal

difficult to forecast [48]. Increasing the accuracy of electricity load forecasting methods is always challenging because it is affected by many factors, such as time factors, including hour of the day, day of the week, holidays, and the season of the year [103], or weather conditions.

From this, the importance is evident to rely on accurate load forecasting models and tools that will be highly beneficial for distributed energy resources (DER) deployment and for grid operators as well.

The load forecasting can be mainly classified into three groups based on timescale (Fig. 1):

- *Short-term load forecast* (STLF), in which the time period can range from few minutes or hours to 1 day ahead or a week. For RES-based energy system applications, STLF usually aims at real-time control and security assessment.
- *Medium-term load forecast* (MTLF), in which the time period goes from a week to 1 year. MTLF has scheduling, coordination of load dispatch, and price settlement as main applications such that demand and generation are balanced all times.
- *Long-term load forecast* (LTLF), in which the time period ranges from few years up to 10 – 20 years ahead. LTLF aims at system planning.

The dramatic increase of RES penetration in power system and of energy consumption defines another challenge for grid operators who need to guarantee the system reliability that strongly depends on proper capabilities to monitor and control the grid. Today, fault detection represents a key factor to ensure power system reliability. In detail, in power systems, a fault is related to an abnormal electric current as, for instance, a short circuit in which the current exceeds the normal operating conditions. With the advent of smart grids, it is essential to enhance the network of transmission lines, equipment, and controls with the aim to manage and integrate information and communication technologies in all the energy supply chain from power generation to consumption while reducing environmental impacts and costs, improving reliability, enhancing efficiency [107], and providing ancillary services to increase power systems' security and adequacy [93].

Faults can occur at different layers of the power system such as, for instance, cables and transmission lines, renewable energy systems, power transformers, power converters, and conventional power generators. Moreover, faults in power systems can be categorized as [107]:

- Physical faults that occur when a physical device or component does not work in normal operating conditions
- Communication faults that occur in communications devices
- Software/hardware faults that occur when a component of the control center fails command and/or operation

In such a context, knowing in advance if a fault will occur within a predetermined time frame allows the system operator to plan maintenance interventions to ensure system reliability while also reducing costs of maintenance interventions.

Machine learning (ML) is considered one of the most promising methods for RES, load, and fault forecasting. It can be considered as a subset of artificial intelligence and refers to those computer systems that can automatically improve their performance in execution of some tasks thanks to the experience [83]. Since the 2010s, the deep learning (DL), which is a subset of ML composed by approaches that learn a hierarchical representation of the data, has demonstrated to be the right paradigm to outperform classical approaches in several contexts, such as computer vision, natural language processing, etc. [45], and recently also some forecasting competitions (e.g., M5) have been dominated by ML-based approaches (top 50 methods are based on ML) [74].

The ML techniques – and in particular the DL ones – have also the capability to take advantage from high amount and variety of available data (e.g., time series data, images, videos, etc.), hence enabling new use cases and opportunities.

Given their dependence by data, the security and privacy issues [69], as well as data quality issues (e.g., representativity, possible presence of bias, adversarial data) [80], have to be considered to have a system that performs well in the real contexts.

2   Novel Forecasting Methods for Renewable Energy Generation

In the literature, there are some works dealing with the application of ML to other RES [15, 110], but most applications are related to wind and solar energy.

There is a vast literature on the solar and wind power generation forecasting, but the proposed methods can be subdivided substantially in three main groups: physical approaches, statistical approaches, and hybrid approaches [11, 57, 121]. The main characteristics of each group are listed briefly in the following and are schematized in Fig. 2 by also highlighting their pros and cons.

The *physical approaches* require the technical specifications of the generation system and the weather forecast obtained through a numerical weather prediction (NWP) module.

For instance, for PV production forecasting, the necessary weather inputs (such as the Global Horizontal Irradiance, the temperature, and, eventually, the wind speed) can be obtained by the weather forecasting and used to compute the irradiance in the plane of the PV array and the temperature of PV modules. Through the PV model (obtained using the manufacturer specifications [71] or fitting historical data [98]), the prediction of the power production can be performed. These approaches can be applied to systems not yet established and, hence, are valuable tools for the initial design phase. The main drawback is the accuracy of the prediction that is dramatically affected by the quality of the weather forecasting that is not very accurate for short timescales (less than a few hours) [53] and the necessity to know the characteristics of the power generation system (also with the necessary simplifications that impact on the final result) [11].

The *statistical approaches* require historical data for training the model to predict the power production, given various inputs (e.g., past power generation values,
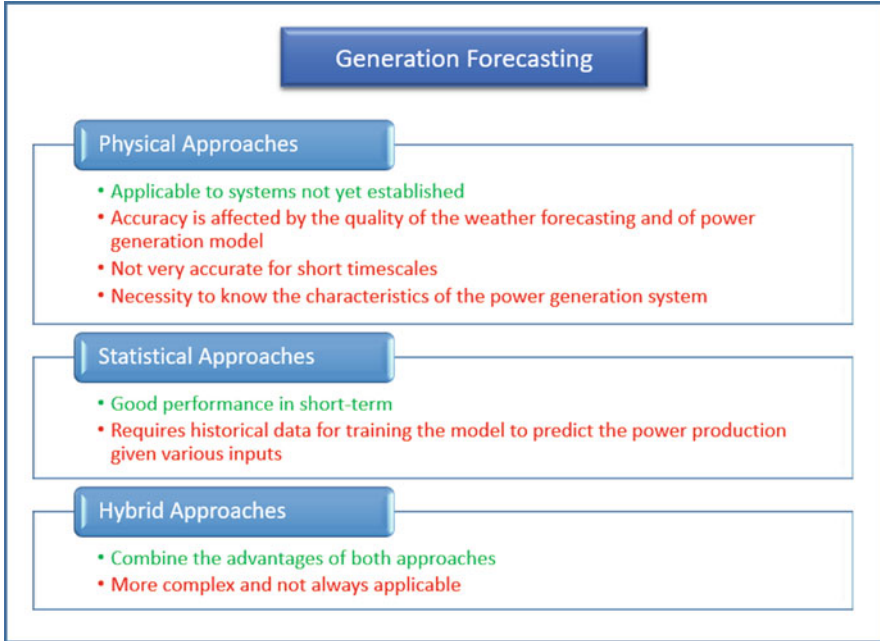
Fig. 2 The main pros (green) and cons (red) of three main groups of generation forecasting

Table 1 Summary of ML approaches for wind and PV power forecasting

Renewable energy source	Methods	Reference
PV	MLP	[38]
PV	GRU	[78]
PV	GRU	[125]
PV	CNN	[52]
Wind	LSTM	[14]
Wind	GRU	[60]
Wind	ConvLSTM	[128]

past weather information, etc.). If historical data of production is available, the *direct forecasting approach* can be applied (forecast the next generated power using past power and meteorological data); otherwise *the indirect forecasting approach* (forecast the next generated power using only meteorological data) has to be selected [47]. The scarcity of historical data can also be overcome by training a model using data made available for similar plants located in the same meteorological region of interest, i.e., using the transfer learning approach [137]. Among the statistical approaches, the ones using ML and, in particular, DL methods have demonstrated to be the most effective. In [77], the authors presented several DL techniques used for PV power forecasting, while in [126], the DL techniques for wind power forecasting are presented. Some of the most used ML methods for PV and wind power forecasting are listed in Table 1.

Physical and statistical approaches can be mixed for obtaining *hybrid approaches*. For instance, in physical approaches, information retrieved from some data could be used to correct the forecasts, or in the statistical approaches, they could inject some knowledge of the application domain. In some situations, the hybrid approaches perform better than the pure physical or statistical approaches [5, 53].

Given their peculiarities, some approaches are more suited for some forecasting horizons (and applications) than others, as described in [121]. For the *intra-hour forecasting* (or very short-term forecasting), the statistical approaches are preferable, while for the *short-term forecasting*, the hybrid approaches are most used. For the *medium-term forecasting*, the physical approaches are most used but with corrections to remove biases in the forecasting. For the *long-term forecasting*, the physical approaches and climatological forecasting are preferable [53].

The great availability of data coming from different sources allows leveraging multimodal data to increase predictive performance. In this context, data fusion techniques [21, 92, 136] are crucial to combine multimodal data and extract useful information for improving the weather forecasting and hence the renewable energy generation forecast (in particular for the very-short term and short-term scale). In recent years, several works have used sky images [95], sky videos [114], or radar observations [105] to improve weather forecasting.

Other most used data can be obtained from geostationary satellites [16] or gathered from other distributed sensors such as mobile cell phones [72] or personal weather stations [34]. To improve the quality of the prediction (in terms of higher spatial and temporal horizon), different spatial and temporal resolutions data could also be used [16].

As the input data, the decisions made by different predictors can also be fused together. These approaches are generally referred to as ensemble methods, and they often improve the overall performance of the forecast [44, 51] since the ensemble reduces the variance of the base models [89].

Recently, some works have shown that the generative models, such as the generative adversarial network (GAN), can be employed to improve the now-cast performance [105] or correct weather prediction in the short and medium term [56].

ML approaches can help the NWP and remote sensing (e.g., speeding up the processing of satellite data, improving the post processing of the models' outputs, etc.) [18], but for their wide adoption, they should have some required characteristics such as reliability, explainability, reproducibility, and trustworthy[1] as depicted in Fig. 3.

Reliability is related to the ability of correctly managing "new" situations that are different respect to the ones the model has been trained on. This aspect is critical for ML models that assume the training and test data follow the same distribution.

---

[1] In this context, reference is made to the concept of the confidence estimate of the predictive models. Recently the term trustworthy ML is used to indicate ML models that are explainable, fair, robust, causal and that preserve privacy.
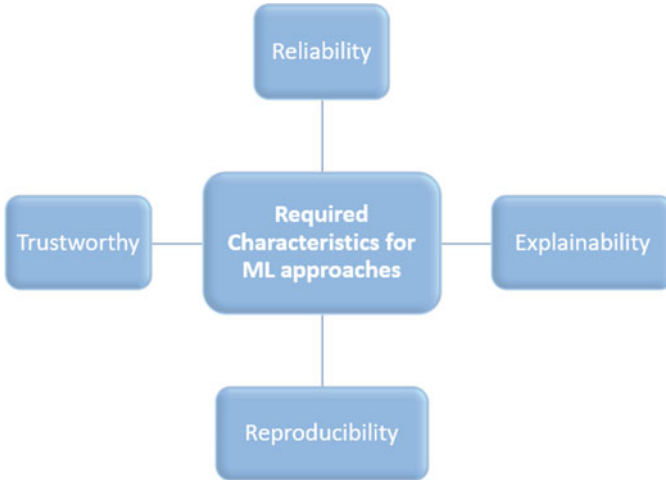
Fig. 3 The main characteristics required to ML approaches

For this reason, the selection of the training set should be made considering the real condition of usage of the deployed model. Moreover, the environment is nonstationary (e.g., climate change scenario), and in some situations, there is a scarcity of real data to use. For these problems, the continual learning approaches can help to build solutions robust to the changes [49], and the already mentioned transfer learning can help in case of scarcity of real data [137].

Explainability is related to the idea that several ML architectures are black boxes. In the last years, a lot of efforts have been devoted in order to improve the explainability of ML models [31, 81, 86, 108] and to make neural networks guided by physics [17, 59].

Reproducibility issues are present in many science fields, and for ML approaches, they are mainly due to the random initialization of the layer weights, shuffling of dataset used for the training process, changes in development frameworks, non-determinism in GPU floating-point computations, etc. [84]. In recent years, many efforts have been made to improve the reproducibility of ML solutions through the usage of tools that track the changes in the code, hyper-parameters, data, and environment during the experimentation (e.g., DVC,[2] Neptune,[3] WandB,[4] etc.) [94].

Trustworthy is related to the estimate of the uncertainty related to the obtained forecast (uncertainty quantification). The recent approaches to generate prediction sets for ML models, known as conformal prediction [10, 118], are pointing in this direction.

---

[2] https://dvc.org/

[3] https://neptune.ai/

[4] https://wandb.ai/

3 Modern Approaches for Electric Energy Consumption Forecasting

According to the literature, the methods most used for electricity load forecasting can be classified into conventional methods or based on artificial intelligence (AI) [79].

Conventional load forecasting techniques, such as linear regression models and autoregressive models, have been used in practice for a long time, providing satisfactory results, being recently often used as baseline models [22, 134]. Among the AI methods, the most used are based on FCNNs [75], RNNs [112], CNNs [66], and LSTM [62]. Other methods used are SVR [132, 133], hybrid methods [103], and the eXtreme Gradient Boosting (XGBoost) [1].

A typical characterization of the methods used for the electricity load forecasting depends on the length of forecast interval. Table 2 summarizes the methods most used in the literature depending on the time horizon used for the prediction.

Table 2 Summary of ML approaches for electricity load forecasting

| Time horizon	Methods	Reference
Short term	Ensemble	[101]
Short term	RNN	[112]
Short term	Multiple kernel extreme learning machine, ensemble	[67]
Short term	Ensemble	[88]
Short term	Factored conditional restricted Boltzmann machine	[48]
Short term	Hybrid	[9]
Short term	FCNN, CNN, LSTM, XGBoost, SVR, multivariate linear regression	[22]
Short term	Linear regression, FFNN, SVR, LS-SVM, HME-REG, HME-FFNN, FCM-FFNN	[37]
Medium term	FCNN	[12]
Medium- term	FCNN	[70]
Medium term	SVR	[104]
Medium- term	CNN, LSTM	[46]
Medium term	Ensemble, LSTM	[35]
Long term	LSTM	[135]
Long term	LSTM	[2]
Long term	Fuzzy, FCNN	[8]
Long term	FCNN, RNN, SVR, k-nearest neighbors, Gaussian process regression, generalized regression neural network	[109]
Long term	LSTM, GRU	[63]
Long term	FCNN, multivariate adaptive regression spline	[90]
Long term	LSTM, GRU	[33]
Long term	LSTM, GRU	[19]
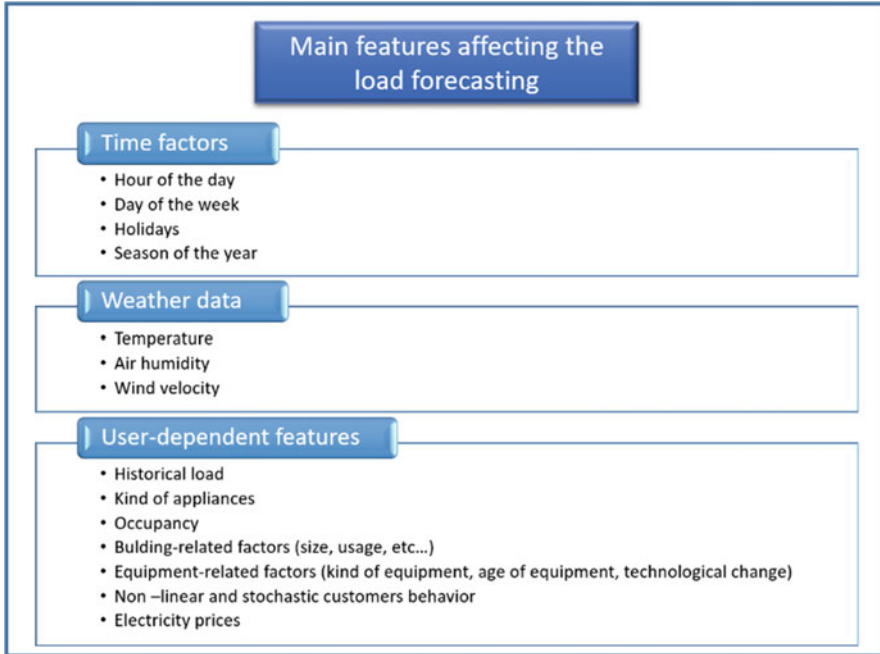
Fig. 4 Main features influencing the electrical load forecasting

The electricity load forecasting is a signal difficult to predict, and the accuracy of methods used for it can be affected by several factors, such as the ones reported in Fig. 4.

Such factors can have a different impact based on the different patterns of electricity use, characterizing the different types of consumers (residential, offices, industry, commercial, etc.). To assess the impact of the features on the prediction and select the most informative ones, the feature selection approaches are considered [116].

Singh et al. [115] tested several methods for forecasting the peak demand for individual households. They observed that considering historic data and data related to the occupancy allowed better prediction with respect to considering temperature and a seasonal time factor.

Gajowniczek and Ząbkowski [43] proposed an approach for predicting the electricity loads of individual households using Classification and Regression Tree (CART), SVR, and MLPs for 24-h ahead load forecasts. They observed that a combination of historical usage data and household behavioral data increased the accuracy of the forecasting, obtaining a mean absolute percentage error (MAPE) of 51% when the neural networks were used and of 48% in case of support vector machine (SVM).

Caliano et al. [22] tested several data-driven approaches, such as persistence, several linear regression methods, FCNNs, CNNs, LSTM, XGBoost, and SVR, for predicting the electricity loads of three individual households, by using data gathered from sensors. They observed that all methods considered performed similarly, while the most performing ones were multivariate linear regression, FCNNs, and XGBoost. The authors stated that the usage of an extended historic load dataset could improve the accuracy of the forecasting performed.

In some cases, to increase the accuracy of the models, an approach based on the decomposition of the forecasting problem can be a valid choice. Depending on the decomposition degree, the problem is split into local subproblems, and for each of them, a specialized predictive model can be used. In the past, several works have also shown how having specialized predictive models for different day types, hour of the day, or month of year can be useful in some conditions.

Papalexopoulos et al. [97] produced seven neural networks, each for each day of the week. Lee et al. [65] considered two load patterns, one for the weekdays and one for the weekend days. Then, each day was divided into three periods, and each of them was modeled using an individual neural network, whose weights had been estimated considering data for each one of the two load patterns. Similarly, [117] produced two separated neural networks, one for forecasting the electricity load of weekdays from Tuesday to Friday and one for Saturdays, Sundays, Mondays, and days after a holiday.

Similar approaches have been used also from [24, 42, 82]. Kalaitzakis et al. [58] and Kodogiannis and Anagnostakis [61] produced 24 neural networks, each for each hour of the day to predict the load of the next days. Deihimi et al. [27] produced 24 individual models, one for each hour of the day, based on wavelet echo state networks for 24-h-ahead short-term load forecasting. Decomposition into 12 months was used in [119] where 12 neural networks have been trained, and each of them performed the final 24-h-ahead load forecasting for 1 month of the year.

Veit et al. [122] tested forecasting methods, such as autoregressive integrated moving average (ARIMA), neural networks, and exponential smoothing considering different strategies for training data selection (e.g., day type) and several forecasting horizons, ranging between 15 min and 24 h. They considered two datasets for evaluation: (i) a German single household and (ii) six households in the United States. The authors observed that the forecasting accuracy was influenced by the choice of the forecasting method and the parameter configuration used. In detail, for the German dataset, the average MAPE was about 30%, while for the American one, it was about 85%.

A similar approach can be used for individual homes for which, thanks to smart meters data, it is possible to capture individual patterns of energy consumption related to home appliances. This allows the decomposition of the overall load into as many loads as the household appliances and equipment used, to predict the load of the single component. The approach proposed can be useful in the presence of appliances with more predictable load, such as the refrigerator. In addition, this will prevent predominant load devices, such as HVAC systems, from submerging the loads of other devices [36, 99].

As stated before, the usage of multimodal data can increase predictive performance. For instance, accessing information about interaction with social media, information from positioning sensors, and/or related to activity in progress (through video streams or using wearable sensors or smartphones) can improve the quality of the forecast [26] and in general improve the energy efficiency of the buildings by recognizing consumers' activities and identifying the associated possible energy saving [3]. However, the access and leveraging of some information pose problems related to user's privacy.

In the context of energy systems composed of a potential large number of customers (and data), the complexity of individual load forecasting can be high due to the multiple time series involved. In such a case, two possible approaches can be used, consisting of a local or a global method. The first one consists in training a single predictive model for each time series involved considering parameters learned separately for each time series. The second one is based on training a single predictive model with parameters learned considering all the available time series. In the last years, the local methods have been the most used approach since they allow to make the forecasting problems simpler to solve, but recently several works have shown the effectiveness of the global approaches, in particular in case of large availability of data thanks to the capacity of global models to leverage patterns that are similar across different time series [50, 55, 64, 73, 74, 87, 123].

Recently, cluster-based approaches have been extensively used demonstrating how the aggregation of customers with similar characteristics in terms of electricity usage patterns can be an effective way to improve the forecasting performance [40, 102, 111, 127, 131] as well as identify the similarity among days [91]. In [131], the load data of more than 1400 industrial customers were grouped in clusters based on the similarity of load features, and a CatBoost model was trained for each cluster obtaining the best performance in comparison with other approaches that did not use the clustering information. When the number of customers becomes very high, the computational complexity of the clustering algorithms becomes prohibitive, and alternative solutions, as dimensionality reduction, must be considered [7].

On the other side, in case the available data were not sufficient for training new prediction models by scratch, an effective data-driven approach to tackle these situations is represented by the transfer learning [96]. This approach allows the models pre-trained on large dataset to be customized and reused. Recently, many studies have used transfer learning for predicting the electricity load of different types of buildings over different time horizons. These works have showed increased accuracy of predictions when data from additional buildings were used, with respect to models using small target datasets [4, 41, 85, 106, 129], especially when source and target data shared some specific characteristics, such as belonging to similar building types or to the same climate zone (but different locations).

Buonanno et al. [20] tested several methods, based on linear regression model, LSTM, temporal convolutional network (TCN), NBEATS, LightGBM, transformer, and persistence, for predicting the 1-h-ahead electricity load for 28 lodging/residential buildings, by using global and local models and a transfer learning-based approach (called global-except). For each method tested, and for

each building considered, a local model was produced, while a unique global model was produced for all 28 buildings together. The aims were (i) comparing the performance of the local and global models produced in predicting the electricity load of a single building and (ii) predicting the energy demand of a single building by using the electricity load data of the other 27 buildings (global-except approach). The authors observed that the global models performed similarly to the local ones, allowing at the same time to reduce the deployment and maintainability effort of the forecasting model. Moreover, the global-except model showed good performance revealing how, without any particular assumption, the load forecasting of a completely new building can be obtained using a global model trained on existing buildings.

4 Predictive Outage Estimation for Renewable-Based Power Systems

Predictive maintenance is fundamental for the operation of power systems, since it allows shifting from the routine maintenance with unnecessary stops of the operations to an "informed" maintenance based on the likelihood that a fault can occur considering the information coming from different sources, such as operational data, weather information, cameras, sensors, etc.

In renewable-based energy systems, the efficiency and functioning under particular conditions should be ensured (e.g., removing the dirt from the PV panels, detecting the crack on PV panels, verifying the bearings in the wind turbines, etc.) to increase the reliability of the overall system and to reduce the operating costs. For that, diagnosis and fault detection for RES systems are necessary.

In the literature, several works have investigated the usage of ML and DL for detecting defects in PV plants or wind farms. In [54], the authors collected a dataset of 71 k images of wind blades captured by drones in different orientations, lighting, and weather conditions. This dataset has been properly labeled and used to train a ResNet50 model to detect blades' damages.

For detecting the bearing defects in wind turbines, [113] analyzed the limitations of human-only and AI-only approaches proposing an AI-assisted fault detection system that, using CNN, classifies images obtained by an endoscope as defect or not.

For defect detection in PV modules, infrared (IR) images or higher-resolution electroluminescence (EL) images can be used. There are many works that use the ML models applied to EL images to detect or classify defects in PV modules such as CNN [6], random forest and SVM [76], CNN and SVM [28], etc. Using image segmentation techniques, it is also possible to quantify the defect as done in [100] where the authors used a U-Net architecture to this scope.

Many power outages are caused by adverse weather conditions such as storms, hurricanes, heath waves, etc., and the outage prediction can be useful to assess the

resilience of the power system, namely, its characteristic to adapt and withstand to external modified conditions. In [39], the authors estimated the outages of the power grid component in response to hurricanes. The proposed approach is based on binary classifier (SVM) trained on historical data considering the resiliency index and distance from the center of the hurricane of various components and the category of the hurricane itself.

In [120], the authors identified the storm using wind gust and pressure fields and classified the storm, using some ML approaches, based on the expected damage it can cause to the power grid.

In [25], an Outer Prediction Model (OPM) leveraged outputs of numerical weather prediction and historical power outage data, spatially distributed information (e.g., soil, vegetation, etc.) to forecast the outages in a power distribution grid and their spatial distribution.

Other works are devoted to the maintenance interventions' feasibility forecasting [124] or on the maintenance planning to reduce users' discomfort [23].

In [13], several ML approaches were used to predict the faults in a power distribution network. In a radial power distribution grid, the current in each line of a middle voltage primary substation is recorded together with the outage data that can occur along the line (the exact position of the fault is unknown). For each fault, the affected line, the time of occurrence, the current in the line, and the weather conditions of the region containing the line are available. Using this information in an observation window of 30 days with a sampling period of 24 h, the tested predictive models can forecast the faults in the next 6 h. The problem has been stated as a binary classification problem since each multivariate time series related to the observation window is associated to "fault" values if in the next 6 h at least a fault has been occurred or "no fault" otherwise. At this scope, several binary classifiers were tested: XGBoost, LightGBM, random forest, k-nearest neighbors, SVM, and a FCNN with only one hidden layer. To assess fairly the results of each classifier at the best of its hyper-parameterization, a 10×5 stratified nested cross validation was used, and the evaluated metrics were the accuracy, the Matthews correlation coefficient, and the receiver operating characteristic area under curve (ROC-AUC). The historical data were available only for the lines that have experimented a fault in the years. For this reason, the authors extracted from the available data "no fault" examples considering the seasonality of the current and weather conditions. The work has shown that LightGBM and XGBoost models outperform other approaches and that, also in small data regime, the predictive models are able to give the power distribution manager informative outcomes.

Even though ML and DL approaches have shown to be very effective for predictive maintenance, research in this field is hindered by the scarcity of historical fault data or of datasets of defects due to several reasons: privacy, security, company reputation, competitive advantage, etc. The available open access datasets contain information with a not sufficient granularity or lack of important information, and hence, many works are tested on simulated or synthetic datasets.

The availability of historical outage dataset with good spatial and temporal granularity could boost the research in this field, and information like the topology

of the grid could enable the possibility of using approaches that leverage this information (refer to the works reviewed in Liao et al. [68]).

5 Conclusions

This chapter presents a critical analysis of machine learning methods used to tackle different challenges present in renewable-based energy system management.

Machine learning techniques can be effective tools in such a context, being employed in forecasting of energy generation and energy demand, in anomaly detection, and in outage forecasting.

The chapter also presents several case studies (applications) for discussing the main advantages of machine learning methods and the critical aspects that have to be taken into consideration.

References

1. Abbasi, R., Javaid, N., Ghuman, M., Khan, Z., & Rehman, S. A. (2019). Short term load forecasting using XGBoost. In L. Barolli, M. Takizawa, F. Xhafa, E. T. In, L. Barolli, M. Takizawa, F. Xhafa, & T. Enokido (Eds.), *Intelligent system and computing*. Springer Cham.

2. Agrawal, R., Muchahary, F., & Tripathi, M. (2018). Long term load forecasting with hourly predictions based on long-short-term-memory networks. In *2018 IEEE Texas power and energy conference (TPEC)*. https://doi.org/10.1109/TPEC.2018.8312088

3. Ahmadi-Karvigh, S., Ghahramani, A., Becerik-Gerber, B., & Soibelman, L. (2018). Real-time activity recognition for energy efficiency in buildings. *Applied Energy, 211*, 146–160.

4. Ahn, Y., & Kim, B. (2022). Prediction of building power consumption using transfer learning-based reference building and simulation dataset. *Energy and Buildings, 258*, 111717.

5. Akhter, M., Mekhilef, S., Mokhlis, H., & Mohamed Shah, N. (2019, March 27). Review on forecasting of photovoltaic power generation based on machine learning and metaheuristic techniques. *IET Renewable Power Generation, 13*, 1009–1023. https://doi.org/10.1049/iet-rpg.2018.5649

6. Akram, M., Li, G., Jin, Y., Chen, X., Zhu, C., Zhao, X., et al. (2019, December). CNN based automatic detection of photovoltaic cell defects in electroluminescence images. *Energy, 189*, 116319. https://doi.org/10.1016/j.energy.2019.116319

7. Alemazkoor, N., Tootkaboni, M., Nateghi, R., & Louhghalam, A. (2022). Smart-meter big data for load forecasting: An alternative approach to clustering. *IEEE Access, 10*, 8377–8387. https://doi.org/10.1109/ACCESS.2022.3142680

8. Ali, D., Yohanna, M., Ijasini, P., & Garkida, M. (2018). Application of fuzzy–neuro to model weather parameter variability impacts on electrical load based on long-term forecasting. *Alexandria Engineering Journal, 57*(1), 223–233.

9. Aly, H. (2020). A proposed intelligent short-term load forecasting hybrid models of ANN, WNN and KF based on clustering techniques for smart grid. *Electric Power Systems Research, 182*, 106191.

10. Angelopoulos, A., & Bates, S. (2021). A gentle introduction to conformal prediction and distribution-free uncertainty quantification. *A gentle introduction to conformal prediction and distribution-free uncertainty quantification*. arXiv. https://doi.org/10.48550/ARXIV.2107.07511

11. Antonanzas, J., Osorio, N., Escobar, R., Urraca, R., Martinez-De-Pison, F., & Antonanzas-Torres, F. (2016). Review of photovoltaic power forecasting. *Solar Energy, 136*, 78–111. https://doi.org/10.1016/j.solener.2016.06.069

12. Askari, M., & Keynia, F. (2019). Mid-term electricity load forecasting by a new composite method based on optimal learning MLP algorithm. *IET Generation, Transmission and Distribution, 14*, 845–852.

13. Atrigna, M., Buonanno, A., Carli, R., Cavone, G., Scarabaggio, P., Valenti, M., et al. (2021, September 7). Effects of heatwaves on the failure of power distribution grids: A fault prediction system based on machine learning. In *2021 IEEE international conference on environment and electrical engineering and 2021 IEEE industrial and commercial power systems Europe (EEEIC/I&CPS Europe)* (pp. 1–5). IEEE. https://doi.org/10.1109/eeeic/icpseurope51590.2021.9584751

14. Banik, A., Behera, C., Sarathkumar, T., & Goswami, A. (2020, October). Uncertain wind power forecasting using LSTM-based prediction interval. *IET Renewable Power Generation, 14*, 2657–2667. https://doi.org/10.1049/iet-rpg.2019.1238

15. Barzola-Monteses, J., Gómez-Romero, J., Espinoza-Andaluz, M., & Fajardo, W. (2021). Hydropower production prediction using artificial neural networks: An Ecuadorian application case. *Neural Computing and Applications, 34*, 13253–13266.

16. Benavides Cesar, L., Amaro e Silva, R., Manso Callejo, M., & Cira, C.-I. (2022, June 14). Review on Spatio-temporal solar forecasting methods driven by In situ measurements or their combination with satellite and numerical weather prediction (NWP) estimates. *Energies, 15*, 4341. https://doi.org/10.3390/en15124341

17. Beucler, T., Pritchard, M., Rasp, S., Ott, J., Baldi, P., & Gentine, P. (2021). Enforcing analytic constraints in neural networks emulating physical systems. *Physical Review Letter, 126*, 098302. https://doi.org/10.1103/PhysRevLett.126.098302

18. Boukabara, S.-A., Krasnopolsky, V., Stewart, J. Q., Maddy, E. S., Shahroudi, N., & Hoffman, R. N. (2019). Leveraging modern artificial intelligence for remote sensing and NWP: Benefits and challenges. In *The 1st NOAA workshop on leveraging AI in the exploitation of satellite earth observations & numerical weather prediction* (pp. ES473–ES491). https://doi.org/10.1175/BAMS-D-18-0324.1

19. Bouktif, S., Fiaz, A., Ouni, A., & Serhani, M. (2020). Multi-sequence LSTM-RNN deep learning and metaheuristics for electric load forecasting. *Energies, 13*, 391.

20. Buonanno, A., Caliano, M., Pontecorvo, A., Sforza, G., Valenti, M., & Graditi, G. (2022). Global vs. local models for short-term electricity demand prediction in a residential/lodging scenario. *Energies, 15*, 2037. https://doi.org/10.3390/en15062037

21. Buonanno, A., Nogarotto, A., Cacace, G., Di Gennaro, G., Palmieri, F., Valenti, M., & Graditi, G. (2021). Bayesian feature fusion using factor graph in reduced normal form. *Applied Sciences, 11*, 1934. https://doi.org/10.3390/app11041934

22. Caliano, M., Buonanno, A., Graditi, G., Pontecorvo, A., Sforza, G., & Valenti, M. (2020). Consumption based-only load forecasting for individual households in nanogrids: A case study. In *Proceedings of the 12th AEIT international annual conference*. https://doi.org/10.23919/AEIT50178.2020.924112

23. Cauchi, N., Macek, K., & Abate, A. (2017, November). Model-based predictive maintenance in building automation systems with user discomfort. *Energy, 138*, 306–315. https://doi.org/10.1016/j.energy.2017.07.104

24. Cecati, C., Kolbusz, J., Rozycki, P., Siano, P., & Wilamowski, B. (2015). A novel RBF training algorithm for short-term electric load forecasting and compararitve studies. *IEEE Transactions on Industrial Electronics, 62*(10), 6519–6529.

25. Cerrai, D., Wanik, D., Bhuiyan, M., Zhang, X., Yang, J., Frediani, M., & Anagnostou, E. (2019). Predicting storm outages through new representations of weather and vegetation. *IEEE Access, 7*, 29639–29654. https://doi.org/10.1109/access.2019.2902558

26. Cuncu, E., Manca, M., Pes, B., & Riboni, D. (2022). Towards context-aware power forecasting in smart-homes. *Procedia Computer Science, 198*, 243–248.

27. Deihimi, A., Orang, O., & Showkati, H. (2017). Short-term electric load and temperature forecasting using wavelet echo state networks with neural reconstruction. *Energy, 57*, 382–401.

28. Deitsch, S., Christlein, V., Berger, S., Buerhop-Lutz, C., Maier, A., Gallwitz, F., & Riess, C. (2019, June). Automatic classification of defective photovoltaic module cells in electroluminescence images. *Solar Energy, 185*, 455–468. https://doi.org/10.1016/j.solener.2019.02.067

29. Di Somma, M., & Graditi, G. (2022a). Challenges and opportunities of the energy transition and the added value of energy systems integration. In *Technologies for integrated energy systems and networks* (pp. 1–14). Wiley. https://doi.org/10.1002/9783527833634.ch1

30. Di Somma, M., & Graditi, G. (2022b, March 25). Integrated energy systems: The engine for energy transition. In *Technologies for integrated energy systems and networks* (pp. 15–40). Wiley. https://doi.org/10.1002/9783527833634.ch2

31. Ding, L. (2018). Human knowledge in constructing AI systems — Neural logic networks approach towards an explainable AI. *Procedia Computer Science, 126*, 1561–1570. https://doi.org/10.1016/j.procs.2018.08.129

32. Dolara, A., Grimaccia, F., Leva, S., Mussetta, M., & Ogliari, E. (2015, February 3). A physical hybrid artificial neural network for short term forecasting of PV plant power output. *Energies, 8*, 1138–1153. https://doi.org/10.3390/en8021138

33. Dong, M., & Grumbach, L. (2019). A hybrid distribution feeder long-term load forecasting method based on sequence prediction. *IEEE Transaction on Smart Grid, 11*, 470–482.

34. Droste, A., Heusinkveld, B., Fenner, D., & Steeneveld, G.-J. (2020, June 15). Assessing the potential and application of crowdsourced urban wind data. *Quarterly Journal of the Royal Meteorological Society, 146*, 2671–2688. https://doi.org/10.1002/qj.3811

35. Dudek, G., Pełka, P., & Smyl, S. (2022). A hybrid residual dilated LSTM and exponential smoothing model for midterm electric load forecasting. *IEEE Transactions on Neural Networks and Learning Systems, 33*(7), 2879–2891.

36. Ebrahim, A. F., & Mohammed, O. A. (2018). Pre-processing of energy demand disaggregation based data mining techniques for household load demand forecasting. *Inventions, 45*(3), 45.

37. Edwards, R., New, J., & Parker, L. (2012). Predicting future hourly residential electrical consumption: A machine learning case study. *Energy and Buildings, 49*, 591–603.

38. Ehsan, R. M., Simon, S. P., & Venkateswaran, P. R. (2017). Day-ahead forecasting of solar photovoltaic output power using multilayer perceptron. *Neural Computation Application, 28*(12), 3981–3992.

39. Eskandarpour, R., Khodaei, A., & Arab, A. (2017, September). Improving power grid resilience through predictive outage estimation. In *2017 North American Power Symposium (NAPS), Morgantown, WV, USA*. IEEE. https://doi.org/10.1109/naps.2017.8107262

40. Fahiman, F., Erfani, S. M., Rajasegarar, S., Palaniswami, M., & Leckie, C. (2017). Improving load forecasting based on deep learning and K-shape clustering. In *2017 international joint conference on neural networks (IJCNN)*. https://doi.org/10.1109/IJCNN.201

41. Fan, C., Sun, Y., Xiao, F., Ma, J., Lee, D., Wang, J., & Tseng, Y. (2020). Statistical investigations of transfer learning-based methodology for short-term building energy predictions. *Applied Energy, 262*, 114499.

42. Fan, S., Chen, L., & Lee, W. (2009). Short-term load forecasting using comprehensive combination based on multimeteorological information. *IEEE Transactions on Industry Applications, 45*(4), 1460–1466.

43. Gajowniczek, K., & Ząbkowski, T. (2015). Data mining techniques for detecting household characteristics based on smart meter data. *Energies, 8*(7), 7407–7427.

44. Gastinger, J., Nicolas, S., Stepić, D., Schmidt, M., & Schülke, A. (2021). A study on ensemble learning for time series forecasting and the need for meta-learning. In *International Joint Conference on Neural Networks (IJCNN)*. https://doi.org/10.1109/IJCNN523

45. Goodfellow, I., Bengio, Y., & Courville, A. (2016). *Deep learning* (Vol. 20). MIT Press. https://doi.org/10.1097/00006223-199507000-00010

46. Gul, M., Urfa, G., Paul, A., Moon, J., Rho, S., & Hwang, E. (2021). Mid-term electricity load prediction using CNN and Bi-LSTM. *The Journal of Supercomputing, 77*, 10942.

47. Gupta, P., & Singh, R. (2021). PV power forecasting based on data-driven models: A review. *International Journal of Sustainable Engineering, 6*, 1733.

48. Hafeez, G., Alimgeer, K., & Khan, I. (2020, July). Electric load forecasting based on deep learning and optimized by heuristic algorithm in smart grid. *Applied Energy, 269*, 114915. https://doi.org/10.1016/j.apenergy.2020.114915

49. He, Y., Zhixin, H., & Sick, B. (2021). Toward application of continuous power forecasts in a regional flexibility market. In *2021 international joint conference on neural networks (IJCNN)*. https://doi.org/10.1109/IJCNN52387.2021.9533626

50. Hewamalage, H., Bergmeir, C., & Bandara, K. (2022). Global models for time series forecasting: A simulation study. *Pattern Recognition, 2022*, 124.

51. Hong, T., Pinson, P., Wang, Y., Weron, R., Yang, D., & Zareipour, H. (2020). Energy forecasting: A review and outlook. *IEEE Open Access Journal of Power and Energy, 7*, 376–388. https://doi.org/10.1109/oajpe.2020.3029979

52. Huang, C.-J., & Kuo, P.-H. (2019). Multiple-input deep convolutional neural network model for short-term photovoltaic power forecasting. *IEEE Access, 7*, 74822–74834. https://doi.org/10.1109/access.2019.2921238

53. Irena. (2020). *Innovation landscape brief: Advanced forecasting of variable renewable power generation*. International Renewable Energy Agency.

54. Iyer, A., Nguyen, L., & Khushu, S. (2021). Learning to identify cracks on wind turbine blade surfaces using drone-based inspection images. In *NeurIPS 2021 workshop on tackling climate change with machine learning* (p. 2021). Retrieved from https://www.climatechange.ai/papers/neurips2021/37

55. Januschowski, T., Gasthaus, J., Wang, Y., Salinas, D., Flunkert, V., Bohlke-Schneider, M., & Callot, L. (2020). Criteria for classifying forecasting methods. *International Journal of Forecasting, 36*, 167–177.

56. Jeong, C., & Yi, M. (2023). Correcting rainfall forecasts of a numerical weather prediction model using generative adversarial networks. *The Journal of Supercomputing, 79*, 1289.

57. Kaaya, I., & Ascencio-Vásquez, J. (2021). Photovoltaic power forecasting methods. In D. M. Aghaei (Ed.), *Solar radiation – measurements, modeling and forecasting for photovoltaic solar energy applications*. IntechOpen. https://doi.org/10.5772/intechopen.97049

58. Kalaitzakis, K., Stavrakakis, G., & Anagnostakis, E. (2002). Shortterm load forecasting based on artificial neural networks parallel implementation. *Electric Power Systems Research, 63*(3), 185–196.

59. Karpatne, A., Ebert-Uphoff, I., Ravela, S., Babaie, H. A., & Kumar, V. (2019). Machine learning for the geosciences: Challenges and opportunities. *IEEE Transactions on Knowledge and Data Engineering, 31*(8), 1544. https://doi.org/10.1109/TKDE.2018.2861006

60. Kisvari, A., Lin, Z., & Liu, X. (2021, January). Wind power forecasting – A data-driven method along with gated recurrent neural network. *Renewable Energy, 163*, 1895–1909. https://doi.org/10.1016/j.renene.2020.10.119

61. Kodogiannis, V., & Anagnostakis, E. (1999). A study of advanced learning algorithms for short-term load forecasting. *Artificial Intelligence, 12*(2), 159–173.

62. Kong, W., Dong, Z., Hill, D., Luo, F., & Xu, Y. (2018). Short-term residential load forecasting based on resident behaviour learning. *IEEE Transactions on Power Systems, 33*, 1087–1088. https://doi.org/10.1109/TPWRS.2017.2688178

63. Kumar, S., Hussain, L., Banarjee, S., & Reza, M. (2018). Energy load forecasting using deep learning approach-LSTM and GRU in spark cluster. In *2018 fifth international conference on emerging applications of information technology (EAIT), Kolkata, India*. https://doi.org/10.1109/EAIT.2018.8470406

64. Laptev, N., Yosinski, J., Erran Li, L., & Smyl, S. (2017). *Time-series extreme event forecasting with neural networks at Uber*. Proceedings of the International Conference of Machine Learning.

65. Lee, K., Cha, Y., & Park, J. (1992). Short-term load forecasting using an artificial neural network. *IEEE Transactions on Power Apparatus and Systems, 7*(1), 124–132.

66. Li, L., Ota, K., & Dong, M. (2017). *Everything is image: CNN-based short-term electrical load forecasting for smart grid*. ISPAN-FCST-ISCC.

67. Li, T., Qian, Z., & He, T. (2020). Short-term load forecasting with improved CEEMDAN and GWO-based multiple kernel ELM. *Complexity, 2020*, 1.

68. Liao, W., Bak-Jensen, B., Radhakrishna Pillai, J., Wang, Y., & Wang, Y. (2022, March). A review of graph neural networks and their applications in power systems. *Journal of Modern Power Systems and Clean Energy, 10*, 345–360. https://doi.org/10.35833/mpce.2021.000058

69. Liu, X., Xie, L., Wang, Y., Zou, J., Xiong, J., Ying, Z., & Vasilakos, A. (2021). Privacy and security issues in deep learning: A survey. *IEEE Access, 9*, 4566–4593. https://doi.org/10.1109/access.2020.3045078

70. Liu, Z., Sun, X., Wang, S., Pan, M., Zhang, Y., & Ji, Z. (2019). Midterm power load forecasting model based on kernel principal component analysis and back propagation neural network with particle swarm optimization. *Big Data, 7*, 130–138.

71. Lorenz, E., Scheidsteger, T., Hurka, J., Heinemann, D., & Kurz, C. (2010). Regional PV power prediction for improved grid integration. *Progress in Photovoltaics, 19*, 757. https://doi.org/10.1002/pip.1033

72. Madaus, L., & Mass, C. (2017, March 3). Evaluating smartphone pressure observations for mesoscale analyses and forecasts. *Weather and Forecasting, 32*, 511–531. https://doi.org/10.1175/waf-d-16-0135.1

73. Makridakis, S., Spiliotis, E., & Assimakopoulos, V. (2020). The M4 competition: 100,000 time series and 61 forecasting methods. *International Journal of Forecasting, 36*, 54–74.

74. Makridakis, S., Spiliotis, E., & Assimakopoulos, V. (2022, January). M5 accuracy competition: Results, findings, and conclusions. *International Journal of Forecasting, 38*, 1346. https://doi.org/10.1016/j.ijforecast.2021.11.013

75. Mandal, P., Senjyu, T., Urasaki, N., & Funabashi, T. (2006). A neural network based severalhour-ahead electric load forecasting using similar days approach. *International Journal of Electrical Power & Energy Systems, 28*(6), 367–373.

76. Mantel, C., Villebro, F., Alves Dos Reis Benatto, G., Rajesh Parikh, H., Wendlandt, S., Hossain, K., et al. (2019, September 6). Machine learning prediction of defect types for electroluminescence images of photovoltaic panels. In *Applications of machine learning* (Vol. 11139, p. 1113904). SPIE. https://doi.org/10.1117/12.2528440

77. Massaoudi, M., Chihi, I., Abu-Rub, H., Refaat, S., & Oueslati, F. (2021). Convergence of photovoltaic power forecasting and deep learning: State-of-art review. *IEEE Access, 9*, 136593–136615. https://doi.org/10.1109/access.2021.3117004

78. Massaoudi, M., Chihi, I., Sidhom, L., Trabelsi, M., Refaat, S., & Oueslati, F. (2019, November). Performance evaluation of deep recurrent neural networks architectures: Application to PV power forecasting. In *2019 2nd international conference on smart grid and renewable energy (SGRE)* (pp. 1–6). IEEE. https://doi.org/10.1109/sgre46976.2019.9020965

79. Mat Daut, M., Hassan, M., Abdullah, H., Rahman, H., Abdullah, M., & Hussin, F. (2017). Building electrical energy consumption forecasting analysis using conventional and artificial intelligence methods: A review. *Renewable and Sustainable Energy Reviews, 70*, 1108–1111.

80. McGovern, A., Ebert-Uphoff, I., Gagne, D., & Bostrom, A. (2022). Why we need to focus on developing ethical, responsible, and trustworthy artificial intelligence approaches for environmental science. *Environmental Data Science, 1*, E6. https://doi.org/10.1017/eds.2022.5

81. McGovern, A., Lagerquist, R., John Gagne, D., Jergensen, G., Elmore, K., Homeyer, C., & Smith, T. (2019, November). Making the black box more transparent: Understanding the physical implications of machine learning. *Bulletin of the American Meteorological Society, 100*, 2175–2199. https://doi.org/10.1175/bams-d-18-0195.1

82. Methaprayoon, K., Lee, W., Rasmiddatta, S., Liao, J., & Ross, R. (2007). Multistage artificial neural network short-term load forecasting engine with front-end weather forecast. *IEEE Transactions on Industry Applications, 43*(6), 1410–1416.

83. Mitchell, T. (1997). *Machine learning*. McGraw-Hill.
84. Ml-Cmu. (2020). *Machine learning – Carnegie Mellon University Blog*. Retrieved from https://blog.ml.cmu.edu/2020/08/31/5-reproducibility/
85. Mocanu, E., Nguyen, P., Kling, W., & Gibescu, M. (2016). Unsupervised energy prediction in a smart grid context using reinforcement cross-building transfer learning. *Energy and Buildings, 116*, 646–655.
86. Molnar, C. (2022). *Interpretable machine learning: A guide for making black box models explainable.* Retrieved from https://christophm.github.io/interpretable-ml-book/
87. Montero-Manso, P., & Hyndman, R. (2021). Principles and algorithms for forecasting groups of time series: Locality and globality. *International Journal of Forecasting, 37*, 1632–1653.
88. Moon, J., Jung, S., Rew, J., Rho, S., & Hwang, E. (2020). Combination of short-term load forecasting models based on a stacking ensemble approach. *Energy and Buildings, 216*, 109921.
89. Murphy, K. (2022). *Probabilistic machine learning: An introduction*. MIT Press.
90. Nalcaci, G., Özmen, A., & Weber, G. (2019). Long-term load forecasting: Models based on MARS, ANN and LR methods. *Central European Journal of Operations Research, 27*, 1033–1049.
91. Nepal, B., Yamaha, M., Yokoe, A., & Yamaji, T. (2019). Electricity load forecasting using clustering and ARIMA model for energy management in buildings. *Japan Architectural Review, 3*, 62. https://doi.org/10.1002/2475-8876.12135
92. Ngiam, J., Khosla, A., Kim, M., Nam, J., Lee, H., & Ng, A. Y. (2011). *Multimodal deep learning*. Bellevue, Washington, USA. https://dl.acm.org/doi/10.5555/3104482.3104569
93. Omitaomu, O., & Niu, H. (2021, April 22). Artificial intelligence techniques in smart grid: A survey. *Smart Cities, 4*, 548–568. https://doi.org/10.3390/smartcities4020029
94. Onose, E. (2021). *Neptune Blog*. Retrieved from https://neptune.ai/blog/how-to-solve-reproducibility-in-ml
95. Paletta, Q., & Lasenby, J. (2019). Convolutional neural networks applied to sky images for short-term solar irradiance forecasting. In *37th European photovoltaic solar energy conference and exhibition* (pp. 1834–1837). https://doi.org/10.4229/EUPVSEC20202020-6BV.5.15
96. Pan, S., & Yang, Q. A. (2010). Survey on transfer learning. *IEEE Transactions on Knowledge and Data Engineering, 22*, 1345–1359.
97. Papalexopoulos, A., Hao, S., & Peng, T.-M. (1994). An implementation of a neural network based load forecasting model for the EMS. *IEEE Transactions on Power Apparatus and Systems, 9*(4), 1956–1962.
98. Pelland, S., Galanis, G., & Kallos, G. (2013). Solar and photovoltaic forecasting through post-processing of the global environmental multiscale numerical weather prediction model. *Progress in Photovoltaics: Research and Applications, 21*, 284–296. https://doi.org/10.1002/pip.1180
99. Pirbazari, A. M., Farmanbar, M., Chakravorty, A., & Rong, C. (2020). Improving load forecast accuracy of households using load disaggregation techniques. In 2020 *International Conferences on Internet of Things (iThings) and IEEE Green Computing and Communications (GreenCom) and IEEE Cyber, Physical and Social Computing (CPSCom) and IEEE Smart Data (SmartData) and IEEE Congress on Cybermatics (Cybermatics), Rhodes, Greece, 2020* (pp. 843–851). https://doi.org/10.1109/iThings-GreenCom-CPSCom-SmartData-Cybermatics50389.2020.00140
100. Pratt, L., Govender, D., & Klein, R. (2021, November). Defect detection and quantification in electroluminescence images of solar PV modules using U-net semantic segmentation. *Renewable Energy, 178*, 1211–1222. https://doi.org/10.1016/j.renene.2021.06.086
101. Qiu, X., Suganthan, P., & Amaratunga, G. (2018). Ensemble incremental learning random vector functional link network for short-term vector functional link network for short-term electric load forecasting. *Knowledge-Based Sytems, 145*, 182–196.
102. Quilumba, F. L., Lee, W.-J., Huang, H., Wang, D. Y., & Szabados, R. L. (2015). Using smart meter data to improve the accuracy of intraday load forecasting considering customer

behavior similarities. *IEEE Transactions on Smart Grid, 6*(2), 911–918. https://doi.org/10.1109/TSG.2014.2364233

103. Rafati, A., Joorabian, M., & Mashhour, E. (2020, June). An efficient hour-ahead electrical load forecasting method based on innovative features. *Energy, 201*, 117511. https://doi.org/10.1016/j.energy.2020.117511

104. Rai, S., & De, M. (2021). Analysis of classical and machine learning based short-term and mid-term load forecasting for smart grid. *International Journal of Sustainable Energy, 40*(9), 821–839.

105. Ravuri, S., Lenc, K., Willson, M., Kangin, D., Lam, R., Mirowski, P., et al. (2021, September 29). Skilful precipitation nowcasting using deep generative models of radar. *Nature, 597*, 672–677. https://doi.org/10.1038/s41586-021-03854-z

106. Ribeiro, M., Grolinger, K., El Yamany, H., Higashino, W., & Capretz, M. (2018). Transfer learning with seasonal and trend adjustment for cross-building energy forecasting. *Energy and Buildings, 165*, 352–363.

107. Rivas, A. E., & Abrao, T. (2020). Faults in smart grid systems: Monitoring, detection and classification. *Electric Power Systems Research, 189*, 106602. https://doi.org/10.1016/j.epsr.2020.106602

108. Samek, W., Wiegand, T., & Müller, K.-R. (2017). *Explainable artificial intelligence: Understanding, visualizing and interpreting deep learning models*. ICT Discoveries. Retrieved from http://handle.itu.int/11.1002/pub/8129fdff-en

109. Sangrody, H., Zhou, N., Tutun, S., Khorramdel, B., Motalleb, M., & Sarailoo, M. (2018). Long term forecasting using machine learning methods. In *2018 IEEE power and energy conference at Illinois (PECI), Champaign, IL, USA*. https://doi.org/10.1109/PECI.2018.8334980

110. Senocak, A. A., & Guner Goren, H. (2022). Forecasting the biomass-based energy potential using artificial intelligence and geographic information systems: A case study. *Engineering Science and Technology, an International Journal, 26*, 100992.

111. Shahzadeh, A., Khosravi, A., & Nahavandi, S. (2015). Improving load forecast accuracy by clustering consumers using smart meter data. In *2015 international joint conference on neural networks (IJCNN), Killarney, Ireland* (pp. 1–7). https://doi.org/10.1109/IJCNN.2015.7280393

112. Shi, H., Xu, M., & Li, R. (2018). Deep learning for household load forecasting – a novel pooling deep RNN. *IEEE Transactions on Smart Grid, 9*, 5271–5280. https://doi.org/10.1109/TSG.2017.2686012

113. Shin, W., Han, J., & Rhee, W. (2021, April). AI-assistance for predictive maintenance of renewable energy systems. *Energy, 221*, 119775. https://doi.org/10.1016/j.energy.2021.119775

114. Siddiqui, T. A., Bharadwaj, S., & Kalyanaraman, S. (2019). A deep learning approach to solar-irradiance forecasting in sky-videos. In *2019 IEEE winter conference on applications of computer vision (WACV)* (pp. 2166–2174). https://doi.org/10.1109/WACV.2019.00234

115. Singh, R., Gao, P., & Lizotte, D. (2013). On hourly home peak load prediction. In *IEEE international conference on smart grid communications*. https://doi.org/10.1109/SmartGridComm.2012.6485977

116. Söderberg, M. J., & Meurling, A. (2019). *Feature selection in short-term load forecasting.*

117. Srinivasan, D. (1998). Evolving artificial neural networks for short term load forecasting. *Neurocomputing, 23*, 265–276.

118. Stankeviciute, K., Alaa, A. M., & Van der Schaar, M. (2021). Conformal time-series forecasting. In *Advances in neural information processing systems 34 (NeurIPS 2021)*.

119. Tamimi, M., & Egbert, R. (2000). Short term electric load forecasting via fuzzy neural collaboration. *Electric Power Systems Research, 56*(3), 243–248.

120. Tervo, R., Láng, I., Jung, A., & Mäkelä, A. (2021, February 11). Predicting power outages caused by extratropical storms. *Natural Hazards and Earth System Sciences, 21*, 607–627. https://doi.org/10.5194/nhess-21-607-2021

121. Tian, T., & Chernyakhovskiy, I. (2016). *Forecasting wind and solar generation: Improving system operations.*

122. Veit, A., Goebel, C., Tidke, R., Doblander, C., & Jacobsen, H. (2014). Household electricity demand forecasting: Benchmarking state-of-the-art methods. In *e-Energy'14: Proceedings of the 5th international conference on future energy systems*. https://doi.org/10.1145/2602044.2602082

123. Wagner, N., Michalewicz, Z., Schellenberg, S., Chirac, C., & Mohais, A. (2011). Intelligent techniques for forecasting multiple time series in real-world systems. *International Journal of Intelligent Computing and Cybernetics, 4*, 284–310.

124. Wang, J., Liang, Y., Zheng, Y., Gao, R. X., & Zhang, F. (2020). An integrated fault diagnosis and prognosis approach for predictive maintenance of wind turbine bearing with limited samples. *Renewable Energy, 145*, 642–650. https://doi.org/10.1016/j.renene.2019.06.103

125. Wang, K., Qi, X., & Liu, H. (2019, December). Photovoltaic power forecasting based LSTM-convolutional network. *Energy, 189*, 116225. https://doi.org/10.1016/j.energy.2019.116225

126. Wang, Y., Zou, R., Liu, F., Zhang, L., & Liu, Q. (2021, December). A review of wind speed and wind power forecasting with deep neural networks. *Applied Energy, 304*, 117766. https://doi.org/10.1016/j.apenergy.2021.117766

127. Wijaya, T. K., Vasirani, M., Humeau, S., & Aberer, K. (2015). Cluster-based aggregate forecasting for residential electricity demand using smart meter data. In *2015 IEEE international conference on big data (big data)*. https://doi.org/10.1109/BigData.2015.73

128. Wilms, H., Cupelli, M., Monti, A., & Gross, T. (2019, March). Exploiting Spatio-temporal dependencies for RNN-based wind power forecasts. In *2019 IEEE PES GTD grand international conference and exposition Asia (GTD Asia)* (pp. 921–926). IEEE. https://doi.org/10.1109/gtdasia.2019.8715887

129. Wu, D., Wang, B., Precup, D., & Boulet, B. (2020). Multiple Kernel learning-based transfer regression for electric load forecasting. *IEEE Transactions on Smart Grid, 11*, 1183–1192.

130. Yang, J., Luo, F., Kong, W., & Dong, Z. (2021). Load forecasting in the short-term scheduling of DERs. In *Distributed energy resources in local integrated energy systems* (pp. 389–417). Elsevier. https://doi.org/10.1016/b978-0-12-823899-8.00003-0

131. Zhang, C., Chen, Z., & Zhou, J. (2020). Research on short-term load forecasting using K-means clustering and CatBoost integrating time series features. In *2020 39th Chinese control conference (CCC)*. https://doi.org/10.23919/CCC50068.2020.9188856

132. Zhang, F., Deb, C., Lee, S., Yang, J., & Shah, K. W. (2016). Time series forecasting for building energy consumption using weighted support vector regression with differential evolution optimization technique. *Energy and Buildings, 12*, 94–103.

133. Zhang, X., Grolinger, K., Capretz, M., & Seewald, L. (2018). Forecasting residential energy consumption: Single household perspective. In *17th IEEE international conference on machine learning and applications, Orlando, FL, USA*. IEEE.

134. Zhao, H., & Magoulès, F. (2012). A review on the prediction of building energy consumption. *Renewable and Sustainable Energy Reviews, 16*, 3586–3592.

135. Zheng, J., Xu, C., Zhang, Z., & Li, X. (2017). Electric load forecasting in smart grids using long-short-term-memory based recurrent neural network. In *2017 51st annual conference on information sciences and systems (CISS), Baltimore, MD, USA*.

136. Zheng, Y. (2015, March 1). Methodologies for cross-domain data fusion: An overview. *IEEE Transactions on Big Data, 1*, 16–34. https://doi.org/10.1109/tbdata.2015.2465959

137. Zhou, S., Zhou, L., Mao, M., & Xi, X. (2020, February). Transfer learning for photovoltaic power forecasting with long short-term memory neural network. In *2020 IEEE international conference on big data and smart computing (BigComp)* (pp. 125–132). IEEE. https://doi.org/10.1109/bigcomp48618.2020.00-87

Bi-objective Optimal Scheduling of Smart Homes Appliances Using Artificial Intelligence

Govind Rai Goyal (iD) **and Shelly Vadhera** (iD)

1 Introduction

There has been a lot of talk about "smart cities." Countries all over the world are striving to build smart cities in order to increase productivity and socioeconomic growth. Although there are several aspects of a smart city, here in this research work we would like to highlight some important things from the energy perspective, i.e., smart homes. A smart home energy management system (EMS) is able to optimize the electricity consumption of the city by being able to record the real-time data pertaining to different residential, commercial, and industrial loads with the help of advanced metering infrastructure (AMI) [1].

Unfortunately, there is not yet a widely adopted and cost-effective strategy for optimizing the EMS available to end users, which would both lower electricity bills and lower peak demand on the grid. Reduction of peak power demand is as important as minimization of electricity bill costs. Peak load demand can be managed by flattening the load curve. Flattening of the load curve is the reduction of power consumption at peak load hours and increasing consumption during the low load periods [2, 3]. Some deferrable home appliances can be scheduled to run during off-peak or mid-peak hours to help flatten the load curve. To flatten the load curve, it is required to bring the actual load curve as close to the objective load curve as possible. So the objective becomes to minimize the difference between the actual load curve and the objective load curve [4]. Smart home appliances can be managed by implementing different programs of demand side management (DSM). DSM is

G. R. Goyal (✉)
University of Engineering & Management, Jaipur, India

S. Vadhera
National Institute of Technology, Kurukshetra, India
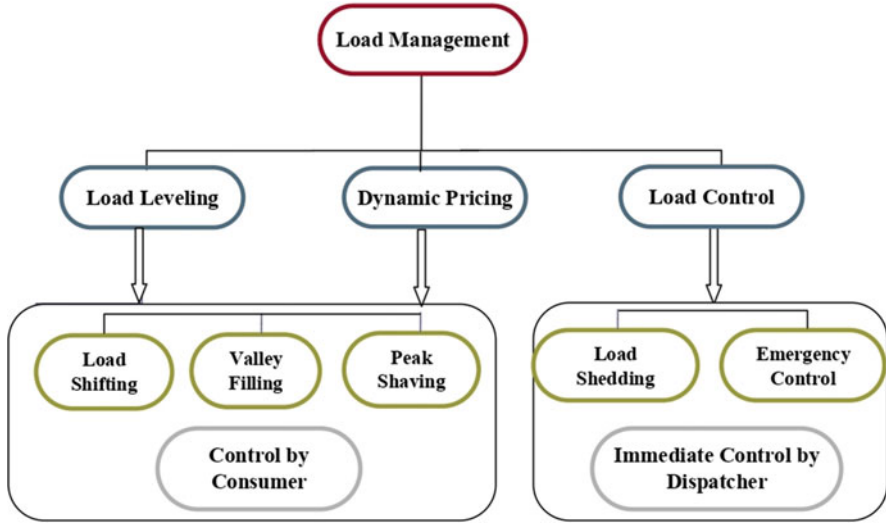
Fig. 1 Objectives of load management

a way for consumers to help the electricity grid with the management of electric power. It is the modification of consumer demand behavior by various methods, such as financial rebates or incentives and differentiated tariffs [5, 6]. There are two terms in DSM, viz., load management and load growth. Load growth involves strategic conservation, or strategic load growth. On the other hand, the term load management has three different types of programs, viz., load leveling, dynamic pricing, and load control, as shown in Fig. 1 [7–10].

Demand response (DR) is also an integral part of demand side management. Demand response can provide a short-term response to energy market conditions, and it can change the regular consumption pattern of electricity in response to the change in electricity prices with time, i.e., dynamic pricing. The classification of DR programs is shown in Fig. 2 [11–14]. The major types of demand response programs are as follows:

- *Load control*: In this type of program, participants allow the load scheduler to manipulate their energy consumption.
- *Emergency program*: In this DR program, consumers are provided incentives for reducing the load when demand exceeds supply.
- *Economic program*: It is employed by utilities to avoid the significantly higher costs of producing energy during peak demand times of the day.
- *Ancillary service program (ACP)*: This program of DR is used to support the reliable and regulated transmission of electricity to loads.
- *Capacity market program (CMP)*: Customers commit to reducing their load by a predetermined amount in order to postpone capacity increase in the capacity market program.

	Operational Planning	Day-ahead Scheduling	Economic Dispatch	Real-Time Dispatch
Price-Based DR	Time-of-Use (ToU) Price	Real Time Pricing (RTP)	Critical Peak Pricing (CPP)	
Incentive-Based DR	Ancillary Services Market Programs (ASMP)		Emergency Demand Response Programs (EDRP)	Direct Load Control (DLC)
	Capacity Market Program (CMP)	Demand Bidding	Interruptible Service Program (ISP)	

Fig. 2 Overview of demand response programs

- *Interruptible service program (ISP)*: In this program consumers are given a rebate for reducing their load in contingency conditions. Consumers can also be penalized for not reducing their load.

All programs of demand response can be categorized as price-based and incentive-based programs. Price-based DR programs rely on the customer's response (change in energy consumption pattern) to the electricity price changing with time in order to reduce electricity bill costs. On the other hand, incentive-based DR programs depend on the rebates or penalties applied to consumers for reducing or raising their power consumption [15]. This research work focuses on price-based as well as incentive-based DR programs in which changes in the electricity prices over time are transmitted to residential customers. Customers may react differently to this dynamic price. One is that their consumption can be reduced only during peak hours and they maintain their normal load pattern during off-peak time. This results in load cutting in peak hours. Another action that could be taken is delaying the use of electricity from peak hours to off-peak or mid-peak hours to minimize the electricity bill cost [16]. This may result in increased load demand in off-peak and mid-peak hours.

Dynamic pricing is one of the building blocks of DR programs. It is a demand- and supply-based pricing strategy, viz., time-of-use (ToU) price; critical peak price (CPP); variable peak price (VPP); peak time rebates/penalties; etc. [17]. All these prices vary at different hours of the day, like off-peak, mid-peak, and peak hours. However, real-time price (RTP) is the most straightforward type of dynamic pricing, in which the cost of electricity is constantly fluctuating in response to variations in the wholesale price. The two types of RTP are day-ahead (DA-RTP) and hourly-ahead (HA-RTP). In contrast to HA-RTP, which communicates the power price signal to the consumer at each interval, DA-RTP lets customers know how much electricity will cost them for the entire day in advance [18]. Implementation of dynamic pricing can be beneficial for all the stakeholders in different ways, like

Fig. 3 Classification of dynamic pricing based on risk involved

monetary benefits for customers [7, 9, 12] and actual cost recovery for suppliers. It is also helpful to postpone the investment in power generation capacity by shifting peak demand from peak hours to off-peak hours [14, 16, 18]. Dynamic pricing has been implemented by various researchers with different strategies of DSM for different objective functions in their studies.

The variation in electricity tariff can be described as a risk for customers; however, it can also be related to the efficiency of the pricing options. Dynamic pricing options can be categorized as low-risk tariff plans, moderate-risk tariff plans, and high-risk tariff plans as shown in Fig. 3 [19–21].

Many programs have limited this risk by assigning customers a baseline for power consumption. The price for the purchase of power below the baseline consumption is usually the ToU rate. Above the baseline consumption, customers pay the real-time price (RTP), and also a rebate can be received for reducing the consumption below its baseline level. Such programs are known as two-part RTP programs with a customer baseline load (CBL) [22]. Demand response (DR) can expand the consumer's participation in the electricity market. A consumer's response towards CBL can be a method of evaluation of the successful implementation of a DR program. In fact, CBL is the expected pattern of customer consumption in the absence of a DR program [23].

1.1 Contribution of Research Work

Key contributions of this research work can be summarized as follows:

- It suggests a way to figure out how much electricity costs that uses prices that change over time and can help both consumers and utilities.
- Single interval programming (SIP) is used to find the best way to schedule appliances when dynamic pricing is used.
- It studies the consequences of optimal scheduling of smart home appliances to minimize the cost of monthly electricity bills.

2 Mathematical Modeling

Smart home appliances under HEMS are categorized as deferrable and non-deferrable [17]. In the smart home energy management system, consumers can define their preferences for the use of appliances through an energy controller.

2.1 Objective Function for Minimization of Electricity Cost

An objective function for the minimization of a consumer's electricity bill costs for 24 h of a day can be given by Eq. (1) [11].

$$\text{Minimize } C_{\text{DEC}} = \sum_{t=1}^{T} x^t(d) \times p^t(d) \ T = 24 \tag{1}$$

$$x^t(d) = \sum_{\ell=1}^{\pounds} \xi_\ell^t y_\ell^t(d) T_\ell \ \ t \in T \tag{2}$$

Here, p^t = Electricity price during time interval $t \in T$.
$x^t(d)$ = Energy consumption schedule in time slot t of the day $d \in N$.
y_ℓ^t = Power demand for a load $\ell \in \pounds$ in time slot t.
ξ_ℓ^t = On/off state of appliances.
T_ℓ = Operational time of load $\ell \in \pounds$.
$\pounds$ = Set of available appliances (deferrable and non-deferrable).

The optimal scheduling of appliances in order to reduce the electricity bill will help to reduce the peak hour's power consumption due to the high electricity price during peak hours. However, shifting appliances from high-priced hours to low-priced homes may result in increased power demand during off-peak or mid-peak hours. Peak load management can be a solution to this problem.

2.2 Objective Function for Peak Demand Management

This research work also aims to manage the peak demand by minimizing the difference between the objective and optimal load curve [2]. The goal is to make the difference between the goal and actual load curves as small as possible. This can be expressed mathematically as Eq. (3) [12].

$$\text{Minimize } f_1 = \sum_{t=1}^{T} x^t(d) - \text{Obj}^t(d) \ T = 24 \tag{3}$$

Here, $\text{Obj}^t(d)$ denotes the objective power demand. Objective power demand for each time slot $t \in T$ on day $d \in N$ can be calculated by Eq. (4) [13].

$$\text{Obj}^t(d) = \frac{1 \Big/ p^t(d)}{\sum\limits_{t=1}^{T} p^t(d)} \sum_{t=1}^{T} y^t(d) \tag{4}$$

Here, $y^t(d)$ is the forecasted demand at interval t.

2.3 Proposed Objective Function for Cost of Electricity

To minimize both the objectives simultaneously, an objective function based on the customer base load (CBL) line model is proposed for both the case studies. The proposed function of electricity cost is given by Eq. (5).

$$\text{Minimize} \quad C_{\text{Total}} = \sum_{t=1}^{T} \begin{Bmatrix} x^t(d)\,p^t_{\text{ToU}}, & \text{if } x^t(d) = \text{Obj}^t(d) \\ 1.2 \times x^t(d)\,p^t_{\text{ToU}}, & \text{if } \text{Obj}^t(d) \leq x^t(d) \\ 0.8 \times x^t(d)\,p^t_{\text{ToU}}, & \text{if } x^t(d) \leq \text{Obj}^t(d) \end{Bmatrix} \tag{5}$$

As per the proposed cost function, if the hourly consumption is equal to the CBL, then time-of-use (ToU) price as usual is applicable. But for the power consumption below this line, a rebate (20% of the ToU price for the respective time slot) can be given. Similarly, for the power consumption above the base line load, a penalty is applied.

2.4 Operational Constraints [18–23]

$$x_\ell^t(d) = 0 \quad t \notin T_\ell \tag{6}$$

$$x_\ell^{\min} \leq x_\ell^t(d) \leq x_\ell^{\max} \quad t \in T_\ell \tag{7}$$

$$\sum_{t=1}^{24} x_\ell^t(d) = DR_\ell \tag{8}$$

3   Solution Methods

In this research work, objective functions are optimized by CS and PSO algorithms. The best results of both algorithms are also compared to the hybrid GA-PSO.

3.1   *Cuckoo Search (CS) Method*

The Cuckoo search method works on the basics of the breeding behavior of cuckoo birds. Based on the breeding behavior of cuckoos, this algorithm works in order to find the most suitable host nest. So this algorithm is designed for the maximization of problems, but it can be used for minimization equally. Thus, it can be used for optimization of any function. Figure 4 shows the flowchart of the CS method [24].

3.2   *Particle Swarm Optimization*

Particle swarm optimization (PSO) is one of the meta-heuristic, population-based search algorithms to solve optimization problems. It is a kind of swarm intelligence that is based on social behavior. This algorithm searches in parallel paths using a group of particles. It contributes to solving any optimization as well as engineering problems. Figure 5 shows the flowchart of the CS method [25].

3.3   *Hybrid GA-PSO Algorithm*

To overcome the limitations of the PSO algorithm, a hybrid GA-PSO has been proposed by [26]. A hybrid approach is expected to combine the merits of PSO with those of GA. The main problem with PSO is its premature convergence to a stable point, but one advantage of PSO over GA is its simplicity. Another clear difference between PSO and GA is the ability of GA to control the convergence. GA crossover and mutation rates can have a subtle effect on convergence, but they are not comparable to the level of control achieved by adjusting the inertia weight of PSO. In fact, the decrease in inertia weight dramatically increases the swarm's convergence. So, in the hybrid GA-PSO algorithm, the best features of GA like mutation and crossover are assorted to improve the performance of PSO. Figure 6 shows the flow chart of the hybrid GA-PSO algorithm [27].
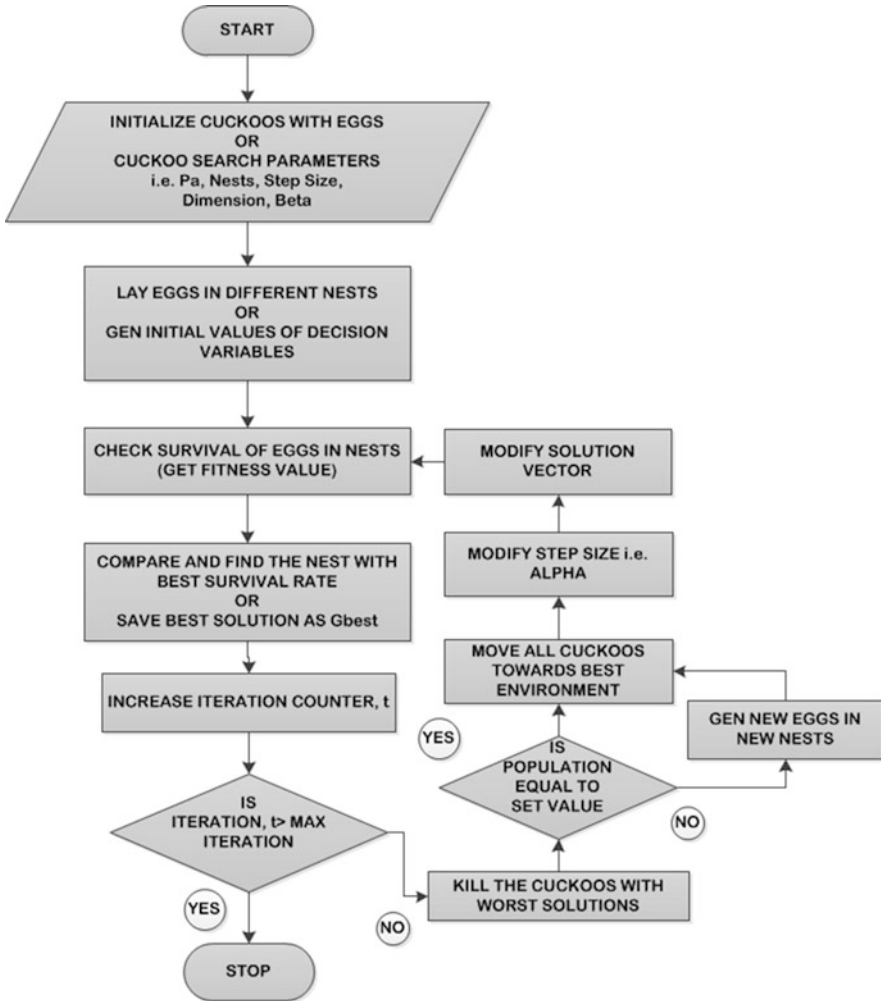
Fig. 4 Optimization procedure of CS method

4 System Data

This model of energy management is applied to smart homes for residential consumers. Details of appliances and monthly power consumption by all the smart home residents are given in Table 1 [28], while Table 2 provides information on power rating and category of appliances [17].

Real data of pricing schemes available in *Tehran Power Distribution Company (TPDC)*, *Iran* (case I), and *Kerala State Electricity Board (KSEB)*, *India* (case II), are studied in this research work. In case study I (TPDC, Tehran) and case study II

```
begin
    Objective function f(x),  x = (x₁, x₂,.....xₐ)ᵀ
    Random initialization of solution vector xᵢ , and velocity vector vᵢ
    Evaluate objective function  f(x) for solution vector xᵢ
    Find local optimum Pᵗbest and global optimum Gᵗbest as per PSO

        while (t < Maximum Iteration)
    Calculate velocity of particles by PSO using the equation

                vᵢᵗ⁺¹ = wvᵢᵗ + c₁R₁(Pᵗbest − xᵢᵗ) + c₂R₂(Gᵗbest − xᵢᵗ)

    Position update of  xᵢ by adding updated velocity (vᵢᵗ⁺¹)
    Evaluate objective function again for updated solution vector
    Update the values of Pᵗbest as well as  Gᵗbest
        end while

            Post process results and visualization
    end
```

Fig. 5 Optimization procedure of PSO algorithm

Table 1 Energy consumption and appliance information of smart homes

S. no.	Household no.	Range (kWh)	Monthly consumption (kWh)	Total appliance	Deferrable appliance
1	1	<600	558.6	8	3
2	2	601–750	654.6	9	3
3	3	751–1000	947.4	14	6
4	4	1001–1250	1142.4	14	6
5	5	1251–1500	1312.5	12	7
6	6	1501–2000	1732.5	14	9
7	7	2001–2500	2392.5	15	10

(KSEB, India), electricity pricing options available for retail consumers are block rate tariff and time-of-use (ToU) price. In this case, pricing data is considered for September 2015, while in case study II (KSEB, India), pricing data is considered for January 2017.
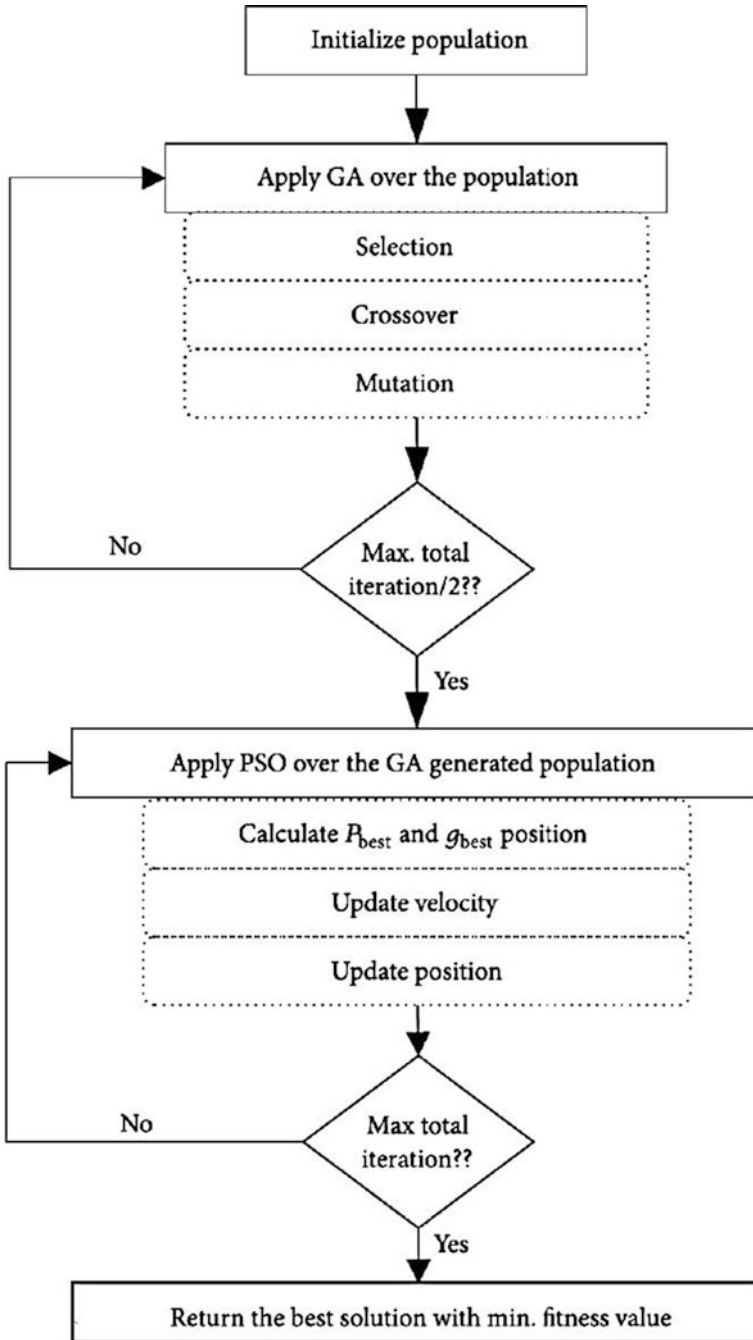
Fig. 6 Flowchart of hybrid GA-PSO algorithm

Table 2 Information of power rating and category of appliances

S. no.	Appliances	Power rating (kW)	Category
1	Light	0.5	NDL
2	Refrigerator	0.125	NDL
3	Personal computer	0.20	NDL
4	TV	0.14	TDL
5	Hairdryer	1.0	TDL
6	Washing machine	1.5	TDL
7	Vacuum cleaner	1.0	TDL
8	Electric stove	1.5	NDL
9	Water heater	1.5	NDL
10	Iron	1.0	TDL
11	Air conditioner	1.0–1.5	PDL
12	Water pump	2.0	TDL
13	Dishwasher	1.0	TDL
14	Air heater	1.5	NDL
15	Cloth dryer	1.5	TDL
16	Fan	0.12	NDL

NDL non-deferrable, *TDL* time deferrable, *PDL* power deferrable

Table 3 Electricity tariff plan in TPDC, Iran

S. no.	Electricity consumption (kWh/month)	Electricity prices (cents/kWh)
1	0–100	1.36
2	100–200	1.59
3	200–300	3.41
4	300–400	6.14
5	400–500	7.05
6	500–600	8.87
7	>600	9.78

Table 4 Time-of-use (ToU) price in TPDC, Iran

S. no.	Category	Extra cost/discount (cents/kWh)
1	Discount for off-peak hours	Electricity consumption (kWh) * 0.68 (cents/kWh)
2	Discount for mid-peak hours	Electricity consumption (kWh) * 0.27 (cents/kWh)
3	Extra cost for peak	Electricity consumption (kWh) * 1.36 (cents/kWh)

4.1 Pricing Data for Case Study I (Tehran Power Distribution Company, Iran)

Tables 3 and 4 show the block rate tariff and time-of-use (ToU) price in Tehran Power Distribution Company, Iran, respectively [29]. In the ToU price plan, an extra cost for peak hours and a discount for mid-peak or off-peak hours are calculated as per Table 4 after calculating the cost of electricity based on Table 3.

Table 5 Block rate tariff plan in KSEB, India

S. no.	Electricity consumption (kWh/month)	Electricity prices (INR/kWh)
1	Up to 300	5.50
2	Up to 350	6.20
3	Up to 400	6.50
4	Up to 500	6.70
5	More than 500	7.50

Table 6 Time-of-day (ToD) price in KSEB, India

S. no.	Category	ToU price (INR/kWh)
1	Normal/mid-peak period	100% of normal charges, i.e., 7.50 INR/kWh
2	Peak period	120% of normal charges, i.e., 9.00 INR/kWh
3	Off-peak period	90% of normal charges, i.e., 6.75 INR/kWh

4.2 Pricing Data for Case Study II (Kerala State Electricity Board, India)

Tables 5 and 6 show the block rate tariff and time-of-day (TOD) price applicable in Kerala State Electricity Board (KSEB), India, respectively [30]. In the KSEB, the rates of TOD tariff given in Table 6 are approved by the Kerala State Electricity Regulatory Commission (KSERC), Thiruvananthapuram, India, for LT domestic consumers having a 6-month average monthly consumption above 500 units in January 2017. The unit rate includes both capacity charges and energy charges. Here, INR 30/month (for single-phase users) and INR 80/month (for three-phase users) are also applicable as fixed charges.

5 Optimal Results of Simulation Study

5.1 Scenario 1: Minimization of Cost of Monthly Electricity Bill

Optimal Results for Case Study I (Tehran Power Distribution Company, Iran)
Results for case I of this study, which includes two pricing schemes, are shown in Table 7. For each of the seven households, the cost of the monthly electricity bill is obtained. The given power costs with ToU pricing in this table are calculated for all the households, both before and after optimization. Here, single interval programming (SIP) is used to attain optimal scheduling, with the fundamental optimization techniques: CS, PSO, and hybrid GA-PSO. It may be concluded from comparing the monthly electricity bill with various pricing plans shown in this table
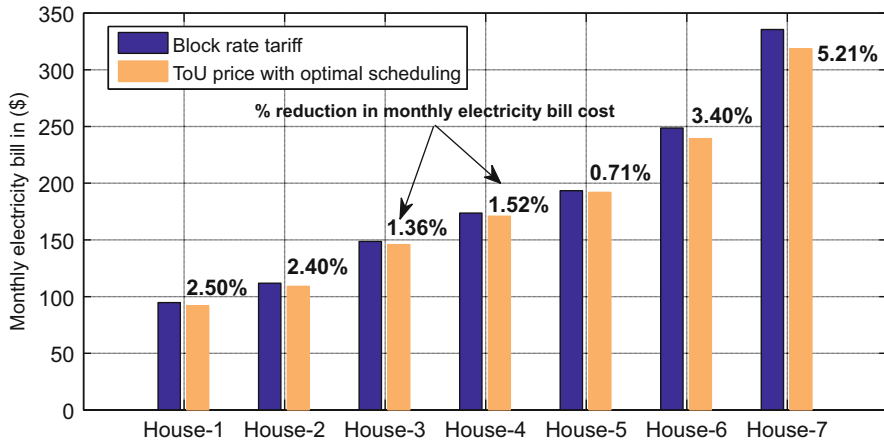
Fig. 7 Reduction of monthly electricity bill with optimal scheduling in case I

that block rate tariffs are more expensive than ToU prices with estimated scheduling; however, this savings can be increased by optimal planning the use of appliances.

According to the comparison of electricity bill costs by block rate tariff (before optimization) and ToU price with optimal scheduling, it can be observed that, on average for all homes, all three algorithms reduced the electricity bill cost by *1.25%*, *1.5%*, and *2.5%*, respectively. Here, it can be said that the hybrid GA-PSO algorithm's optimal scheduling can lead to a minimum electricity bill for all levels of power consumption. Figure 7 compares the electricity cost before optimization to the monthly electricity bill with ToU price and optimal scheduling to show the % reduction in electricity bill expense.

Table 8 gives the comparison of peak-to-average ratio (PAR) for seven households with estimated and optimal scheduling obtained for cost minimization. Figure 8 gives a graphical representation of the PAR obtained by estimated scheduling and optimal scheduling with ToU price. From this comparative representation, it can be noticed that planning of appliances after optimization in order to minimize the bill costs may result in increased peak power consumption due to the scheduling of various appliances at low-cost time slots.

Optimal Results for Case Study II (KSEB, India)

Similar to case study I, Table 9 provides the best electricity cost results for case II. In this case study, the block rate tariff and TOD price are both applied. For each of the seven study households, the cost of the monthly electricity bill is obtained here. In this table, estimated scheduling (before to optimization) and optimal scheduling are used to determine the provided power costs with TOD pricing for all the households (after optimization). This table also includes a comparison of electricity expenses with respect to the best scheduling of appliances. It may be concluded that block rate tariffs are more expensive than TOD prices with anticipated scheduling by

Table 7 Comparative results of minimized electricity bill for case I

Household no.	Monthly consumption in kWh	Monthly electricity bill in ($)					
		Before optimization		After optimization with ToU price			
		Block rate tariff	ToU price	CS	Hybrid GA-PSO	PSO	
1	558.6	93.92	92.45	92.0	91.59	91.68	
2	654.6	111.29	110.13	109.70	108.61	109.21	
3	947.4	147.85	147.16	146.85	145.83	146.52	
4	1142.4	172.87	171.82	171.32	170.23	170.43	
5	1312.5	192.42	193.33	192.15	191.05	191.50	
6	1732.5	247.63	246.45	244.85	239.22	244.03	
7	2392.5	334.70	329.92	327.10	317.26	326.58	

Table 8 Peak demand and peak to average ratio (PAR) for case I

Household no.	By estimated scheduling		Resulted by optimal scheduling	
	PAR	Peak demand (kW)	PAR	Peak demand (kW)
1	2.990	2.33	3.389	2.63
2	3.203	2.92	4.443	4.04
3	2.689	3.35	*1.965*	2.41
4	2.325	3.68	2.935	3.97
5	2.184	3.98	2.469	5.25
6	2.450	5.88	4.208	10.12
7	1.983	6.59	3.724	12.37
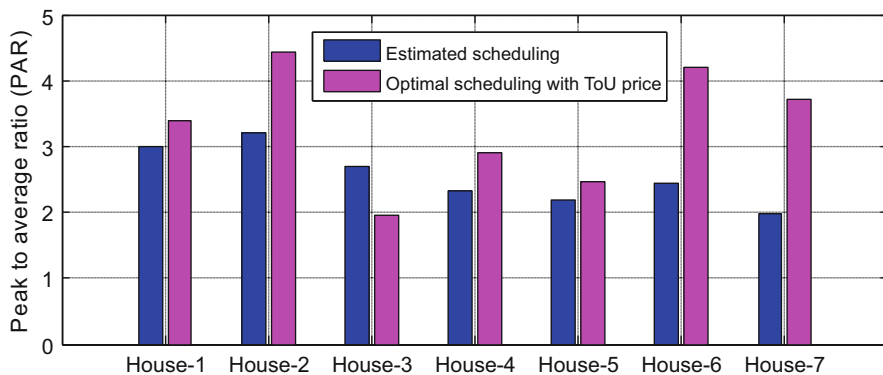
Fig. 8 Comparison of PAR before and after optimal scheduling for case I

comparing the monthly power bill with various pricing schemes prior to optimal scheduling, which is shown in Table 9. This savings can be enhanced by optimal planning of appliances.

However, for all of the households, the average monthly expense was reduced by *1.15%*, *1.65%*, and *3.0%*, respectively, using the CS, PSO, and hybrid version of PSO. By comparing the pre-optimization monthly electricity bill cost by block rate tariff with the post-optimization monthly electricity bill cost by TOD price, it is observed that hybrid GA-PSO algorithm's optimal scheduling resulted in the lowest possible monthly electricity bill cost regardless of the level of power consumption. Figure 9 shows the reduction in electricity bill cost after optimization by the hybrid GA-PSO algorithm in comparison of estimated scheduling with block rate tariff and TOD price.

Peak-to-average ratio (PAR) for estimated and optimal scheduling for cost minimization using hybrid GA-PSO algorithm are compared in Table 10 for seven homes. The PAR achieved by approximated scheduling and optimal scheduling with TOD pricing is graphically depicted in Fig. 10. Here, it is clear that the best appliance scheduling for bill savings resulted in greater PAR and peak power consumption.

Table 9 Comparative results of minimized electricity bill for case II

Household no.	Monthly consumption in kWh	Monthly electricity bill in (INR/month)					
		Before optimization		After optimization with TOD price			
		Block rate tariff	TOD price	CS	Hybrid GA-PSO	PSO	
1	558.6	4374.09	4362.78	4342.5	4276.8	4302.75	
2	654.6	5120.66	5107.40	5084.0	5023.5	5066.25	
3	947.4	7397.69	7378.51	7378.5	7150.23	7287.50	
4	1142.4	8914.68	8891.0	8897.0	8591.4	8891.25	
5	1312.5	10236.98	10210.41	10166.0	9950.0	10140.0	
6	1732.5	13503.21	13468.14	13419.0	13350.0	13356.75	
7	2392.5	18635.87	18587.43	17744.0	17640.4	17677.50	
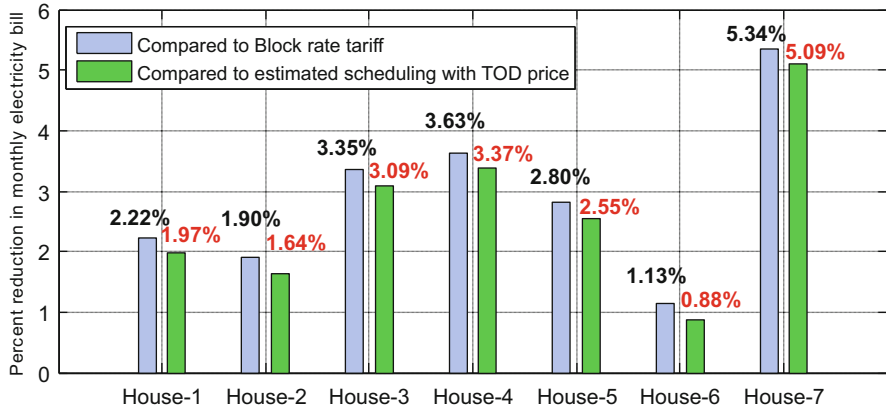
Fig. 9 Reduction in monthly electricity bill using TOD price with optimal scheduling

Table 10 Peak demand and peak-to-average ratio (PAR) for case II

Household no.	By estimated scheduling		Resulted by optimal scheduling	
	PAR	Peak demand (kW)	PAR	Peak demand (kW)
1	2.990	2.33	4.567	3.56
2	3.203	2.92	4.443	4.05
3	2.689	3.35	2.835	3.53
4	2.325	3.68	3.039	4.81
5	2.184	3.98	3.436	6.26
6	2.450	5.88	4.321	10.37
7	1.983	6.59	3.724	12.38
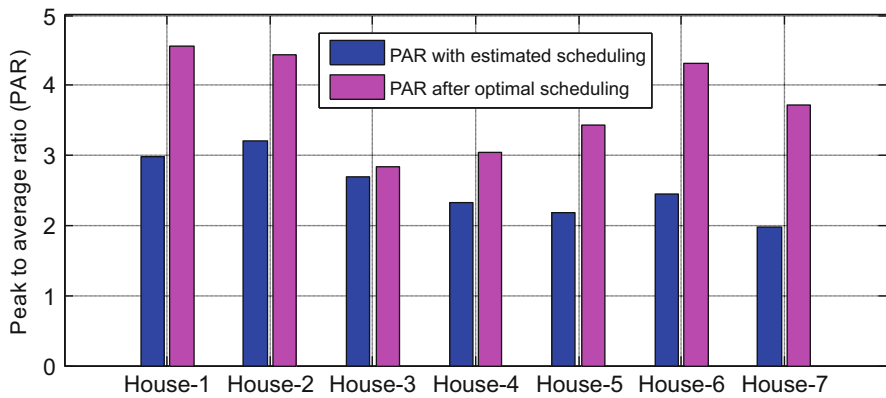
Fig. 10 Comparison of PAR before and after optimal scheduling for case II

Table 11 Objective and optimal load obtained with ToU price

Time slot	Power demand (kW)		Time slot	Power demand (kW)	
	Objective	Optimal		Objective	Optimal
T1	8.82	7.46	T13	18.18	13.88
T2	8.82	7.39	T14	18.18	14.55
T3	8.82	8.21	T15	18.18	14.52
T4	8.82	9.00	T16	18.18	13.36
T5	8.82	9.00	T17	18.18	13.25
T6	8.82	10.48	T18	12.75	14.38
T7	8.82	10.35	T19	12.75	14.38
T8	12.75	14.50	T20	8.82	12.31
T9	12.75	15.38	T21	8.82	12.31
T10	12.75	15.72	T22	8.82	10.83
T11	12.75	15.25	T23	8.82	10.58
T12	18.18	13.87	T24	8.82	10.42
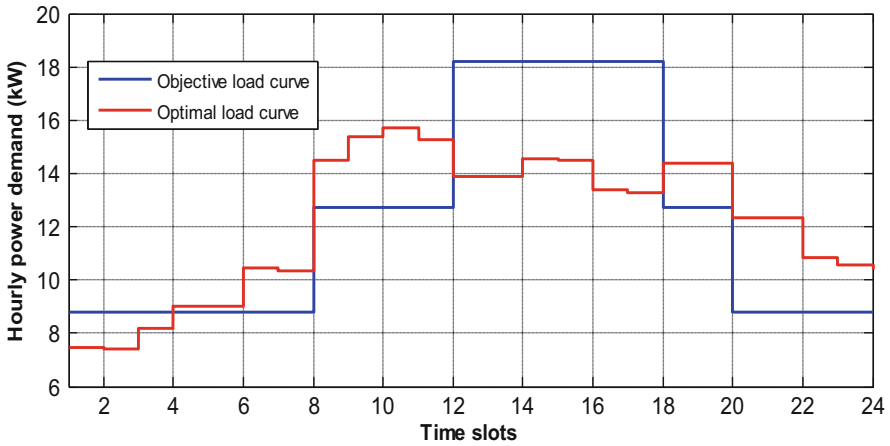
Fig. 11 Comparison of objective and optimal hourly power demand (kW)

5.2 Scenario 2: Minimization of Peak Demand and Electricity Cost Simultaneously

For the peak demand management, an objective load curve is prepared for 24 hours using Eq. (4) with a ToU price for all the seven households. Then optimal power demand is observed by minimizing the difference between optimal and objective load curves using Eq. (3). Table 11 gives the objective and optimal power demand collectively for all seven households. Figure 11 represents the comparison of objective and optimal load demand for both cases.

Figures 12, 13, and 14 represent the objective and optimal load curves, respectively, for household 4, household 5, and household 6. Similar curves can also be
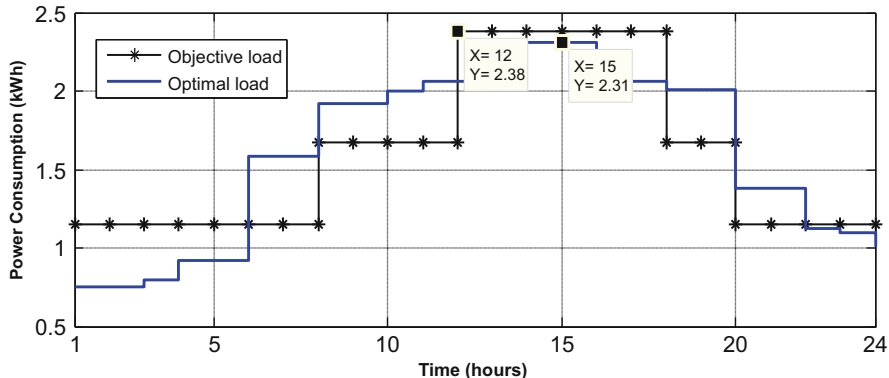
Fig. 12 Objective and optimal load curves for household 4
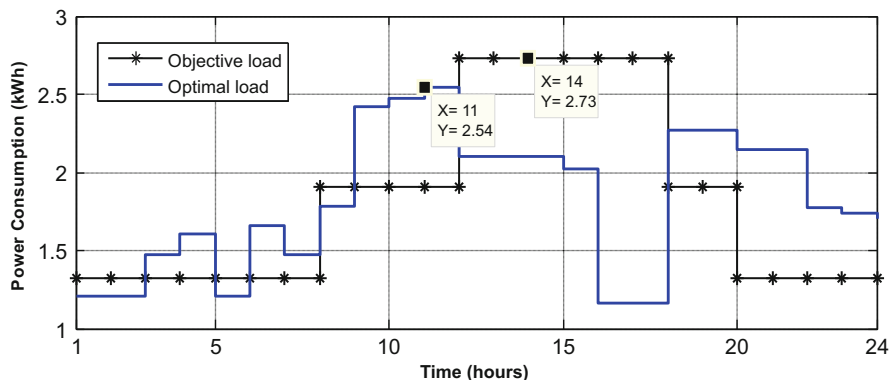
Fig. 13 Objective and optimal load curves for household 5

drawn for other households. The data tips given on the scheduling curves show the peak power consumption. Here, X shows the time slot, and Y represents the value of peak demand that can be verified with the results given in Table 12. Table 12 provides information on PAR and peak demand with optimal scheduling for all the households obtained by hybrid version of PSO as optimization algorithm for both the case studies. Table 13 displays the best values of the monthly power cost with optimal allocation of appliances for both the cases.

As compared to the electricity costs with block rate tariff and ToU price (before optimization), the average power costs for all homes after optimization in scenario 2 are reduced by *9.10%* and *8.44%*, respectively (results are given in Tables 7 and 13). Similarly, by comparing the results for case II given in Tables 9 and 13, it is observed that optimal scheduling in scenario 2 minimized the electricity cost by *7.98%* and *7.74%* as compared to the electricity cost with block rate tariff and TOD price before optimal scheduling. Optimal scheduling of smart home appliances in
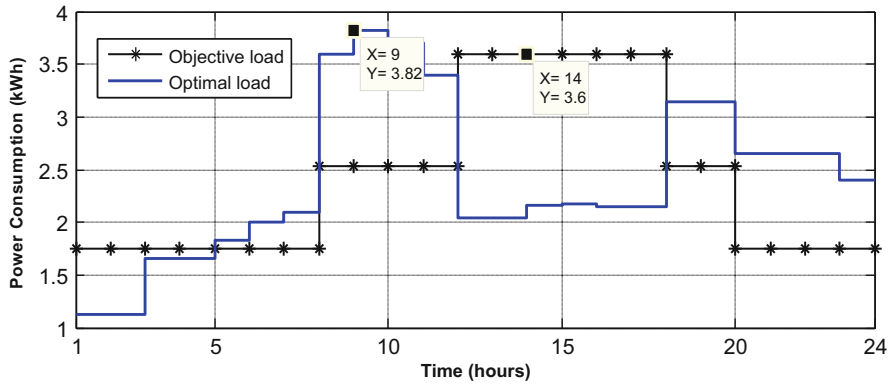
Fig. 14 Objective and optimal load curves for household 6

Table 12 PAR and peak power demands by optimal scheduling

		Before optimal scheduling		After optimal scheduling	
S. no.	Household no.	PAR	Peak demand (kW)	PAR	Peak demand (kW)
1	1	2.990	2.33	2.552	1.98
2	2	3.203	2.92	2.626	2.39
3	3	2.689	3.35	1.965	2.41
4	4	2.325	3.68	1.952	2.31
5	5	2.184	3.98	1.823	2.54
6	6	2.450	5.88	2.137	3.82
7	7	1.983	6.59	1.957	6.51

Table 13 Monthly electricity cost in case I and case II by optimal scheduling

S. no.	Household no.	Optimal electricity cost in case I ($/month)	Optimal electricity cost in case II (INR/month)
1	1	85.13	4061.45
2	2	100.56	4712.96
3	3	135.92	6882.51
4	4	152.46	8192.48
5	5	181.29	9241.30
6	6	225.74	12650.63
7	7	300.53	16839.41

scenario 2 also resulted in reduced PAR and peak power demand in comparison with estimated scheduling of *15.18%* and *24.41%*, respectively.

6   Conclusion

In this research work, a number of simulations were performed under two scenarios using real data of different pricing schemes applicable to Tehran Power Distribution Company, Iran, and Kerala State Electricity Board (KSEB), India. The problem of optimal scheduling of household appliances in order to minimize two objectives, viz., monthly electricity bill cost and peak power demand, while considering the consumer's preferences of use, is solved by single interval programming using MATLAB. The efficiency and effectiveness of the suggested model are represented by a comparison of results obtained using artificial intelligence-based optimization algorithms. A person using a smart home energy controller with dynamic pricing will have great control over how much electricity he or she uses.

References

1. Anees, A., Dillon, T., Wallis, S., & Chen, Y.-P. P. (2021). Optimization of day-ahead and real-time prices for smart home community. *International Journal of Electrical Power & Energy Systems, 124*, 106403, ISSN 0142-0615.
2. Goyal, G. R., & Vadhera, S. (2020). Challenges of implementing demand side management in developing countries. *Journal of Power Technologies, 100*(1), 43–58, ISSN: 2083-4187.
3. Albadi, M. H., & El-Saadany, E. F. (2007). Demand response in electricity markets: An overview. In *2007 IEEE Power Engineering Society General Meeting*. IEEE.
4. Barbato, A., & Capone, A. (2014). Optimization models and methods for demand-side management of residential users: A survey. *Energies, 7*(9), 5787–5824.
5. Rasheed, M. B., et al. (2016). Real time information based energy management using customer preferences and dynamic pricing in smart homes. *Energies, 9*(7), 542.
6. Ahmad, S., et al. (2020). Joint energy management and energy trading in residential micro grid system. *IEEE Access, 8*, 123334–123346.
7. Mahmood, A., et al. (2014). A new scheme for demand side management in future smart grid networks. *Procedia Computer Science, 32*, 477–484.
8. Vidal, A. R. S., Jacobs, L. A. A., & Batista L. S. (2014). An evolutionary approach for the demand side management optimization in smart grid. In *IEEE Symposium on Computational Intelligence Applications in Smart Grid (CIASG)*.
9. Sharma, A. K., & Saxena, A. (2019). A demand side management control strategy using Whale optimization algorithm. *SN Applied Sciences, 1*, 870.
10. Zhao, Z., Lee, W. C., Shin, Y., & Song, K.-B. (2013). An optimal power scheduling method for demand response in home energy management system. *IEEE Transactions on Smart Grid, 4*(3), 1391–1400.
11. Goyal, G. R., & Vadhera, S. (2021). Multi-interval programming based scheduling of appliances with user preferences and dynamic pricing in residential area. *Sustainable Energy, Grids and Networks, 27*, 100511, ISSN: 2352-4677.
12. Mellouk, L., et al. (2018). Genetic algorithm to solve demand side management and economic dispatch problem. *Procedia Computer Science, 130*, 611–618.
13. Yahia, Z., & Pradhan, A. (2020). Multi-objective optimization of household appliance scheduling problem considering consumer preference and peak load reduction. *Sustainable Cities and Society, 55*, 102058, ISSN 2210-6707.
14. Ahmad, S., Muhammad, N., & Ayaz, A. (2020). Unified optimization model for energy management in sustainable smart power systems. *International Transactions on Electrical Energy Systems, 30*(4), e12144, ISSN: 2050-7038.

15. Hussain, H. M., Javaid, N., Iqbal, S., Hasan, Q. U., Aurangze, K., & Alhussein, M. (2018). An efficient demand side management system with a new optimized home energy management controller in smart grid. *Energies, 11*, 190.
16. Goyal, G., & Vadhera, S. (2019). Solution of combined economic emission dispatch with demand side management using meta-heuristic algorithms. *Journal Européen des Systemes Automatisés, 52*(2), 143–148.
17. Hamed, S. G., & Kazemi, A. (2017). Multi-objective cost-load optimization for demand side management of a residential area in smart grids. *Journal of Sustainable Cities and Society, 32*, 171–180.
18. Samuel, O., Javaid, S., Javaid, N., Ahmed, S. H., Afzal, M. K., & Ishmanov, F. (2018). An efficient power scheduling in smart homes using Jaya based optimization with time-of-use and critical peak pricing schemes. *Energies, 11*, 3155.
19. Saravanan, B. (2015). DSM in an area consisting of residential, commercial and industrial load in smart grid. *Frontiers in Energy, 9*, 211–216.
20. Bedia, A. S., Aditya, P. V., Waseem Ahmada, M., Swapnil, S., Rajawat, K., & Anand, S. (2018). Online algorithms for storage utilization under real-time pricing in smart grid. *Journal of Electrical Power and Energy Systems, 101*, 50–59.
21. Hussain, H. M., Javaid, N., Iqbal, S., Hasan, Q. U., Aurangzeb, K., & Al-Hussein, M. (2018). An efficient demand side management system with a new optimized home energy management controller in smart grid. *Energies, 11*, 190.
22. Nguyen, H. K., Song, J. B., & Han, Z. (2012). Demand side management to reduce peak-to-average ratio using game theory in smart grid. In *Proceedings*. IEEE INFOCOM, pp. 91–96.
23. Ahmad, S., et al. (2018). A compendium of performance metrics, pricing schemes, optimization objectives, and solution methodologies of demand side management for the smart grid. *Energies, 11*(10), 2801.
24. Yang, X.-S., & Deb, S. (2009). Cuckoo search via Lévy flights. In *World Congress on Nature & Biologically Inspired Computing, NaBIC*. IEEE, pp. 210–214.
25. Goyal, G. R., & Mehta, H. D. (2015). Multi-objective optimal active power dispatch using swarm optimization techniques. In *2015 5th Nirma University International Conference on Engineering (NUiCONE)*, pp. 1–6.
26. Cheng, Z., Wang, J., Zhang, M., Song, H., Chang, T., Bi, Y., & Sun, K. (2019). Improvement and application of adaptive hybrid cuckoo search algorithm. *IEEE Access, 7*, 145489–145515.
27. Singhal, K., & Goyal, G. R. (2018). Comparative study of power consumption minimization in analog electronic circuit using AI techniques. *European Journal of Electrical Engineering, no. 427*, 438.
28. Electricity prices in Canada. https://www.energyhub.org/electricity-prices/. Accessed 09 Dec 2019.
29. Faisal, T., Salem, A., & Ghulam, A. (2020). Solving renewables-integrated economic load dispatch problem by variant of metaheuristic bat-inspired algorithm. *Energies, 13*, 6225, ISSN: 1996-1073.
30. Samuel, O., Javaid, N., Ashraf, M., Ishmanov, F., Afzal, M. K., & Khan, Z. A. (2018). Jaya based optimization method with high dispatchable distributed generation for residential microgrid. *Energies, 11*, 1513.

Optimal Placement of Photovoltaic Systems and Wind Turbines in Distribution Systems by Using Northern Goshawk Optimization Algorithm

Bach Hoang Dinh (iD)**, Thuan Thanh Nguyen** (iD)**, and Thang Trung Nguyen** (iD)

1 Introduction

In modern power systems, distribution networks have a vital role in transferring electricity from national transmission networks to customers, especially at major loads in high/medium voltages. Recently, due to many benefits in economics and engineering, integrating distributed generators (DGs) into distribution networks becomes an emerging trend, especially with the presence of renewable power sources. The installation of DGs could reduce the burden on generating side which most power is produced from bundle generating sources located far from demand side as well as requiring a lot of financial resources in a long time. In addition, the amount of power supplied locally by DGs also scales down the current value circulated through transmission and distribution lines, and then the power loss as well as power quality will be significantly improved and optimized substantially. Moreover, if DGs are renewable energy type, e.g., wind, solar, and hydrogen, they also contribute to environment protection by reducing emission and improving the

B. H. Dinh
Faculty of Electrical and Electronics Engineering, Ton Duc Thang University, Ho Chi Minh City, Vietnam
e-mail: dinhhoangbach@tdtu.edu.vn

T. T. Nguyen
Faculty of Electrical Engineering Technology, Industrial University of Ho Chi Minh City, Ho Chi Minh City, Vietnam
e-mail: nguyenthanhthuan@iuh.edu.vn

T. T. Nguyen (✉)
Power System Optimization Research Group, Faculty of Electrical and Electronics Engineering, Ton Duc Thang University, Ho Chi Minh City, Vietnam
e-mail: nguyentrungthang@tdtu.edu.vn

reliability of network operation. Therefore, the research field regarding optimal integrating DGs into distribution networks has attracted many researchers all over the world. These studies aim to determine the optimal location and size of DGs in distribution networks so that the considered systems reach the minimization of one or more objective functions while satisfying the limitations. They are primarily classified into sub-items, such as integrating general DGs [1–10], analyzing DG-based wind [11–18], allocating DG using solar energy [19–26], and combining solar and wind energy DGs [27–33].

As the main purpose of installing DGs in distribution systems is to produce active power locally, most studies have focused on searching for optimal positions of DGs and how to reduce active power loss rather than to obtain a better voltage profile. In [1], the objective of power loss as well as loss sensitivity index was analyzed to optimize sizes and locations of DGs for IEEE 33-node configuration. Another way of allocating DGs according to reconfiguration of distribution networks to minimize the power losses was mentioned in [2]. It was accomplished by combining between load flow analysis and metaheuristic algorithms where traditional load flow analysis methods, e.g., Newton-Raphson or Gauss-Seidel, were used to analyze the power flow and a metaheuristic method selected optimal size and location for each DG in the network. In study [3], various benchmark networks, including IEEE 33 nodes, IEEE 69 nodes, and IEEE 85 nodes, were applied to determine the appropriate size and position of DGs to minimize the total power loss. Besides reducing the power loss, the presence of DGs can enhance voltage stability. In the study [4], an IEEE 33-node configuration was applied to demonstrate the general effect of installing DGs for distribution networks in both aspects of active and reactive power. Another study in [5] focused on solutions to combine DGs of photovoltaic systems and wind energy so that the network was avoided from overload in lines as well as voltage stagnation at loads, and an IEEE 33-node configuration was tested by applying a new planning method with different stages. Similarly, to reduce the voltage stagnation and switching number during network reconfiguration, installing DGs has been considered in [6] where an IEEE 69-node configuration was used to investigate the effectiveness of the applied method.

In operation of distribution networks, wind-based generators (WGs) have a better contribution to the grid than that of solar-based generators (SGs) because they can simultaneously control active and reactive power. Moreover, a wind power source has also higher power capacity than that of a solar source. However, it is not flexible in setting location and capacity. Doubly-fed induction generator (DFIG), which stator windings are connected to the grid and rotor windings are connected to the converter via slip rings and back-to-back voltage source converter that controls both the rotor and the grid currents [11], is widely used in wind turbine industry. In [12], particular benefits of installing WGs appropriately in distribution networks were analyzed, and the study in [13] discussed the cutting edges of energy storage system in the unbalanced distribution network. More specifically, the steady-state operation of DFIG has been analyzed in various conditions corresponding to several types of turbines which were placed in the unbalanced distribution network in [14]. One of the most comprehensive studies about WGs integrating in distribution networks was described by [15] in which various computing methods have been applied to

determine the optimal size and the suitable location of wind turbines, and a wide range of setting parameters has been analyzed in various models of wind turbines as well as considered the power factor of wind turbines at PPT point. Another trend, integrating wind power in combined heat and power systems, has been mentioned in [16] where the operation results were significantly improved by reducing the fuel cost by 8% and power loss by 5% and improving the voltage profile better than 0.5% in an IEEE 33-node configuration.

Photovoltaic module-based generators (PVGs) are the most popular DGs in renewable types due to high flexibility in setting location and capacity as well as cost-effectiveness. In [19, 20], small-scale PVGs were applied to assess the influences of these sources on load curve at the peak time. Another study [21] has focused on how to reduce the investment cost of distribution networks efficiently by placing PVGs appropriately. The impact of placing PVGs on active and reactive power loss and node voltage amplitudes was investigated by the optimization methods, and three benchmark distribution networks including IEEE 33-node, IEEE 69-node, and IEEE 84-node systems have been applied in [11]. Another research in [22] has considered two different objective functions including total installing and operating PVGs and energy purchase cost at slack bus. In [18], the research has investigated the combination of PVGs and the hydrothermal systems in short-term period within 1 day. Total generation cost and polluted emission of thermal generating sources of the hybrid systems have been minimized effectively by different metaheuristic methods.

Recently, to maximize the advantages of both PVGs and WGs, a new trend of integrating multi-renewable sources in distribution networks has been taken much attention of researchers in optimal power system problems. For example, the optimized integration of wind turbines and solar panels has been applied to solve the optimal load flow problem with different objective functions in IEEE 33-node configuration [27, 28]. In addition, the uncertainties of solar energy and wind power have been considered. In the studies [29, 30], the process of optimizing size and location of PVGs and WGs in distribution network has been considered under the consideration of demand-side response with many different objective functions, such as total power loss, annual cost, and annual demand response compensation as well as voltage stability index. Another trend integrating wind turbines and solar panels to solve the reconfiguration problems of distribution networks has been investigated in [31] where the unpredictable variation of load demand and the uncertainties of renewable generating sources were also considered. Moreover, to resolve the problem of unpredictable power output from renewable sources, a hybrid wind-solar system combined with battery storage [32] has been proposed and optimized in terms of design and allocation of each source type.

To determine the optimal size and location for DGs, most of the mentioned studies have applied metaheuristic algorithms, the combination among those such algorithms or hybrid methods which are combined between a metaheuristic algorithm and a non-metaheuristic method. However, for more complicated optimization problems, e.g., integrating both PVGs and WGs in distribution networks, metaheuristic algorithms are essentially sole approaches to determine the optimal solutions, for example, whale optimization algorithm (WOA) [1]; PathFinder algorithms (PA) [2];

the Manta ray foraging optimization algorithm [3]; symbiotic organism search algorithm (SOSA) [4]; shuffled frog-leaping algorithm (SFLA) [6]; marine predators algorithm (MPA) [8]; hybrid artificial bee colony algorithm (HABC) [11]; genetic algorithm (GA) and social welfare, multi-objective genetic algorithm (MOGA) and non-dominated sort GA-II (NSGA-II) [12]; inherited competitive swarm optimizer (ICSO) [13]; quantum-inspired particle swarm optimization (QPSO) [16]; and multi-objective artificial electric field algorithm (MOAEFA) [17]. Other popular methods can be list as Newton metaheuristic algorithm (NMA) [19], student-based optimization algorithm (SBOA) [20], particle swarm optimization (PSO) which was applied in [21], Cuckoo search algorithm (CSA) which was utilized in [22], modified gradient-based metaheuristic optimizer (MGMO) [24], and improved salp swarm algorithm (ISSA) [31]. Another approach was proposed in [27], a hybrid method including Ant Lion Optimizer (ALO) and Fuzzy Logic Controller (FLC), combining between differential evolution (DE) and improved whale optimization algorithm (IWOA) [28].

This study investigates three metaheuristic algorithms including Northern Goshawk Optimization (NGO) [34], Bonobo optimizer (BO) [35], and Transient Search Optimization (TSO) [36] in solving the optimal size and location of the photovoltaic power plant (PVG) and wind power plant (WG) integrating in distribution networks. The main contributions of the study can be summarized as follows:

- Evaluate the optimal results to determine the best method among three applied methods according to the purpose of minimizing the power loss value.
- Investigate and analyze quantitatively the impact caused by PVGs and WGs for the power loss of distribution networks.

The structure of the entire study can be organized in five sections consisting of the following:

Section 1 – Introduction: Generally, reviews about the considered problem and existing approaches.
Section 2 – Problem description: Mentions about the main goal and related restrictions on the considered problem.
Section 3 – Proposed optimization algorithm: Describes how the proposed methods are applied to solve the problem.
Section 4 – Results: Depicts, evaluates, and discusses the results in different case studies.
Section 5 – Conclusion.

2 Problem Formula

One of the most popular structures of electric distribution networks is the radial distribution network configuration (RDNC) which consists of distribution lines, source buses, and load buses. The main goal of this study is to locate and select

the capacity of PVGs and WGs appropriately to shorten total power loss value of a specific radial distribution network consisting of N_{br} distribution lines, N_{no} buses, and N_{Ld} load buses. WGs are supposed to generate both active and reactive power into RDNC, while PVGs only supply active power. Optimally placing DGs in RDNC will decrease the electric currents circulated in the distribution lines as well as total power loss value.

In the next subsections, the mathematical expressions of the main goal as well as related constrains will be presented and described in detail. The entire process of the considered problem can be summarized as follows: metaheuristic algorithms will be applied to determine the optimal size and location of PVGs and WGs so that the power loss value is minimized as much as possible. However, the computation of power loss value is obtained by applied backward/forward sweep (BFS) [3].

2.1 The Main Goal and Its Mathematical Expression

Two of the most concerns in RDNC operation are voltage drop and current on distribution lines. Voltage and current have a mutual relationship where if voltage magnitudes between the sending end and receiving end are high, the value of current sent through the conductor is low and vice versa. In addition, the power loss is also greater if the current is high. Hence, shortening power loss in distribution networks is always an important target, and the mathematical expression for this objective can be described by:

$$\text{Minimize } \Delta\text{AP} = \sum_{x=1}^{N_{\text{br}}} \Delta\text{AP}_{\text{br}x} \tag{1}$$

where $\Delta AP_{\text{br}x}$ is the active power loss in the xth branch of the considered RDNCs.

2.2 Renewable Energy Sources

2.2.1 The Electricity Generation of Photovoltaic Power Generators (PVGs)

The power output produced by PVGs is based on the solar irradiance and embedded temperature of the site. If the solar irradiance is determined, the generated power will be calculated by using solar radiation function [26] as follows:

$$\text{SP}_q = \begin{cases} \text{SP}_q \times \frac{(\text{Ra}_q)^2}{(\text{Ra}_{\text{CIP}}.\text{Ra}_{\text{st}})}, & \left(0 < \text{Ra}_q < \text{Ra}_{\text{st}}\right) \\ \text{SP}_q \frac{\text{Ra}_q}{\text{Ra}_{\text{CIP}}}, & \left(\text{Ra}_q \geq \text{Ra}_{\text{st}}\right) \end{cases} \tag{2}$$

where SP_q is the power output produced by the qth PVG, Ra_q is the solar radiation of the location where the qth PVG is located (W/m^2), Ra_{CIP} is the solar radiation in standard environment (W/m^2), and Ra_{CIP} is the certain irradiance point (W/m^2).

2.2.2 The Electricity Generation of Wind-Based Generators

In this study, the type of wind generators installed in distribution networks is DFIG technology. It allows WGs to inject both active and reactive power into grids. Suppose that the power factors of all WGs are all the same and fixed at 0.95. According to [30], the power output of WGs can be determined by:

$$P_{wj} = \begin{cases} 0, & v_j < v_{j,in} \text{ or } v_j > v_{j,out} \\ P_{wj,max} \times \frac{v_j - v_{j,in}}{v_{j,rate} - v_{j,in}}, & v_{j,in} \leq v_j < v_{j,rate} \\ P_{wj,max}, & v_{j,rate} \leq v_j < v_{j,out} \end{cases} \tag{3}$$

where P_{wj} is the active power generated by WT j; $P_{wj,max}$ is the maximum active power generated by WT j; $v_{j,in}$ and $v_{j,out}$ are, respectively, the cut-in and cut-out wind velocity for the jth WT; and $v_{j,rate}$ is the rate of wind velocity belonging to WT j.

2.3 The Operational Constraints

Power system is a very complicated engineering system with many restrictions in balanced and unbalanced conditions to keep the system in stable operation. The occurrence of PVGs and WGs in distribution networks will affect the original operation states of the systems, such as voltage magnitude at buses, current value at each distribution line, and active and reactive power flows of electric sources and lines. The change of these parameters must be restricted in allowed ranges to assure that the entire system will operate safely, efficiently, and economically. Constraint of parameters is expressed as follows:

- Voltage magnitude constraint: This condition means that the voltage magnitude at all nodes of RDNCs must be restricted in the boundaries between the maximum and minimum values. It can be described by the expression below:

$$V_{min} \leq V_{nodey} \leq V_{max}; y = 1, \ldots, N_{no} \tag{4}$$

where V_{min} and V_{max} are, respectively, the minimum and maximum voltage magnitudes and V_{nodey} is the voltage value of node y.

- Line current constraint: Unlike bus voltages, the current through each distribution line is only restricted by its designed capability corresponding to the size and

material of conductors. That parameter can be seen as the maximum current capability of the line without overload or damage. In a normal condition, an operation current of a specific distribution line must be not higher than its designed current capability and presented by:

$$I_{brx} \leq I_{brx}^{Cap}; x = 1, \ldots, N_{br} \tag{5}$$

where I_{brx}^{Cap} is the designed capability of the distribution line x.

• Constraint of installation places of PVGs and WGs: The location of PVGs and WGs can be placed at nodes in distribution networks except for Node 1 (source node), which is the traditional generating source of the system. The location limits are formulated as follows:

$$2 \leq LC_{PV,q} \leq N_{no} \tag{6}$$

$$2 \leq LC_{WT,n} \leq N_{no} \tag{7}$$

where $LC_{PV, q}$ and $LC_{WT, n}$ are, respectively, the locations of PVS q and WT n in RDNC.

3 The Northern Goshawk Optimization

3.1 The Main Inspiration

The main idea of the Northern Goshawk Optimization (NGO) has been primarily inspired from hunting actions of the Northern Goshawk bird in nature. The species is a member of Accipiter family and mainly dwell on Eurasia and North America. The potential prey of Northern Goshawk could be any small creatures such as mice, rabbits, and squirrels or even several bigger animals such as raccoons and foxes. NGO is a natural behavior-based metaheuristic algorithm, and it is also acknowledged as a population-based algorithm. After running and comparing NGO with 8 other metaheuristic algorithms including genetic algorithm (GA), particle swarm optimization (PSO), teaching-learning-based optimization (TLBO), grey wolf optimizer (GWO), gravitational search algorithm (GSA), tunicate swarm algorithm (TSA), whale optimization algorithm (WOA), and marine predators algorithm (MPA) for solving 68 benchmark functions and 4 engineering design optimization problems [34], NGO was stated to be superior to these compared algorithms. So, NGO is suggested to be an effective algorithm for obtaining solutions of the considered problem in the study.

3.2   The Candidate Solution-Searching Process of NGO

Suppose that P_z is the population and each particle in the population is called P_j. At the initial state, each particle (also each solution) P_j ($j = 1, \ldots, P_z$) can be randomly created within the search space $[P^{\min}, P^{\max}]$ where $P^{\min}$ and $P^{\max}$ are, respectively, the minimum and maximum solutions in the search space. According to the specified objective function, each particle has a fitness value F_j. Then, NGO continues the searching process by creating new solutions as the update mechanism below.

3.2.1   The Update Mechanism

The main difference between NGO and other algorithm in the same class is its special update mechanism where a new solution is implemented by two main stages including target selection and offensive maneuver as subsections below:

- Stage 1: Target selection

  At the beginning of the stage, NGO will randomly select a particular solution Pr from the initial population (i.e., $Pr \in P_Z$). Then, each control variable in the particle P_j can be newly updated by:

$$a_{j,k}^{\text{new}1} = \begin{cases} a_{j,k} + rd_1 \left(b_k - rd_2 a_{j,k} \right), & F_{\text{Pr}} < F_j \\ a_{j,k} + rd_1 \left(a_{j,k} - b_k \right), & F_{\text{Pr}} \ge F_j \end{cases} ; k = 1, \ldots, K \& j = 1, \ldots, P_Z \tag{8}$$

  where $a_{j,k}^{\text{new}1}$ and $a_{j, k}$ are the kth new and old variables owned by the jth solution; b_k is the kth variable of the selected solution P_{pr} and $k = 1 \ldots K$ where K is the dimensions featured according to the considered problem; rd_1 is a random number in the interval between 0 and 1; rd_2 is a natural random number, either 1 or 2; and F_{Pr} is the fitness value of the selected solution P_{pr}.
- After generated by Eq. (8), each new solution is compared to its older one, and a better solution is retained to make a new group of the high-quality solutions. The detail of the first evaluation step is described by:

$$P_j = \begin{cases} P_j^{\text{new}1} & \text{if } F_j^{\text{new}1} < F_j \\ P_j & \text{else} \end{cases} \tag{9}$$

  where $P_j^{\text{new}1}$ and $F_j^{\text{new}1}$ are the jth new solution and fitness value of the jth new solution, respectively.
- It is the first evaluation step to update new solutions, called target selection, of the whole update process.
- Stage 2: The offensive maneuver

    In this stage, new variables of an updated solution can be generated by using following expressions:

$$a_{j,k}^{\text{new2}} = a_{j,k} + \text{PHR} \left(2rd_1 - 1\right) a_{j,k} \tag{10}$$

where $a_{j,k}^{\text{new2}}$ is the kth new variable owned by the jth solution in the population and PHR is the possible hunting area formulated as follows:

$$\text{PHR} = 0.02 \left(1 - \frac{It}{IT^{\text{max}}}\right) \tag{11}$$

where It and IT^{max} are the current value of iterations and the maximum number of iterations, respectively.

- Thus, the second evaluation step to update new solutions, called offensive maneuver, is completed by:

$$P_j = \begin{cases} P_j^{\text{new2}} \text{ if } \ F_j^{\text{new2}} < F_j \\ P_j \quad \ \ \text{else} \end{cases} \tag{12}$$

3.2.2   The Terminated Condition

Like all other metaheuristic algorithms, the searching process of NGO is also an iterative mechanism. So, the termination condition is established according to the maximum number of iterations.

    The entire searching process for the optimal solution of NGO is described step by step as a flowchart in Fig. 1.

4   Numerical of Results

Three metaheuristic algorithms, including Bonobo optimizer (BO), Transient Search Optimization (TSO), and Northern Goshawk Optimization (NGO), have been applied to determine the optimal sizes and locations of one PVG and one WG in the IEEE 85-node distribution network configuration to minimize energy loss. After that, the best algorithm is applied to investigate the impact of energy loss on the quantity of PVGs and WGs installed in the grid. The data for wind speed [11] and solar radiation [26] are presented in Tables A.1 and A.2 of the Appendix. The structure of the IEEE 85-node distribution network [21] is shown in Fig. 2.

    The implementation of proposed approaches for the considered problem is performed on a personal computer with 2.2 GHz of the central processing unit (CPU), 8GB of RAM. The code is built and simulated on MATLAB software
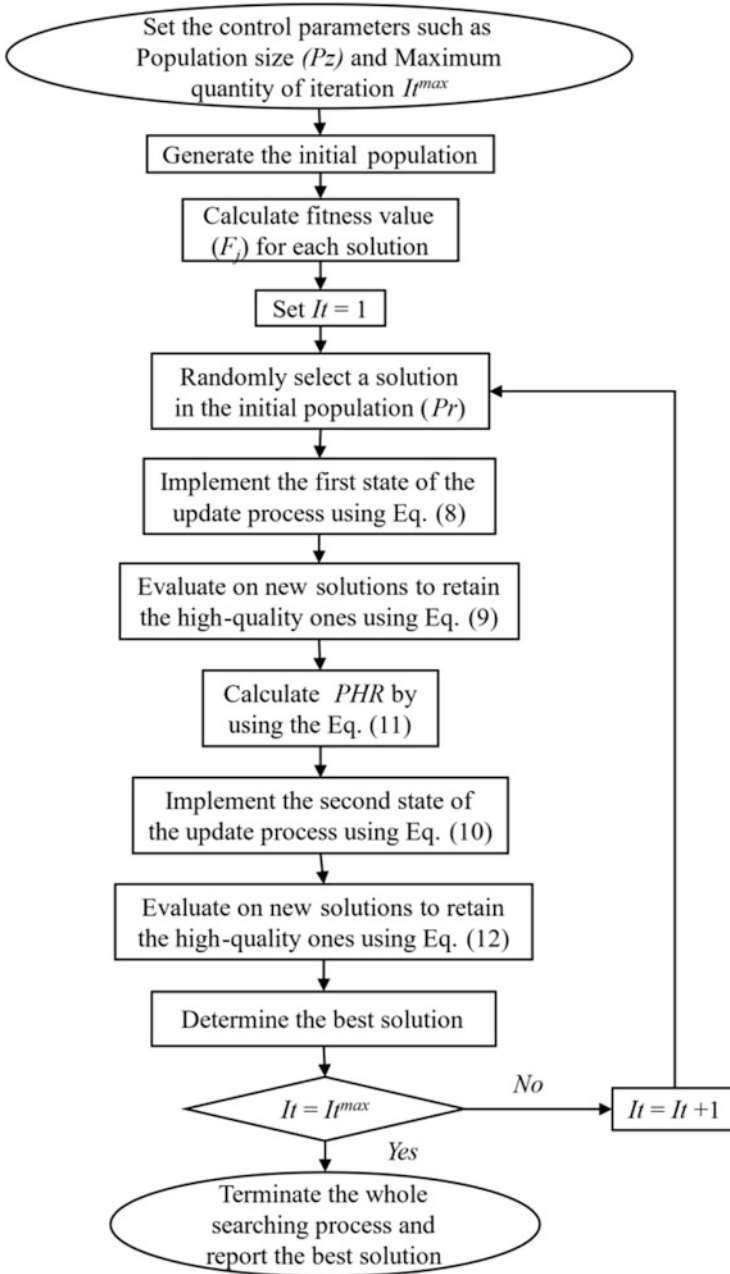
Fig. 1 NGO flowchart
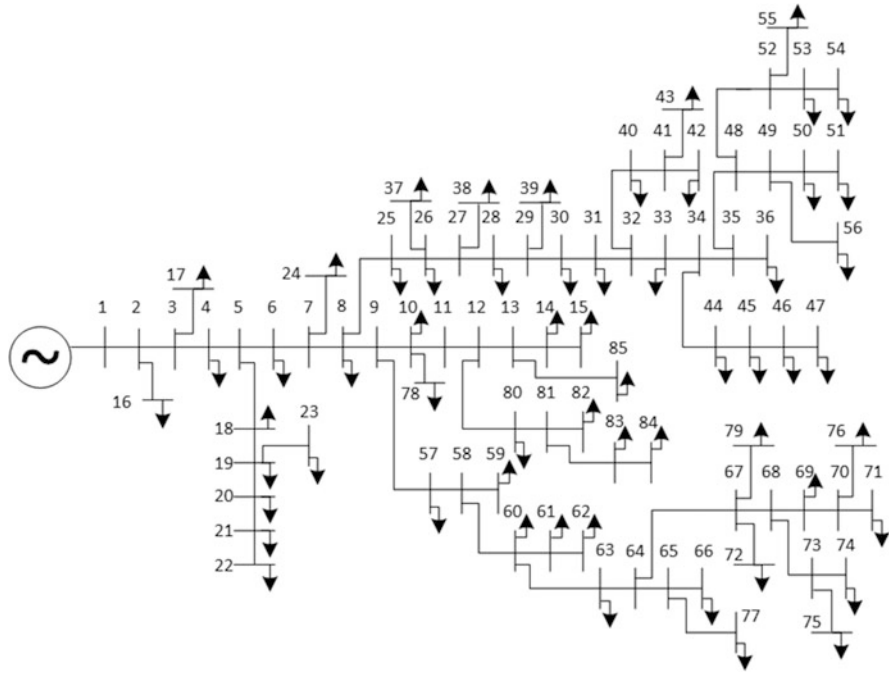
Fig. 2 The configuration of IEEE 85-node distribution network

version R 2019a. For each metaheuristic method, the evaluation is tested over 50 independent runs, and the statistical analysis is conducted for all obtained results. The control parameters of the search processes such as population size (P_z) and maximum quantity of iterations (It^{max}) are set by intuition and experiment experiences via many trials. In this research, the populations of TSO, BO, and NGO can be set as 20, 20, and 10, respectively; meanwhile It^{max} of them is set to 50.

4.1 The Determination of the Best Method for Solving the Considered Problem

The results obtained by three applied methods will be presented and analyzed in different criteria to determine the best method. The specific values in terms of optimal size and position belonging to PVG and WT are shown in Table A.3 in the Appendix. Figure 3 describes the energy loss resulted from 3 applied methods over 50 runs. The blue line represents the energy loss diagram of NGO, while the dashed black line and the dotted red line are, respectively, illustrated for those of TSO and BO. As we can see in the figure, the fluctuation of energy loss values among runs given by NGO is the smallest and that of TSO is highest among three
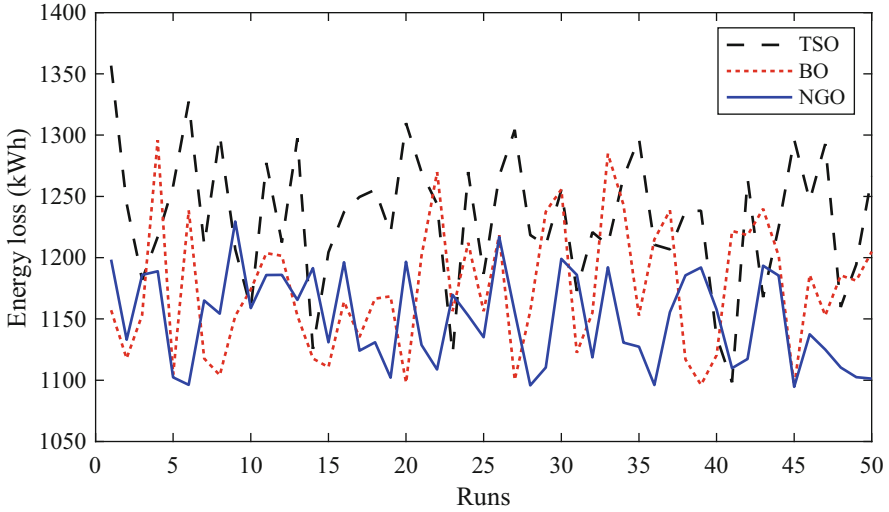
Fig. 3 The energy loss values obtained after 50 independent runs
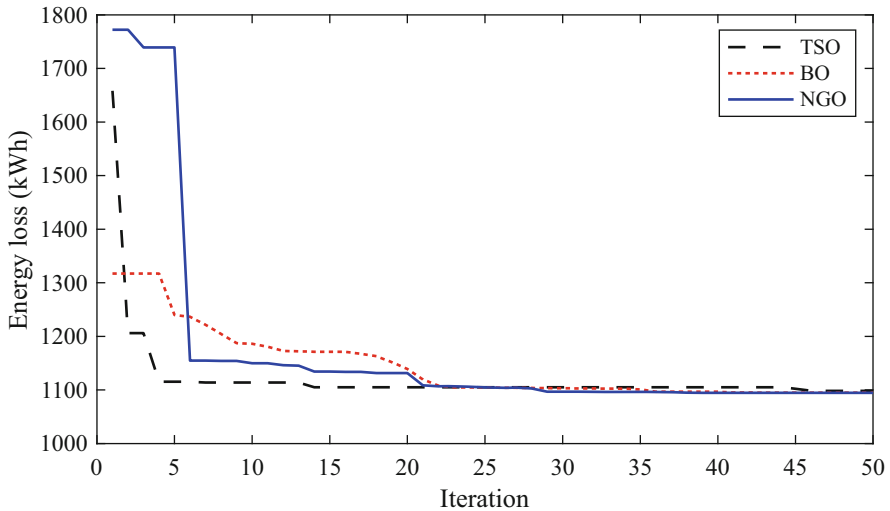
Fig. 4 The minimum convergences given by three applied methods

applied methods. It means that the optimal results obtained from many different runs of NGO vary only in a small range or, in other words, the obtained results are more reliable.

Figure 4 shows the minimum convergence curves of three applied methods. It indicates that the best convergence of these algorithms is different and NGO seems to have an outstanding performance over others. In fact, NGO only requires 30
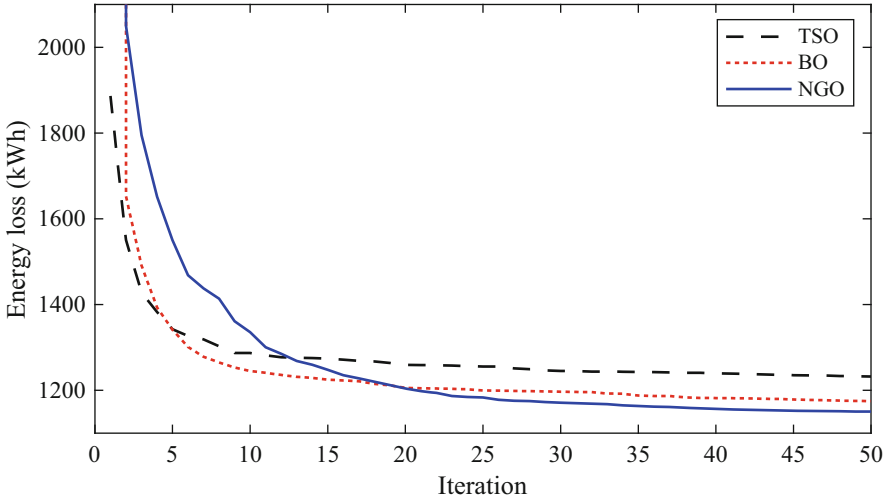
Fig. 5 The mean convergences given by three applied methods

iterations for reaching the optimal solutions, while BO utilizes over 40 iterations. On the contrary, TSO cannot determine the optimal solution even if the last iteration is reached.

The mean convergence curves obtained by three applied methods are displayed in Fig. 5. From the independent runs of 25 to the end, the blue line illustrated for NGO is always much lower than the two other ones which are displayed for BO and TSO. That means the energy loss saved by the solution determined by NGO is better than the ones reached by BO and TSO. In the considered problem, the lower the value of energy loss is determined, the more efficient the corresponding proposed method is.

Figure 6 proves the outperformance of NGO among the three applied methods in terms of the performance risk due to randomly searching solutions as indicated by the maximum convergence curves. By observing Fig. 6, it is easy to realize that the maximum values of energy loss resulting from NGO are substantially lower than both BO and TSA over 50 runs. It means that even in the poorest case, the obtained result of NGO is also better than those of BO and TSA, and it has the smallest risk among the three applied methods due to uncertain and random characteristics of metaheuristic algorithms.

Table 1 shows the comparison among three applied methods by statistical values in terms of minimum loss (min. loss), mean loss (mean loss), maximum value (max. loss), and standard deviation (STD). By looking at min. loss values, NGO gives the best result with 1094.60 kWh, while the corresponding results reached by BO and TSO are 1094.96 kWh and 1098.30 kWh, respectively. Next, while the mean energy loss obtained by NGO is only 1150.27 kWh, the relevant value given by BO is 1174.64 kWh and by TSO is 1232.10 kWh. In other words, mean loss of NGO is lower than that of BO, about 24.37 kWh, as well as lower than that of TSO by
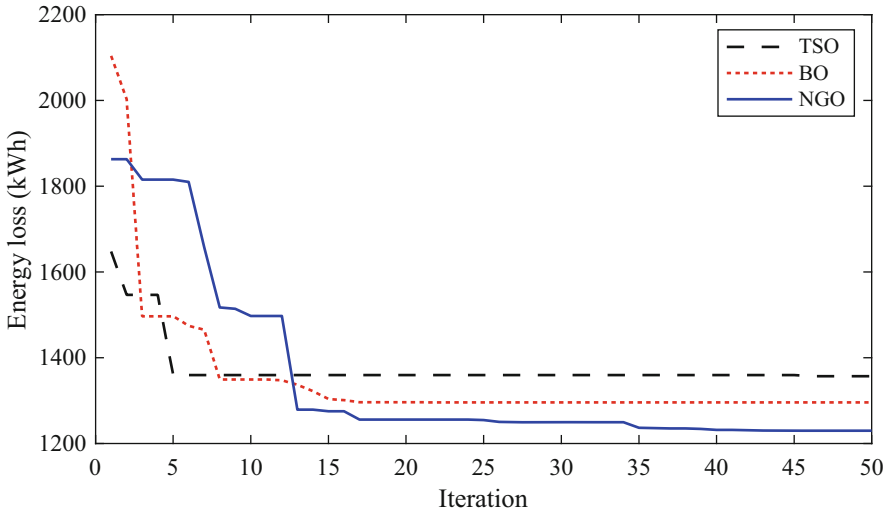
Fig. 6 The maximum convergences given by three applied methods

Table 1 The comparison on specific values resulted by three applied methods in different criterion

Method	TSO	BO	NGO
Min. loss (kWh)	1098.30	1094.96	1094.60
Mean loss (kWh)	1232.10	1174.64	1150.27
Max. loss (kWh)	1356.64	1295.93	1229.54
STD	55.14	53.34	38.01

81.83 kWh or 2.12% and 7.11% in percentage, respectively. Regarding the max. loss, we can see that NGO is the best reliable method because even in the poorest case, NGO can also reach a better solution than that of both BO and TSO. In more detail, the max. loss of NGO is smaller than that of BO, about 66.39 kWh, and that of TSO up to 127.1 kWh or 5.40% and 10.43% in percentage, respectively. Finally, by observing the STD of the three applied methods, it is easy to know that NGO is the most stable method with the STD value of only 38.01 and TSO is the poorest stable one with STD of 55.14.

According to statistical comparisons presented in Table 1, NGO is the most effective and stable method for solving the considered problem, while TSO seems to be an ineffective one due to poorer performance in all aspects.

Figure 7 presents the optimal solution of NGO, which determines the necessary amount of active and reactive power supplied by both PVG and WG. The red dotted line depicts the active power supplied by PVG, while the blue and the pink ones, respectively, describe the amount of active and reactive power injected into the grid by WG.
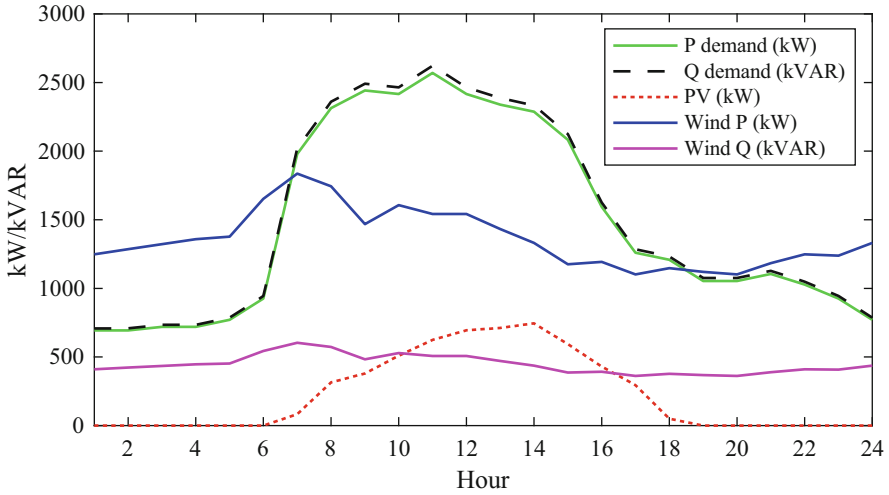
Fig. 7 The contribution of injected power from PVS and WG within 24 h
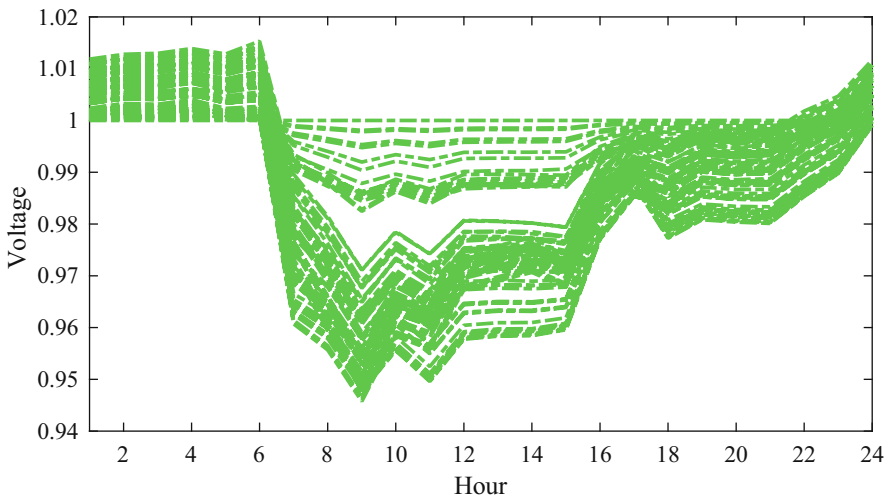
Fig. 8 Voltage profile in 24 h given by NGO

The voltage values obtained by NGO during a day for 24 h are presented in Fig. 8. These voltage values completely comply with the voltage constraints as described in Eq. (4) in Sect. 2.3. Particularly, voltage values are always located inside the upper and lower boundaries. These boundary values are preset at 0.9 and 1.1 pu, respectively.

4.2   The Investigation on Quantity of PVGs and WGs to Power Loss Value

The investigation will be conducted based on the obtained results of the considered problem in three different cases where the power loss of the IEEE 85-node distribution network is evaluated via various installation plans of PVGs and WGs in the grid. Every case has a different quantity of PVGs and WGs integrated into grid, e.g., the base case with no PVGs and WGs installed and three others, as mentioned earlier, Case 1, Case 2, and Case 3.

Figure 9 illustrates the power loss during 24 hours of the IEEE 85-node distribution network according to the specific number of PVGs and WGs installed. The black line presents the base case which no DGs is installed, the dotted red line describes the power loss of Case 1, and the blue line and the pink line, respectively, depict the obtained results from Case 2 and Case 3. As we can see in the figure, the power loss of the base case is obviously too high due to no DGs installed in the grid, while the remaining cases can significantly reduce the power loss thanks to the contribution of DGs in the grid. In addition, the different quantities of PVGs and WGs installed in the distribution network also cause different impacts on total power loss values. The greater the number of DGs installed in the grid, the more saving power/energy is obtained. However, from the economic point of view, the higher the number of DGs installed in the grid, the more investment is needed. Thus, before deciding any chosen case, we need to establish a full cost-benefit balance sheet to generally compare between saving energy cost and investment plus operation cost for each installation case of DGs.
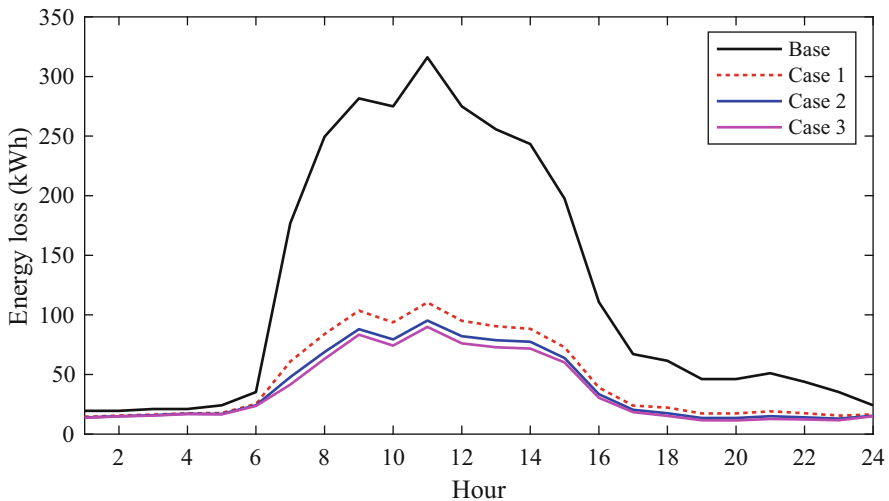
Fig. 9 Loss values given by different cases without/with PVGs and WGs
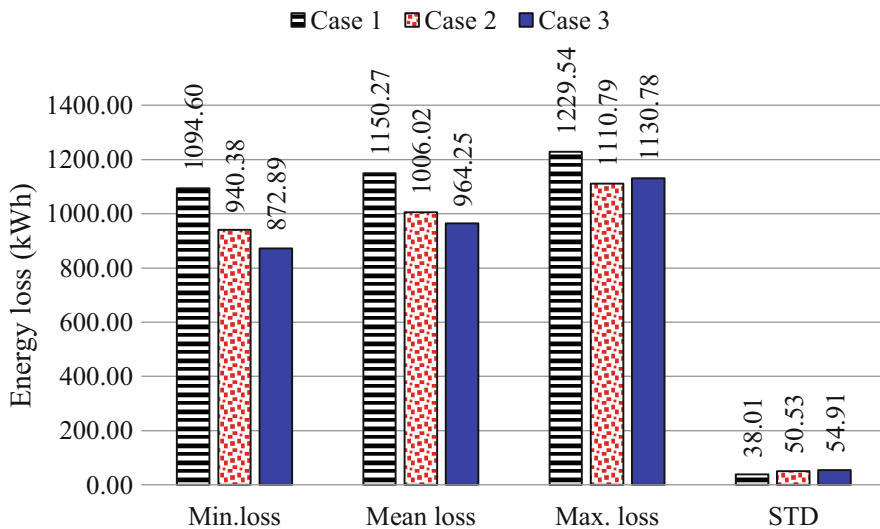
Fig. 10 The performance comparison among three installation cases in statistical criteria

Furthermore, as NGO is a metaheuristic algorithm, the impact of different quantities of PVGs and WGs to power loss value should be statistically analyzed in detail. The particular values achieved by NGO regarding optimal size and position of PVGs and WGs in Case 2 and Case 3 are presented in Table A.4 in Appendix. Figure 10 describes the investigation of power loss value over 50 runs corresponding to different numbers of PVGs and WGs in the grid.

The performance comparison among three installation cases is shown by Fig. 10 in terms of different criteria such as minimum loss (min. loss), mean loss (mean loss), maximum loss (max. loss), and standard deviation (STD). As shown in the figure, the blue bars illustrate the obtained results of Case 1, while the red bars and the black bars represent the reported results of Case 2 and Case 3, respectively. Regarding min. loss, Case 3 obtains the lowest power loss value of 872.89 kWh, while the corresponding value of Case 2 is 940.38 kWh and that of Case 1 is 1094.60 kWh. The improvement level of Case 3 compared to Case 2 and Case 1 is 7.73% and 25.40% in percentage, respectively. For another criterion, mean loss, Case 3 is also better than the ones given by Case 2 and Case 1. The mean values reported from Case 3, Case 2, and Case 1 are, respectively, 964.25 kWh, 1006.02 kWh, and 1150.27 kWh. Similar to the min. loss evaluation, the improvement levels of mean loss between Case 3 and Case 2 as well as between Case 3 and Case 1 are 4.33% and 19.29% in percentage, respectively. Regarding max. loss, Case 2 obtains the best power loss of only 1110.79 kWh, while the relevant results from Case 3 and Case 1 are 1130.78 kWh and 1229.54 kWh, respectively. Finally, the STD values show that Case 1 has the smallest value of 38.01, while the other relevant values from Case 2 and Case 3 are 50.53 and 54.91, respectively.

5 Conclusion

In this study, three metaheuristic methods are applied successfully to determine the optimal size and location of PVGs and WGs installed in the IEEE 85-node distribution network to minimize the total power loss. In addition, the study has considered the data of both solar radiation and wind speed within a day's operation for 24 h as well as respected all restrictions of the considered problem. Among the three applied methods, NGO is the outstanding method compared with other methods, including BO and TSO in terms of all aspects. Specifically, for the minimum loss value – the main target of the entire study – NGO obtained the smallest solution, while TSO reached the poorest one. Besides, other evaluation criteria including mean loss, maximum loss, and standard deviation determined by NGO are all completely superior to those values calculated by BO and TSO. Furthermore, to analyze the impact of the number of installed PVGs and WGs, the investigation through three different cases has been conducted using NGO. The optimal solutions for power loss resulting from different quantities of PVGs and WGs have proved that the greater the number of DGs is installed in the grid, the more power/energy is saved. Therefore, NGO has demonstrated to be a powerful searching method and can be highly recommended for solving the optimization problem of placing PVS and WG in distribution networks.

Appendix

To simulate the impact of PVGs and WGs on the power loss of the IEEE 85-node distribution network, solar radiation and wind speeds are used as input data for 24 hours. The solar radiation data and the wind speed data are given in Tables A.1 and A.2. Finally, the obtained results including position and size of both PVG and WG, and power loss of the system are reported in Table A.3.

Table A.1 The radiation data in 24 h within a day

Time (hour)	Gt (W/m^2)	Time (hour)	Gt (W/m^2)
1	0	13	703
2	0	14	736
3	0	15	586
4	0	16	425
5	0	17	291
6	0	18	86
7	111	19	0
8	311	20	0
9	375	21	0
10	503	22	0
11	617	23	0
12	686	24	0

Table A.2 The wind speed data in 24 h within a day

Time (hour)	Gt (W/m^2)	Time (hour)	Gt (W/m^2)
1	0	13	703
2	0	14	736
3	0	15	586
4	0	16	425
5	0	17	291
6	0	18	86
7	111	19	0
8	311	20	0
9	375	21	0
10	503	22	0
11	617	23	0
12	686	24	0

Table A.3 Optimal solutions given reported by three applied methods in Case 1

Methods	TSO	BO	NGO
Position of PVG	35	34	34
PVG size	837.445	1030.718	1012.114
Position of WG	9	9	9
WG size	1903.952	1790.142	1835.554
Energy loss	1098.30	1094.96	1094.60

Table A.4 Optimal solutions in Case 2 and Case 3

Case	Case 2	Case 3
Position of PVGs	6; 68	7; 8; 24
PVG size	1024.332; 893.433	98.488; 984.915; 337.912
Position of WGs	10; 35	13; 35; 65
WG size	1089.943; 670.594	411.510; 680.718; 623.675
Energy loss	940.38	872.89

References

1. Suyarov, A., Hasanov, M., Boliev, A., & Nazarov, F. (2021). Whale optimization algorithm for intogreting distributed generators in radial distribution network. *SSRN Electronic Journal*.
2. Alnabi, L. A., Dhaher, A., & Essa, M. (2022). Optimal allocation of distributed generation with reconfiguration by genetic algorithm using both Newton Raphson and Gauss Seidel methods for power losses minimizing. *International Journal of Intelligent Engineering and Systems, 15*.
3. Hemeida, M. G., Ibrahim, A. A., Mohamed, A.-A. A., Alkhalaf, S., & El-Dine, A. M. B. (2021). Optimal allocation of distributed generators DG based Manta Ray Foraging Optimization algorithm (MRFO). *Ain Shams Engineering Journal, 12*(1), 609–619.

4. Quoc, S. N., & Ngoc, D. V. (2020). Symbiotic organism search algorithm for power loss minimization in radial distribution systems by network reconfiguration and distributed generation placement. *Mathematical Problems in Engineering, 2020*, Article ID 1615792, 22 pages.

5. Sun, B., Li, Y., Zeng, Y., Chen, J., & Shi, J. (2022). Optimization planning method of distributed generation based on steady-state security region of distribution network. *Energy Reports, 8*, 4209–4222.

6. Asrari, A., Wu, T., & Lotfifard, S. (2016). The impacts of distributed energy sources on distribution network reconfiguration. *IEEE Transactions on Energy Conversion, 31*(2), 606–613.

7. Prakash, P., Meena, D. C., Malik, H., Alotaibi, M. A., & Khan, I. A. (2022). A novel analytical approach for optimal integration of renewable energy sources in distribution systems. *Energies, 15*(4), 1341.

8. Eid, A., Kamel, S., & Abualigah, L. (2021). Marine predators algorithm for optimal allocation of active and reactive power resources in distribution networks. *Neural Computing and Applications, 33*(21), 14327–14355.

9. Heng, P., Prasatsap, U., Polprasert, J., & Kiravittaya, S. (2019). Optimal placement of distributed generation using analytical approach to minimize losses in a university. *GMSARN International Journal, 13*(2), 81–85.

10. Kaewvata, C., Sirisamphanwong, C., & Suriwong, T. (2021). Simulation of the appropriate capacity and mouthing position of distributed battery storage systems for maintaining the power quality in Maesariang Microgrid System. *GMSARN International Journal, 15*(3), 166–174.

11. Hao, X., Jiang, C., Wu, L., & Zhang, L. (2015). Based on the power factors of DFIG wind farm for power flow optimization. *Lecture Notes in Electrical Engineering, 334*, 157–165.

12. Mokryani, G., & Siano, P. (2015). Evaluating the benefits of optimal allocation of wind turbines for distribution network operators. *IEEE Systems Journal, 9*, 629–638.

13. Nayak, M., Behura, D., & Kasturi, K. (2021). Optimal allocation of energy storage system and its benefit analysis for unbalanced distribution network with wind generation. *Journal of Computational Science, 51*, 101319.

14. Datta, T., & Bajpai, P. (2021). Steady-state modeling of DFIG-based wind energy system for unbalanced operation. In *Handbook of renewable energy technology & systems* (pp. 3–35). World Scientific (Europe).

15. Chen, P., Siano, P., Chen, Z., & Bak-Jensen, B. (2010). *Optimal allocation of power-electronic interfaced wind turbines using a genetic algorithm – Monte Carlo hybrid optimization method*. Presented at the June.

16. Pazouki, S., Mohsenzadeh, A., Haghifam, M.-R., & Talebian, M. E. (2013). Optimal allocation of wind turbine in multi carrier energy networks improving loss and voltage profile. In *ELECO 2013 - 8th International Conference on Electrical and Electronics Engineering* (pp. 67–71).

17. Naderipour, A., Abdul-Malek, Z., Mustafa, M., & Guerrero, J. (2021). A multi-objective artificial electric field optimization algorithm for allocation of wind turbines in distribution systems. *Applied Soft Computing, 105*, 107278.

18. Yao, F., Dong, Z. Y., Meng, K., Xu, Z., Iu, H., & Wong, K. (2012). Quantum-inspired particle swarm optimization for power system operations considering wind power uncertainty and carbon tax in Australia. *IEEE Transactions on Industrial Informatics, 8*, 880–888.

19. Calero, I., Canizares, C., Bhattacharya, K., & Baldick, R. (2021). Duck-curve mitigation in power grids with high penetration of PV generation. *IEEE Transactions on Smart Grid, 13*, 314–329.

20. Adeagbo, A. P., Ariyo, F. K., et al. (2022). Integration of solar photovoltaic distributed generators in distribution networks based on site's condition. *Solar, 2*, 52–63.

21. Montoya Giraldo, O., Grisales-Noreña, L., Alvarado-Barrios, L., Arias-Londoño, A., & Alvarez, C. (2021). Efficient reduction in the annual investment costs in AC distribution networks via optimal integration of solar PV sources using the Newton Metaheuristic Algorithm. *Applied Sciences, 11*, 11525.

22. Montoya Giraldo, O., Grisales-Noreña, L., & Giral-Ramírez, D. (2022). Optimal placement and sizing of PV sources in distribution grids using a modified gradient-based metaheuristic optimizer. *Sustainability, 14*, 3318.
23. Janamala, V. (2021). A new meta-heuristic pathfinder algorithm for solving optimal allocation of solar photovoltaic system in multi-lateral distribution system for improving resilience. *SN Applied Sciences, 3*, 1–17.
24. Dash, S., & Mishra, S. (2021). Optimal allocation of photo-voltaic units in radial distribution networks using a new student psychology based optimization algorithm. *International Journal on Electrical Engineering and Informatics, 13*, 318–335.
25. Alhayali, R., Hasan, G., Salih, Z., Mohammed, M., Klib, M., & Ali, A. (2019). *Study the effect of integrating the solar energy source on stability of electrical distribution system*. Presented at the June.
26. Augusteen, W., Geetha, S., & Rengaraj, R. (2016). *Economic dispatch incorporation solar energy using particle swarm optimization*. Presented at the June.
27. Samala, R., & Kotapuri, M. (2020). Optimal allocation of multiple photo-voltaic and/or wind-turbine based distributed generations in radial distribution system using hybrid technique with fuzzy logic controller. *Journal of Electrical Engineering & Technology, 16*, 1–13.
28. Arasteh, A., Alemi, P., & Beiraghi, M. (2021). Optimal allocation of photovoltaic/wind energy system in distribution network using meta-heuristic algorithm. *Applied Soft Computing, 109*, 107594.
29. Rawat, T., Niazi, K., Gupta, N., & Sharma, S. (2020). Impact analysis of demand response on optimal allocation of wind and solar based distributed generations in distribution system. *Energy sources. Part B Economics, Planning and Policy, 16*, 75–90.
30. Taha, H., Alham, M., & Youssef, H. (2022). Multi-objective optimization for optimal allocation and coordination of wind and solar DGs, BESSs and capacitors in presence of demand response. *IEEE Access, 10*, 16225–16241.
31. Fathi, R., Tousi, B., & Galvani, S. (2021). A new approach for optimal allocation of photovoltaic and wind clean energy resources in distribution networks with reconfiguration considering uncertainty based on info-gap decision theory with risk aversion strategy. *Journal of Cleaner Production, 295*, 125984.
32. Aliabadi, M., & Radmehr, M. (2021). Optimization of hybrid renewable energy system in radial distribution networks considering uncertainty using meta-heuristic crow search algorithm. *Applied Soft Computing, 107*, 107384.
33. Farzamnia, A., Marjani, S., Galvani, S., & Kin, K. (2022). Optimal allocation of soft open point devices in renewable energy integrated distribution systems. *IEEE Access, 10*, 9309–9320.
34. Dehghani, M., Hubalovsky, S., & Trojovsky, P. (2021). Northern Goshawk optimization: A new swarm-based algorithm for solving optimization problems. *IEEE Access, 9*, 162059–162080.
35. Das, A., & Pratihar, D. (2022). Bonobo Optimizer (BO): An intelligent heuristic with self-adjusting parameters over continuous spaces and its applications to engineering problems. *Applied Intelligence, 52*, 2942–2974.
36. Qais, M., Hasanien, H., & Alghuwainem, S. (2020). Transient search optimization: A new meta-heuristic optimization algorithm. *Applied Intelligence, 50*, 3926–3941.

Granulated Silicon and Thermal Energy Converters on Its Basis

B. M. Abdurakhmanov, M. M. Adilov, O. V. Trunilina, and Valeriy Kharchenko (iD)

1   Introduction

The study of the behavior of solar cells (SC) made of mono- (MS) and polycrystalline silicon (PS) at high summer temperatures, and then at even higher temperatures, i.e., beyond the range typical for operation, revealed a non-monotonous change in the energy characteristics of the PS SC. Abnormal temperature changes in the parameters were detected for the temperature dependences of dark currents and voltages of the PS SC at temperatures ~400 K and above, namely, the occurrence of peaks of short-circuit current and no-load voltage of significant magnitudes [1]. The observed phenomena were explained from the standpoint of the manifestation of the thermal-voltage effect theoretically predicted in [2], consisting in generation of charge carriers in a heated polycrystalline semiconductor with participation of deep energy levels due to grain boundaries, impurities, and other structural defects. This conclusion was confirmed by the measurement results of dark currents and voltages for samples of technical silicon (TS) remelted in a solar furnace up to temperatures of 400 K and above [3] and even for MS SC irradiated by fast electron flows ($E = 1$ MeV) or ion implanted with alkali metal ions at *p-n* transition, but in both cases without subsequent annealing of induced radiation defects [4]. Then the relationship between dark current and voltage was established, namely, their growth with an increase in the density of various type defects in the material, as well as an increase in the Seebeck coefficient by two to four times in samples made of fine-grained PS.

B. M. Abdurakhmanov · M. M. Adilov (✉) · O. V. Trunilina
Institute of Ion-Plasma and Laser Technologies of the Academy of Sciences of the Republic of Uzbekistan, Tashkent, Uzbekistan

V. Kharchenko
Federal Scientific Agroengineering Center VIM, Moscow, Russian

Based on these facts, we proposed the use of granular silicon (GS), i.e., silicon powder having the particles not sintered and not fused but simply mechanically pressed together with a certain effort to develop thermoelements. This approach has fully justified itself. It was found for GS samples that their specific thermal EMF is ten or more times higher than that of MS.

2   The Physical Mechanism of the Observed Effects

The competitiveness of a particular thermal energy converter and, accordingly, the material from which this device is made will be indisputable if TEC, in addition to accessibility and manufacturability, which in the case of silicon can be considered a solved problem, has high values of conductivity σ and, conversely, small values of thermal conductivity χ, which, along with α, determines the main parameter of the thermoelectric material – Q-factor Z [5, 6].

$$Z = \frac{\alpha^2 \, \sigma}{\chi} \tag{1}$$

The Seebeck coefficient α is considered one of the main parameters of a thermoelectric material and amounts to ~200–300 mV/K for traditional and most used thermoelectric materials such as alloys (BiTe, PbTe, SiGe) [7]. In MS, α is ~44–50 mV/K at 300 K [5].

The expediency and prospects of using GS, that is, micrograin Si powder, are undoubted, since the specific thermal EMF at 300 K was 500 microvolts per degree [8], which, as indicated above, is more than ten times higher than the tabular value of this indicator per MS and is comparable or exceeds this value for a number of traditional thermoelectric materials.

The reason for such high rates is the impurity thermal-voltage effect that, according to the theory [2], consists in the fact that isovalent impurities, or defects, a priori present in the GS and giving deep energy levels in the forbidden zone, participate in generating the electron-hole pairs, which occurs due to the absorption of heat, or photons having less energy, than the band gap width of the semiconductor. At the same time, the concentration, the degree of filling, and the position of these energy levels in the forbidden zone are very important. To fully realize the impurity thermal-voltage effect, it is necessary that the rate of generation of electrons and holes with the participation of deep levels has close values [2].

Of considerable interest is the use of data from [9] to explain the characteristics of GS, where it is shown that one of the promising directions in thermoelectricity is the creation of "electron-crystal phonon-glass" structures. Our GS object fits exactly this definition, since in GS "electronic crystal" is the grain itself – a granule or particle of silicon powder – and "phonon glass" is an oxide layer, SiO_2, on the surface of a powder particle.

By controlling the grain size, and in fact the ratio of the sum of the volumes of all grains and the sum of the volumes of all oxide layers at the intergrain boundaries, we can control the thermal conductivity of this thermoelectric material.

Recall that the experimentally estimated thermal conductivity of c micrograined silicon with a grain size of about 1–30 microns, at 300–350 K, was from 10 to 15 W/m • K, which is at least 7 times less than that of monocrystalline silicon and ~3.5 times less than that of silicon samples obtained by powder metallurgy, including operations of pressing silicon powders followed by sintering at 1500 K [10]. It should be noted that this is not the limit and there is a further possibility to reduce the value of the thermal conductivity of GS. In [10], our approach and the prospect of developments in the field of granular semiconductor materials were physically justified by considering a model of such a semiconductor.

As a result, expression (2) was obtained from which it follows that, in contrast to expression (1) for homogeneous thermoelectric materials [5], the thermoelectric Q-factor Z of granular semiconductor depends both on the characteristics of the grain itself, which determine the Seebeck coefficient, and on the properties of the nanoscale layer of silicon dioxide covering each particle, which determine the thermal conductivity and conductivity of GS.

$$Z_{\text{eff}} = \frac{\alpha_1^2 \, \sigma_2}{\chi_2} \tag{2}$$

It should be noted that theoretical estimates [10] of the thermoelectric Q-factor Z_{eff} of granular semiconductors indicate their undoubted superiority in comparison with their monocrystalline modifications.

This conclusion confirms the correctness of the present-day trend of replacing monocrystalline materials with polycrystalline ones in the field of thermoelectricity, which was first theoretically substantiated back in [11], but from completely different physical prerequisites. This conclusion is also confirmed by our experimental results in terms of increasing α and decreasing χ [10].

It should be particularly noted that silicon, despite its mastery in production and the content in the rocks of the earth's crust >25%, was practically not considered as a thermoelectric material, except in the form of alloys with germanium, due to the relatively small value of α in its single-crystal modification. However, based on the above results, we can assume that the proposed new modification in the form of GC can be used as a thermoelectric material and create new types of thermal energy converters (TEC), as well as develop prerequisites for finding new, nontrivial ways to increase the conductivity of GS, as described below.

Figure 1 presents a scheme of the electron-crystal phonon-glass (ECPG) system consisting of semiconductor particles in contact with each other, separated by a thin film of a substance with the properties sharply different from those of semiconductor. In the system, the current can only run at places of mechanical contact of semiconductor particles with each other by tunneling charge carriers through a nanoscale layer of the substance film enveloping each of them from all sides. GS can be considered as one of the real examples of the system under

Fig. 1 Structure of thermoelectric composite. (1) Granules (2) SiO$_2$ matrix (3) Tunnel contact
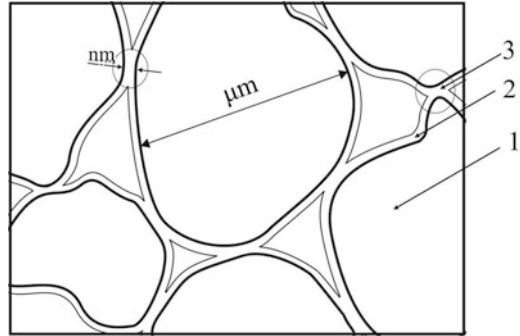
consideration where the silicon powder particles (grains) are the "electronic crystal." The role of "phonon glass" is played by a nano-thickness film of silicon dioxide naturally occurring on the surface of silicon powder particles when they come into contact with oxygen in the air.

Of the values σ_{eff}, α_{eff}, and χ_{eff}, it is possible to form an important dimensionless expression in thermoelectricity that characterizes the conversion efficiency:

$$ZT = \frac{\sigma_{\text{eff}}\, \alpha_{\text{eff}}^2}{\chi_{\text{eff}}} T \tag{3}$$

where Z is the Q-factor and T is the average temperature of the thermoelement.

In our case, when one of the "phases" is actually a tunnel contact, then we can talk about a heterosurface with tunnel contacts. As shown by the studies in [12], the most important element in terms of increasing Z_{eff} is tunnel contacts. In our case, such tunnel contacts are SiO$_2$-isthmuses between Si grains. The essence of the whole problem is to find conditions for optimizing the process of tunneling charge carriers through tunnel contacts [12, 13].

It is important to note that in these works we are talking about the usual ("Gamow") tunneling of an electron with probability:

$$D^{(1)}(E) = \exp\left[-\frac{2}{h}\sqrt{2m\,(V-E)x}\right] \tag{4}$$

Here, $V - E$ is the distance from the top of the potential barrier to the energy level of the particle and x is the barrier width. Since the tunnel contact conductivity is determined by the following expression [13]:

$$\sigma_{\text{TK}}^{(1)} = \text{const} \int_0^\infty \frac{D\,(\varepsilon^*)}{1 + \exp\left(\varepsilon_x^* - \mu^*\right)}\, d\varepsilon^* \tag{5}$$

where $\varepsilon^* = E/\kappa T$, $\mu^* = \mu/\kappa T$ is the reduced level of energy and chemical potential, and then the expression (5) as $D(\varepsilon^*)$ leads to a rather sharp drop with the growth of x.

In [10], we modified the "Gamow" tunneling model by introducing two incoherent electron jumps through an intermediate defective state inside the tunnel contact. It has been shown that in this case:

$$D^{(2)}(E) = \frac{1}{2} \exp \left[-\frac{2}{h} \sqrt{2m \left(V - E\right)}^x \Big/ 2 \right] \tag{6}$$

From the comparison of (4) and (6), it follows that this contributes to an increase in conductivity, but, unfortunately, not significantly. This conclusion was partially confirmed by our experiment during which an "island" film of conductive transition metal oxides, in particular, based on tin dioxide, was created on the surface of silicon particles coated, as mentioned above, with a nano-replaceable layer of its dioxide, outside of the mentioned silicon dioxide [14]. That is, according to [14], in order to tunnel charge carriers through a nanoscale gap of silicon dioxide, a kind of conducting "springboard" was created for each single grain from an island of tin dioxide of nanoscale thickness as well.

More promising is the organization of the so-called resonant tunneling of charge carriers through an intermediate state inside the tunnel contact itself, that is, the organization of optimal tunneling conditions in the SiO_2 nanotool film itself [10, 15].

It should be noted that resonant tunneling is fundamentally different from the "Gamovsky" one used in [12, 16], and judging by the review [17] devoted to the latest achievements in the field of composite thermoelectric materials, it is proposed in [10, 15] for use in thermoelectricity for the first time.

For the case of resonant tunneling in [10], it was shown that the probability of charge carrier tunneling with the use of a local resonant energy level specially created in a nanoscale layer of silicon dioxide with an occurrence near the bottom of the conduction band is much higher than in the case of Gamow tunneling [12, 13].

One of the ways to create such local energy levels can be irradiation, for example, with protons, neutrons, or gamma quanta. However, the process of radiation is not easy to run, especially and most importantly selection of the right dose. Our estimates show that for effective current transfer through resonant levels in silicon dioxide nanotubes, it is necessary that their number, i.e., the density of levels or states, should be an order of 10^{17}–10^{18} cm^{-3}. The desired density can be provided as a result of various types of irradiations, for example, neutron and proton irradiation strongly displacing regular atoms and gamma irradiation strongly ionizing strained chemical bonds. Using the concept of accumulated radiation through the so-called effective dose, which makes it possible to uniformly describe various types of radiation in rads [18], it can be stated that the characteristic, i.e., necessary, doses ensuring the appearance of levels at the bottom of the conduction band of silicon grains are 10^7 rad. However, firstly, this dose can be clearly insufficient for the

appearance of the desired energy levels in the forbidden zone of silicon dioxide. Secondly, if we draw an analogy with the conductivity of irradiated monocrystalline silicon, it is possible that the SiO_2 conductivity increases due to irradiation, while for the same reason, the conductivity of the silicon powder particles themselves drops sharply due to induced radiation defects causing a sharp increase in recombination of charge carriers.

At least, our irradiation of granular silicon with gamma quanta of Co^{60} within the dose range of 10^7–10^9 rad did not lead to a significant improvement in its electrical conductivity. Nevertheless, the results we obtained made it possible to formulate other technological approaches to solving the problem of increasing the conductivity of silicon dioxide covering Si powder particles in GS.

3   Application of Granular Silicon in New Types of Thermal Energy Converters

We have proposed a TEC containing a working body made of granular silicon material of the same type with impurities giving deep levels.

The TEC design is presented in Fig. 2 where it is shown in the section.

It can be seen that the TEC contains a working body (1) made of silicon powder of *n* or *p* type of conductivity. Figure 2 shows a TEC variant with a working body made of *p*-type silicon powder placed in a form-forming tubular hollow housing (2) made of a dielectric heat-conducting material, for example, ceramics. To the *p*-type silicon powder made by grinding the SHB 10 and SHB 0.5 plates, followed by sieving and selecting a part of the powder with a grain size of 10–30 microns, we added a powder made from technical silicon (TS) shown by asterisks in the shading of the working body (1). The Kr0-brand TS was used in the form of a powder with dispersion similar to that of the Si powder of electronic purity. TS contains

Fig. 2 Thermovoltaic converter of thermal energy with a working body from isotype GS according to the Patent of the Republic of Uzbekistan № IAP 05121 [19]. (1) Working body (2) Ceramic housing (3) Ohmic contact
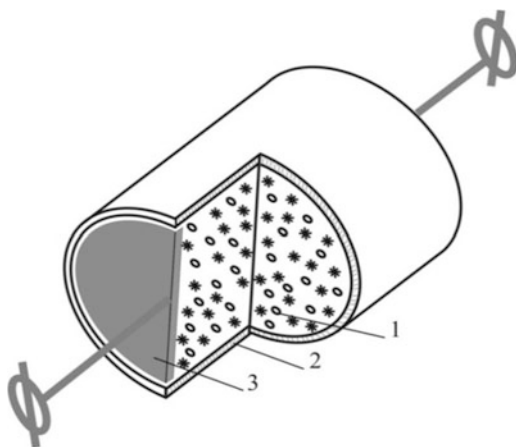
impurities giving deep energy levels, specifically an iron admixture at the 0.5% level. The working body (1) is equipped with ohmic contacts (3) connected at the edges of the housing (2) with terminals for connection to an external circuit. Ohmic contacts (3) are made of metal giving deep energy levels in silicon, namely, steel being an alloy consisting of >85% iron. TEC can operate from thermal radiation, as well as from contact with a heated body, hot gases, liquids, vapors, liquid metal, or an open flame. The heat supply is schematically shown by bold arrows.

We have also developed a device in which the above-described individual TECs are switched into a battery. The battery [20] contains single TECs electrically connected in series with each other with a working body of GS of the same type of conductivity as in [19]. The single TECs are placed in a common housing in such a way that when the housing is rotated by the working side with a selective coating in the direction of the thermal radiation source, the unipolar ohmic contacts, namely, positive, are also turned towards the radiation source. Switching of the multipolar contacts into a serial electrical circuit is provided by connecting electrodes having a smaller cross-sectional area as compared to that of the multi-named ohmic contacts; each pair of ohmic contacts directly connected to each other does not have direct thermal contact with each other, which is achieved by their spatial separation.

As is known, the solar cells (SC) convert only a part of the solar radiation reaching the Earth's surface within the wavelength range of 0.4–1.1 microns, while only within the range from 0.4 to 3 microns, there are up to 44% of the total solar radiation energy [21]. Therefore, the conversion of this part of solar radiation, as well as the heat of heated bodies, liquids, and gases of natural or man-made origin, is an important issue to be solved with the help of thermal converters of various designs. One of such hypothetical energy converters [2] named by the author as a thermoelectric element is made from a non-monocrystalline material with *p-n* conductivity with the efficiency of ~80% and higher radiation resistance.

By analogy with [2], we have created a TEC whose operation is also based on the processes characteristic of non-monocrystalline silicon. The working body of the TEC [22] consists of two regions mechanically contacting with each other; each of the regions is formed from silicon of *p* and *n* types of the same dispersion.

The TEC working body [22] (Fig. 3) contains *p* and *n* regions 1 and 2, respectively, made equal in size, formed from silicon powders with different types of conductivity; the TEC working body is placed in housing 3 of a dielectric heat-conducting material, for example, ceramics, with a selective coating 4; each of the different types of regions is equipped with an ohmic contact 5, which, in turn, is equipped with terminal 6 for connection to an electrical circuit. The impurity giving deep energy levels in silicon is intentionally introduced only into the *p* region 1 in the form of an additive to the *p*-type silicon powder from which it is formed, a powder from TS containing an admixture of iron (schematically shown by asterisks in the hatching of the *p* region). The typical energy characteristics of TEC with the size of the p and n GS regions ~6 mm in length and 1.7 mm in diameter, for example, at temperature of 650 K, are $U_{oc} \sim 200$ mV and $J_{sc} \sim 200$ mA/cm^2.

This TEC is operable when heated by solar radiation or radiation from heated bodies; the heat can be supplied to the housing 3 in any known way: in the form of
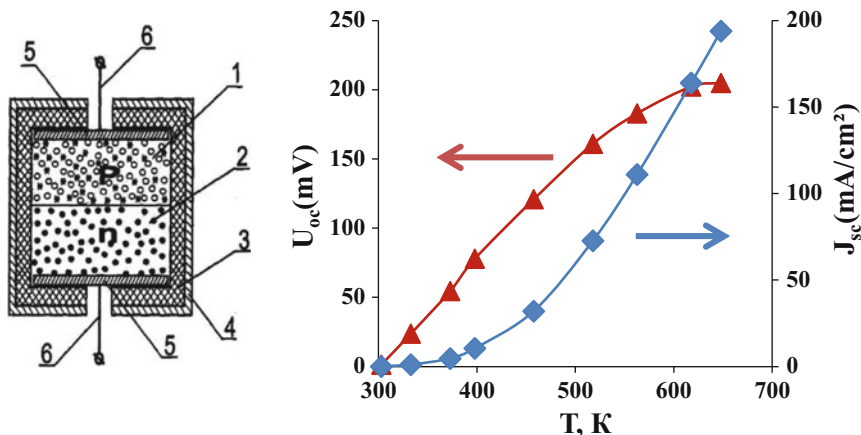
Fig. 3 Thermal energy converter with *p* and *n* areas made of granular silicon according to the Patent of the Republic of Uzbekistan No. IAP 04831 [22]. (1) *p* region, (2) *n* region, (3) tubular housing made of dielectric material, (4) selective coating, (5) ohmic contact, (6) output. Sizes of *p* and *p* areas: length 6 mm each, diameter 1.7 mm

direct or concentrated solar radiation; in the form of a stream of heated gas, steam, and liquid; and through thermal contact with a heated body or by direct contact with an open flame, etc. The best results have been obtained when a temperature gradient is created, for example, from the TEC center, i.e., the contact point of Si powders made from raw materials with different types of conductivity to its edges or at least to one of the edges.

Of interest are the new TEC designs developed by us, which use such an environmentally friendly source of thermal energy as concentrated solar radiation (CSR) and, accordingly, modules in which, unlike photovoltaic devices of this type, a non-photoactive component of CSR is applied.

One of the new module designs is actually a GS-type TEC [19] having the heat supply to the working body from one of the ends of the dielectric housing; it is placed in a focal spot of the parabolic solar radiation concentrator with a 500-mm diameter, and this device with the solar radiation intensity of ~800 W/m^2 can be heated an area of 80 mm in diameter up to ~800 K.

Figures 4 and 6 show the designs of new-type devices with a working body from GS; they are very interesting because their work is based on the use of electricity:

- Simultaneously heat and outer pressure arising, among other things, due to the use of CSR and acting on the TEC working body, made of TS-grinding GS.
- The heat received from the CSR coming from a truncated conical concentrator focused on the boundary of the *n*- and *p*-type areas of the working body made of TS-grinding GS with the addition of powder made by grinding, respectively, silicon of n^+ and p^+ types, providing a temperature gradient along the length of the working body.
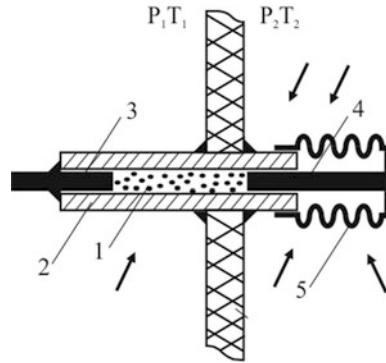
Fig. 4 A new type of TEC from GS working on boundary of two media with $T_2 > T_1$ and $P_2 > P_1$, separated by an insulating wall. (1) Working body from GS, (2) carcass, (3) fixed electrode, (4) movable electrode connected to bellows (5), placed in an environment with a higher pressure P_2 and transmitting compression force working body (1). The arrows show not uniform heat supply to the TEC

- Heat received from the CSR source and focused on the boundary between TS-grinding GS and a contact material also providing a temperature gradient along the length of the working body.

Figure 4 shows a section of the heat and pressure converter. Figure 5 shows the temperature dependences of current density J_{sc} when placing the device on the boundary of two media with different pressures ($P_2 > P_1$) and temperatures ($T_2 > T_1$). The developed TEC has a number of modifications. One of them contains two bellows and two movable electrodes placed along the edges of the housing 2. This TEC is completely placed in a high-pressure medium and outer pressure acts on the GS working body 1 from two sides.

It is important to note that TEC of this type can operate under extreme operating conditions, for example, open space or on the surface of celestial bodies, such as Venus, the lower layers of the atmosphere characterized by high values of temperature, pressure, and radiation levels. So, the TEC quite operable at temperatures of ~900 K and pressures of ~60 atm, characteristic of the Venus surface, is shown in Fig. 4. The statement regarding the GS resistance to radiation is based on our experimental data where the high radiation resistance of GS has been proven by special experiments. In particular, from comparing the results of measurements of the characteristics of TEC from GS before and after irradiation with gamma quanta of Co_{60} with a dose of 10^9 rad, which is certainly destructive for all types and kinds of semiconductor devices, no changes were noted.

Another option for using this type of TEC is a new solar module using a parabolic concentrator as a source thermal energy that provides heating of the TEC working body to the required temperatures and simultaneous creation of outer pressure.

The calculation results [23] show that with the help of such a concentrator made by sagging a glass billet with 500 mm in diameter, a focal length of 500 mm, and a
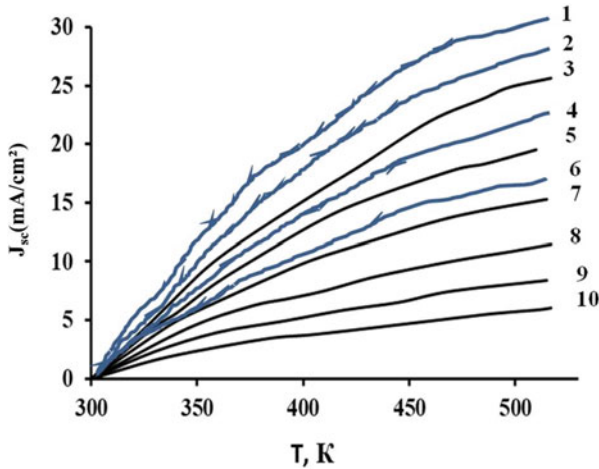
Fig. 5 Typical dependences of current density of GS-TEC at various pressures P_2 and temperatures T_2 at a fixed temperature $T_1 \sim 300$ K. Pressure P_2, MPa: (1) 270; (2) 235; (3) 205; (4) 185; (5) 170; (6) 155; (7) 135; (8) 95; (9) 55; (10) 25. GS contains 30% Kr00-grade TS powder sifted with separation fractions 10–30 microns

sprayed aluminum coating having the reflection coefficient of ~0.8, it is theoretically possible to obtain with the solar radiation intensity of ~1000 W/m^2 the temperature of ~800 K on the area ~80 mm in diameter and ~1300 K on the area 7.1 cm^2, and the possible maximal temperature ~2800 K at a "point focus" with a diameter of <1 cm^2.

The actual temperature value measured by the chromel-alumel thermocouple mounted on a blackened round steel plate with a diameter of ~80 mm and a thickness of 5 mm placed behind the focus of this parabolic concentrator at a distance of ~80 mm at a solar radiation intensity of 800 W/m^2 did not exceed ~500 K. However, that was quite enough for testing the operation of TEC manufactured in two variants. The first variant of TEC was a system [19] in which the working body was made of the GS particles pressed together with a fixed mechanically generated force of ~35 MPa; GS consisted of ~70% of silicon p-type waste of electronic purity and 30% of the same size particles of Kr00-brand TS powder. The heating of the working body was due to the use of the parabolic concentrator described above. This variant of TEC was used by us as a reference.

The scheme of the module [24], in which the CSR is used both as a source of heating of the TEC working body and to create pressure on it, is shown in Fig. 6. The compression force of the GS particles is provided by the pressure of superheated water vapor placed in the cavity of the silphon 8; to one of its ends, the receiving platform 6 heated by the CSR is hermetically attached, and the second end is hermetically connected to a movable, "hot" electrode 3 equipped with a heat-conducting shank 9. For the ratio of the silphon end area (50 cm^2) and the end area of the "hot" electrode ~ (0.3 cm^2), the calculated force of GS compression was
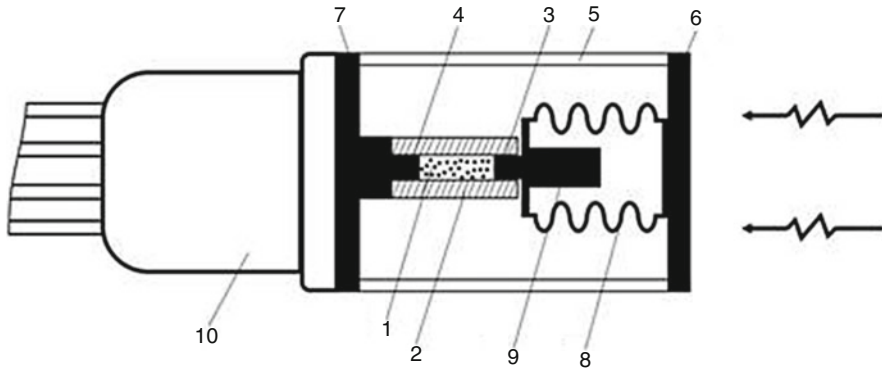
Fig. 6 A new type of solar module with CSR. (1) Working body from the GS, (2) ceramic carcass of TEC, (3) movable "hot" electrode with a shank (9), (4) fixed "cold" electrode, (5) dielectric carcass, (6) reception area heated by CSR (shown arrows), (7) copper plate, (8) bellows with H_2O vapor, (10) heat pipe

~270 MPa. The "cold" electrode 4 is connected to a platform 7 made of copper and cooled by a heat pipe 8 like a gravity thermosiphon thermostabilizing its surface and hence the "cold" electrode 4 at a boiling point of 336 K, used in the heat pipe 8 as a refrigerant, acetone up to the supplied heat capacity of 250–260 Wt.

The temperature of the "hot" electrode 3 was 475 K. The current density J_{sc} of TEC with the size of the GS working body Ø6 mm and a length of 12 mm was 20 mA/cm^2, and the voltage was $U_{oc} \sim 80$ mV. These values turned out to be ~30% lower than expected ones, which is explained by a loss of thermal energy through the device dielectric housing 5, as well as by a decrease in the absolute value of the current when the area of the TEC working body is increased, which occurs due to recombination currents running in GS and associated with charge states at the grain boundaries.

Once again noting the improvement in the energy characteristics of TEC when creating a temperature gradient over the working body, we give an example of using this fact. Figure 7 shows the scheme and characteristics of a solar module containing a concentrator 1 in the form of a truncated cone; TEC 2 converting the CSR thermal energy is placed in its focal band; the TEC working body is equipped with electrodes 3 and 4 that are brought into mechanical contact with the areas 5 and 6 made of GS manufactured by TS grinding with the addition of Si powders of n^+ and p^+ types, respectively.

A sectional view of the module is shown in Fig. 7a; it can be seen that the CSR from the truncated conical concentrator 1 is directed to the receiver 7 being a narrow (~1 mm) metal ring with a blackened surface and mounted on the outer surface of the converter housing 2. The calculation shows that for the ratio of the diameter of the receiver 7 and that of the concentrator 1 ~ 1/100, the working body temperature in the area of the junction of n and p regions 5 and 6 when the receiver is illuminated 7 by CSR from the transatmospheric Sun can be at a level of 1000 K even with
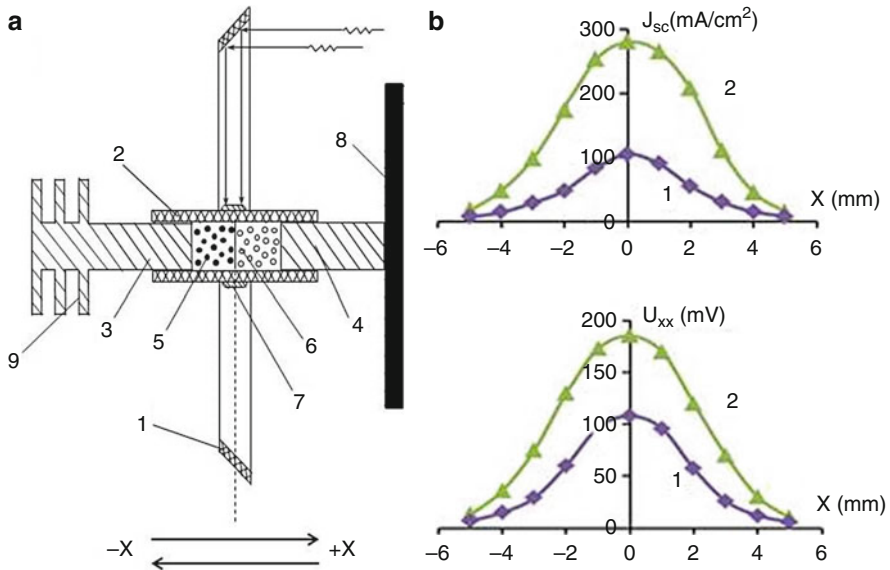
Fig. 7 (**a**) This is a sectional view of the solar module. (1) Conical concentrator, (2) TEC carcass, (3 and 4) electrodes, (5) working body made of silicon with the n and p areas brought into contact, (6) working body made of granular silicon, (7) CSR receiver in the form of a ring, (8) screen, (9) radiator; (**b**) the change in current density I_{sc}; (**c**) voltage U_{oc} when the converter is moved to directions $(-X) – (+X)$ at temperatures of 1–500 K and 2–700 K measured on the receiver (7) when it is illuminated with CSR at $P_0 = 700$ W/m^2 and $P_0 = 850$ W/m^2, respectively

insufficiently accurate execution of the concentrator 1 and a reflection coefficient of ~0.8. The radiation resistance of the module is ensured not only due to the TEC working body from GS but also due to the macroscopic screen 8 on the electrode 4, which excludes any direct hit of charged particles going in the direction from the Sun to the TEC working body 2. Figure 7b, c show the changes in the short-circuit current density (I_{sc}) and the no-load voltage (U_{oc}) when moving the TEC housing, i.e., displacement of the boundary between the n and p regions 5 and 6 to the right $(+X)$ or to the left $(-X)$ relative to the midline (mid-height) of the truncated conical concentrator 1. Curves (1) in Fig. 7b, c were measured under conditions of AM 1.5 for the solar radiation intensity $P_0 = 700$ W/m^2 and curves (2) for $P_0 = 850$ W/m^2 and air temperature 300 K. It can be seen that the maximum energy indicators of the module setup are observed when the middle line of the concentrator 1 coincides with the boundary between the different-type GS regions 5 and 6. The experiments with variation of the concentrator height within the range from 2 to 15 mm and with creation of temperature gradients along the working body length not only due to the TEC uneven illumination with CSR from the truncated conical concentrator but also due to heat transfer from the heated screen 8 and heat removal through the developed surface of the radiator 9 on the electrode 3 showed that it is possible to increase the value of I_{sc} at temperature of 700 K up to ~6.6 mA for $U_{oc} = 200$ mV,

which was demonstrated by a pilot converter with a working body of 12 mm in length and 1.7 mm in diameter only. The ratio of the TEC-produced energy to the mass of the GS working body with the density of 0.69 of the monocrystalline silicon density under Earth conditions is ~30 mW/g, and the expected one, i.e., under transatmospheric Sun illumination, can be at least 48 mW/g with an unlimited service life.

The described module can also be equipped with a TEC with a working body made of isotype GS, i.e., from Si powder of the *n* or *p* type only. In this case, the area of GS-metal contact is exposed to CSR illumination, i.e., local heating. It was found that when heating this region of the width from ~0.5 to 1 mm, the TEC with the length of only 6 mm and the diameter of 1.7 mm has a short-circuit current density of 200 mA/cm^2 at a voltage of 60 mV.

4 Ways to Improve the Energy Characteristics of Heat Energy Converters Based on Granular Silicon

The most important issue for further development of TEC and modules is to increase the GS conductivity; its solution is based on increasing the probability of charge carrier tunneling through a nanoscale oxide layer covering silicon particles. We believe that this can be achieved either by creating for tunneling carriers a kind of "bridgeheads" made in the form of nanoscale islands of SnO_2 on the surface of a nanoscale layer of silicon dioxide covering the GS particles [15] or by adding nanoscale particles of amorphous silicon to the GS powder, as well as by special alloying of a silicon dioxide film [25]. The solution in [25] implies two implementation options. The first is to select such an alloying impurity that would be a deep impurity in silicon and at the same time dissolve well in SiO_2, creating energy levels at the bottom of the conduction band of silicon dioxide. In our opinion, such an admixture should be sought among those responsible for the color centers of SiO_2-based glass, i.e., Co, Mo, Fe, etc. This can also be small impurities highly soluble both in Si and SiO_2. We also believe that alkali metal impurities are very promising because of their easily diffusion in silicon and highly soluble in oxide. The second option assumed irradiation with a dose of at least 10^9 rad, leading to appearance of energy levels with the density of 10^{17}–10^{18} cm^{-3} in the Si particle and in the nanoscale SiO_2 film. These levels are near the ceiling of the silicon conduction band and the bottom of the SiO_2 conduction band; through them the resonant tunneling of charge carriers through a nanoscale SiO_2 film takes place with more probability as compared to "Gamovsky" one. The introduction of impurities soluble in SiO_2 and in silicon itself into GC was more productive. This idea was first formulated in [26], and then after the experiments was performed, a patent for this specific technical solution was granted.

For different types of GS, including those with different types of conductivity and with different grain sizes, we used impurities of Fe, Ni, and a number of

alkali metals (AM). The originality of our approach lies in the fact that not the GS itself was doped, but GS was made from raw materials with one or another of the mentioned admixture introduced into it in advance.

At the same time, the most important conditions determined by us were fulfilled, namely, raw materials for the GS manufacturing; the samples of PS of various technological origins were selected but with the grain sizes comparable to the GS particle size we planned to obtain by grinding this raw material. That is, the basis was, firstly, the fact of the predominant destruction of the polycrystals during mechanical grinding along grain boundaries, which happened, according to the results of optical microscopy of Si powder before sieving, from which a conclusion about relative uniformity of the powder particle sizes can be made. Secondly, we assumed that the GS particles obtained by grinding inherit from the grains of non-monocrystalline raw materials the impurity clusters at their boundaries, which is automatically accompanied by doping the surface of the SiO_2 film of the obtained silicon particles contacting with air oxygen. It is easy to notice that we use a well-known physical effect of impurity segregation at the grain boundaries during crystallization of polysilicon that is used in practice for polysilicon cleaning by grinding and subsequent etching of the powder particle surface.

This assumption is confirmed by the data of instrumental estimation of the distribution in volume of a single Si granule with ~18 microns in size, oxygen and natrium introduced into the raw material in the form of PS. It was found that the silicon concentration decreases to the granule surface and the oxygen concentration, on the contrary, increases sharply. The Na content turns out to be minimal in the granule center and, as expected, increases towards the surface, reaching a maximum at the granule boundaries.

The operational capability of a new method of increasing the GS conductivity is confirmed by Fig. 8 where the temperature dependences of GS resistivity are presented: Curve 1, standard, is for Si powder of electronic purity; Curve 2 is for a mixture of TS powders (30%) and p-type PS with the grain size of 10–30 microns; Curve 3 is for GS from p-type PS plates pre-doped with Na by ion implantation; and Curve 4 is for GS from p-type multi-silicon plates doped with nickel and Curve 5 with iron before grinding. It can be seen that when Na is introduced into the initial PS, the conductivity of GS obtained from it by grinding is two times higher than that of the standard within the heating temperature range of 300–650 K. This is even better seen at a temperature ($\geq 430\,°C$), when there takes place intensive decomposition of oxygen-containing SiO_4 complexes initially located at grain boundaries and after grinding mainly at the boundaries of GS particles.

The increase in the conductivity of the grain boundaries obviously increases the probability of resonant tunneling of charge carriers through the nanoscale SiO_2 layer, which leads to the observed growth in the GS conductivity. In the case of Ni impurity introduction into the raw material (Curve 4), the increase in conductivity is less noticeable about 1.5 times less, which is explained by the fact that in the case of Na impurity introduced into the initial PS by ion implantation, it is possible to achieve a much higher degree of grain boundary doping than when introducing a nickel impurity by "rubbing" the Si surface [27] with subsequent diffusion. Perhaps
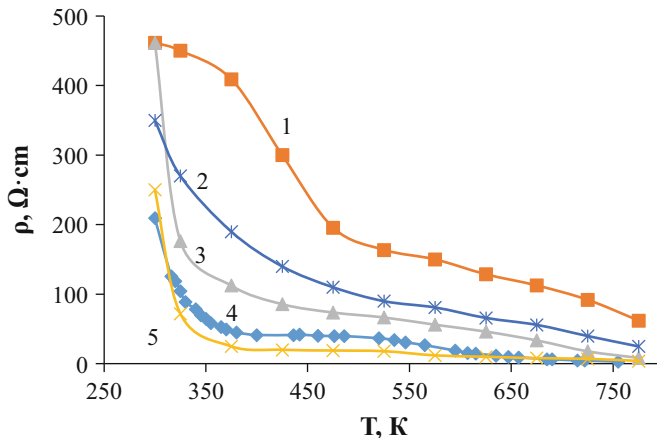
Fig. 8 Dependence of the specific resistance of GS samples on temperatures: (1) GS from electronic purity Si powder; (2) GS from a mixture of powders TS (30%) and PS; (3) GS from PS doped with Ni; (4) initial PS doped with Na; (5) GS from multi-silicon melted from a charge with the addition of TS

the low solubility of Ni in Si also plays a role. On the contrary, in the case of doping of the initial polycrystalline raw materials with an iron admixture from multi-silicon obtained from the charge with TS addition, the obtained GS has the highest conductivity (Curve 5). Similarly, the samples obtained by PS grinding and pre-doped with an iron admixture introduced by diffusion after "rubbing" the surface according to [27] have a sufficiently high conductivity. It is important to note that all the samples have a very high Seebeck coefficient (~490–520 at 350–375 K) measured independently in two organizations.

The best raw material option for creating GS with minimal resistance turned out to be a mixture of TS and PS powders in the ratio of three to four parts of TS to six to seven parts of PS, pre-doped before grinding with an iron admixture, as well as grinding of multi-silicon manufactured by one remelting of TS with the addition of highly alloyed p^+ plates of the SHB-0.003 grade with boron content $3 \cdot 10^{19}$ cm^{-3} with an additional two- or threefold doping of the plates cut from it by "rubbing" [27] of their surfaces with Al of CP grades and Ni followed by aluminum burning in nitrogen flow. That is, the intergrain boundaries in this case are doped with fine and two, at least, deep impurities simultaneously. This is confirmed by estimates of the elemental composition of the GS samples obtained by grinding of such raw materials by X-ray spectral microanalysis with the Aztec Energy Advanced X-Max 80 spectrometer (Oxford Instruments, UK).

5 Conclusions

A new scientific direction has been proposed and justified concerning development of a new type of the thermoelectric material based on granular silicon in the form of Si powder. In the working body of the thermal energy converter, the Si powder particles are simply brought into mechanical contact with each other without destroying the nanoscale silicon dioxide film on the surface of particles arising from their contact with air oxygen in the process of mechanical grinding of the initial silicon material.

The experimental results concerning abnormally high values of the Seebeck coefficient in samples of granular silicon have been physically justified, as well as values of thermal conductivity lower than that of monocrystalline silicon.

The original ways of increasing the conductivity of granular silicon and EMF of thermal energy converters based on it have been physically justified.

A number of fundamentally new types of thermal energy converters have been created and tested. Their energy characteristics increase under conditions of outer pressure on the working body, as well as modules equipped with them using concentrated solar radiation. A number of converter designs operable under conditions of high temperature, pressure, and radiation have been developed.

The economic benefits of using granular silicon as a thermoelectric material, despite the so far modest energy characteristics of the converters created on its basis, have been obvious. Silicon is an affordable material and widely distributed chemical element in terrestrial rocks; it is the most mastered semiconductor in production. Moreover, a wide range of silicon production waste can be used in heat energy converters based on granular silicon, including sludge, i.e., a precipitate of silicon powder from a mixture of water-oil waste from cutting operations of silicon ingots into plates in any semiconductor production.

References

1. Saidov, M. S., Abdurahmanov, B. M., & Olimov, L. O. (2007). Impurity thermovoltaic effect in the grain boundaries of a polycrystalline silicon solar cell. *Applied Solar Energy, 43*(4), 203–206. https://link.springer.com/article/10.3103/S0003701X07040019
2. Saidov, M. S. (2003). Possible impurity voltaic effects in semiconductors. *Geliotehnika, 3*, 3–6. (in Russian). http://geliotekhnika.uz/en/articles/1142
3. Saidov, A. S., Abakumov, A. A., Saidov, M. S., Usmonov, S. N., & Kholikov, K. T. (2007). Thermovoltaic properties of technical silicon melted by solar radiation. *Applied Solar Energy, 43*(4), 266–267. https://link.springer.com/article/10.3103/S0003701X07040184
4. Abdurahmanov, B. M., & Olimov, L. O. (2009). Obnaruzhenie primesnyh vol'taicheskih jeffektov v monokristallicheskih kremnievyh solnechnyh jelementah «DAN RUz», № 1, 26–29 (in Russian).
5. Ioffe, A. F. (1957). *Semiconductor Thermoelements and thermoelectric cooling*. London, 103 p.
6. Abdurahmanov, G., Zahidov, R. A., & Mamatkulova, S. A. (2012). Advanced materials for solar thermoelectric transducers. *Applied Solar Energy, 48*(1), 10–13. https://link.springer.com/article/10.3103/S0003701X12010021

7. Matchanov, N. A., Farhan, M., Angelo, J. D., & Timm, E. J. (2011). Investigation of the hot side contacts to nanostructured LASTt(T) material. *Applied Solar Energy, 47*(2), 90–97. https://link.springer.com/article/10.3103/S0003701X11020137

8. Ashurov, M. H., Abdurahmanov, B. M., Adilov, M. M., & Ashurov, H. B. (2012). Termo-jelektricheskie harakteristiki preobrazovatelej teplovoj jenergii s izotipnym rabochim telom iz mikrozernistogo kremnija, «DAN RUz», № 1, 27–30 (in Russian).

9. Fedorov, M. I. (2009). Thermoelectric silicides: Past, present and future. *Journal of Thermo-electricity, 2*, 51–60. https://www.elibrary.ru/item.asp?id=16406523

10. Abdurakhmanov, B. M., Adilov, M. M., Ashurov, M. K., Ashurov, K. B., Kuchkanov, S. K., Maksimov, S. E., Oksengendler, B. L. (2015). Thermoelectrical characteristics of granular semiconductors with resonance tunnelling charge carriers for conversion of the solar radiation heat component. *Applied Solar Energy, 51*(4), 253–257. https://link.springer.com/article/10.3103/S0003701X15040039

11. A.I. Karchevskogo Termojelektricheskie materialy i preobrazovateli. «Mir». Moskva. 1954. 353 p. (in Russian).

12. Snarskij, A. A., Sarychev, A. K., Bezsudnov, I. V., & Lagar'kov, A. N. (2012). Termo-jelektricheskaja dobrotnost' ob#emnyh nanostrukturirovannyh kompozitov s raspredelennymi parametrami. *Fizika i tehnika poluprovodnikov, 46*(5), 677–683 (in Russian).

13. Mahan, G. D. (1994). Thermoelectric devices using semiconductor quantum wells. *Journal of Applied Physics, 76*, 4362–4366. https://aip.scitation.org/doi/10.1063/1.357715

14. Abdurahmanov, B. M., Abdurahmanov, T. B., Adilov, M. M., Ashurov, M. H., Ashurov, R. H., Ashurov, H. B., Maksimov, S. E., Morozov, O. B., & Oksengendler, B. L. (2016). *Sposob izgotovlenija poluprovodnikovyh zagotovok dlja preobrazovatelej jenergii*, Patent RUz IAP No 05288 (in Russian).

15. Adilov M. M. (2019). *Thermoelectric properties of granular silicon Abstract of dissertation of the doctor of Philosophy (PhD) On Physical And Mathematical Sciences*, Tashkent.

16. Silin, A. R., & Truhin, A. N. (1985). *Tochechnye defekty i jelementarnye vozbuzhdenija v kristallicheskom i stekloobraznom SiO₂*. Riga, 244 p.

17. Dmitriev, A. V., & Zvjagin, I. P. (2010). Sovremennye tendencii razvitija fiziki termojelektrich-eskih materialov. *Uspehi Fizicheskih Nauk, 180*(8), 821–838. (in Russian).

18. Korshunov, F. P., Gatal'skij, G. V., & Ivanov, G. M. (1978). Radiacionnye effekty v poluprovod-nikovyh priborah. Minsk, "Nauka i Tehnika" (in Russian).

19. Abdurahmanov B. M., Adilov, M. M., & Ashurov, H. B. (2013). *Preobrazovatel jenergii*. Patent RUz IAP No 04824 (in Russian).

20. Abdurahmanov B. M., Adilov, M. M., Ashurov, H. B., & Alad'ina, Z. N. (2014). *Preobrazo-vatel' jenergii*. Patent RUz IAP No 04831 (in Russian).

21. Bakhadyrkhanov, M. K., Valiev, S. A., & Zikrillaev, N. F. (2016). Silicon photovoltaic cells with clusters of nickel atoms. *Applied Solar Energy, 52*, 278–281. https://link.springer.com/article/10.3103/S0003701X1604006X

22. Abdurahmanov, B. M., Adilov, M. M., Alad'ina, Z. N., Ashurov, M. H., & Ashurov, H. B. (2015). *Teplovol'taicheskij preobrazovatel' jenergii*, Patent RUz IAP No 05121 (in Russian).

23. Abdurahmanov, B. M., Bajdakov, S. G., Solovejchik, V. I., & Chirva, V. P. (1993). Moduli i jelementy solnechnyh fotojelektricheskih stancij s koncentraciej izluchenija. Tashkent: FAN 200 p. (in Russian).

24. Abdurahmanov, B. M., Adilov, M. M., Ashurov, H. B., Kurbonov, M. S., & Trunilina, O. V. (2022). *Preobrazovatel' koncentrirovannogo solnechnogo izluchenija (SolarConver)*, Patent RUz IAP No 06853 (in Russian).

25. Abdurahmanov, B. M., Adilov, M. M., Ashurov, M. H., Ashurov, H. B., Maksimov, S. E., Oksengedler, B. L., Alad'ina, Z. N., Kuchkanov, S. K. (2018). *Termojelektricheskij material i sposob ego izgotovlenija*, Patent RUz IAP No 05615 (in Russian).

26. Abdurahmanov, B. M., Oksengendler, B. L., Ashurov, H. B., & Adilov, M. M. (2017). Novye aspekty termojelektrichestva: jelektronnye skutterudity. *Geliotehnika, 2*, 37–40. http://geliotekhnika.uz/ru/articles/149

27. Abdurahmanov, B. M., & Shopen, V. I. (1995). *Sposob formirovanija jelektricheskogo kontakta na kremnievoj zagotovke*. Patent RUz IAP No 3864 (in Russian).

Security-Constrained Unit Commitment with Wind Energy Resource Using Universal Generating Function

Robert T. F. Ah King and Doorgesh Balgobin

Abbreviations

a	Particle number
C_1	Cognitive parameter
C_2	Social parameter
COST_{ji}	Cost of i-th generator at j-th time period
D	Dimension
D_{ij}	Shutdown cost for i-th generator at j-th time period
M	Number of wind scenarios
MDT_i	Minimum downtime of i-th generator
MUT_i	Minimum uptime of i-th generator
N	Number of thermal generators available for dispatching ($i = 1, \dots N$)
NW	Numbers of wind turbines
$P_{\text{D}j}$	Load demand at j-th time period
P_{ij}	Output of i-th generator during j-th time period
$P_i^{\max}$	Maximum generation capacity of i-th generator
$P_i^{\min}$	Minimum generation capacity of i-th generator
P_{jsce}	Probability of wind at j-th time period for scenario sce
$P_{\text{L}j}$	System losses at j-th time period
$P_{\text{R}j}$	Spinning reserve required at j-th time period
P_{wc}	Total power curtailed
$P_{\text{W}j}$	Power produced by wind turbine
S.D.C	Shutdown cost of the system
S.U.C	Total startup cost of the system

R. T. F. Ah King (✉) · D. Balgobin
Department of Electrical and Electronic Engineering, University of Mauritius, Reduit, Mauritius
e-mail: r.ahking@uom.ac.mu

Sce   Scenarios of wind modelling
S_{ij} Startup cost for i-th generator at j-th time period
t Current iteration
T Number of time periods making the schedule
T_{ij}^{OFF} Off time of unit i at j-th time period
T_{ij}^{ON} On time of unit i at j-th time period
U_{ij} 'On/off' status of i-th generator during j-th time period. ON = 1,OFF = 0
w Weight
W.C.C   Total wind curtailment cost
W_c Cost of curtailed wind power per MW for a unit NW

1   Introduction

Wind power, itself being a renewable and clean source of energy, is a major field of study in the power sector. The need for optimising generation from wind power is due to its renewability and the ability to lower total operating costs. The optimisation of wind power is not fully well defined due to the dimension of a power system and the uncertainty associated with it, and it is still an ongoing research. Unit commitment analysis, which is a planning process, becomes mandatory to deal with the volatile nature of wind power. Wind power forecasting in unit commitment will help to maintain the reliability and safety of supply. Wind power flow adds network constraints to the already present technological constraints in the unit commitment problem. In fact, in power supply systems, use of wind and other renewable sources is limited to a small percentage of power grids to account for stability reasons.

Thus, it is important for wind power to be modelled in order to illustrate its randomness. Atwa and El-Saadany [2] modelled wind speed behaviour as the Rayleigh probability density function where they used a stochastic approach for optimal allocation of wind-based distribution system. While many of wind modelling methods rely on Monte Carlo simulation, Li and Zio [10] used the universal generating function technique, which is a convolution computation. They used a complex UGF function which combines mechanical and renewable generation states. Solar generators and wind turbines among others are all presented using UGF technique, and the advantage of the latter is that computation time is much lesser than simulation methods. Also, the computational effort used to solve the model was critical. The objective was to find reliability indices such as loss of load expectation and expected energy not supplied. Jin et al. [8] also modelled wind using UGF, due to its handling of discrete random variable and computational time. The fact that probability distribution of wind is non-identical from time to time, a multiple-period, multiple-state was used to model the wind system.

Bender's decomposition was proposed by Wang et al. [15] to solve the optimisation process. Due to the random nature of wind, different scenarios and probability of wind power were included in the subproblem. The master problem was consisted of rightly forecasted wind power generation, and the unit commitment problem was

solved in the master problem. There exists an iterative process between the two problems until the scenarios can be accommodated by redispatch. A simulation technique instead of analytical technique was used to model the wind distribution; Monte Carlo simulation was performed in accordance with Latin hypercube sampling. Wang et al. [16] presented two unit commitment methods, deterministic and stochastic, to provide the linkage between day-ahead unit commitment and real-time dispatching. The paper analysed the effects of wind power forecasting errors on the power system that is the uncertainty and variability of the wind power. The stochastic approach was found to be better in terms of cost and reliability. Therefore for future works, stochastic approach will be used to describe wind power. The deterministic approach showed similar result when more reserve requirements were used. No wind curtailment occurred because transmission constraints were not considered.

The computational results of Wang et al. [17] suggested that a combined sample average approximation (SAA) algorithm can solve this complex power grid optimisation problem. The risk of wind curtailment was minimised by setting risk levels for different probabilities. Chance constraint was exercised to describe policies to allow the utilisation of wind power output together with security constraints. Traditionally, researchers aimed for considering constraints when optimising the unit commitment problem. One of the main improvements that are addressed by Nasrolahpour and Ghasemi [12] is that transmission constraints together with the traditional generating constraints are considered. This constitutes the security constraints problem. The wind power generation being unpredictable and random makes the problem a stochastic one. The objective function was divided into two parts, one with forecasted wind power and the other with different wind scenarios. In addition, reconfigurable networks are proposed and compared with other solutions obtained. Bender's decomposition is applied due to the nature of power systems which is a mixed integer type. The proposed model succeeded in maximising wind use and exploiting reconfiguration capability to distribute energy.

Gupta et al. [7] proposed the use of line outage distribution factor to reduce the number of nonzero coefficients of post contingency DC security constraints for improving computational requirement. The authors considered a complex mixed integer linear programming problem which was solved using benders decomposition for modified IEEE reliability test system and 118-bus system. Guo et al. [6] built the uncertainty model for each main component in generation-grid-load-energy storage and combined with these models the production simulation method based on improved universal generating function. Thus, the flexibility evaluation tool and flexibility metrics are proposed based on flexibility definition and physical mechanism. The method was tested on the IEEE RTS-79 and on Zhangjiakou system which has serious renewable energy curtailment problems. Alqunun et al. [1] presented a modified formulation for the wind-battery-thermal unit commitment problem that combines battery energy storage systems with thermal units to compensate for the power dispatch gap caused by the intermittency of wind power generation. A chance constraint was used to model the uncertainty of wind power in order to overcome the probabilistic infeasibility generated by classical

approximations of wind power. The unit commitment problem was solved using a mixed-integer linear programming algorithm.

Most research involved was to solve the problem of unit commitment in order to dispatch loads correctly. Many of them included evolutionary algorithms [9, 11, 14], and due to widespread calls to use wind energy, it is therefore advantageous to investigate unit commitment while maximising wind power generation. It was noted that none of the evolutionary algorithms mentioned had a recurring optimal solution. For modelling of a proper power system, transmission and generation constraints should be considered in addition to power losses. However, only a few studies have considered this aspect, and those who have used it did not use a comparative approach. Therefore to validate the findings, evolutionary algorithms such as GA and PSO could be helpful.

The chapter is organised as follows. The mathematical formulation of the unit commitment problem is described in Sect. 2. Wind modelling using UGF is presented in Sect. 3. Section 4 gives the methodology adopted in this study. The results are presented in Sect. 5, and conclusion is made in Sect. 6.

2 Mathematical Formulation of the Unit Commitment Problem

2.1 Constraints

The barrier of the unit commitment problem finds its source in the constraints that should be dealt with for the optimal solution to be feasible. To maintain reliability of supply and safety, constraints should be considered when optimising.

2.1.1 Generation Limit

A committed generator can supply only power within its allowable range. The generator output is therefore bounded by minimum and maximum limits.

It can be classified as:

$$P_i^{\min} \leq P_{ij} \leq P_i^{\max} \tag{1}$$

2.1.2 Power Balance

It is of paramount importance that demand is equal to generation during a period. Transmission losses are catered, and the inequality becomes:

$$\sum_{i=1}^{N} U_{ij} P_{ij} = P_{Dj} + P_{Lj} \tag{2}$$

Since wind power is also contributing to the grid, the constraint is modelled as:

$$\sum_{i=1}^{N} U_{ij} P_{ij} + \sum_{i=1}^{NW} P_{Wj} = P_{Dj} + P_{Lj} \tag{3}$$

2.1.3 Minimum Uptime

Once a generator is turned on, it should remain so during a certain time, known as minimum uptime.

$$T_{i(j-1)}^{ON} - MUT_i \times \left[U_{i(j-1)} - U_{ij} \right] \geq 0 \tag{4}$$

2.1.4 Minimum Downtime

Once a generator is turned off, it should remain so for a certain time.

$$-MDT_i \times \left[U_{ij} - U_{i(j-1)} \right] \geq 0 \tag{5}$$

The objective function is the total generation cost. The latter includes the production cost (fuel), the transition cost and wind curtailment cost. Wind is assumed to be the generation cost free and hence be used as maximum as permitted. The objective function must be minimised, taking into consideration the constraints mentioned in the previous section.

2.2 Transition Cost

Transition implies the change of states of generators. The *energy* used for switching on and off is not used for power generation and hence is listed as costs.

2.2.1 Startup Cost

Since thermal generators are being used, the startup cost is divided into two types:
The startup cost for *i*-th generator is modelled as:

$$S.U.C_i = \sum_{j=1}^{T} \left(1 - U_{i(j-1)} \right) \times U_{ij} \times S_{ij} \left(T_{i(j-1)}^{OFF} \right) \tag{6}$$

The total S.U.C of the power system is the sum of starting costs of all generators for the schedule. It is obtained by summing S.U.C$_i$ over all i in the range [1, 2 … N].

$$\text{S.U.C} = \sum_{i=1}^{N} \sum_{j=1}^{T} \left(1 - U_{i(j-1)}\right) \times U_{ij} \times S_{ij} \left(T_{i(j-1)}^{\text{OFF}}\right) \tag{7}$$

2.2.2 Shutdown Cost

An i-th generator incurs shutdown costs when the generator is switched off and is given by the equation:

$$\text{S.D.C}_i = \sum_{j=1}^{T} U_{i(j-1)} \times \left(1 - U_{ij}\right) \times D_{ij} \tag{8}$$

The total shutdown cost for all generators for the schedule is thus modelled as:

$$\text{S.D.C} = \sum_{i=1}^{N} \sum_{j=1}^{T} U_{i(j-1)} \times \left(1 - U_{ij}\right) \times D_{ij} \tag{9}$$

2.3 Wind Curtailment

Since wind is assumed to be cost-free, maximum wind generation should be used. However, the transmission constraints cause the wind to be curtailed and hence using thermal engines thereby incurring additional costs. Wind curtailment cost equation is given below:

$$\text{W.C.C} = \sum_{w=1}^{NW} P_{wc} \times W_c \tag{10}$$

For this paper, wind curtailment costs represent excess power that thermal generating units need to be produced, and load shedding is not included as it involves extreme cases.

Therefore, total generation cost (objective function) amounts to the sum of

1. Total production cost
2. Shutdown costs of generators
3. Startup costs of generators
4. Wind curtailment costs

2.4   Objective Function

The fact that wind power depends on wind which is unpredictable makes the unit commitment problem to consider other scenarios. The wind that is being forecasted has the probability of 1 compared to other scenarios. The objective function is as follows:

$$
\text{Objective function} = \text{MIN} \sum_{j=1}^{T} \left(\sum_{i=1}^{N} \left(S_{ji} + D_{ji} + \text{COST}_{ji} \right) \right.
$$
$$
\left. + \sum_{\text{Sce}=1}^{M} P_{\text{jsce}} \sum_{i=1}^{N} \left(S_{ji} + D_{ji} + \text{COST}_{ji} \right) \right)
\tag{11}
$$

The 1st line of Eq. (11) considers the correct prediction of wind energy, while the 2nd line of the equation considers different scenarios due to its random nature.

3   Wind Modelling

As mentioned wind power output is highly fluctuating and intermittent unlike traditional power generators. With the insertion of wind power generating units, the randomness of a power system is increased further. This eventually makes the power system probabilistic production simulation more significant in the power system scheduling. Jin et al. [8] divided random modelling of wind power into two techniques:

- Multistate model of universal generating function which is an analytical technique
- Monte Carlo simulation which is a simulation technique

Since numerous wind turbine generators (WTGs) are required and considering the high wind power penetration, simulation techniques have a major drawback in the long computational time. Hence analytical techniques like universal generating function (UGF)-based methods are more efficient than the simulation approaches for evaluating the average values of reliability indices in power system planning [4].

For this work, data has been taken from Atwa and El-Saadany [2].

A wind turbine is modelled as:

$$
P_w = 0 \text{ if } V \leq V_{\text{in}} \text{ or } V \geq V_{\text{out}}
\tag{12}
$$

$$
P_w = \frac{V - V_{\text{in}}}{V_{\text{rated}} - V_{\text{in}}} \times P_{\text{rated}} \text{ for } V_{\text{in}} \leq V \leq V_{\text{rated}}
\tag{13}
$$

$$
P_w = P_{\text{rated}} \text{ for } V_{\text{rated}} \leq V \leq V_{\text{out}}
\tag{14}
$$
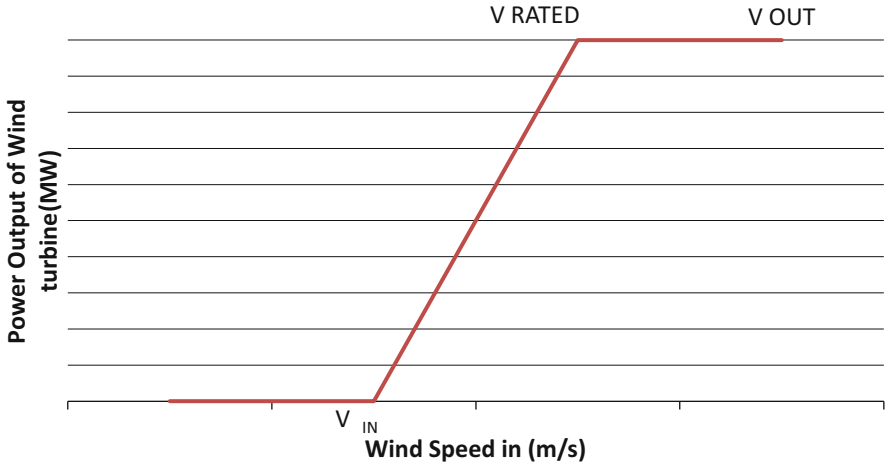
Fig. 1 Power output of a wind turbine

where V, V_{in}, V_{rated} and V_{out} are the actual average speed, the cut-in speed, rated speed and cut-off speed of the wind turbine, respectively. Figure 1 illustrates the power output variation with wind speed.

3.1 Universal Generating Function

UGF is an efficient computational tool handling discrete random variable and is based on simple recursive procedures. It provides a systematic method for the system state enumeration that can substitute very complicated combinational algorithms and diminish the computational burden. In addition, a flexible approach is provided by the UGF to represent the various reliability models and their correlation in a power system with high wind power penetration [4].

Two random variables X_1 and X_2 are expressed in UGF form as:

$$U_1(z) = \sum_{i=1}^{k_1} P(1, i) Z^{x(1,i)} \tag{15}$$

$$U_2(z) = \sum_{j=1}^{k_2} P(2, j) Z^{x(2,j)} \tag{16}$$

where $U_1(Z)$ and $U_2(Z)$ represent the u-model of X_1 and X_2.

The purpose of 'Z' is to distinguish between the value and probability of random variables.

Considering that X_1 and X_2 are independent of each other, their functional operation result will be obtained through operation of UGF. For example, if $X_3 = X_1 + X_2$, X_3 can be expressed in the UGF model as:

$$U_3(z) = \sum_{i=1}^{k_1} \sum_{j=1}^{k_2} P(1, i) \, P(2, j) \, Z^{x(1,i)+x(2,j)} \tag{17}$$

In our case, X_1 and X_2 represent the output of wind turbine generators. The above equation clearly expresses the distributions of the generators. Mechanical state representations are neglected in our approach as only external sources of randomness (wind speed) are considered.

Data taken from Atwa and El-Saadany [2] is as follows (Refer to Table 8 in the Appendix):

- Maximum wind speed = 22 m/s
- Mean wind speed = 6.07 m/s

The wind turbine data is as follows:

- Cut-in speed = 4 m/s
- Rated speed = 14 m/s
- Cut-off speed = 25 m/s

The data of the wind turbine is used to create the probabilistic wind power output model.

From the Appendix, some states such as 0–4 m/s, 14–25 m/s and wind speed greater than 25 m/s are aggregated together because they represent the same power output either rated for the 2nd case or zero for the 1st and 3rd cases.

Since a 10-MW wind turbine is assumed to be used, the generating power will be divided into five states, namely, 10 MW, 8 MW, 4.5 MW, 1.5 MW and 0 MW. These correspond to the performance rates.

The probability should also be divided into five states, and the wind speed and probabilities are rearranged as shown in Table 1.

The values of power output were obtained from wind turbine power equation by plugging mean values of wind speed. The wind speed limits were discretised such that wind speed limits were summed from the Appendix with their probabilities adding together.

The load curve's maximum wind power is around 100 MW and one Wind turbine is realistically made to produce 10 MW. Thus, in order to cater for demand, ten wind turbines will hence make the wind farm.

Table 1 States and their probabilities

Wind speed limits, m/s	Probabilities	Power output/MW
14–25	0.078425	10
10–14	0.152853	8
7–10	0.280708	4.5
4–7	0.282078	1.5
0–4	0.205936	0

For ten wind turbines and five states, there will be 5^{10} (9765625) variables for both probabilities and state variables.

Therefore for one wind turbine, the UGF function corresponds to:

$$U_1(z) = 0.078425z^{10} + 0.152853z^8 + 0.280708z^{4.5} + 0.282078z^{1.5} + 0.2059936z^0 \tag{18}$$

Since the summing operator is used $\otimes_+$, for ten wind turbines, the overall u-function is termed as:

$$U_W(z) = U_1(z)\otimes_+U_2(z)\otimes_+U_3(z)\otimes_+U_4(z)\ldots\otimes_+U_{10}(z) \tag{19}$$

$$U_1(z)\otimes_+U_2(z) = \left(0.078425 \times 0.078425z^{10+10}\right) + \ldots \\ + \left(0.2059936 \times 0.2059936z^{0+0}\right) \tag{20}$$

Modelling two wind turbines will result in the following u-function:

The above equation will consist of 25 terms and, for example, states that a $(10 + 10)$ MW will have a probability of 0.078425×0.078425. Henceforth, the overall u-function consists of 9,765,625 terms.

$$U_w(z) = \underbrace{8.81e - 12z^{100} + \cdots + 1.372e - 7z^0}_{9,765,625 \text{ terms}}$$

The probability density function is plotted using the data obtained, and the result is shown in Fig. 2.
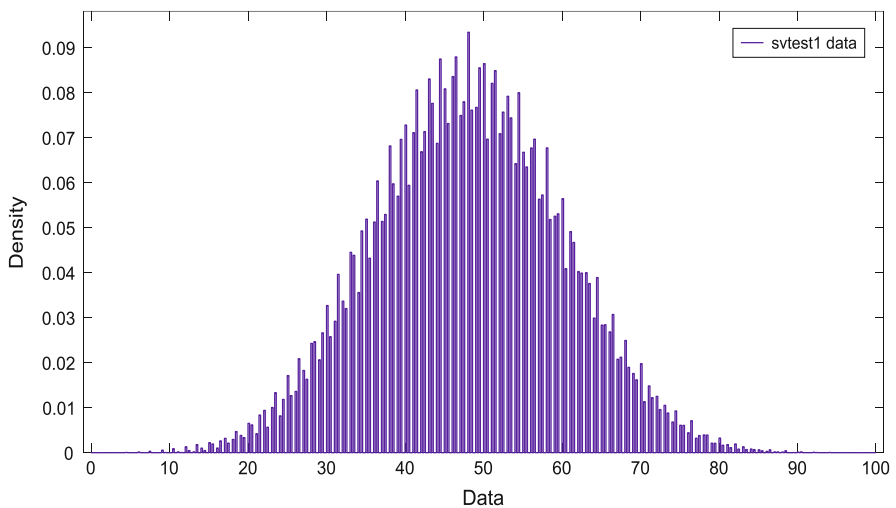
Fig. 2 Probability density function obtained from UGF

4 Methodology

4.1 Genetic Algorithm

The three operators [3] (selection, crossover, mutation) that define GA were applied with default settings.

In the case of Genetic Algorithm, principles used by Matlab software are as shown in Fig. 3.
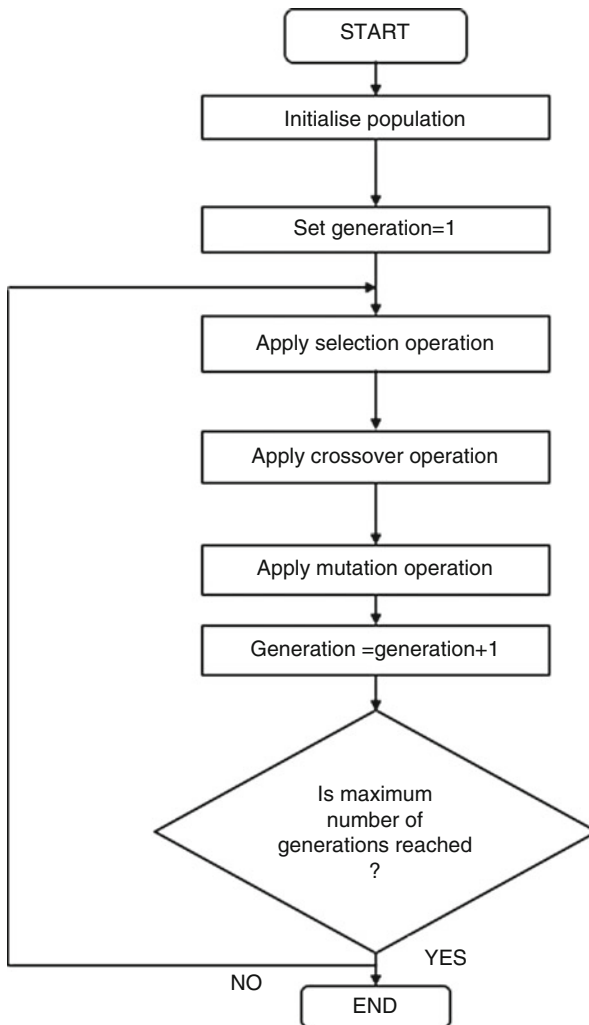
Fig. 3 GA flowchart

4.2   Particle Swarm Optimisation

The procedures to find global best particle are summarised as follows:

Step I: Swarm and velocity initialisation
The number of populations is randomly initialised, and the dimension is stated according to the optimisation problem. Furthermore, the particles' velocities are randomly initialised, and these lie within the maximum and minimum limit of the velocities.

Step II: Pbest, Gbest and iteration initialisation
The maximum number of iteration is set. Using initial set of particles position, Pbest is the actual position as no iterations have been run as of now. The particle with the best (lowest) evaluation function is used to generate Gbest.

Step III: Performing iteration
At each iteration, new velocities are calculated using Eq. (21) and corrected to satisfy the velocity limits stated by $V^{\max}$ and $V^{\min}$. New solutions are obtained using Eq. (22). The latter are used to evaluate new evaluation function.

$$V_{ia}^{(t)} = w \times V_{ia}^{(t-1)} + c_1 \times \mathrm{ran\,d}_{ia}^{(t)} \times \left(\mathrm{pbest}_{ia}^{(t-1)} - \mathrm{particle}_{ia}^{(t-1)} \right)$$
$$+ c_2 \times \mathrm{ran\,d}_{ia}^{(t)} \times \left(\mathrm{gbest}^{(t-1)} - \mathrm{particle}_{ia}^{(t-1)} \right) \quad \text{where } i \in [1, 2 \dots D] \tag{21}$$

$$\mathrm{particle}_a^{(t)} = \mathrm{particle}_a^{(t-1)} + V_{ia}^{(t)} \tag{22}$$

Step IV: Updating Pbest and Gbest
Each new solution is compared to the best position. If the new solution has a lower evaluation value, it becomes the best solution and is termed Pbest. Among Pbests, the Gbest is chosen by selecting the lowest evaluation function.

Step V: Stopping criterion
The PSO algorithm is run for a number of iterations. If stopping criterion is not met, step III is repeated; otherwise the algorithm is ended. The flowchart of the PSO algorithm is shown in Fig. 4.

MATLAB codes were written for the unit commitment problem, and the principles are illustrated as follows:

Saadat's power flow toolbox [13] was used and the generator on bus 1 was considered to be a slack bus. Therefore generator 1 was removed from optimisation to later implement power losses. The difficulty of the coding was the minimum generating power constraint, and to solve the optimisation problem, several times PSO and GA codes were run for a program. For example, to decide which generator should be on, codes are run to decide the maximum generating unit, or for adjusting power capacity under wind curtailment. Codes for comparison of costs are inserted to decide the power dispatch. If with power loss, maximum generator limit is exceeded, excess power is dispatch, and codes are re-run. Multiple scenarios are analysed, and with the probabilities obtained from UGF, the total cost is calculated.

Fig. 4 PSO flowchart
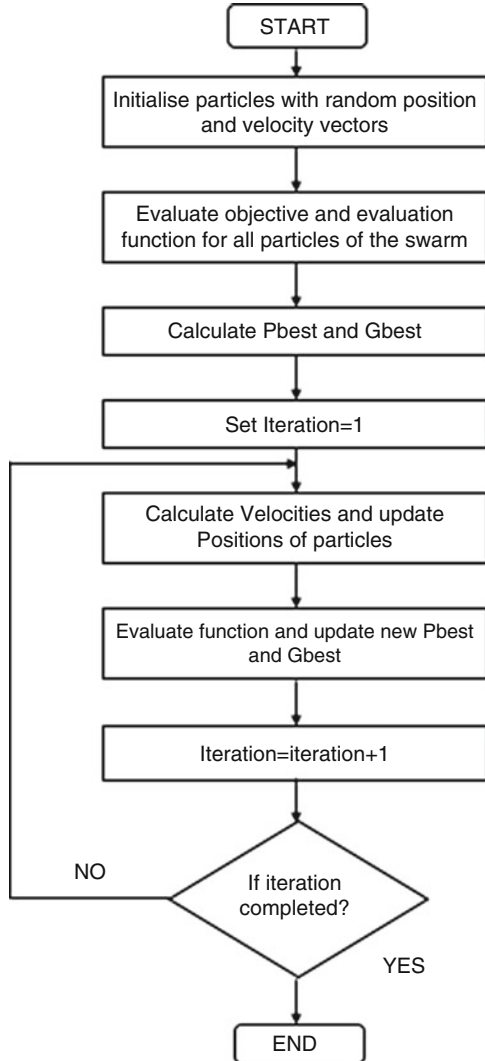
The above methodology applies to both PSO and GA. The coding flowchart is shown in Fig. 5.

5 Results

Unit commitment was solved using genetic algorithm and particle swarm optimisation. For the methods to be comparable, the following criteria were set the same:
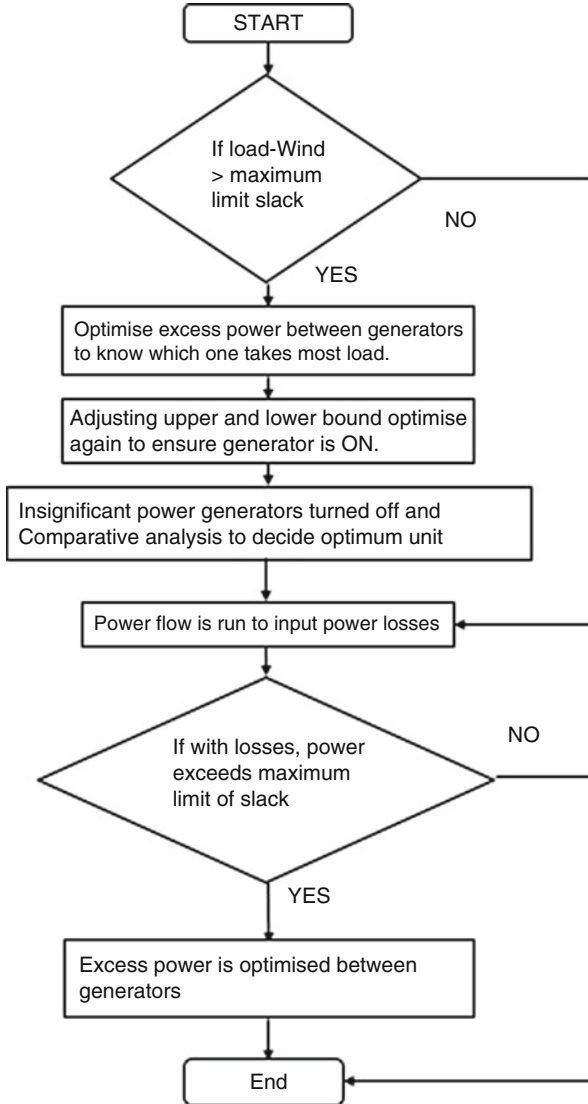
Fig. 5 Coding flowchart

- Maximum iteration
- Number of particles/population size

The codes were written in MATLAB due the ability of implementing Saadat's power flow toolbox [13] with the code. The 6-bus system was solved as a normal unit commitment problem, while the 30-bus system was solved as a security-constrained unit commitment problem. The 30-bus data set was taken from Gaddam [5]. Both

were incorporated with power flow toolbox and wind energy resources, and results, particularly for the 6-bus system, are compared with Wang et al. [15] where the data has been acquired (Refer to Table 9 in the Appendix).

It should be noted that simulations were performed on an Intel(R) Core(TM) i3 CPU, 2.40 Ghz and 3 GB of RAM personal computer.

The following cases have been considered:

  (i) Case 1: 6-bus system with GA
 (ii) Case 2: 6-bus system with PSO
(iii) Case 3: 30-bus system with GA
(iv) Case 4: 30-bus system with PSO

Case 1: 6-Bus System with GA

As shown from Table 2, for hours 1 to 9, generator 1 is sufficient to cater for demand and losses. Generators 2 and 3 are optimised for hours 10–22 because of increased load. For the remaining hours, generator 1 is run only.

Table 2 Unit commitment of generators of 6-bus system with GA

Hour	G1/MW	G2/MW	G3/MW	Production costs/$	Transition costs/$
1	177.57	0	0	2853.96	0
2	167.18	0	0	2712.28	0
3	160.52	0	0	2621.52	0
4	156.47	0	0	2566.33	0
5	156.80	0	0	2570.87	0
6	162.36	0	0	2646.55	0
7	175.56	0	0	2826.64	0
8	193.05	0	0	3065.32	0
9	208.80	0	0	3280.44	0
10	210.60	0	10	3481.60	0
11	220	0	12.30	3650.79	0
12	220	10	10.09	3937.83	300
13	220	10	16.14	4045.10	0
14	220	10	17.63	4071.56	0
15	220	13.11	20.00	4214.95	0
16	220	20.54	20.00	4457.61	0
17	220	20.90	20.00	4469.17	0
18	220	10	12.87	3987.00	0
19	220	10.37	20.00	4125.65	0
20	216.25	10	10	3884.85	0
21	220	10	11.39	3960.69	0
22	210.67	10	10	3808.58	0
23	204.14	0	0	3216.72	0
24	199.80	0	0	3157.42	0
				8.09×10^4	300
Total cost/$					8.39×10^4

Table 3 Unit commitment of generators of 6-bus system with PSO

Hour	G1/MW	G2/MW	G3/MW	Production costs/$	Transition costs/$
1	177.57	0	0	2853.96	0
2	167.18	0	0	2712.28	0
3	160.52	0	0	2621.52	0
4	156.47	0	0	2566.33	0
5	156.80	0	0	2570.87	0
6	162.36	0	0	2646.55	0
7	175.56	0	0	2826.64	0
8	193.05	0	0	3065.32	0
9	208.80	0	0	3280.44	0
10	210.60	0	10	3481.61	0
11	219.94	0	12.22	3648.51	0
12	219.83	0	19.87	3782.92	0
13	219.91	11.23	14.81	4060.57	300
14	219.89	10.08	17.43	4069.06	0
15	219.87	12.86	19.95	4204.25	0
16	219.88	19.99	20.00	4437.84	0
17	219.88	20.32	20.00	4448.86	0
18	219.86	10.04	12.85	3986.16	0
19	219.87	10.21	19.96	4118.12	0
20	216.29	10	10	3718.93	0
21	219.84	10.01	11.46	3960.21	0
22	219.97	0.50	10.41	3633.33	0
23	204.14	0	0	3216.72	0
24	199.80	0	0	3157.42	0
				8.31×10^4	300
Total cost/$					8.34×10^4

Case 2: 6-Bus System with PSO

As shown from Table 3, for hours 1 to 9, generator 1 is sufficient to cater for load demand and losses. The value is obtained from power flow analysis. For hours 10–12, generator 3 is needed to cater for demand, and during peak times, all three generators are run. Since demand and losses are less than generator 1 maximum power limit, the latter is run only at hours 23 and 24.

Case 3: 30-Bus System with GA

As shown in Table 4, wind curtailment occurs at time period 7, 8 and 11 due to the line limit. For hours 1 to 7, power flow analysis finds the value of generator 1. GA is employed for hours 8 to 23.

At the end of iteration, all individuals should have same fitness values as the genetic operators have acted upon the chromosomes. The results are shown in Fig. 6.

Table 4 Unit commitment of 30-bus system with GA

Hour	G1/MW	G2/MW	G3/MW	G4/MW	G5/MW	G6/MW	P wind/MW	Pcurtailed/MW
1	176.97	0	0	0	0	0	44	0
2	165.74	0	0	0	0	0	70.2	0
3	158.83	0	0	0	0	0	76	0
4	154.61	0	0	0	0	0	82	0
5	154.93	0	0	0	0	0	84	0
6	160.61	0	0	0	0	0	84	0
7	183.70	0	0	0	0	0	100	90.98
8	180.38	20.00	0	0	0	0	100	92.35
9	187.51	20	0	0	0	0	78	0
10	200	20.30	0	0	0	0	64	0
11	200	20.10	15.10	0	0	0	100	95.42
12	200	21.65	16.65	0	0	0	92	0
13	200	25.29	20.30	0	0	0	84	0
14	200	27.44	22.44	0	0	0	80	0
15	200	29.66	24.66	0	0	0	78	0
16	200	50.87	15	0	0	0	32	0
17	200	50.16	15	0	0	0	4	0
18	200	24.18	19.18	0	0	0	8	0
19	200	29.00	24.00	0	0	0	10	0
20	200	20.96	15.96	0	0	0	5	0
21	200	23.51	18.51	0	0	0	6	0
22	194.42	20	15	0	0	0	56	0
23	182.63	20	0	0	0	0	82	0
24	199.74	0	0	0	0	0	52	0
Total cost/$								1.4028×10^4

Case 4: 30-Bus System with PSO

From Table 5, with the PSO algorithm, generators 1, 2 and 3 are sufficient and the cheapest way to deliver electricity. Using a limit for power flow on the wind turbine line, wind curtailment occurs at time period 7, 8 and 11. For hours 1 to 8, power flow analysis calculates generator 1's output power.

Figure 7 shows the case for hour 17 where after the 1st initialisation, particles take up entire space:

After the final iteration, the solution space is shown in Fig. 8.

Tables 6 and 7 summarise the results obtained for GA and PSO, respectively. It is found that PSO is slightly better than GA for both test systems. Results for the 6-bus system are comparable to Wang et al. [15].
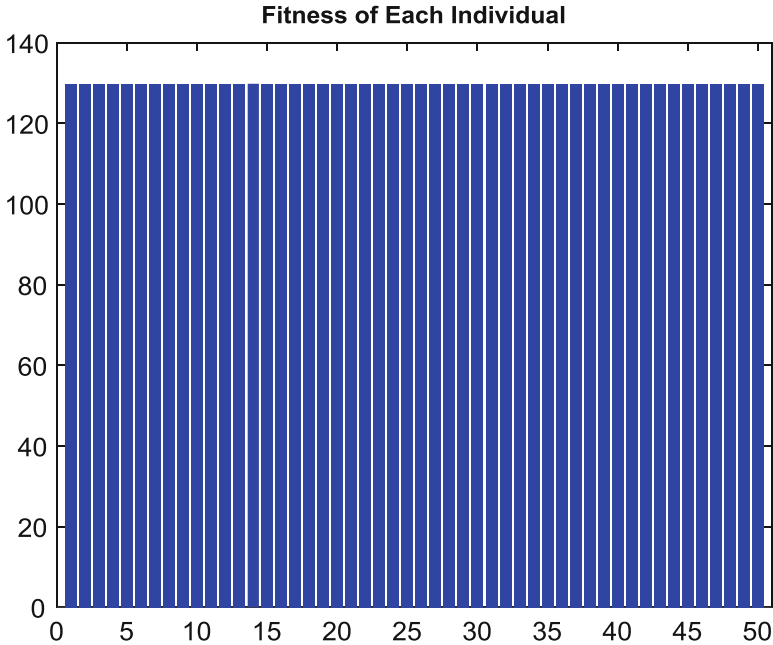
Fig. 6 Final fitness values of individuals

6   Conclusion

The evolutionary methods GA and PSO were successfully applied as an optimisation method in a security-constrained unit commitment with wind energy resource. The two algorithms succeeded in linking with the load flow program to cater for power losses.

For the 6-bus system, unit commitment with transmission losses and with wind power was solved using the two mentioned approaches. Both methods were able to locate the global optimum. It was found that PSO was slightly better than GA in this test system. The 24-hour unit commitment dispatch yielded the same result as Wang et al. [15] for both methods.

For the 30-bus system, security constraint was applied, and PSO was also found to be slightly better than GA. Both unit commitment dispatches yielded nearly the same result. This result also seconds that the algorithms used in the 6-bus system were correct since the same conclusions were drawn.

It can be concluded that the universal generating function (UGF) can effectively model wind power and its associated probabilities.

Table 5 Unit commitment of generators of 30-bus system with PSO

Hour	G1/MW	G2/MW	G3/MW	G4/MW	G5/MW	G6/MW	P wind/MW	P curtail/MW
1	176.97	0	0	0	0	0	44	0
2	165.74	0	0	0	0	0	70.2	0
3	158.83	0	0	0	0	0	76	0
4	154.61	0	0	0	0	0	82	0
5	154.93	0	0	0	0	0	84	0
6	160.61	0	0	0	0	0	84	0
7	183.70	0	0	0	0	0	100	90.98
8	200	0	0	0	0	0	100	92.35
9	187.51	20	0	0	0	0	78	0
10	200	20.30	0	0	0	0	64	0
11	200	20	15	0	0	0	100	95.42
12	200	23.33	15.00	0	0	0	92	0
13	200	29.64	15.02	0	0	0	84	0
14	200	30.91	14.77	0	0	0	80	0
15	200	35.80	16.03	0	0	0	78	0
16	200	43.74	18.34	0	0	0	32	0
17	200	44.98	18.79	0	0	0	4	0
18	200	28.47	15.00	0	0	0	8	0
19	200	34.75	15.88	0	0	0	10	0
20	200	20	15	0	0	0	5	0
21	200	27.09	15.00	0	0	0	6	0
22	194.42	20	15	0	0	0	56	0
23	182.63	20	0	0	0	0	82	0
24	199.74	0	0	0	0	0	52	0
Total cost/$								1.3978×10^4
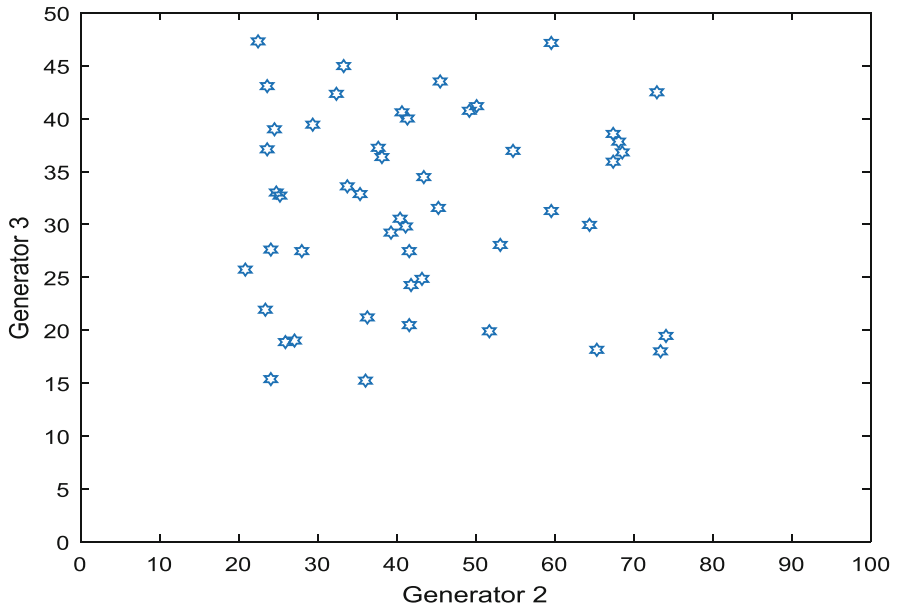
Fig. 7 Initial search space
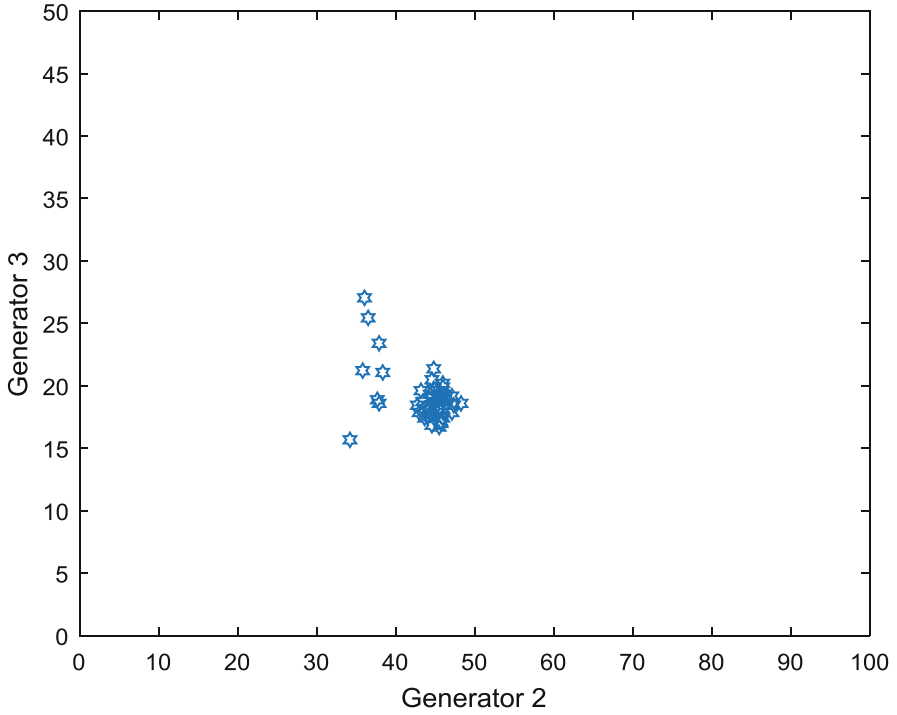
Fig. 8 Final search space

Table 6 Comparison table for 6-bus system

Method	Costs/$
Genetic algorithm	8.39×10^4
Particle swarm optimisation	8.34×10^4

Table 7 Comparison table for 30-bus system

Method	Costs/$
Genetic algorithm	1.4028×10^4
Particle swarm optimisation	1.3978×10^4

Appendix

Table 8 Annual wind speed data

Wind speed limits, m/s	Hours/year	Probability
0–4	1804	0.205936
4–5	579	0.066096
5–6	984	0.112329
6–7	908	0.103653
7–8	983	0.112215
8–9	799	0.09121
9–10	677	0.077283
10–11	439	0.050114
11–12	395	0.045091
12–13	286	0.032648
13–14	219	0.025
14–25	687	0.078425
Greater than 25	0	0

Table 9 Load demand and wind profile

Hour	Power demand/MW	Q demand/MVar	Wind power/MW
1	219.19	50.4	44
2	235.35	47.4	70.2
3	234.67	45.6	76
4	236.73	44.5	82
5	239.06	44.6	84
6	244.48	46.1	84
7	273.39	49.9	100
8	290.40	51.1	100
9	283.56	53.7	78
10	281.20	59.5	64
11	328.61	65.7	100
12	328.10	67.9	92
13	326.18	69.6	84
14	323.60	70.0	80
15	326.86	71.6	78
16	287.79	73.5	32
17	260.00	73.6	4
18	246.74	70.9	8
19	255.97	70.7	10
20	237.35	68.2	5
21	243.31	68.2	6
22	283.14	66.9	56
23	283.05	56.3	82
24	248.75	56.2	52

References

1. Alqunun, K., Guesmi, T., Albaker, A. F., & Alturki, M. T. (2020). Stochastic unit commitment problem, incorporating wind power and an energy storage system. *Sustainability, 12*(23), 10100.

2. Atwa, Y. M., & El-Saadany, E. F. (2011). Probabilistic approach for optimal allocation of wind-based distributed generation in distributions systems. *IET Renewable Power Generation, 5*(1), 79–88.

3. Deb, K. (1999). Introduction to genetic algorithms. *Sadhana - Academy Proceedings in Engineering Sciences, 24*(4–5), 293–315.

4. Ding, Y., Wang, P., Goel, L., Loh, P. C., & Wu, Q. (2011). Long-term reserve expansion of power systems with high wind power penetration using universal generating function methods. *IEEE Transactions on Power Systems, 26*(2), 766–774.

5. Gaddam, R. R. (2013). *Optimal unit commitment using swarm intelligence for secure operation of solar energy integrated smart grid* (Thesis). Power Systems Research Center International Institute of Information Technology.

6. Guo, Z., Zheng, Y., & Li, G. (2020). Power system flexibility quantitative evaluation based on improved universal generating function method: A case study of Zhangjiakou. *Energy, 205*, 117963.

7. Gupta, P. P., Jain, P., Kalkhambkar, V., Sharma, K. C., & Bhakar, R. (2020). Stochastic security constrained unit commitment with battery energy storage and wind power integration. *International Transactions on Electrical Energy Systems, 30*, e12556.

8. Jin, T., Zhou, M., & Li, G. (2017). Universal generating function based probabilistic production simulation for wind power integrated power systems. *Journal of Modern Power Systems and Clean Energy, 5*(1), 134–141.

9. Kazarlis, S. A., Bakirtzis, A. G., & Petridis, V. (1996). A genetic algorithm solution to the unit commitment problem. *IEEE Transactions on Power Systems, 11*(1), 83–92.

10. Li, Y. F., & Zio, E. (2012). *A multi-state model for the reliability assessment of a distributed generation system via universal generating function* (pp. 5–15). Ecole Centrale Paris.

11. Logenthiran, T, & Srinivasan, D. (2010). Particle swarm optimization for unit commitment problem. In *IEEE 11th International Conference on Probabilistic Methods Applied to Power Systems, 2010*, pp. 642–647.

12. Nasrolahpour, E., & Ghasemi, H. (2014). A stochastic security constrained unit commitment model for reconfigurable networks with high wind power penetration. *Electric Power Systems Research*, 341–350.

13. Saadat, H. (2011). *Power system analysis*. PSA Publishing LLC.

14. Senjyu, T., Yamashiro, H., Uezato, K., & Funabashi, T. (2002). A unit commitment problem by using genetic algorithm based on unit characteristic classification. *IEEE Power Engineering Society Winter Meeting, 1*, 58–63.

15. Wang, J., Shahidehpour, M., & Li, Z. (2008). Security-constrained unit commitment with volatile wind power generation. *IEEE Transactions on Power Systems, 23*(3), 1319–1327.

16. Wang, J., Botterud, A., Miramda, M., Monteiro, C., & Sheble, G. (2011). Impact of wind power forecasting on unit commitment and dispatch. *Applied Energy, 88*(11), 4014–4023.

17. Wang, Q., Guan, Y., & Wang, Y. (2012). A chance-constrained two-stage stochastic program for unit commitment with uncertain wind power output. *IEEE Transactions on Power Systems, 27*, 206–215.

Index